STREAK DETECTION AND PHOTOMETRY WITH THE NASA WIDE-FIELD INFRARED SURVEY EXPLORER

DÉTECTION DE TRACES ET PHOTOMÉTRIE AVEC LE SATELLITE NASA WIDE-FIELD INFRARED SURVEY EXPLORER

A Thesis Submitted to the Division of Graduate Studies
of the Royal Military College of Canada
by

Joshua Fitzmaurice, B.Sc.

Flight Lieutenant, Royal Australian Air Force

In Partial Fulfillment of the Requirements for the Degree of
Master of Science in Physics - Space Science

May, 2018

To my family - Clare, Ned and Violet. Thank you. Without your love and support this whole adventure would not have been possible.

Acknowledgements

I would like to thank my supervisor, Major Donald Bédard, for his unwavering support and guidance throughout my time at RMC, and in particular during completion of this thesis. Your enthusiasm, encouragement, patience and friendship are greatly valued.

I would also like to thank Dr. Patrick Seitzer and Chris Lee, from the University of Michigan. Pat and Chris inspired the topic of this thesis through their novel space surveillance research using WISE data, and have provided unending advice and assistance throughout. I look forward to continuing the WISE journey with you.

Finally, I would like to thank members of DRDC - Dr. Martin Lévesque, Dr. Lauchie Scott, Dr. Brad Wallace and Stefan Thorsteinson - for provision of code segments that vastly improved the outcomes of this research. Thank you all for your patience and advice as I slowly comprehended your excellent work.

Abstract

Photometric analysis of Resident Space Objects (RSOs) in the infrared offers some advantage over more prevalent optical analyses; in particular, objects are typically brighter at infrared wavelengths. An algorithm was developed that utilises image background subtraction, pixel connectedness and moments to scan imagery from the NASA Wide-field Infrared Survey Explorer (WISE) mission for the presence of Geostationary (GEO) RSO streaks. NASA WISE scanned the entire infrared sky with a space-based 4m telescope, in four bands at 3.4, 4.6, 12 and 22 μm wavelengths. The algorithm developed in this research allows for automatic photometric measurement of detected streaks in all four bands, and for correlation to satellites, rocket bodies or debris in the public satellite catalogue. In an initial subset of 82,208 WISE images, 1,696 GEO RSO streaks were serendipitously observed and analysed. Multiple infrared bands yielded magnitude and colour index data for these streaks. Preliminary results suggest a correlation between colour index values and several RSO characteristics, including age, size and shape, that shows promise for the utility of infrared sensors for space surveillance. Expansion of this research into almost six million images accessible in the NASA WISE database is planned, to increase the veracity of outcomes and the breadth of data available for analysis.

Résumé

L'analyse photométrique des objets spatials en orbite (OSO) dans l'infrarouge offre certains avantages comparée aux méthodes prévalentes dans la partie visible du spectre électromagmétique. Un algorithme a été développé afin de détecter la présence de traces de satellites en orbite géosynchrone des images acquises avec le télescope spatial de la NASA Wide-Field Infrared Survey Explorer (WISE). Ce télescope, ayant un aperture de 0.4 mètre, a scanné le ciel entier dans quatre bandes de l'infrarouge, soit à 3.4, 4.6, 12 et 22 μm. L'algorithme, élaboré dans le cadre de ce projet de recherche, calcule automatiquement des mesures photométriques des traces de satellites dans les quatre bandes et identifie les objets par l'entremise d'une corrélation entre les détections et les satellites et débris spatiaux dans le catalogue publique d'objets spatiaux. Dans un sous-ensemble initial de 82,208 images acquise par le télescope spatial WISE, un total de 1,696 traces d'OSO en orbite géosynchrone furent détectées et analysées. L'analyse photométrique dans les quatre bandes infrarouges a permis de produit des indices de couleurs pour chacunes des traces détectées. Les résulats préliminaires démontrent une corrélation entre l'indice de couleur et plusieurs caractéristiques des OSS tels que l'age, la dimension, la forme. Ces résultats laissent croire un avenir prometteur pour l'utilisation de capteurs infrarouges pour des missions de surveillance de l'espace. L'expansion de cette recherche à une analyse complète de la banque d'image WISE, qui contient presque 6 millions d'images, est prévue afin de confirmer les conclusions de la recherche présentées dans cette thèse.

Contents

List of Tables

List of Figures

List of Acronyms

CCD	Charge Coupled Device
DEC	Declination
DRDC	Defence Research and Development Canada
FIR	Far Infrared
FITS	Flexible Image Transport System
GEO	Geostationary Orbit
HEO	Highly Elliptical Orbit
IPAC	Infrared Processing and Analysis Center
IR	Infrared
ITU	International Telecommunications Union
LEO	Low Earth Orbit
LWIR	Long-Wave Infrared
MEO	Medium Earth Orbit
MWIR	Mid-Wave Infrared
NaN	Not-A-Number
NIR	Near Infrared
RA	Right Ascension
RSO	Resident Space Object
SNR	Signal-to-Noise Ratio
SSA	Space Situational Awareness
SSM	Sidereal Stare Mode
STK	Systems Tool Kit
SWIR	Short-Wave Infrared
TLE	Two-Line Element
TRM	Track Rate Mode
WISE	Wide-field Infrared Survey Explorer
WISEstreakDET	WISE Streak Detection

1 Introduction

1.1 Background

The first artificial satellite to be placed in orbit around the Earth, Sputnik 1, was launched in October of 1957. The following decades witnessed a tremendous growth in launches, heralding the now ubiquitous use of space. Satellites, however, account for only 7% of tracked space objects - the number of rocket bodies, fragments and other debris associated with the launch of satellites is growing at an unprecedented rate. Over 21,000 objects greater than 10cm in diameter are tracked and catalogued, while the number of smaller, non-traceable objects is estimated to be in the millions [1]. This has resulted in a cloud of near-Earth debris, depicted in Figure 1.1, that has the potential to damage or destroy operational space-based assets.
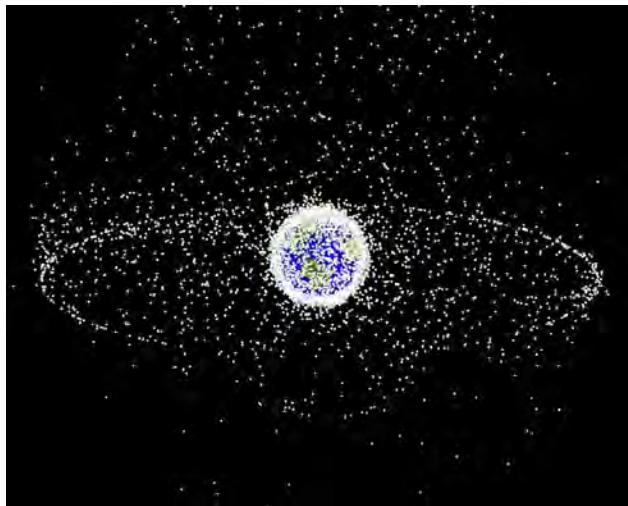
Figure 1.1: Depiction of tracked objects in orbit around the Earth, approximately 95% of which are debris [2].

The world has become increasingly reliant upon the services delivered by space-based assets. Position, Navigation and Timing (PNT) satellites such as GPS not only deliver pinpoint location information to billions of people, but also time synchronisation functions critical to banking, power and other industries [3]. Communication and entertainment, weather observation, and remote sensing are further examples of space-based services. The military also heavily replies upon these, in addition to utilising space for Intelligence, Surveillance and Reconnaissance (ISR). The protection of space-based assets, therefore, is essential. To achieve this, knowledge of potential threats must be gained.

Threats to space-based assets come in two forms: accidental, and deliberate. The risk of deliberate threat to assets has already been realised. In 2007, China launched an Anti-Satellite (ASAT) missile at Fengyun-1C, its own weather satellite. This military demonstration created an unprecedented debris field, with close to 3,500 pieces large enough to be tracked, and hundreds of thousands more estimated to be of non-traceable size [4, 5]. The rapidly increasing population of RSOs, travelling at speeds in excess of 3 km/s, has raised the probability of accidental conjunction - that is, two objects colliding. This risk was realised in 2009, when the US Iridium 33 and retired Russian Kosmos 2251 communication satellites collided at a relative velocity of 11.7 km/s [5]. This collision created a debris field of more than 2,000 large objects, resulting in damage to space assets, and forcing the International Space Station (ISS) to take collision avoidance measures.

This reliance upon Earth-orbiting RSOs, and their proliferation in the days since Sputnik 1, has driven a need for their observation - the genesis of space surveillance, or Space Situational Awareness (SSA). SSA focuses upon the ability to detect RSOs, calculate their orbit (position and velocity), and to perform some level of identification [6]. Such information may assist in avoiding further RSO conjunctions, by allowing active satellites to conduct collision-avoiding manoeuvres. Current efforts to remove debris from orbit, such as the experimental REMOVEdebris mission equipped with nets and harpoons to capture and de-orbit debris, will also benefit from precise debris location and characteristic data [7].

Infrared sensors have shown promise to contribute to these SSA efforts, building upon similar work performed by the many optical telescopes located at sites across the globe [6]. Enhanced determination of RSO location, status and identifying characteristics may be offered, due to the combination of reflected and thermal energy at wavelengths outside of the visible spectrum.

By way of example, Figure 1.2 shows the M51 'Whirlpool Galaxy' in five different bands of the electromagnetic spectrum. It is clear that for the same object, different wavelengths of observation provide distinctive information. It is hoped that infrared sensors may do the same for observations of RSOs.

(a) X-Ray   **(b)** Visible   **(c)** Near-IR   **(d)** Mid-IR   **(e)** Far-IR
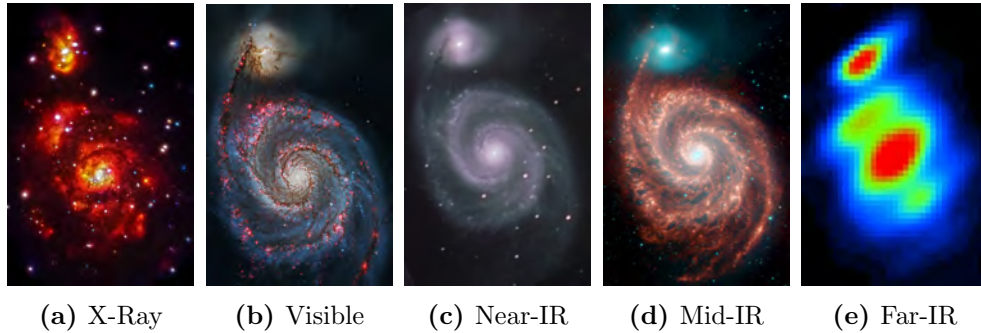
Figure 1.2: A demonstration of the distinct information presented by observations in different wavelengths. Images are of the M51 Whirlpool Galaxy [8].

This chapter will seek to provide an understanding of the requisite theory that will be discussed and utilised throughout the remainder of this thesis.

1.2   Electromagnetic Spectrum

The infrared (IR) electromagnetic spectrum is divided into several bands, the definitions of which vary according to context and author. There is also often overlap between the visible and IR bands. For the purposes of this thesis, the definitions shown in Table 1.1 will be utilised [9, 10]. Near Infrared (NIR) and Short-Wave Infrared (SWIR) are often grouped together as reflected IR, while longer IR wavelengths are known as thermal IR. Observations in the visible spectrum will be referred to as optical.

Band	Subdivision	Wavelength (μm)
Optical	-	0.40 - 0.70
Reflected	Near Infrared (NIR)	0.70 - 1.40
Infrared	Short-Wave Infrared (SWIR)	1.40 - 3.00
Thermal	Mid-Wave Infrared (MWIR)	3.00 - 8.00
Infrared	Long-Wave Infrared (LWIR)	8.00 - 15.00
	Far Infrared (FIR)	15.00 - 1000

Table 1.1: Visual and infrared band definitions [9, 10].

A common filter system used in astronomical observations is the Johnson-Cousins-Glass standard photometric system of filters. When referring to these filters, their wavelengths are as shown in Table 1.2 [11].

Filter	λ_{eff} (μm)	λ_{range} (μm)	Filter	λ_{eff} (μm)	λ_{range} (μm)
U	0.366	0.30 - 0.43	**J**	1.22	1.01 - 1.43
B	0.438	0.35 - 0.53	**H**	1.63	1.32 - 1.94
V	0.545	0.46 - 0.63	**K**	2.19	1.80 - 2.58
R	0.641	0.48 - 0.80	**L**	3.45	2.98 - 3.92
I	0.798	0.64 - 0.95	**M**	4.74	4.29 - 5.21

Table 1.2: The Johnson-Cousins-Glass standard photometric system of filters [11].

When comparing the respective abilities of optical and IR sensors for use in SSA, an awareness of how electromagnetic energy is attenuated by the atmosphere is required. Figure 1.3 shows the typical percentage of energy, or flux, that is transmitted through the atmosphere at different wavelengths for a specific observatory. Atmospheric windows exist within which transmission percentages are high comparable to neighbouring wavelengths. Telescope sensor design is able to benefit from selecting bandwidths in these atmospheric windows, where attenuation is minimised. For both reflected and thermal infrared wavelengths, it can be seen that atmospheric transmission levels vary greatly - at 1μm for example, approximately 90% of IR energy makes its
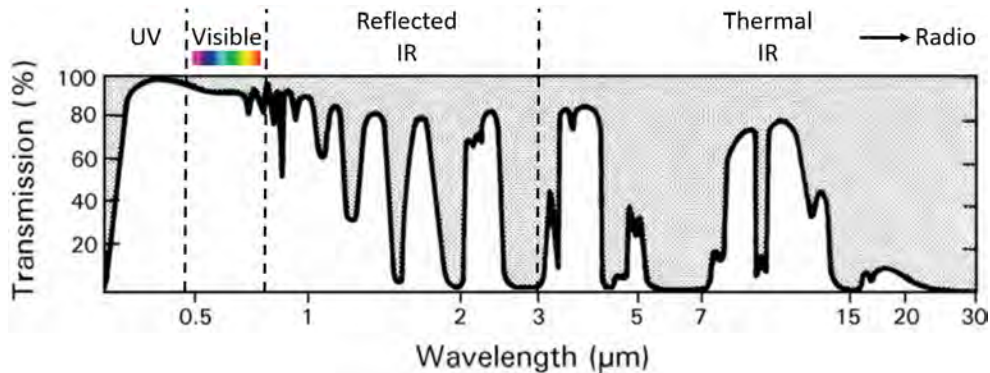
Figure 1.3: Atmospheric windows (adapted from [12]).

way through the atmosphere to ground-based sensors, while almost all of the infrared energy with wavelengths near 6μm is attenuated.

If infrared observations at highly attenuated wavelengths is desired, sensors need to be at high altitude where the atmosphere is thin, or in space. Observatories are located on high mountain peaks, such as the Infrared Telescope Facility on Mauna Kea, Hawaii. Infrared sensors are also placed in airborne observatories, such as the NASA Stratospheric Observatory for Infrared Astronomy (SOFIA). Flying at altitudes of 45,000 feet, SOFIA avoids much of the attenuation of longer wavelengths, with average transmission rates of around 80% observed at wavelengths greater than 0.3 μm [13].

To avoid atmospheric attenuation altogether, however, observatories must be placed into orbit. While space-based optical observations have been popularised by the famous Hubble telescope, many infrared missions have also been launched. The NASA Wide-Field Infrared Survey Explorer (WISE), launched in 2009 and the focus of this thesis, is one such system. WISE will be presented in detail in Chapter 2.

1.2.1 Irradiance, Emissivity and Temperature

RSOs may be observed due to the energy that they reflect, and energy that they emit. Reflected energy is typically supplied by the Sun - upon contact with an RSO, some of this energy will be absorbed, and some reflected. If a component of that reflected energy is toward an observing sensor, it may be detected. For any object that is warmer than absolute zero ($0°$K), energy will also be emitted [14]. The amount of energy emitted is dependent upon both the wavelength of observation, and temperature of the object being observed.

This relationship was observed by Max Planck early in the twentieth century, and is given by Planck's radiation equation, shown in Equation 1.1 [15]. Here, S is the amount of irradiated energy, h is Planck's constant (6.626×10^{-34} Js), T the object temperature in kelvin, λ the wavelength of observation, c the speed of light in metres per second, and k the Boltzman constant (1.381×10^{-23} JK^{-1}).

$$S(\lambda, T) = \frac{2\pi hc^2}{\lambda^5 \left(e^{hc/\lambda kT} - 1\right)} \tag{1.1}$$

For an object at a given temperature, the wavelength at which irradiance peaks is given by Equation 1.2, where T is temperature in kelvin [15]. This is determined by setting the differentiation of Plank's radiation equation to zero, and is known as Wien's displacement law. This law tells us that the warmer an object is, the shorter its wavelength of peak irradiance. This relationship may be observed in Figure 1.4 [14], which plots Planck's radiation equation as a function of varying wavelength for different temperatures.

$$\lambda_{max} = \frac{2.898 \times 10^{-3}}{T} \tag{1.2}$$
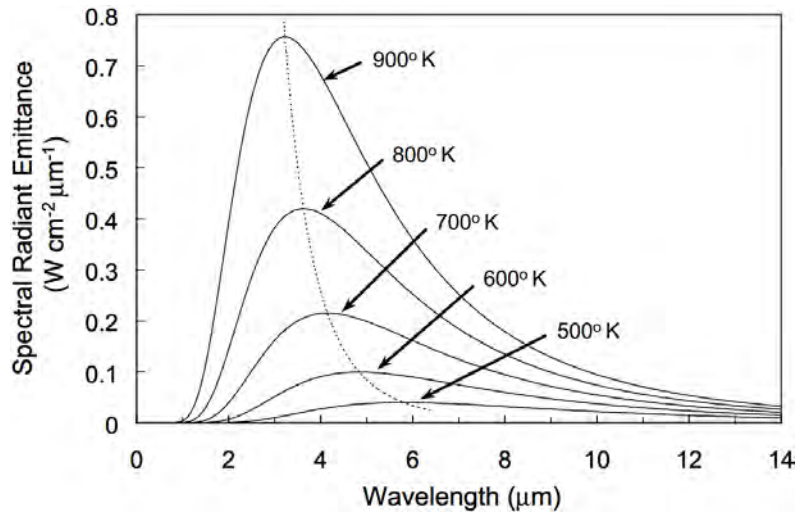
Figure 1.4: Planck's radiation equation, showing the change in irradiance with variance in wavelength. Peak irradiance varies, depending upon the temperature of the object, per Wien's displacement law [14].

Both Planck's radiation equation, and Wien's displacement law, are based upon the object in question being a blackbody. A blackbody is an ideal emitter - that is, it converts heat energy to radiant energy with maximum efficiency [15]. However, in reality most objects do not emit energy at maximum efficiency. The measure of an objects ability to efficiently emit energy is known as emissivity (ε), and is determined by the ratio of energy emitted by an object (S'), compared to the energy it would emit as a blackbody (S), per Equation 1.3 [15]. Emissivity is therefore a value between zero and one, with one being a perfect emitter (blackbody). If the emissivity of an object is a constant < 1 over all wavelengths, that object is said to be a greybody; if emissivity varies with wavelength, as it does for most objects, it is said to be a selective emitter [14]. This concept is diagrammatically represented in Figure 1.5.

$$\varepsilon(\lambda) = \frac{S'(\lambda, T)}{S(\lambda, T)} \qquad (1.3)$$
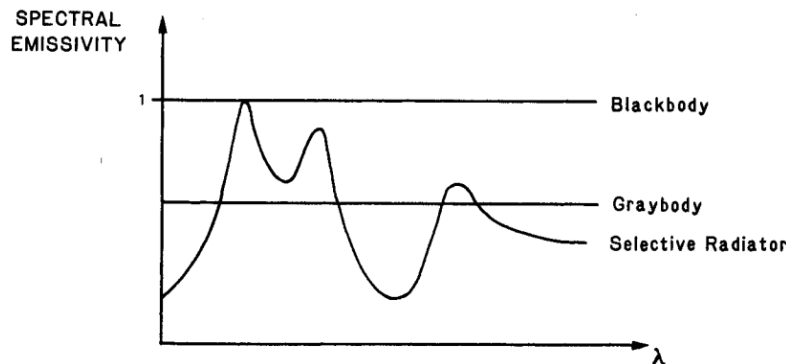
Figure 1.5: An object that perfectly converts heat energy to radiant energy is known as a blackbody, with emissivity = 1. An object with emissivity < 1 though constant at all wavelengths is a greybody, while if emissivity varies with wavelength the object is a selective emitter [14].

When considering the thermal infrared wavelengths observed by WISE, the concept of Planck's radiation equation, combined with irradiance measurements of an RSO, may be applied to determine the brightness temperature (T_B) of that object. For an object with irradiance S at a specific wavelength λ, T_B is the equivalent temperature at which a blackbody would also emit irradiance S. T_B is determined by Equation 1.4; if the emissivity of the object is known, its true temperature (T_T) is also able to be determined via

Equation 1.5 [15]. Both T_B and T_T are useful characteristics that allow for characterisation of RSOs.

$$T_B = \frac{hc}{\lambda k} \cdot \frac{1}{ln[\frac{2\pi hc^2}{S'(\lambda,T)\cdot\lambda^5)} + 1]} \tag{1.4}$$

$$T_T = \frac{hc}{\lambda k} \cdot \frac{1}{ln[\frac{\epsilon 2\pi hc^2}{S'(\lambda,T)\cdot\lambda^5)} + 1]} \tag{1.5}$$

1.3 Infrared Sensors

To understand the method by which sensors such as those aboard WISE observe infrared energy, a comparison to the ubiquitous Charge Coupled Device (CCD), used as a detector in the visible portion of the electromagnetic spectrum, is useful.

1.3.1 Comparison to the Charge Coupled Device (CCD)

CCDs are constructed as an array of pixels, in columns and rows, with each pixel consisting of a semiconducting silicone substrate. On top of each pixel are a number of electrodes called gates [16]. A simplified CCD pixel layout is shown in Figure 1.6a. When a photon with sufficient energy is incident upon a pixel within a CCD array, the photoelectric effect is observed. An electron within the silicon substrate is able to break its covalent bond, and jump the band gap to move from the valence band into the conduction band, as illustrated in Figure 1.6b (adapted from [9]).

An electron will only be freed from the valence band if it is supplied energy greater than the energy difference between the top of the valence band and bottom of the conduction band, known as the band gap energy (E_G) [9]. An incident photon is only able to supply this energy if its wavelength is less than the cutoff wavelength criterion, shown in Equation 1.6 [9], where h is Planck's constant, c the speed of light, and λ_c the cutoff wavelength. For silicon, E_G = 1.14 electron volts (eV); therefore, as shown by the workings of Equation 1.7, incident photons can have wavelengths of no longer than 1.11 μm if the photoelectric effect is to occur in a CCD with silicon substrate. While this

8

(a) A simplified CCD pixel layout is shown, consisting of a semiconducting silicone substrate on top of which lies a number of electrodes called gates.

(b) An electron is shown jumping from the valence band to the conduction band of silicon when a photon is incident (adapted from [9]).
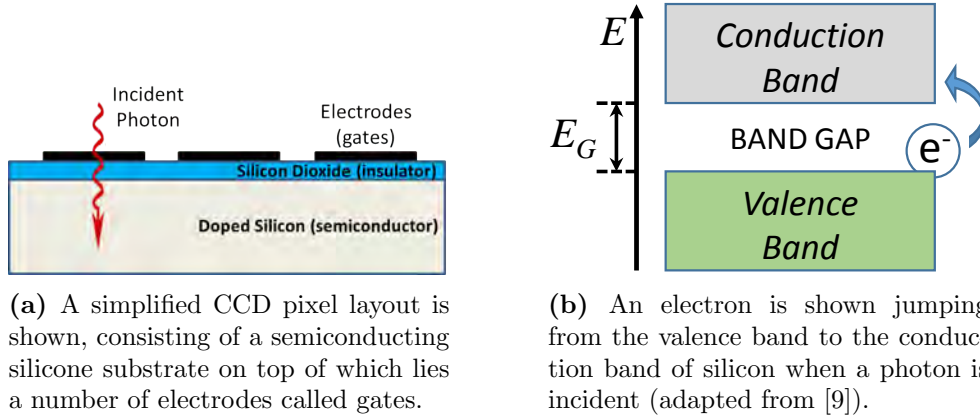
Figure 1.6: Illustration of the photoelectric effect within a CCD array.

may allow for some observations in the NIR, observations of longer infrared wavelengths are not achievable.

$$\lambda_c = \frac{hc}{E_G} \tag{1.6}$$

$$\lambda_c = \frac{1.24\mu m}{1.14 eV} = 1.11\mu m \tag{1.7}$$

To allow observations in the longer infrared wavelengths, changes to the CCD design seen in Figure 1.6a are required. CCDs use silicon as the substrate material, however alternate materials achieve a different band gap between the valance and conduction bands of the semiconductor [17]. Due to the different values of E_G that are found in varying substrate materials, the cutoff wavelength of incident light will change per Equation 1.6. Materials with smaller band gaps (and therefore smaller values of E_G) are sought for longer wavelengths being observed.

Near infrared detectors have made use of indium antimony (InSb) and mercury-cadmium telluride (HgCdTe, often referred to as MCT) photodiodes for observations in the 0.6 - 5 μm bandwidth. Mid and long-wave infrared detectors dope with other elements, such as antimony (Si:Sb) or arsenic (Si:As) for observations in the 5 - 28 μm bandwidth. In the far infrared, germanium doped with various impurity elements (Ge:Ga, Ge:B, Ge:Sb) are used to achieve observations up to cutoff wavelengths of 190 μm.

Two types of noise - unwanted additional electrons in the system - are introduced within both CCD and infrared detector systems. The first is read noise, where charge is introduced during the conversion of signal from analogue to digital, and from the workings of electronic components [16]. The second is dark current, whereby electrons are freed from the valence band due to heat within the system. To minimise dark current, infrared detectors in particular often required active cooling.

Dark current is higher in infrared sensors, due to the reduced band gap of materials used in order to achieve higher cutoff wavelengths, per Equation 1.6. This reduced band gap means that lower levels of energy are required to free electrons. To counteract this, cooling of instrumentation is required - the longer the wavelength of observation, the smaller the band gap and therefore the more cooling required. Rieke [17] gives examples of near-infrared sensors cooled to 78 K, mid-wave infrared sensors to 18 K, and far-infrared sensors as low as 6.7 K. By comparison, CCDs utilised by the Gemini Optical Observatory are cooled to just 170 K [18]. This level of cooling comes at great financial penalty to the design, operation and maintenance of infrared sensors.

Another disadvantage of infrared sensors when compared to optical is reduced spatial resolution. Spatial resolution may be defined as the minimum angular separation of two objects that allows them to be individually resolved. To determine the spatial resolution of a telescope, the Rayleigh Criterion is applied, which states that the centre of two Airy discs produced by individual light sources must be separated by at least the angular radius of those Airy discs (α_A) [9]. α_A may be calculated from Equation 1.8, and is dependent upon the diameter of the telescope aperture (D) and the wavelength of incident energy (λ).

Consider a 4 m telescope with optical sensor viewing energy centred at 0.55 μm, compared to a 4 m telescope with infrared sensor viewing energy centred at 6.0 μm. Spatial resolution calculations for the optical sensor and infrared sensor are shown in Equations 1.9 and 1.10 respectively. It can be seen that the optical sensor is able to resolve objects approximately $0.035''$ apart, while the infrared sensor requires objects to be almost 10-times further separated ($0.38''$). This spatial resolution limit is known as the diffraction-limit, as the Rayleigh-criterion is based upon the diffraction of a planar wavefront of light by a circular telescope aperture [9]. However it does not tell the whole story - optical telescopes are often not able to resolve objects as well as the diffraction-limit suggests. Instead, they are usually limited by atmospheric conditions. This is referred to as seeing, where a loss of spatial resolution

occurs due to the disturbance of the planar wavefronts of light by atmospheric turbulence and molecular interaction [9]. Longer infrared wavelengths are typically not as affected by atmospheric conditions (seeing), and are often able to achieve observations near or at the limit of diffraction [19]. This then means that although theoretically optical telescopes are capable of much higher spatial resolutions than infrared, they are seeing-limited, reducing much of the theoretical advantage.

$$\alpha_{\mathrm{A}} = \frac{1.22\lambda \times 206,265}{\mathrm{D}} \quad \text{[in arcseconds]} \tag{1.8}$$

$$\begin{aligned} \alpha_{\mathrm{A}} &= \frac{(1.22)(0.55 \times 10^{-6})(206,265)}{4} \\ &= 0.035'' \end{aligned} \tag{1.9}$$

$$\begin{aligned} \alpha_{\mathrm{A}} &= \frac{(1.22)(6.0 \times 10^{-6})(206,265)}{4} \\ &= 0.38'' \end{aligned} \tag{1.10}$$

1.3.2 Digital Imagery

Once an infrared sensor is exposed to a source of flux a digital image is formed. This image is made of a number of rows and columns of pixels, each with a different value determined by the amount of photons incident upon their surface during the exposure time. As such, an infrared image is much like an image captured with a CCD camera in visible wavelengths. The different images, however, present the same object differently. See Figure 1.7, in which a garbage bag is opaque in a visible image, and transparent in an infrared image [8]. Conversely, the man's glasses allow transmission of visible wavelengths to the camera, while blocking infrared energy.

Infrared detectors differ in another important way from CCDs: the read-out method. The gates on each pixel within a CCD store incident photons throughout the image exposure time. Then, one column at a time, these photons are shifted down from pixel to pixel, and a count made upon reaching a register at the bottom. Counting pixel values is this manner often results in energy losses and error.

Infrared sensors typically retain the use of silicon in readout segments, due to the low cost and complexity of manufacturing with this material. However,

(a) Visible image.
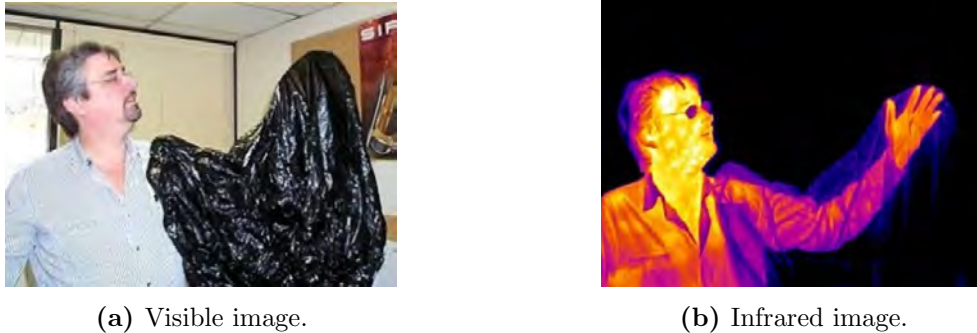
(b) Infrared image.

Figure 1.7: A comparison of visible and IR digital images shows the different information offered by each [8].

each pixel contains its own silicon readout amplifier, bonded to the chosen infrared sensitive substrate material for detection of photons [9, 17]. The result is that each pixel is read out individually. This carries certain advantages over the CCD transfer process - photon saturated pixels do not spill into other pixels, avoiding streaks from blooming, and dead pixels do not impact whole columns or rows [9].

1.4 Orbits

To understand how a space-based asset such as WISE is able to make observations of other RSOs, an examination of the various orbital regimes into which satellites are placed is required.

1.4.1 Orbital Regimes

Orbits may be classified by type, according to various different criteria. A simple, convenient and frequently used classification is by altitude. These regimes are summarised in Table 1.3, and shown in Figure 1.8. Altitude refers to height above the surface of the Earth at the equator. Orbital radius, meanwhile, refers to the distance between a satellite and the Earth's centre.

Regime	Altitude (km)
Low Earth Orbit (LEO)	160 - 2,000
Medium Earth Orbit (MEO)	2,000 - 35,486
Geostationary Orbit (GEO)	35,486 - 36,086
Highly Elliptical Orbit (HEO)	Apogee > 36,286

Table 1.3: Summary of the four main orbital regimes [20, 21].
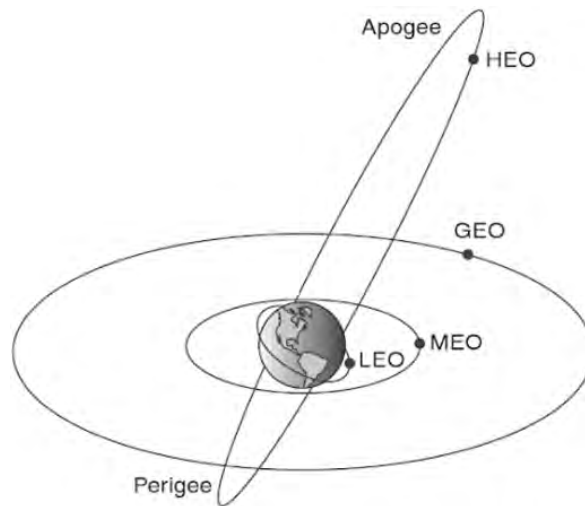
Figure 1.8: The four main orbital regimes, classified by altitude [22].

Although officially ranging from 160 - 2,000km, satellites in LEO are typically placed above 300km due to the significant atmospheric drag experienced below this altitude [20]. Drag removes energy from the satellites orbit, causing decay, or a lowering of orbital altitude. Above 1,000km, the upper atmosphere becomes sufficiently thin for drag effects to be considered negligible.

MEO extends from LEO, to the lower limit of the GEO region. The most well-known occupants of the MEO regime are spacecraft providing PNT services, such as GPS satellites. GEO is a special type of geosynchronous orbit, in which satellites share the same period of rotation as the Earth. For this reason, satellites in GEO appear to remain stationary over the same location on Earth, making them ideal for communication and broadcast services.

The radius (r) of GEO may be derived by starting with the known parameter of orbital period T, being equal to one sidereal day: 23 hours 56 minutes, or 86,164 seconds. Equation 1.11 is then used, along with Earth's gravitational parameter (μ) which equals 398,600 km^3/s^2 [23]. The orbital radius of 42,164 km corresponds to an orbital altitude of 35,786 km after subtracting the equatorial Earth radius (6,378 km). The International Telecommunications Union (ITU) allows a 300 km buffer either side of 35,786 km for the definition of GEO, giving the figures shown in Table 1.3.

$$
\begin{aligned}
T_{\text{sidereal day}} &= \frac{2\pi}{\sqrt{\mu}} \, r^{3/2} \\
\Rightarrow r &= \left(\frac{\sqrt{\mu}}{2\pi} \, T \right)^{2/3} \\
&= \left(\frac{\sqrt{398,600 \text{ km}^3/\text{s}^2}}{2\pi} \, (8.6164 \times 10^4 \text{ seconds}) \right)^{2/3} \\
&= 42,164 \text{ km}
\end{aligned}
\tag{1.11}
$$

The Inter-Agency Space Debris Coordination Committee (IADC) guidelines for space debris mitigation [24] state that the region extending 200 km above and below GEO is protected. This is done with the aim of preservation for safe and sustainable use. With this aim in mind, there are strict guidelines for the disposal of satellites upon their retirement. A 'graveyard orbit' is defined as 235 km above GEO, with the additional 35 km above the protected region allowing for orbital perturbations of retired satellites. Following these guidelines, the vast majority of GEO satellites are moved to the graveyard orbit upon retirement.

Finally, satellites with Highly Elliptical Orbits (HEO) are defined as having their highest point of orbit (the apogee) at least 200 km above GEO [20]. Due to the highly elliptical nature of these orbits, the point of lowest orbital height (perigee) often encroaches upon the LEO regime. HEO satellites have variable orbital velocity due to Kepler's second law of planetary motion, which states that orbits sweep out equal areas in equal lengths of time. The lowest orbital velocity is realised at apogee, which allows for extended dwell times over particular points on Earth.
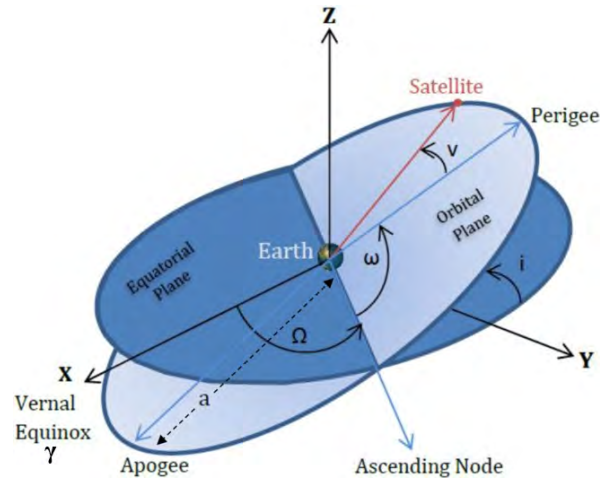
Figure 1.9: Pictorial representation of the six classical orbital elements [25].

1.4.2 Orbital Elements

Orbits may also be defined by a set of parameters, shown in Figure 1.9 [25]. These classical orbital elements combine to define the position of a satellite in space, as well as the shape, size and orientation of its orbit [26].

The first three parameters are used to define the orientation of the orbital plane, with reference to the equator and vernal equinox (γ). The vernal equinox may be defined as the point at which the plane of Earth's orbit around the Sun crosses the equator from south to north. Inclination (i) refers to the angle between the orbital and equatorial planes. The Right Ascension of the Ascending Node (Ω) is the angle between the vernal equinox, and the point at which the satellite orbit crosses the equatorial plane from south to north (the ascending node). The argument of perigee (ω) is the angle between the ascending node and the orbit perigee.

The next two parameters define the shape of the orbit. Eccentricity (e) simply refers to the ratio of orbit length and width - a value of zero is a perfectly circular orbit, elongating as values approach one. The semi-major axis (a) is defined as half of the elliptical orbit length.

The final parameter, true anomaly (ν), gives the current location of the satellite within its orbit, and is defined as the angle from perigee to the satellite, along the orbital plane.

1.4.3 Orbital Perturbations

Orbital dynamics in its simplest form assumes that the motion of a satellite around Earth is the product of their interacting gravitational fields [20]. The reality, however, is much more complex. Several disturbing forces act upon the satellite, known as perturbations, affecting its orbital parameters.

Figure 1.10 shows some of the major perturbing forces that act upon satellites, and how these forces vary with altitude [27]. As previously discussed, atmospheric drag is a prevailing force acting upon satellites in LEO, particularly below 500 km. As altitude increases above 500 km, variations in the Earth's gravitational field become the predominant perturbing force. The Earth is not a perfect sphere, but an oblate spheroid - it is around 20 km wider at the equator than at the poles. Gravitational acceleration therefore varies depending upon the satellite's location above the Earth, resulting in a constantly changing orbit [20]. To a lesser extent, the gravitational fields of other bodies also exert force upon satellites in orbit. The Moon, due to its proximity, and the Sun, due to its large gravitational field, are most influential, however other planets also minimally perturb orbits. Radiation pressure may be considered as a force exerted by photons, emitted by the Sun and planets, impacting and reflecting away from a satellite.

While this is not an exhaustive list of the disturbing forces exerted upon a satellite, it is clear that orbital parameters are constantly changing as a result of perturbations. This adds complexity to the task of space surveillance, as a level of uncertainty will always exist when predicting the position of an RSO for observation purposes.

1.4.4 Reference Frames

The classical orbital elements, as shown in Figure 1.9, are based upon a reference frame which places the Earth at its centre. Such frames of reference are known as Earth Centred Inertial (ECI), or Geocentric Inertial (GCI) [20]. Taking this concept further, imagine a sphere surrounding the Earth, upon which objects in the sky appear to be positioned. This is known as the celestial sphere, where north and south poles are aligned with the Earth's, as shown in Figure 1.11 [23]. The celestial equator is a plane that extends from the Earth's equator to the celestial sphere. Using this frame, a coordinate system for the position of objects in the sky may be defined. The science of providing accurate positional information for astronomical objects, using such coordinate systems, is known as astrometry.
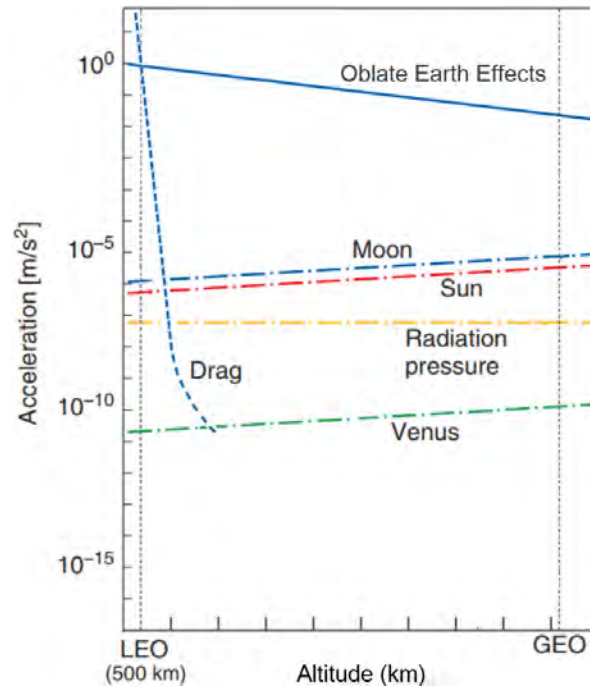
Figure 1.10: Disturbing forces acting upon a satellite in orbit, as a function of altitude (adapted from [27]).

The angle measured eastward from the vernal equinox (γ) along the celestial equator to an object is known as the right ascension (RA, or α). RA is measured in hours, rather than degrees, where 24 hours is equivalent to 360 degrees. The north-south angle between the celestial equator and an object is known as declination (DEC, or δ), and is measured in positive degrees to the north, negative to the south.

Specific cases of ECI reference frames exist, their use dependent upon the field of application. The J2000 reference frame, for example, is an ECI frame using the position of the celestial equator and vernal equinox as they existed at noon on January 1st, 2000 [23]. The True Equator, Mean Equinox (TEME) frame, used by the United States when reporting space object positions, differs from J2000 in that it uses an alternate, 'uniform' position of the vernal equinox [26].
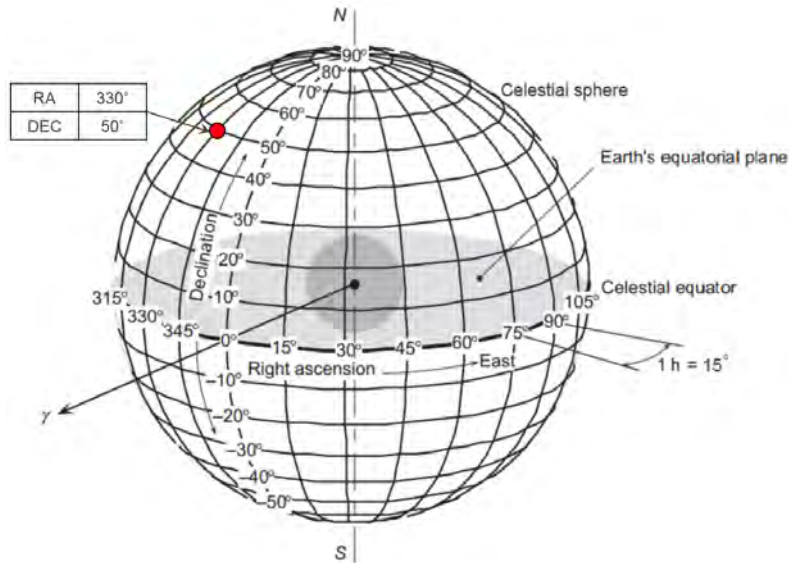
Figure 1.11: An Earth Centred Inertial (ECI) frame of reference, showing the right ascension and declination coordinate system (adapted from [23]). A red dot shows an example of a space object, with position in RA and DEC.

1.5 Surveillance of Space

Space surveillance consists of an ability to detect RSOs, calculate their orbit (position and velocity), and to perform some level of identification. This section will describe the conduct of these activities.

1.5.1 Sensor Types

The primary sensors contributing to SSA are radar and optical. Radar surveillance systems consist of a transmitter that emits radio waves, some of which reflect from an RSO, to be measured by a receiver [6]. More recently, passive radar technology is also employed for SSA, whereby non-cooperative sources of energy such as television and radio towers are used as the source of transmitted energy [28]. Radar systems, unlike optical, are able provide range measurements. However, the high cost of development and sustainment make wide-scale distribution of sensors prohibitive. Detection and tracking of RSOs beyond 5000km in altitude also becomes overly complex [6].

Optical and infrared sensors typically consist of a focal plane array, that directs incident energy onto a detector. The primary disadvantage of optical

18

and infrared sensors, as previously discussed, is the attenuation of energy by the atmosphere at various wavelengths. Placing an infrared sensor in space, as with WISE, therefore provides an ideal opportunity to observe RSOs in orbits higher than LEO.

The remainder of this section will focus on optical observation, which may be considered similar to infrared. As radar is not the focus of this thesis, its theory or application to space surveillance will not be further discussed.

1.5.2 Illumination and Observation Geometry

The principle of optical SSA observations may be described as the measurement of photon flux, as a result of sunlight reflecting off the surface of an RSO. The angles involved in this transmission of light, and its reflectance off the RSO toward a sensor, are shown in Figure 1.12 [29]. θ_{obs} and θ_{sun} are the azimuth angles (x-y plane) to the sensor (observer) and the Sun, respectively. ϕ_{obs} and ϕ_{sun} are the zenith (z-plane) angles. These definitions place the RSO as the frame of reference - as the RSO moves in its orbit, the angles to Sun and sensor constantly change [29].
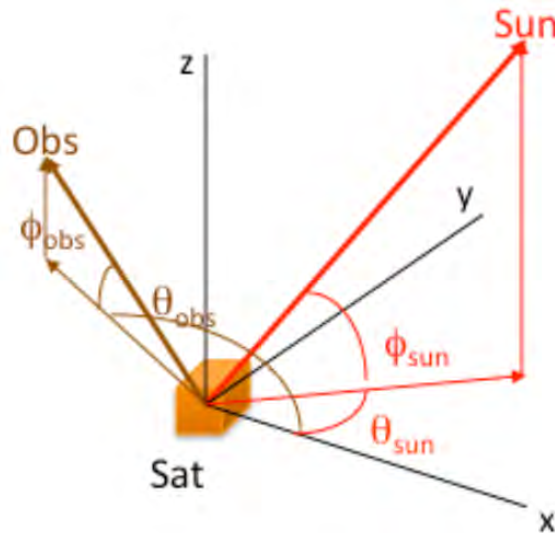
Figure 1.12: The four angles involved in solar illumination and observation geometry are shown [29].

This Sun-RSO-sensor geometry requires knowledge of the RSO shape and attitude, in order to understand the direction in which light is reflected. As

these RSO parameters are often not known, a simplified Sun-RSO-sensor geometry may be used. This simplified model replaces the four angles shown in Figure 1.12 with one - the angle between the sensor and Sun, from the point-of-view of an observed RSO. This is known as the phase angle, an example of which is shown in Figure 1.13.
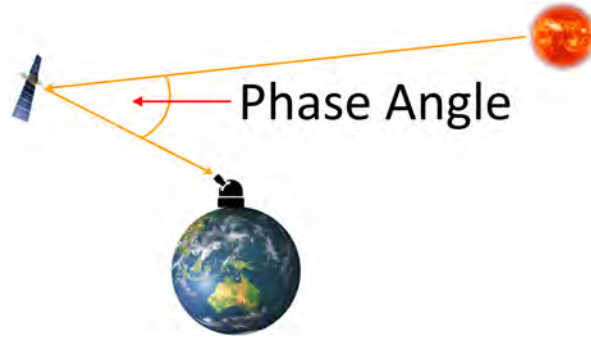
Figure 1.13: The angle formed between light from the Sun, reflected off an RSO toward a sensor, is known as the phase angle.

Kervin et al. [29], using simulated optical observations of satellites in LEO, MEO, GEO and Molniya (HEO) orbits, explored the assumption that irradiance of an RSO will peak at minimum phase angle. Satellites in LEO, MEO, GEO and Molniya (HEO) orbits were modelled, with varying complexities in shape, physical properties and dynamic orientation. The authors found that as phase angle does not take into account orientation or physical properties of a target satellite, the assumption was reliable under only limited circumstances. Specifically, phase angle was recommended as an observation prediction tool for objects approximating diffuse spheres, and that are stable at or near GEO. RSOs that are unstable or in other orbit regimes are less likely to exhibit a predictable relationship between peak irradiance and phase angle.

1.5.3 Satellite Design

Satellites consist of two major subsystems: a payload (communication or mission-specific sensors), and the bus, to which the payload, power and other systems are attached. This construct is summarised in Figure 1.14 [30].

There are many companies that manufacture satellite buses, each having multiple designs to facilitate the varying requirements of individual customers. Space Systems/Loral (SSL), for example, produce several variants of their SSL
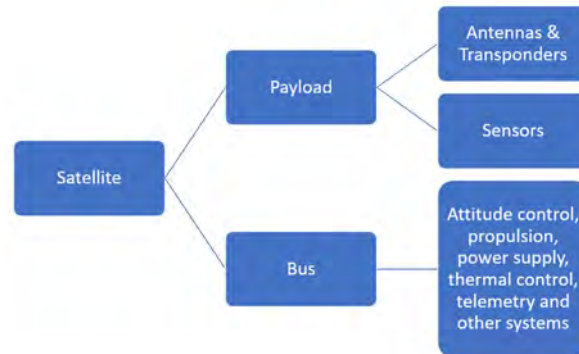
Figure 1.14: Structure of a satellite, showing the two major subsystems - payload and bus (adapted from [30]).

1300 bus that about a third of existing large communications satellites are built upon [31].

However, satellite buses may generally be categorised into one of two shapes: box-wing, or cylindrical. Box-wing satellites consist of a rectangular-prism bus, with solar panels arranged in a horizontally spread 'wing' configuration. Cylindrical satellites, conversely, typically have solar panels on the bus surface. An example of each shape, displaying their different profiles, is given in Figure 1.15.

1.5.4 RSO Operational Status

An operational GEO satellite is controlled, and maintained in its assigned orbital position via station keeping manoeuvres. Conversely, a retired satellite is no longer operated - it may have been moved to the graveyard orbit, and may also be tumbling or otherwise not orbiting in an optimal flight profile. Rocket bodies and debris at or near GEO may also exhibit unstable orbits.

Figure 1.16 shows a WISE image in two different infrared bands (2.8 - 3.8 μm and 4.1 - 5.2 μm), captured on 12 June 2010. This image contains a streak from the satellite Thaicom 1, which was moved to a graveyard orbit at the end of January 2010 [33, 34]. The strobing effect seen in band W1 (Figure 1.16a) is indicative of the satellite tumbling - as the surface facing the WISE sensor constantly changes, so does the level of flux it reflects or transmits toward the sensor. The longer infrared band W2 does not exhibit this strobing effect, likely due to this band predominantly observing thermal emissions.

(a) HS-601 box-wing.

(b) HS-376 cylinder.

Figure 1.15: Examples of a *(a)* HS-601 box-wing and *(b)* HS-376 cylindrical satellite bus [32]

(a) W1

(b) W2

Figure 1.16: Image frame 05454a150 in bands *a* W1 and *b* W2, show the satellite Thaicom 1 which was moved to the graveyard orbit over 5 months before the date of image capture. A strobing effect is evident in band W1, indicating that the satellite is in an unstable, tumbling profile.

The reported status of satellites is susceptible to inaccuracy, as commercial operators may be reluctant to share this information with the public, and may do so months after their satellite was actually retired. Additionally, operators may be enticed to keep a retired satellite in its ITU assigned GEO slot, until they are able to launch a replacement; if they allow the slot to become empty their ITU allocation may be lost. In this instance, companies may maintain east-west station keeping, but not north-south [35]. This all means that although a GEO satellite might be listed as operational in a database, it may recently have been retired. Conversely, an RSO listed as retired may exhibit an orbit profile similar to an operational satellite, if it had not yet succumbed to perturbations without the benefit of station keeping. In summary, operational status may not be an accurate indicator of the orbital stability of a satellite.

1.5.5   RSO Observation

Two options are presented when attempting to observe an RSO with optical or infrared sensors: Sidereal Stare Mode (SSM), or Track Rate Mode (TRM) [36]. For SSM, the sensor is moved across the sky at the same speed and direction as stars in the field of view. This allows stars to appear as points in the image, while RSOs appear as streaks. Conversely, TRM moves the sensor with the predicted speed and direction of the observed RSO, streaking stars while focusing the RSO to a point. Examples of both SSM and TRM images are shown in Figure 1.17.

(a) SSM   **(b)** TRM
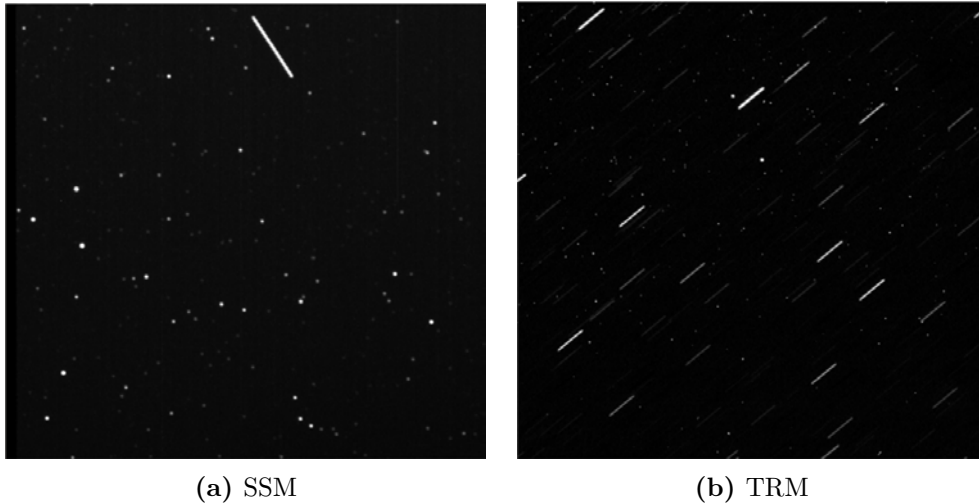
Figure 1.17: *(a)* Stars appear as points in SSM imagery, while RSOs appear as streaks. *(b)* The opposite is true of TRM imagery. Two satellites are evident as points in the centre-top of the image [37].

LEO objects, when observed in SSM, traverse the field of view rapidly, leading to minimal energy being captured by each individual pixel in the detector [36]. SSM is therefore more suited to regimes above LEO, where the decreased orbital velocity of RSOs allow them to remain in the sensor field of view for enough time that sufficient energy is captured. Given that WISE operates in SSM, the focus of this thesis will be the detection of satellites in this regime.

1.5.6 Space Surveillance Objectives

When observing RSOs, there are two primary objectives that may be carried out. The first objective is metrics, which involves the tracking of an RSO to update its orbital parameters, such that RSO catalogues may be maintained. The second objective, which is the focus of this thesis, is characterisation of the RSO via analysis of its signal.

1.6 Photometry

The process of measuring the amount of flux emitted by an object as a function of wavelength, and how that flux changes over time, is known as photometry [16]. This practice is a fundamental component of astronomy, shedding light on the construct of stars, planets, galaxies and other celestial objects. However, photometry also applies to the measurement of flux reflected or emitted by RSOs.

The flux incident upon an infrared sensor pixel, from the direction of an RSO, is not solely from that RSO. Stars or galaxies in the same line-of-sight also contribute to the total flux counted by that pixel. Atmospheric particles outside the RSO line-of-sight may reflect flux from the Moon in the direction of the sensor, again increasing that pixels total count. Finally, the sensor itself, through heat and other energetic processes, may contribute flux counts via dark current and read noise. These additional sources of flux are collectively referred to as background [9].

Those wishing to analyse RSO streaks must therefore take the background into account, in order to isolate flux attributable to the RSO. Once this is achieved, the flux levels of different RSOs, under different conditions, may be compared to provide identifiable trends.

1.6.1 The Magnitude System

In isolation, the measurement of flux from an RSO does not provide much meaning. Measurements are therefore converted to a standard scale, such that they may be compared to other known objects.

This process began with the Greek astronomer Hipparchus, c. 130 BC [9]. Hipparchus published a catalogue of 600 observed stars, that he assigned to one of six classes based upon their perceived brightness. The first class of stars were considered the brightest, the sixth faintest. These classes from one to six came to be known as magnitudes, a system that although improved upon, is still in use today.

With the invention of the telescope, observation of fainter stars became possible, leading to the introduction of magnitudes seven and beyond. In 1856, William Pogson proposed that the scale become logarithmic, such that a magnitude difference of five corresponds to an increase in brightness of 100:1. For example, a star of magnitude 5 is 100 times brighter than a star of magnitude 10. This logarithmic magnitude scale is represented in Figure 1.18; magnitude

is represented by m, with a subscript for the wavelength of observation, in this case v for visual.
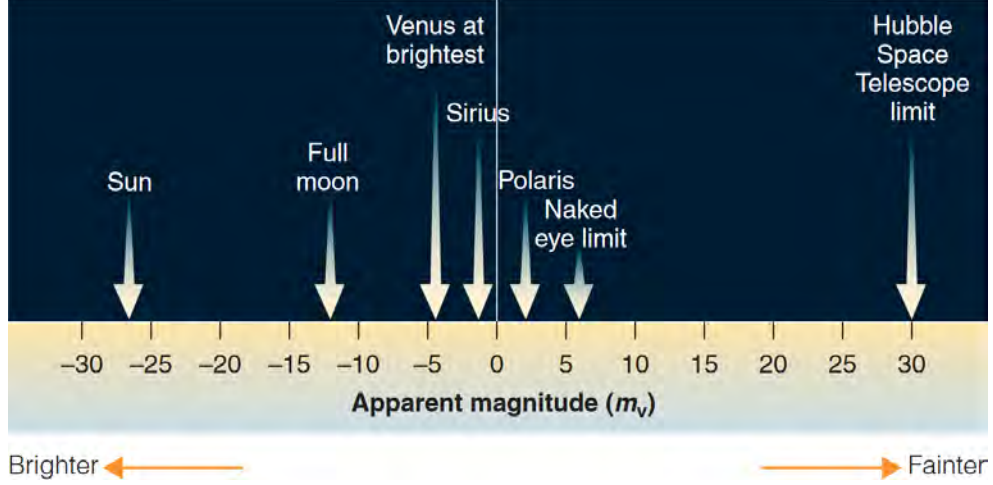
Figure 1.18: Apparent magnitude in the V band, with reference points [38].

To allow flux measurements of RSOs to be represented on this scale, Equation 1.12 is used, based upon the logarithmic scale introduced by Pogson [9]. F is the measured flux, while the inclusion of a constant, K, allows a measurement to be adapted such that it conforms to previous measurements. For example, the star Vega is often used as its known magnitude is $\approx$ zero. Therefore, if sensors aboard WISE were to measure the flux from Vega, K in Equation 1.12 would be set such that m was equal to zero. Once this process is conducted for a number of known (standard) stars, a final value for K may be set, and the apparent magnitude of observed RSOs determined.

$$m = -2.5 \log_{10}(F) + K \tag{1.12}$$

When the magnitude of an object is measured in more than one band, useful information may be obtained through the use of colour indices. The colour index of an object is found by subtracting the longer wavelength magnitude from the shorter. For example, if an object is measured using both B and V filters from the Johnson-Cousins-Glass system shown in Table 1.2, its B-V colour index is determined per Equation 1.13.

$$m_{B-V} = m_B - m_V \tag{1.13}$$

26

1.7 Aim of the Masters Thesis

The primary aim of this thesis is to investigate the use of infrared sensors for the purposes of SSA, using archival imagery from the NASA WISE mission.

The primary goal in achievement of this aim is the investigation of streak detection methods, culminating in the development of a streak detection algorithm that is customised to detect the serendipitous presence of RSOs in WISE imagery. A secondary goal is to conduct photometric analysis of identified RSOs, adding to extensive characterisation efforts already carried out with infrared, optical and radar sensors.

1.8 Thesis Outline

Chapter 2 will commence with a brief description of the NASA WISE mission and system, giving context for the remaining Chapters. A review of relevant literature will follow in Chapter 3, focussing upon research in the fields of optical and infrared photometry. Chapter 4 will describe in detail the streak detection algorithm developed for the purposes of identifying RSOs in WISE imagery. Chapters 5 and 6 will provide results of the photometric analysis conducted on detected RSOs, validating the streak detection algorithm and providing insight to the potential benefits of infrared sensors for the purposes of SSA. Finally, Chapter 7 will summarise thesis outcomes, and provide suggestions for future work in this field.

2 NASA WISE

There are currently no space-based infrared sensors conducting SSA operations. That said, in 2009 NASA launched the WISE spacecraft as an astronomical mission, which captured serendipitous observations of RSOs. The expansive data set of infrared images offered by the WISE mission therefore provides an ideal opportunity to detect and characterise RSOs, which is the premise of this thesis.

Before commencing this research, an understanding of the WISE mission is useful. This chapter will describe in detail the mission objectives, system specifications, data processing, and how WISE may be used for the purposes of SSA.

2.1 Mission Objectives

The WISE satellite mission was launched by NASA on 14 December 2009, into a Sun-synchronous Low Earth Orbit (LEO), with a mean altitude of 540km and inclination of 97.5° [39]. The mission objective was to scan the entire sky in infrared wavelengths, to obtain insight into star formation, the existence of planets outside our solar system, and the origins of the universe.

WISE utilises IR sensors, as the wavelength of energy from such distant cosmological objects, in an expanding universe, is lengthened from the visible spectrum into the infrared - the process of redshift [36]. Infrared sensors also allow observation of cosmological objects not possible with optical sensors. Wien's displacement law tells us that the cooler an object is, the longer its wavelength of peak irradiance. Therefore, as observations move from visible to near-infrared wavelengths, cooler stars become more prominent [8]. As observations move towards longer infrared wavelengths, stars fade, and cooler objects such as planets and asteroids become the focus.

Observations are made in four different infrared bands, allowing the production of colour-colour plots such as in Figure 2.1. This plot, revealing interesting features in various categories of cosmological objects, is an example of the many astronomical outcomes produced by the WISE mission.
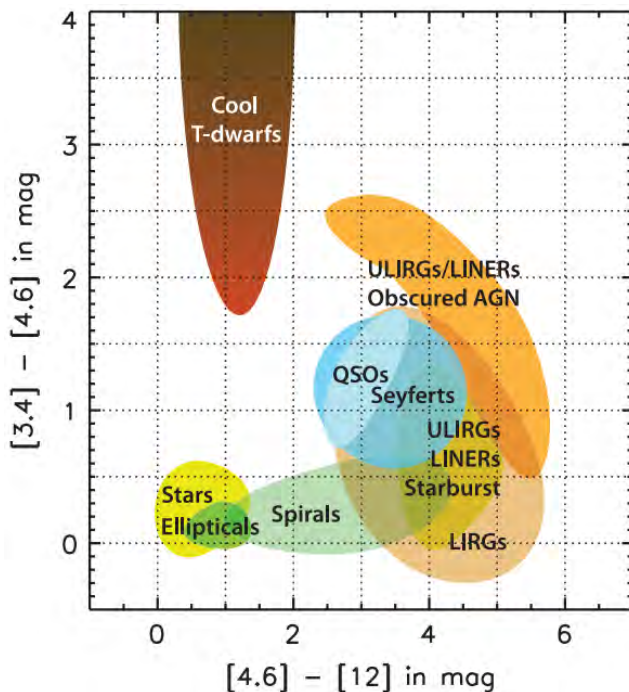
Figure 2.1: This colour-colour plot is an example of the many astronomical outcomes of the WISE mission [39]

2.2 Telescope and Sensor Specifications

Wright et al. [39] and Larsen et al. [40] provide an in-depth description of the WISE mission payload, and the initial performance in orbit. The WISE payload consists of a 40 cm telescope aperture, and three beam splitters that focus incident energy onto four separate focal plane arrays. These arrays take measurements in four infrared bands, W1-4, centred at 3.4, 4.6, 12 and 22 μm [40] respectively. A depiction of the WISE spacecraft and components is shown in Figures 2.2 and 2.3.

Figure 2.2: Depiction of the NASA WISE satellite [41].
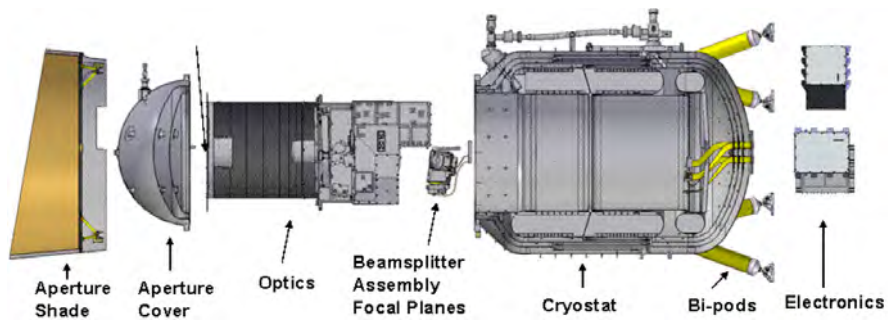
Figure 2.3: NASA WISE satellite components [42].

HgCdTe (MCT) detectors are used for bands W1 and W2, while Si:As detectors are used for bands W3 and W4. The wavelengths observed by WISE, particularly band W4 centred at 22 μm, are not typically observable using ground based telescopes. As can be seen from Figure 1.3, energy at such wavelengths is almost completely absorbed or scattered before reaching a ground-based sensor.

A drawback of observations at such long wavelengths is the increase in dark current due to reduced band gaps in the sensor materials used (HgCdTe and Si:As). To counter this, the WISE payload includes a solid hydrogen cryogenic cooling system that keeps the W1/W2 sensors cooled to 32.0 ± 2.0 K and W3/W4 sensors cooled to 7.8 ± 0.5 K, resulting in dark current levels of < 1 and < 100 electrons per second respectively [40].

Cooling systems such as that used on WISE have limited lifespans, as their cryogenic materials are not able to be replenished on orbit. Following commencement of operations, the cryogen tanks aboard WISE were depleted in 10-months [39], less than the expected operational life of 12.8 months [40]. As a result, W3 and W4 band operations ceased in September 2010, while operations in W1 and W2 continued until February 2011. The spacecraft was then placed into a state of hibernation.

In December 2013, the WISE spacecraft was reactivated, and re-branded as NEOWISE. The renewed mission focusses upon detection and analysis of Near-Earth Objects (NEOs), specifically asteroids and comets [43]. Due to the lack of cryogenic cooling, NEOWISE operations are conducted solely in bands W1 and W2, which are passively cooled by pointing the telescope near zenith, which allows sensors to radiately cool.

WISE is able to capture images while in motion through the use of a scanning mirror mechanism. Mirrors move synchronously with the telescope, holding the desired field-of-view steady for the entire exposure time [39]. Images in band W3 and W4 have 8.8 second exposure times, while W1 and W2 have a shorter 7.7 second exposure time due to a different readout process in the HgCdTe detector [44]. At the end of each image exposure, it takes 1.06 seconds to read each of the four arrays, and 1.1 seconds for the mirror to assume its new observational position. In practice, this means that an observational frame of four images (one for each band) is captured every 11 seconds.

Detailed specifications of the WISE mission instrumentation are found in Table 2.1

TELESCOPE	
Telescope Aperture	40 cm
Field of View	46.9 x 46.9 arcmin
Focal Length	1.35 m
f/	3.375

FOCAL PLANE ARRAY				
	W1	**W2**	**W3**	**W4**
Wavelength (μm)	2.8 - 3.8	4.1 - 5.2	7.5 - 16.5	20 - 26
Airy Disk Radius (μm)	14.0	18.9	49.4	90.6
Sampling Ratio (pixels / Airy disk)	1.56	2.10	5.49	10.1
Pixel Scale (arcsec / pixel)	2.75	2.75	2.75	5.5
Quantum Efficiency (%)	> 70		> 60	
Noise (e$^-$)	20		100	
Dark Current (e$^-$/s)	< 1		< 100	
Dynamic Range (e$^-$)	100,000			
Image Dimensions (pixels^2)	1024	1024	1024	512
Pixel Size (μm)	18			

Table 2.1: WISE focal plane array and telescope specifications. The W4 band is binned 2×2, resulting in a pixel scale and image dimensions different to bands W1-W3. Specifications are compiled from literature [39, 40, 45], and from calculations based upon texts by Chromey [9] and Howell [16].

2.3 WISE Image Reduction and Calibration

Astronomical data collected from the WISE and NEOWISE missions is managed by the Infrared Processing and Analysis Centre (IPAC), a division of NASA. Specifically, data is available through the Infrared Science Archive (IRSA), which provides access to more than 20 billion astronomical measurements [46]. IRSA maintains data from all stages of the WISE mission, including operations prior to cryogenic depletion, W1 and W2 operations post-depletion, and the reactivated NEOWISE mission. Data releases are summarised in Table 2.2.

Data Release	Bands	Notes
All-Sky	W1-4	Jan - Aug 2010.
3-Band Cryo	W1-3	Aug - Sep 2010. Reduced functionality of the W3 sensor.
Post-Cryo	W1-2	Sep 2010 - Feb 2011.
ALLWISE	W1-4	Jan 2010 - Feb 2011. Combines data from previous releases, enhancing photometric sensitivity and accuracy.
NEOWISE	W1-2	Commenced in Dec 2013. On-going mission to observe Near-Earth Objects, specifically asteroids and comets.

Table 2.2: WISE data releases, from the various phases of operations pre and post cryogenic depletion [46].

Initially, photometric analysis of all four WISE bands is desired, to thoroughly investigate the utility of each wavelength for SSA. The ALLWISE dataset was therefore selected for this research. Individual images from ALLWISE are passed through a series of data processing steps, prior to release. These include artefact detection and tagging, identification and photometric cataloguing of astronomical sources, and other quality assessment processes.

Once an individual image has passed through this processing pipeline, it becomes known as a Level 1b calibrated single-exposure image. Every time that WISE conducted an 11 second observational frame of a segment of the sky, four single-exposure images were produced, one for each band W1-W4.

Each frame is given a unique name - for example 01274a129. Single-exposure images have their specific band appended, such as 01274a129-w1.

An additional product available from IRSA is the image atlas, which is made by combining images from all four bands into larger image segments of the entire sky. Atlas images are not suitable for the purposes of RSO detection, as dynamic objects have been deliberately removed to improve clarity near astronomical sources - RSO streaks are therefore not present.

An astronomical source database is also provided, that contains astrometry and photometric data for over 747 million astronomical objects detected by WISE. This database is useful for calibrating algorithm measurements to known star magnitudes, prior to conducting photometric measurements of RSOs.

Bulk download of single-exposure images, for use in this research, is made possible by an Automated Programming Interface (API) to IRSA [47]. First, an ASCII format table is created with a list of images required for download. This table may be built by conducting a search within the IRSA image database [48], for example by searching for all images within an angular radius from a celestial coordinate. A URL query was then built as Python code, and run using the cURL command line tool.

2.4 Serendipitous Observations of RSOs

WISE's 540km orbital altitude was chosen to minimise transmission path distance to Earth for the large quantities of data being captured, and also to avoid the South Atlantic Anomaly such that radiation exposure was minimised [39]. The low orbital altitude of WISE also carries an unintended benefit - the orbit of higher altitude RSOs occasionally fall within its field-of-view. WISE imagery, therefore, becomes a suitable source of data for the purposes of SSA.

The Sun-synchronous orbit of WISE, and the radial pointing of the sensor, means that GEO RSOs are typically observed at a similar phase angle, near $90°$. To visualise this, WISE and a sample GEO spacecraft (Galaxy 11) were modelled using Systems Tool Kit (STK). Figure 2.4 gives a visual representation of how WISE is able to view GEO satellites, and the typical $\sim90°$ phase angle of observations.
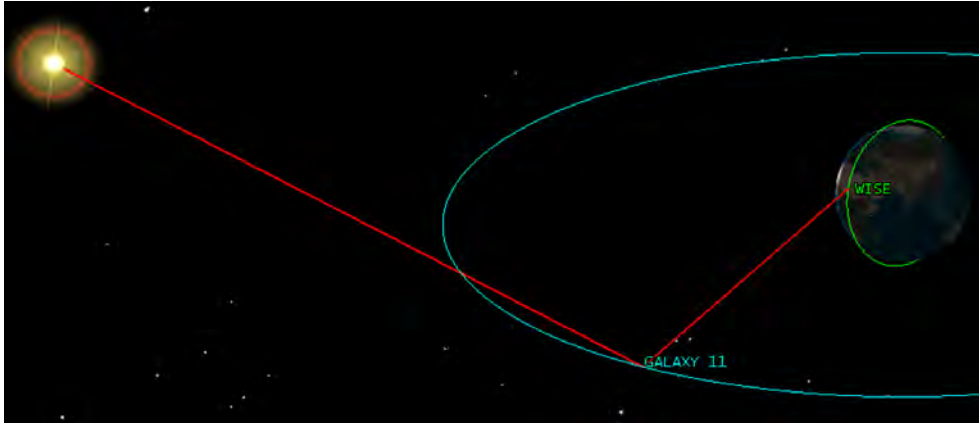
Figure 2.4: *(a)* Energy emitted from the Sun is incident upon a GEO satellite (Galaxy 11), and reflected toward WISE. This Sun-object-sensor relationship defines the phase-angle, around 90° for GEO spacecraft observed by WISE.

The multiple wavelengths utilised by WISE sensors may be of particular advantage for observing RSOs. Unlike optical observations, the infrared flux from an RSO does not greatly depend upon reflecting solar energy, or upon phase angle [13]. While band W1 falls in the reflective IR regime at 3.4 μm, bands W2-W4 detect thermal emissions. This means that while an RSO is in eclipse, shielded by the Earth from solar illumination, it is still emitting at thermal IR wavelengths. Consequently, the RSO appears bright to thermal IR sensors during these portions of their orbits, while the visible signature becomes almost invisible.

2.4.1 RSO Characterisation Capability

RSO characterisation typically relies upon plots of time resolved flux variation, which are known as light curves. This is the ultimate goal in observing RSOs, preferably in multiple bands, with results such as that of Bédard et al. [49] shown in Figure 2.5. An RSO photometric measurement taken from WISE imagery, however, represents a single data point for that RSO. Therefore, flux variation as a factor of time is not given.
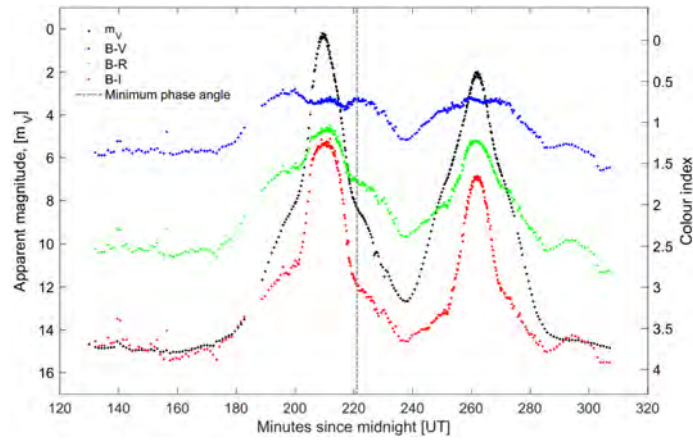
Figure 2.5: An example of a time-resolved light curve [49].

Technically, a light curve is able to be produced using WISE data. See Figure 2.6, in which several individual photometric measurements of the Astra-5A GEO satellite are plotted, over the January to August period of four-band observations. Such plots, however, are not useful, as the time resolution between data points is too large to provide any meaningful insight into spacecraft characteristics.
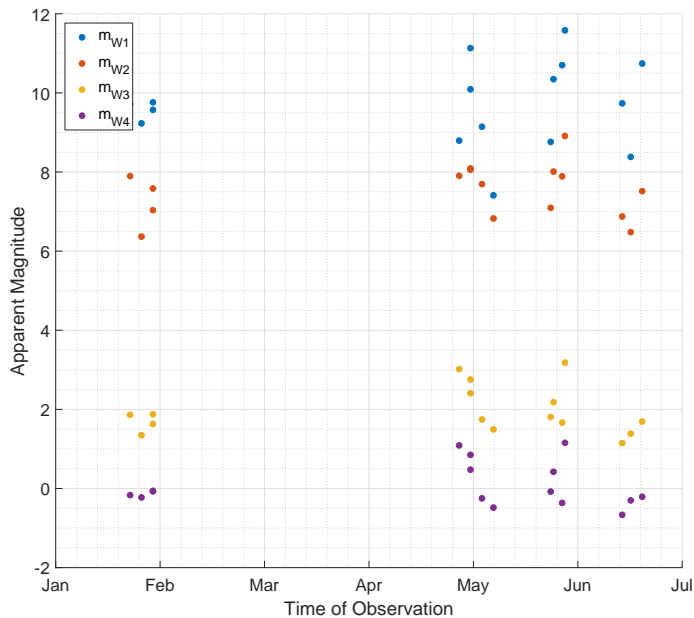
Figure 2.6: Light curves created with WISE data, such as this one for the Astra-5A GEO satellite, are not useful due to the large time period between observations of individual RSOs.

Light curves are typically produced in Track-Rate Mode (TRM), where the ground or space-based sensor follows the RSO. This allows RSO flux to be concentrated on a small number of image pixels, increasing the sensitivity of measurements. The creation of light curves is also possible in Sidereal Stare Mode (SSM), where sensors such as WISE remain still while RSOs streak across the field of view. To obtain enough time-resolved measurements of an RSO in SSM, the sensor must move between each image exposure to retain the RSO in its field of view.

However, WISE was not developed as an SSA sensor - although many RSOs were serendipitously captured, the sensor was not moved to follow them in order to produce time-resolved measurements. Despite this, it is hoped that a clear indication of the utility of infrared sensors for RSO characterisation will be obtained from this research. This information may then be used to direct the efforts of future infrared SSA sensors, be they ground or space-based, in the creation of light curves.

2.4.2 Thermal Infrared Characterisation

WISE not only observes infrared energy emitted by the Sun and reflected off objects, but also energy emitted by those objects in the thermal infrared regime. The concepts of Planck's radiation equation as it relates to temperature may therefore be analysed. Satellites are typically designed to operate in specified temperature ranges; sensitive electronic components operate at around 0 to 50°C, while solar panel temperatures range from -100 to 125°C [50]. Using Equation 1.1, spacecraft at temperatures of 0°C (273K) and 100°C (373K) were modelled, and the four WISE bands overlaid, as shown in Figure 2.7. Peak irradiance, according to Wien's displacement law, falls at 10.61μm at 273K, and 7.77μm at 373K. It can be observed that these peak wavelengths fall within band W3 at both temperatures. This band may therefore provide the best opportunity for analysis of RSO temperature.
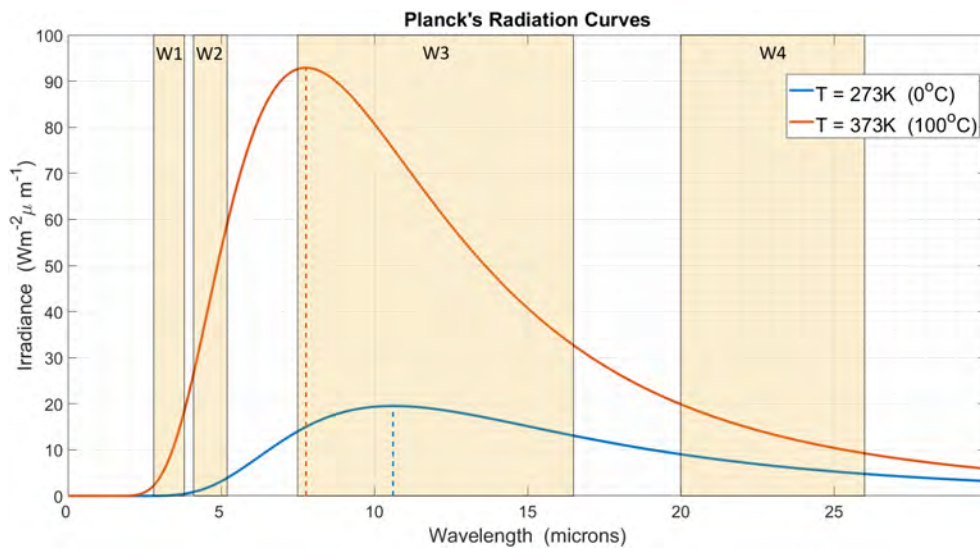
Figure 2.7: Planck radiation curves, at typical spacecraft operating temperatures of 0°C (273K) and 100°C (373K), are modelled. The wavelength ranges of WISE bands W1 - W4 are overlaid, showing that the peak irradiance of spacecraft falls within band W3.

The spectral emittance of the Sun, whose surface temperature is approximately 6000K (5727°C), was also plotted as shown in Figure 2.8. Irradiance peaks at 0.48μm, in visible wavelengths. Although the four WISE bands fall in the tail of the spectral curve, reflected sunlight is still the predominant

source of irradiance, as shown in Table 2.3. For photometric measurements of an RSO, the ratio of reflected to emitted infrared energy in each band will depend upon the specific orientation of that RSO during image capture, and consequently the overall Sun-RSO-WISE observational geometry.
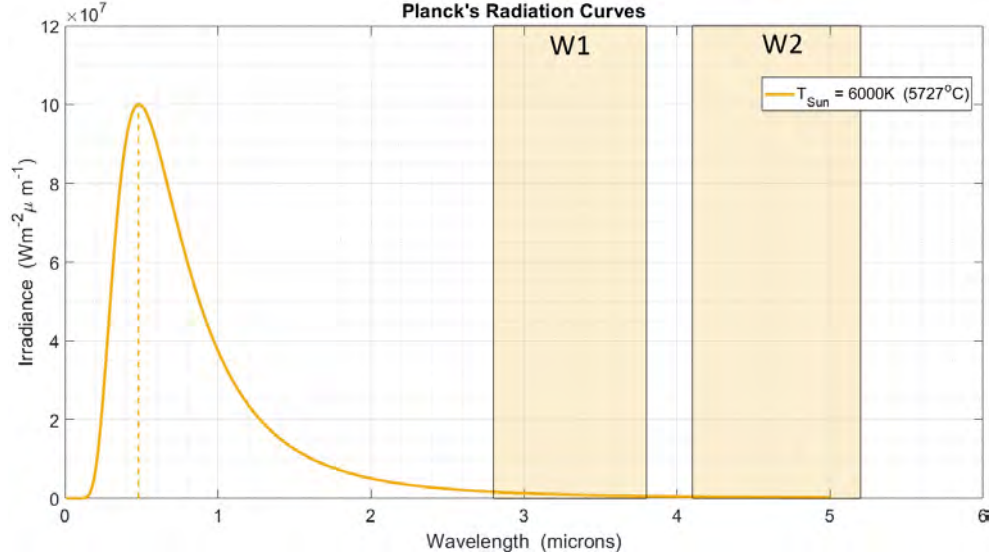
Figure 2.8: Planck radiation curve for the surface temperature of the Sun. Although peak irradiance is in visible wavelengths at 0.48μm, irradiance in the four WISE bands (only W1 and W2 shown) is still higher than thermal emissions at RSO surface temperatures of 273K and 373K.

Band (Wavelength)	6000K $(\text{Wm}^{-2}\mu\text{m}^{-1})$	373K $(\text{Wm}^{-2}\mu\text{m}^{-1})$	273K $(\text{Wm}^{-2}\mu\text{m}^{-1})$
W1 $(3.4\mu\text{m})$	803,900	9.74	0.15
W2 $(4.6\mu\text{m})$	265,500	41.46	1.92
W3 $(12\mu\text{m})$	6,798	62.95	18.85
W4 $(22\mu\text{m})$	630.5	15.21	7.28

Table 2.3: Irradiance figures at the four WISE central wavelengths are given, for the Sun's surface temperature (6000K) and indicative RSO surface temperatures (273K and 373K).

3 Literature Survey

This chapter presents a summary of previous research conducted in the areas of streak detection and infrared space surveillance. Firstly, various methods implemented to detect and measure streaks in astronomical images will be examined, in order to assess their utility with imagery from the WISE database. The ability to identify various characterising traits of RSOs will then be explored, via an in-depth review of research conducted in the fields of optical and infrared SSA. Finally, following a summation of the literature review findings, the overarching goals of this thesis will be stated.

3.1 Streak Detection

In order to obtain photometric measurement of RSOs within astronomical images, they must first be found. This may be achieved by searching images for the streaks that their incident photons create when capturing images in Sidereal Stare Mode (SSM) - the process of streak detection.

3.1.1 Near-Earth Asteroid Detection

Streak detection processes are not only used for the identification of RSOs - astronomers seeking to observe and characterise Near-Earth Asteroids (NEAs) also need to identify these moving objects. Waszczak et al. [51], for example, developed a streak detection algorithm called *findStreaks* to identify faint asteroid trails that were not adequately detected by the more commonly utilised commercial software *Source Extractor* [52]. *findStreaks* was developed in conjunction with researchers from IPAC, the NASA division that catalogues WISE image data.

A methodology similar to that implemented by Laher et al. [53] for removal of streaks and transient events in the WISE image atlas was used. First, two images of the same or similar area of the sky are stacked, with the position

of point sources astrometrically aligned. By subtracting one image from the other, a 'differenced image' is created in which objects that were in both images, such as point sources, are removed. Objects that were in only one of the images - such as the streak of an RSO or asteroid - remain. This process is shown in Figure 3.1. Personal email communication with Laher [54] led to an offer of the use of *findStreaks* for this research. However, the software is built upon the C programming language, and it was consequently determined that sufficient time to learn the required programming was not available in the set thesis time-frame. Future work involving the analysis of WISE imagery for the purposes of SSA may include utilisation of the *findStreaks* algorithm.
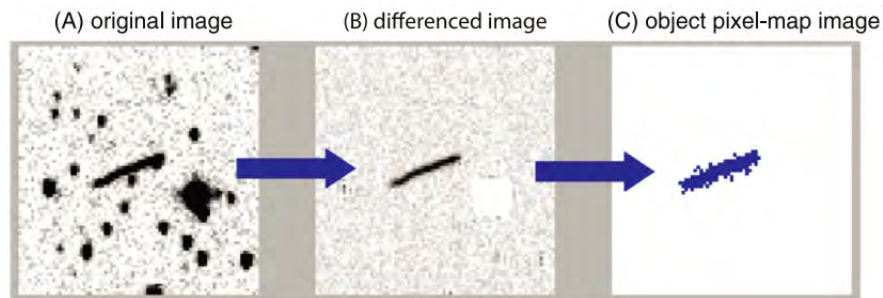
Figure 3.1: To detect the faint streaks left by Near-Earth Asteroids (NEAs), two images of the same sky-view are subtracted, removing point-sources (adapted from [51]).

3.1.2 Hough and Radon Transforms

A widely-used process by which to detect straight lines is the Hough transform [55]. Using the equation for a straight line, $y = ax + b$, each pixel at location (x,y) in a binary image is transformed into a straight line in (a,b) parameter space, with slope equal to -x and intercept y. When points along a straight line in the image are transformed, their corresponding lines in the (a,b) space intersect at the same point. The Hough transform uses these points of intersection to detect the presence of straight lines in an image.

Ciurte and Danescu [56] developed an algorithm based upon the Radon transform, a process very similar to the Hough transform. The difference is that the Hough transform minimises the amount of features to be analysed in an image via a process of voting and thresholding, making it quicker though

less reliable than the Radon transform. Using a series of images with both simulated and real MEO RSOs, the authors were able to accurately identify streaks in 100% of cases. The transformation from image to Radon parameter space is shown in Figure 3.2, with the cyan line in the final frame representing the peak value in the Radon transform. The choice between Hough or Radon transforms is a trade-off between speed and accuracy; testing of each method with WISE imagery may reveal the best process by which to detect streaks.

(a) Image space.

(b) Parameter space.

(c) Line of local maximum.
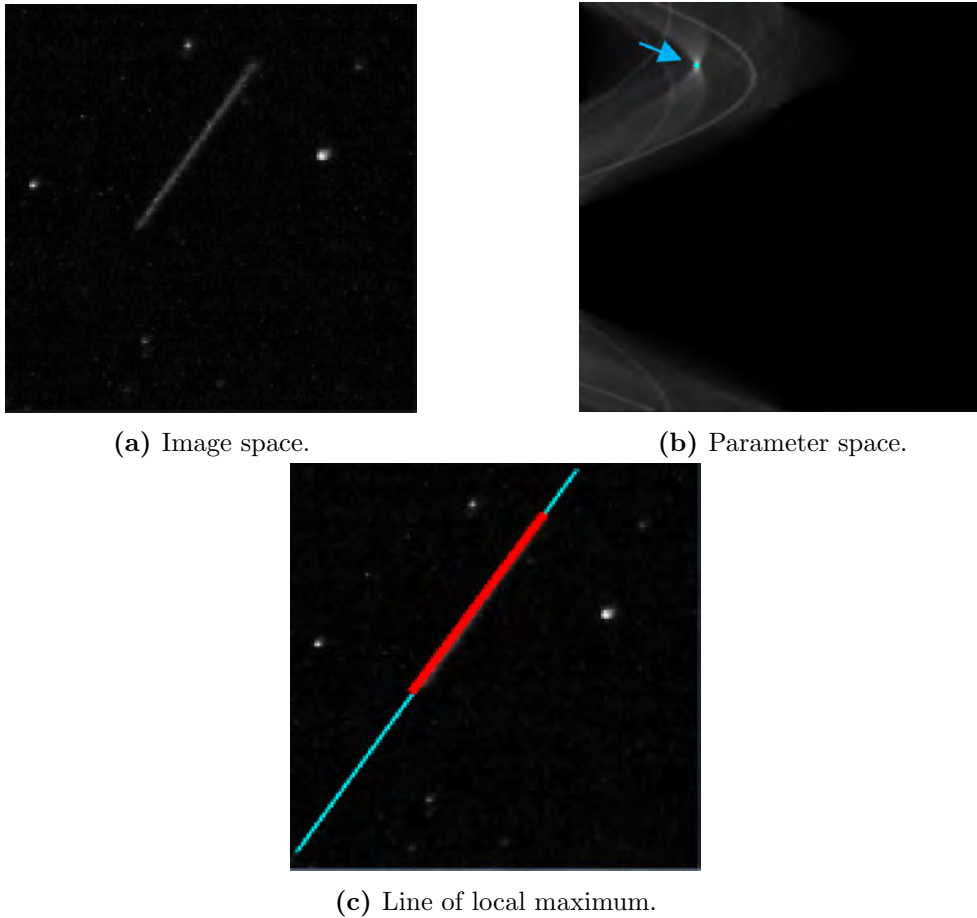
Figure 3.2: The Radon transform is used to detect a streak within an astronomical image. Transformation from *(a)* the image space to *(b)* the Radon parameter space allows detection of a local maximum, shown by the arrow and *(c)* the straight line [56].

3.1.3 Matched-Filter Process

Lévesque et al. [57–62] implemented a unique matched-filter process for the detection of streaks in images produced by the three Surveillance of Space Concept Demonstrator observatories in Kingston, DRDC Suffield and DRDC Valcartier, Canada. The matched-filter process relies upon a-priori knowledge of the RSO being observed - an estimate of its position and orbital trajectory must already be known. This is a situation faced when wishing to reacquire an RSO whose orbital parameters may have drifted since last being observed due to orbital perturbations or station-keeping manoeuvres.

Observations are set up such that the RSO will streak from positions P_1 to P_2 in the image exposure time (t+dt), as shown in Figure 3.3a. Based upon the line between these two points, a filter is created, at Figure 3.3b. The captured image and the streak filter are then compared using convolution integrals, resulting in a convolution peak at the site of the detected streak. The full process is shown in Figure 3.4.

(a) Predicted RSO path. **(b)** Resultant filter.
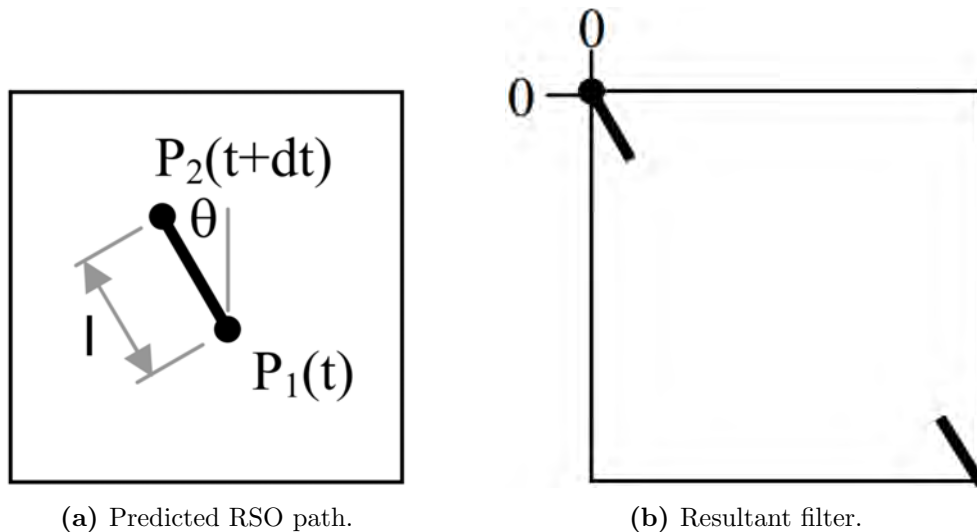
Figure 3.3: A matched-filter process developed by Lévesque and Buteau [57] takes *(a)* the predicted start and end points (P_1 and P_2) of an RSO within an image, over the exposure time (t+dt), to generate *(b) a filter.*
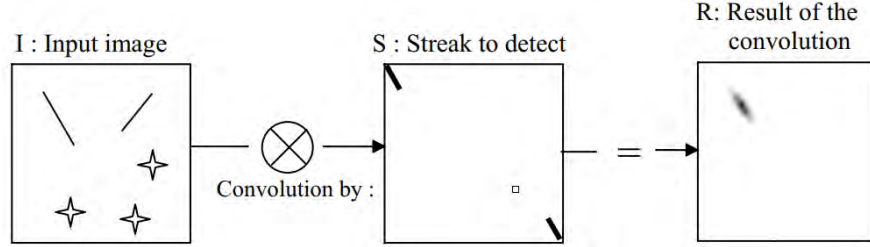
Figure 3.4: Comparison of the astronomical image and generated filter using convolution integrals results in detection of the RSO streak [57].

Lévesque and Leliévre [59] found an exceptional ability to detect faint RSOs - streaks with signal-to-noise ratio (SNR) as low as 0.1 were detected. Reliable detection without false alarms was achieved for streaks with SNR ≥ 0.5. Although the ability to detect such faint streaks in WISE imagery is highly desirable, application of the matched-filter method is not directly applicable to this research, as there is no a-priori knowledge of RSO position and orbital trajectory. However, these authors also developed a stringent process of background subtraction that was necessary for successful image convolution [57]. This background subtraction algorithm was generously provided by Lévesque for use in this thesis. The algorithm was adapted to suit the specifics of WISE imagery, and integrated into WISEstreakDET. The background subtraction process is described in detail within Chapter 4.

3.1.4 Image Segmentation

Wallace et al. [63] developed an algorithm, also used for astronomical images obtained with the three Canadian Surveillance of Space Concept Demonstrator observatories. Following background subtraction using the process developed by Lévesque and Buteau [57], objects above a determined noise floor are retained, and characterised as either streaks or point sources based upon their individual distribution of pixels (image moments). This algorithm, not requiring a-priori knowledge of RSOs, showed the most promise for application to the WISE image database. Wallace also generously provided code segments for use in this thesis, which were adapted and integrated into WISEstreakDET. Associated algorithm processes are described in detail throughout Chapter 4.

3.2   Ground-Based Optical Characterisation

Efforts to observe artificial satellites have existed as long as artificial satellites themselves. With the launch of Sputnik 1 in 1957, the Smithsonian Astrophysical Observatory utilised twelve tracking cameras as part of a larger global 'MOONWATCH' network. The Sputnik 1 satellite ('1957 Alpha 2') and its carrier rocket ('1957 Alpha 1') were detected, tracked, and their orbits subsequently derived [13].

Photometric observations, studying the light reflected or emitted by artificial satellites, were being conducted by the USSR as early as 1958 using specialised SBG satellite cameras developed by VEB Carl Zeiss [64]. The following decades heralded vast improvements in the sensitivity of these photometric measurements. The 1960s saw the introduction of technologies such as electro-optical photometers, while the invention of the CCD in 1969 set a new standard in imaging technologies that persists today.

Modern optical photometric measurements are abundant, with precise data from RSOs in all orbital regimes catalogued by various agencies. The Joint Space Operations Centre (JSpOC), for example, maintains a database with over 3.5 million photometric measurements of RSOs, allowing advanced modelling and prediction capabilities [65].

3.2.1   Illumination and Observation Geometry

Optical photometric methods have led to many RSO characteristics being discovered. Based upon over a decade of data from photometric observations, Payne et al. [66] developed a model of several GEO satellites in order to study their signatures under varying illumination geometries. The generalisation that flux peaks at lowest phase angle was found to hold true, under modelled and observed conditions, resulting in the 'canonical' signature shown in Figure 3.5a. However, some satellites such as those built upon the BSS-702 bus type display non-canonical signatures, with alternate peaks away from zero phase angle as shown in Figure 3.5b. This was attributed to solar concentrators unique to this model being at an angle normal to the solar panels. These findings allow the timing of observations for specific satellites to be planned, to coincide with phase angles representing the highest reflectance, such that measurements are optimised.

(a)   **(b)**
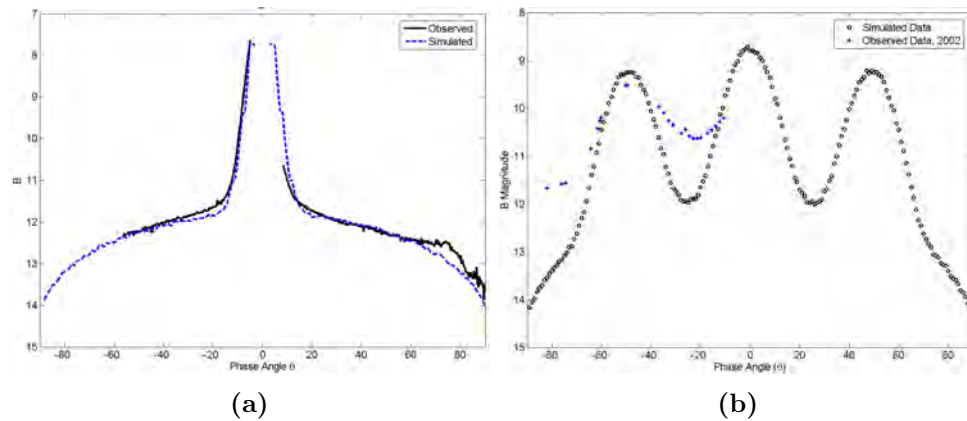
Figure 3.5: Modelled and observational data show that while some satellites display *(a)* 'canonical' signatures, with peak flux around zero phase angle, others *(b)* have peaks at angles off-zero [66].

For stable, box-wing GEO satellites in particular, generalisations about illumination geometry and flux profiles may be made. For example, as solar panels actively track the Sun, when phase angle approaches 90° they are viewed edge-on, as shown in Figure 3.6a. This minimises the amount of flux that the large, flat panels are able to reflect toward an observing sensor. Figure 3.6b shows the respective component contributions to flux for RSOs with solar arrays, based upon observational data modelling by Cognion [67]. While this is modelled upon optical observations, it is also applicable to the reflective IR regime. WISE measurements, typically at phase angles of around 90°, may therefore provide an opportunity for enhanced observation of satellite bodies, as opposed to more acute or obtuse geometries that are dominated by solar panel reflections.

46

(a)

(b)
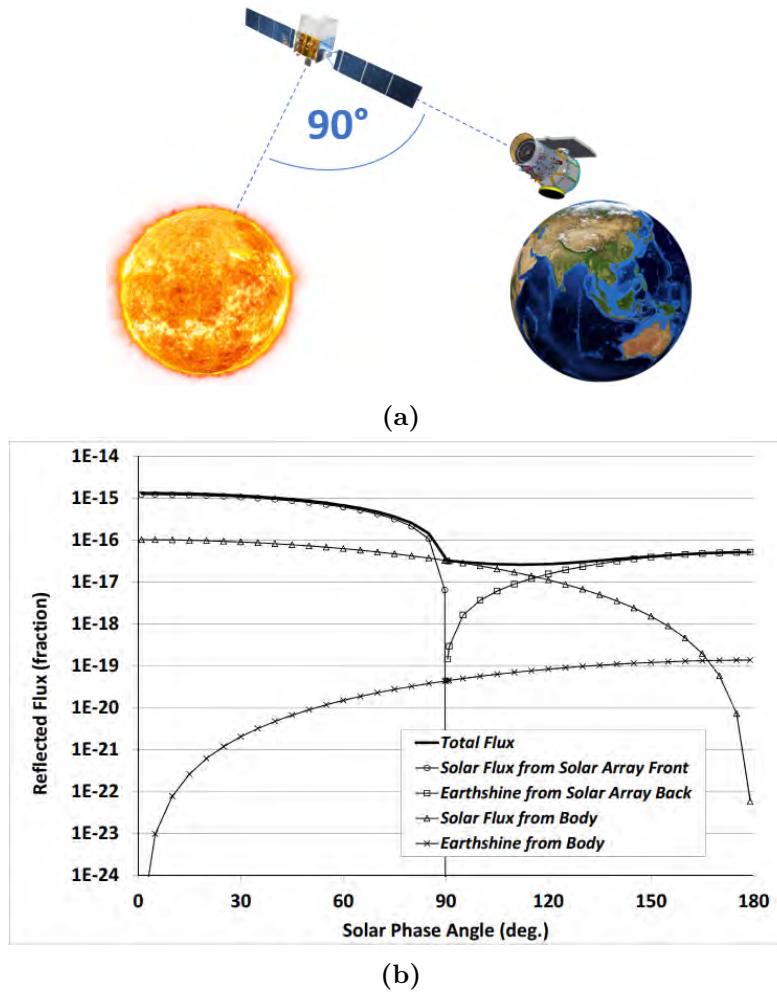
Figure 3.6: *(a)* At a phase angle of 90°, the solar panels of active GEO spacecraft are typically viewed edge-on. *(b)* The flux contribution of various RSO components is shown at various phase angles [67].

3.2.2 RSO Identification

Variance in the photometric signature of different satellites has been used to identify individual spacecraft in clustered formations. Scott and Wallace [68] observed Canadian GEO satellites with a small aperture telescope at the Defence Research and Development Canada (DRDC) Space Surveillance Observatory (SSO). Signature varied with bus type, showing that observations at

various phase angles could potentially offer the ability to differentiate between individual satellites in a cluster.

A clustered pair of satellites - Anik-F1 and Anik-F1R - were observed, and identified based upon NORAD TLE data. However, the photometric signature of Anik-F1, built upon the BSS-702C bus, appeared similar to a satellite with Eurostar 3000S bus. Conversely, Anik-F1R which is built upon Eurostar 3000S appeared similar to BSS-702C satellites. This led the authors to believe that satellite identities had been erroneously swapped - a 'mistag' - which was reported to Space Surveillance Network analysts. Photometric signatures for the respective satellites are shown in Figures 3.7 and 3.8.

The ability to individually identify two or more closely-spaced satellites based upon their photometric measurements will be of increasing benefit to the SSA community. Recent developments in On Orbit Servicing (OOS), whereby satellites are refuelled, repaired or re-purposed by a second servicing satellite, will see a rise in close-proximity satellite operations [69]. There are also recent concerns regarding intentional approaches to satellites for the purpose of intelligence gathering. The merit of infrared RSO observations may therefore be proven, should they offer a similar or enhanced ability to differentiate between satellite bus types for these purposes.
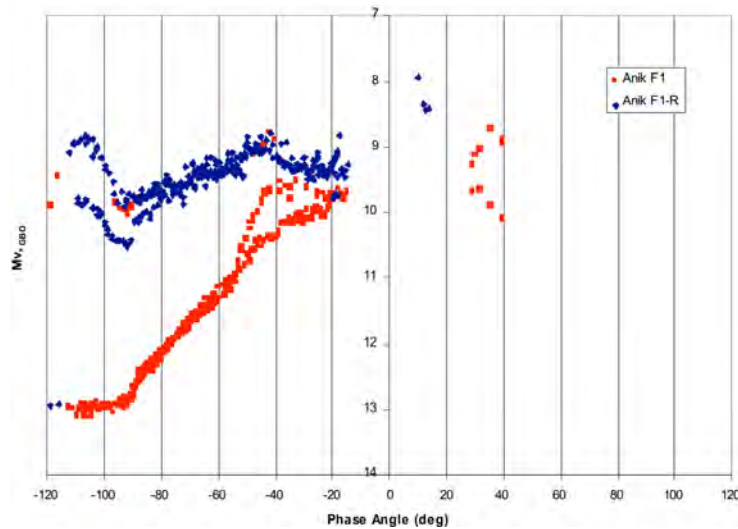
Figure 3.7: Anik-F1 measurements were in fact of Anik-F1R, and vice-versa, due to a mistag event [68].
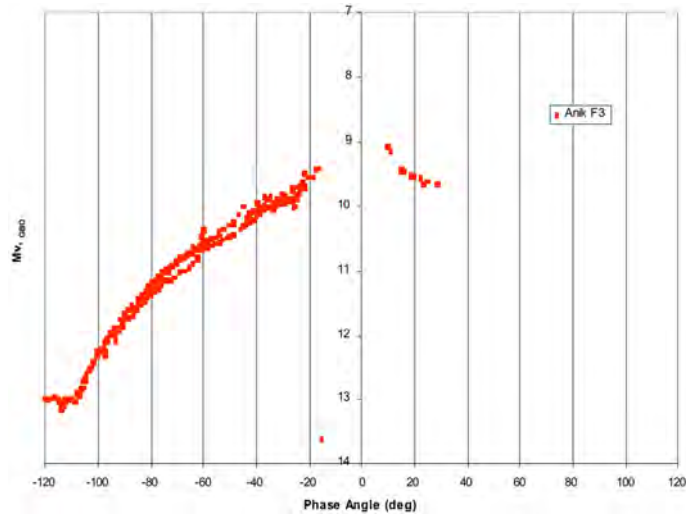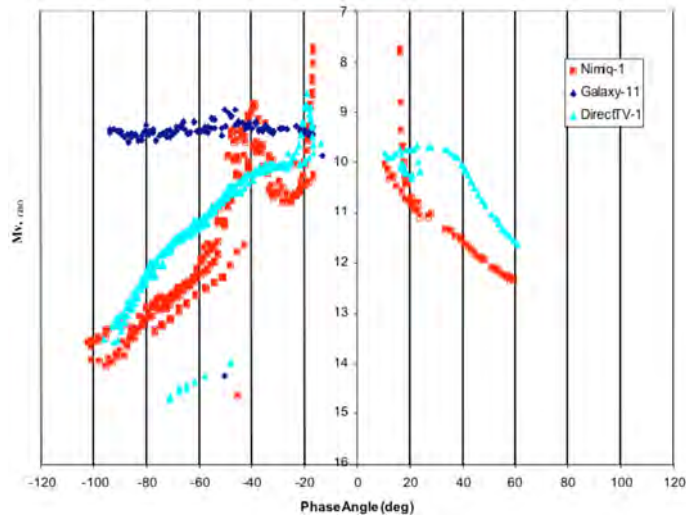
(a) Anik-F3

(b) Galaxy-11

Figure 3.8: Figure 3.7 shows the photometric signatures of two clustered satellites, Anik-F1 and Anik-F1R, which appear quite different. Anik-F1R should appear similar to Anik-F3 in *(b)*, as they each use the Eurostar 3000S bus. Likewise, Anik-F1 should appear similar to Galaxy-11 in *(c)*, with each using the BSS-702C bus. However, observations show the opposite, suggesting that the two satellites in *(a)* had been mis-identified [68].

3.3 Space-Based Optical Characterisation

WISE is not the first space-based sensor to be used for SSA purposes. There have been several optical sensors aboard spacecraft whose mission was to perform observations of RSOs, in order to gain both characteristic and metric data.

3.3.1 The Space Based Visible Sensor

Initial technology demonstrations were conducted with the Space-Based Visible (SBV) sensor on the Midcourse Space Experiment (MSX) satellite. MSX was launched in 1996, into a near Sun-synchronous 898 km altitude orbit, and comprised a distinctive suite of ultraviolet, visible and infrared sensors shown in Figure 3.9 [70]. While the primary mission of MSX was to demonstrate detection and tracking of ballistic missiles from space, inclusion of the SBV sensor allowed a secondary mission of optical space-based space surveillance [71].
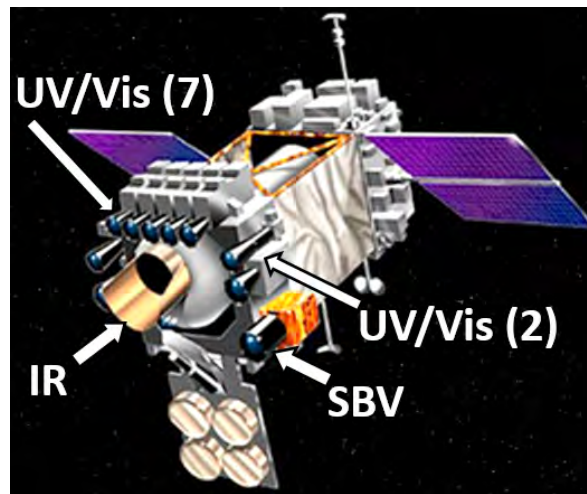
Figure 3.9: The MSX satellite, with multiple sensors covering the ultraviolet, visible and infrared spectrums (adapted from [72]).

The SBV sensor, operating in the 0.3 - 0.9 μm spectral range, possessed a wide 6.6° × 1.4° field-of-view that allowed for large sections of the sky to be searched for RSO streaks in each image exposure [70]. Using the SBV sensor, over 100,000 observations and photometric measurements of 2,300 RSOs were conducted. Stokes et al. [70], using this photometric data, were able to observe

a difference when comparing the signature of active, stable GEO satellites to those that are uncontrolled. As shown in Figure 3.10a, satellites appear brighter at smaller phase angles, when reflection from solar panels is highest. This phase angle relationship is not evident for tumbling satellites, as shown in Figure 3.10b, due to the observational geometry to solar panels constantly changing. Although WISE is not able to provide observations at such a broad range of phase angles, the higher distribution of data points around 90° for tumbling satellites may allow WISE imagery to discriminate between stable and unstable satellites, particularly in the reflective W1 band.

(a) Stable satellites   **(b)** Unstable satellites
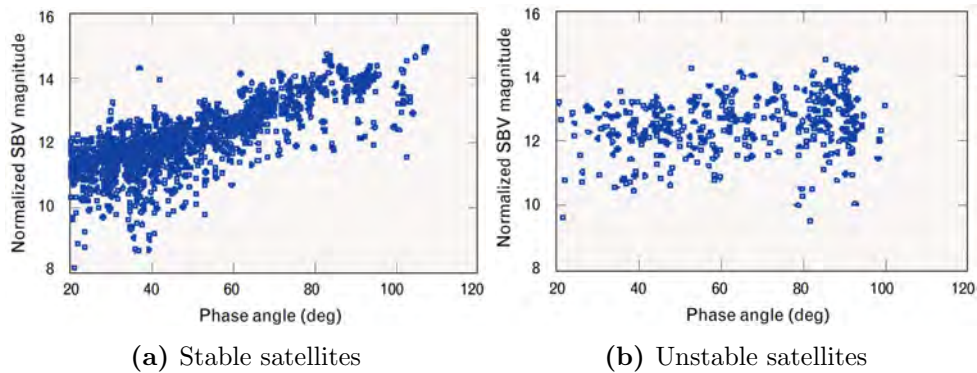
Figure 3.10: The photometric signatures of *(a)* stable GEO satellites show a linear relationship between phase angle and brightness, peaking at small phase angles. *(b)* Tumbling satellites do not demonstrate such a relationship [70].

Stokes et al. [70], using SBV data, were also able to establish a difference in magnitude based upon the size of observed satellites, when normalised for range. Photometric measurements of stable Telstar 401 and Symphonie A/B satellites were made and compared, as shown in Figure 3.11. The larger Telstar 401 spacecraft often appeared brighter than the smaller Symphonie satellites.

(a) Large satellite   **(b)** Small satellite
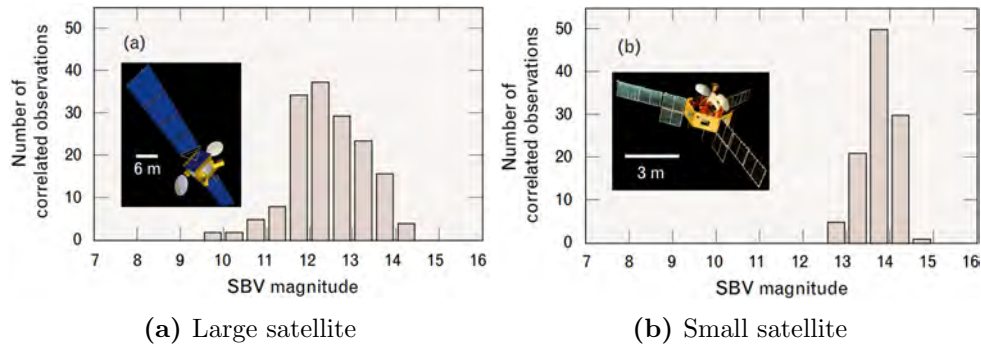
Figure 3.11: The photometric signatures of *(a)* large and *(b)* small satellites, when normalised for range, show that larger spacecraft often appear brighter [70].

3.3.2 The MOST Space Surveillance Experiment

The Microvariability and Oscillations of Stars (MOST) microsatellite, designed and built in Canada, was launched in 2003 to conduct astronomical observations in the broadband filter range of 0.35 - 0.75 μm. In October of 2005, MOST conducted a first for a microsatellite - space-based observation of another spacecraft. Scott et al. [73] report on photometric measurements taken of two GPS satellites, compared to empirical measurements of the same spacecraft taken by a ground-based optical observatory. The two data sources were shown to agree to within 0.2 magnitudes, offering further validation of the merit of space-based optical SSA sensors.

3.3.3 Other Space-Based Assets

The success of SBV and MOST as technology demonstrators validated the use of space-based optical sensors for the purposes of SSA. The U.S. subsequently launched the first of a planned network of Space-Based Space Surveillance (SBSS) satellites in 2010, expected to provide 14,000 RSO observations per day [74]. Canada, meanwhile, launched two small satellites in 2013 that are utilised for SSA - Sapphire, and the Near Earth Object Surveillance Satellite (NEOSSat) [75]. As these follow-on space-based telescopes are predominantly military controlled assets, little published research is available for review.

3.4 Ground-Based Infrared Characterisation

Since the discovery of infrared radiation in 1800 by Sir William Herschel, astronomers have conducted observations with infrared sensors to unveil characteristics not seen in the visible spectrum [76]. Analogous endeavours have been made for the purposes of SSA, with practitioners seeking characterisation abilities outside of those possible with optical telescopes alone.

3.4.1 Determination of RSO Size

Following the example set by infrared astronomers observing asteroids, Lambert et al. [77] obtained optical and thermal infrared measurements of space debris objects in 1993 using the Space Command Maui Optical Tracking and Identification Facility (MOTIF). The temperature and albedo of observed debris, defined as the percentage of incident energy reflected by those objects, was used to estimate cross-sectional area. Data obtained by the thermal infrared sensors matched well with known radar cross-section measurements for all but very large debris objects.

3.4.2 Daylight Observations

A major advantage of infrared sensors over optical is the ability to observe during daylight hours. Optical telescopes require a target to be illuminated by the Sun, and to reflect incident energy in the direction of the telescope - night observations are typically required to ensure that this reflected energy is stronger than background noise [36]. Background noise during the day, primarily caused by Rayleigh and particle scattering of light in the atmosphere, greatly inhibits the efficacy of optical observations [78]. However in the infrared regime, the dominant source of background is thermal emissions from the telescope and sky. Telescope sensors may be cooled to overcome this, making daylight observation of RSOs a theoretical possibility. Work by Jim et al. [79] and others have proven this theory, by demonstrating daytime observations of GEO satellites in the infrared.

3.4.3 Brightness

Simultaneous observation of satellites in the optical and infrared allows for a direct comparison of brightness in each band. Gibson et al. [80] conducted such a comparison in 2012. Optical V band observations were captured using the 0.4m Oceanit MStar telescope, paired with a 1024 × 1024 Alta U47 camera. Infrared K band (2.58 μm) observations were taken with the 2.2m

University of Hawaii telescope, paired with the HANDS-ION camera that utilises a short-wave IR (1.40 - 3.00 μm) 1280 $\times$ 1024 sensor. Images were captured in track-rate mode, with exposures of 2, 3 or 4 seconds in the optical and between 0.05 and 2.00 seconds for infrared. Figure 3.12 shows apparent magnitude at various phase angles for observations of the Tracking and Data Relay Satellite (TDRS) 5 spacecraft. This satellite was 2.6 - 3.8 magnitudes brighter in K band infrared than optical, while all observed GEO satellites were on average 2.5 magnitudes brighter.
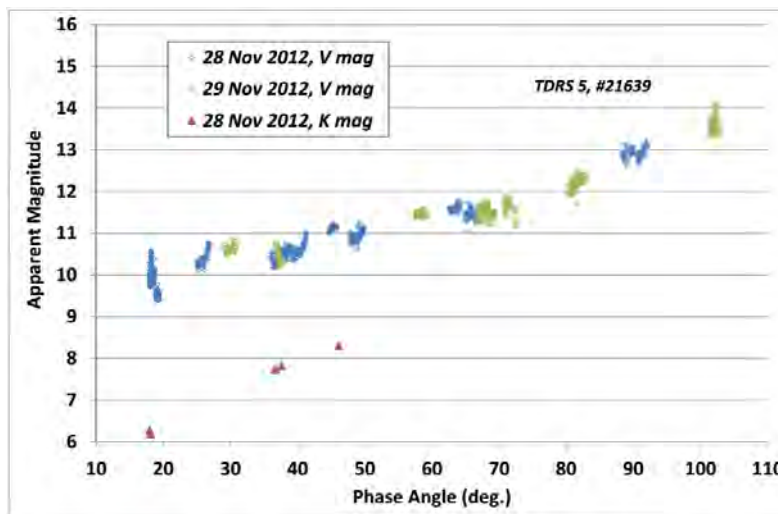
Figure 3.12: Apparent magnitude of the TDRS 5 GEO satellite at varying phase angles. Infrared observations (K band, denoted by red triangles) were 2.6 - 3.8 magnitudes brighter than V band optical observations [80].

Should measurements using WISE photometric data also show that RSOs appear brighter in the infrared regime than in the optical, the utility of infrared sensors for detection of small or faint RSOs may be demonstrated.

3.4.4 Illumination and Observation Geometry

Research conducted by Skinner et al. [81] demonstrates that the assumption of peak irradiance at minimum phase angle does not always hold true. The authors conducted optical and thermal infrared observations active GEO satellites, and an inactive satellite (DIRECTV-2) in the 'graveyard orbit'.

DIRECTV-2 has not been given altitude control or station-keeping com-

mands since decommissioning - the orbit is therefore typically unstable, subject to natural torques and perturbations. Figure 3.13 [81] shows observed flux values at varying phase angles, for a series of active satellites and DIRECTV-2. The active satellites display expected phase angle to flux relationships, with flux values decreasing as observations move away from zero degrees. Minimum flux values were observed at around 90°, where it was interpreted that large solar panels on the satellites were being viewed side-on, minimising their flux contribution. Flux values increase either side of 90° as the front or rear of the solar panels start to contribute to the flux received at the sensor, in line with the modelling of Cognion [67] shown in Figure 3.6b. For the inactive satellite however, despite data being restricted to phase angles between 15-50°, much different behaviour is evident. As stated by Kervin et al. [29], factors other than phase angle come into consideration - in this case, the unstable nature of the satellites attitude and orientation.
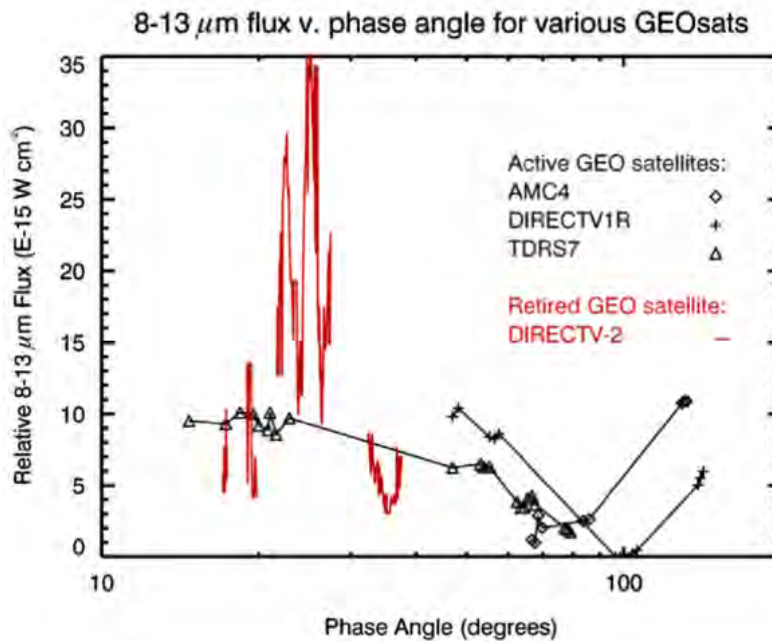
Figure 3.13: Thermal infrared observations by Skinner et al. [81] show that the assumption of peak irradiance at minimum phase angle does not hold true for unstable satellites.

3.4.5 Spectrometric Observations

More recent work [82–86] has focussed upon the use of infrared spectrometers, offering measurements across a broad range of infrared wavelengths. While not directly relevant to the photometric measurements obtained by WISE, inferences may be made from results at a single wavelength.

For example, Frith et al. [87] conducted observations in 2014 of non-active satellites using the HS-376 bus with the United Kingdom Infrared Telescope (UKIRT). UKIRT is situated at 14,000 feet in Mauna Kea, Hawaii, above much of the atmosphere causing attenuation of energy in the 0.9 - 2.4 μm bandwidth of observations. The authors were able to demonstrate a correlation between the mean J-K colour values of HS-376 satellites and their respective ages - the longer a spacecraft has been in space, the more red (large) its colour index. This relationship is shown in Figure 3.14, also showing the small sample of observations, warranting further investigation with WISE data.
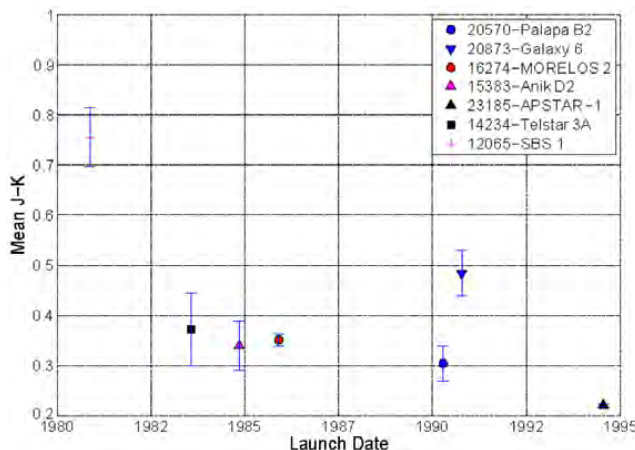
Figure 3.14: Observations by Frith et al. [87] suggest that mean J-K colour index values become more red (larger) with increase in spacecraft age.

Observations in the infrared regime may also allow for enhanced determination of RSO composition, with infrared spectral data revealing information not evident in visible wavelengths. Robinson [88], for example, show the difference in observed reflectance for various black paint types in the visible/near-infrared regime compared to a wider bandwidth up to 14 μm. Longer wavelength infrared measurements exhibit an increased variation and separation between spectra lines of the different paint types, as shown in

Figure 3.15. Such distinction may therefore be possible in photometric measurements of RSOs from WISE imagery, particularly in the longer wavelength W2-W4 bands.
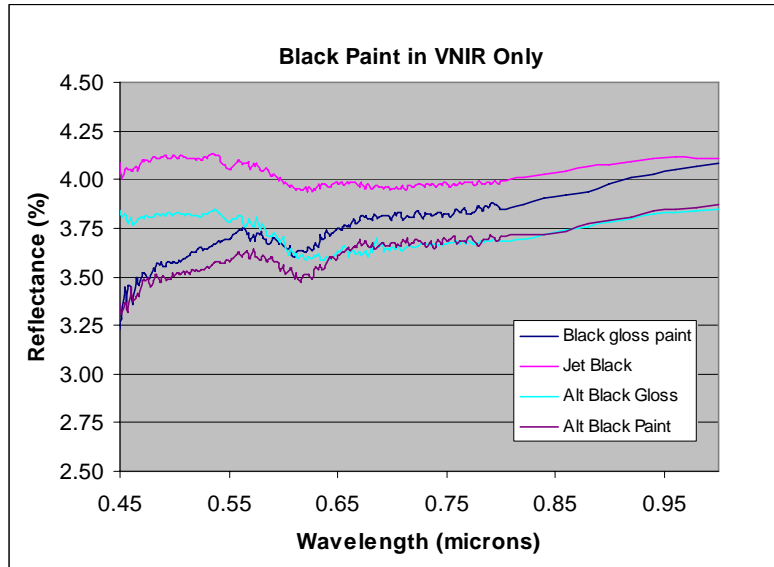
(a) Narrower spectrum showing little differentiation.
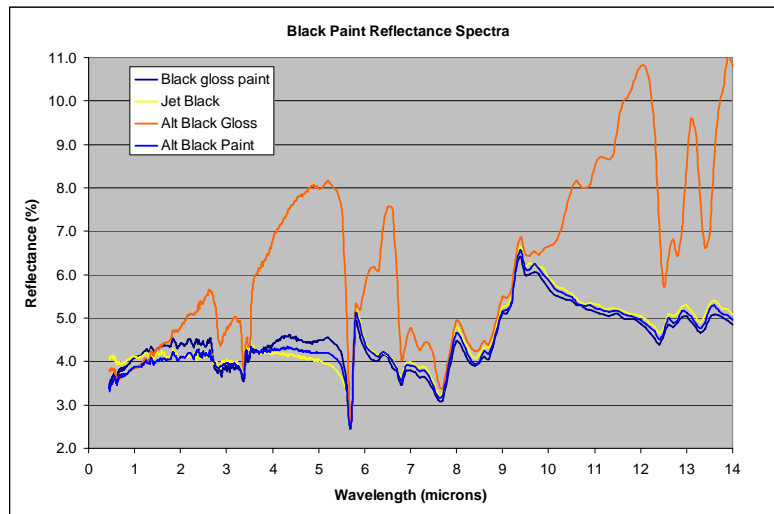
(b) Wider spectrum allows for greater differentiation.

Figure 3.15: Paint type characterisation in visual and infrared bands [88].

Abercromby et al. [89] also demonstrated the increased brightness of RSOs at infrared wavelengths relative to optical, via spectroscopic observations in the 0.65 - 2.5 μm band of various objects in the GEO or near-GEO planes. Results of this study are shown in Figure 3.16, showing a clear increase in reflectivity for spacecraft, rocket bodies and debris in the infrared regime above 0.7 μm.
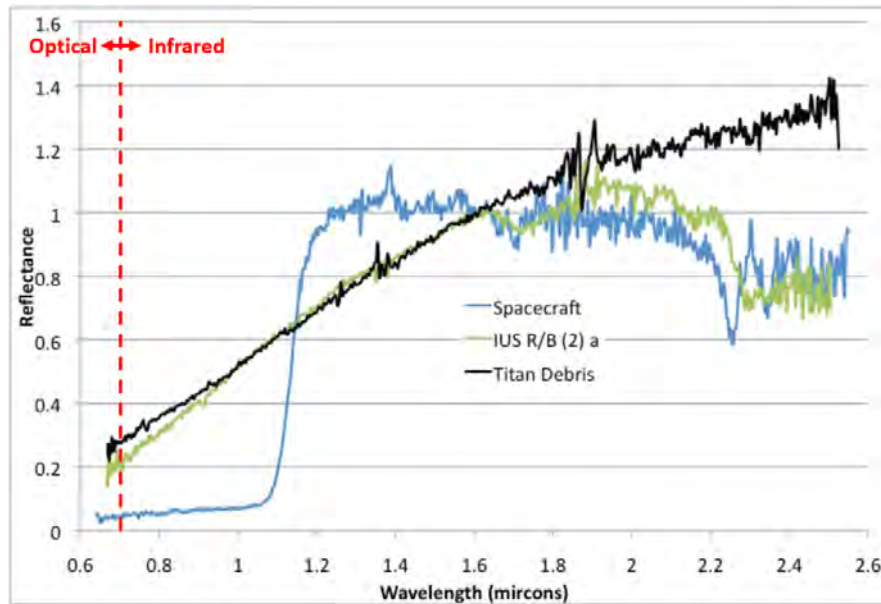
Figure 3.16: The increased reflectance for RSOs viewed in the infrared regime (>0.70 μm), as compared to optical observations (<0.70 μm), is evident (adapted from [89]).

3.5 Space-Based Infrared Characterisation

While the attenuation of energy at by the atmosphere prevents ground-based observations at many infrared wavelengths, space-based sensors are not subject to such restrictions. Although no dedicated space-based infrared SSA assets have been launched to date, serendipitous observations of spacecraft from astronomical satellites allow insight into the characteristics of RSOs in the infrared.

The earliest example of serendipitous spacecraft observations from a space-based infrared sensor come from the Infrared Astronomical Satellite (IRAS). Launched in 1983, IRAS conducted operated from March to November until running out of cryogen used to cool the sensors [90]. IRAS operated in a 800km altitude Sun-synchronous orbit, inclined at 99.2°. Four long-wavelength infrared sensors, centred at 12, 25, 60 and 100μm were aboard to conduct an all-sky survey of celestial objects. During operations, 190,000 RSOs were detected, with 2,047 correlated to catalogued objects. This extensive dataset was used by Gaposchkin and Bergemann [90] of the Massachusetts Institute of Technology Lincoln Lab to perform a statistical analysis of the temperature, absorptivity and emissivity of RSOs.

The future of space-based infrared sensors may allow for extended operations, due to the use of pyroelectric materials in long-wave IR detectors [91]. These materials do not require active cooling, such as the use of cryogenic tanks which deplete in relatively short periods of time. The end result is a longer baseline of observations than seen in missions such as IRAS and WISE.

3.5.1 WISE Characterisation

Similar to its space-based infrared predecessors such as IRAS, data from the WISE mission has been used by researchers for the purposes of SSA. Lee et al. [45] conducted an analysis of WISE image data to determine the colour temperature of GEO satellites. A subset of WISE images were selected, with inclination of $\pm$ 15° for the GEO regime, and separated from both the galactic plane and Moon to avoid excessive star and light contamination. From the database subset analysed, approximately 10% of images were found to contain streaks corresponding to controlled objects in GEO. Streaks were detected using *Source Extractor* [52], and photometric measurements obtained with a custom streak aperture-fitting algorithm. An example of a detected GEO satellite pair is shown in Figure 3.17 [45].
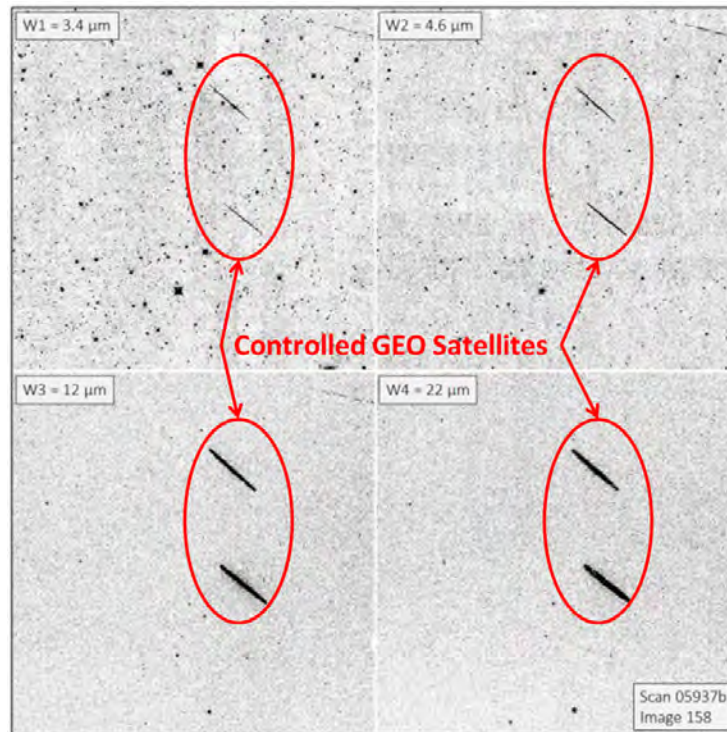
Figure 3.17: Four band WISE imagery, showing a pair of GEO spacecraft (adapted from [45]).

The space occupied by GEO spacecraft colour indices was shown to be different to that of astronomical objects viewed by WISE in previous research by Wright el al. [39] and Masiero et al. [92]. An example of this is shown in Figure 3.18.

(a) Wright el al. [39]
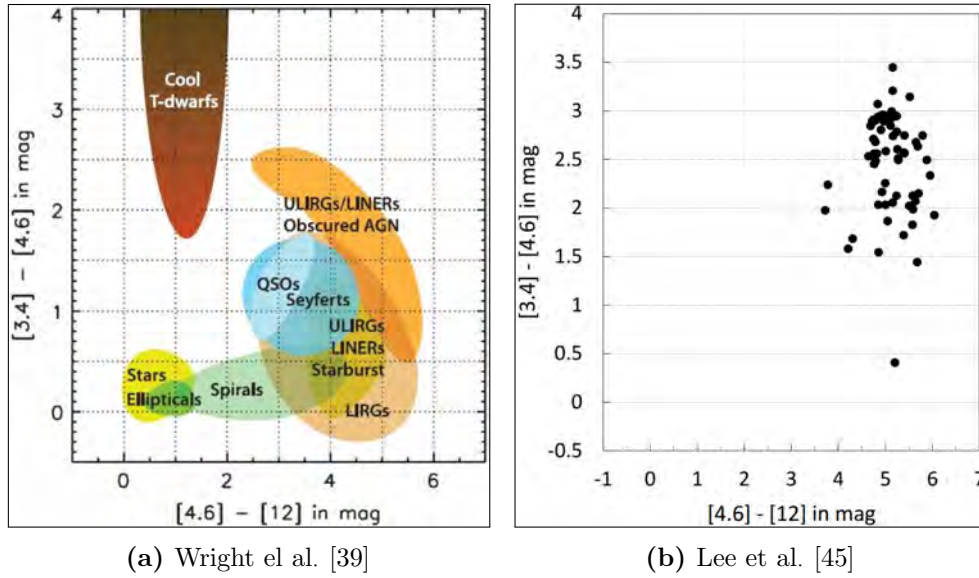
(b) Lee et al. [45]

Figure 3.18: *(a)* Wright el al. [39] show the respective colour indice space occupied by various astronomical objects. *(b)* Lee et al. [45] demonstrate that GEO spacecraft occupy a different subspace.

More recently, Lee et al. [93] compared box-wing and cylindrical active satellites, using photometric results obtained from WISE imagery. 245 active box-wing and 18 cylindrical satellites were detected and measured. Colour indices, in particular W2 - W3, were shown to provide an ability to discriminate between the two different RSO bus shapes, as shown in Figure 3.19.
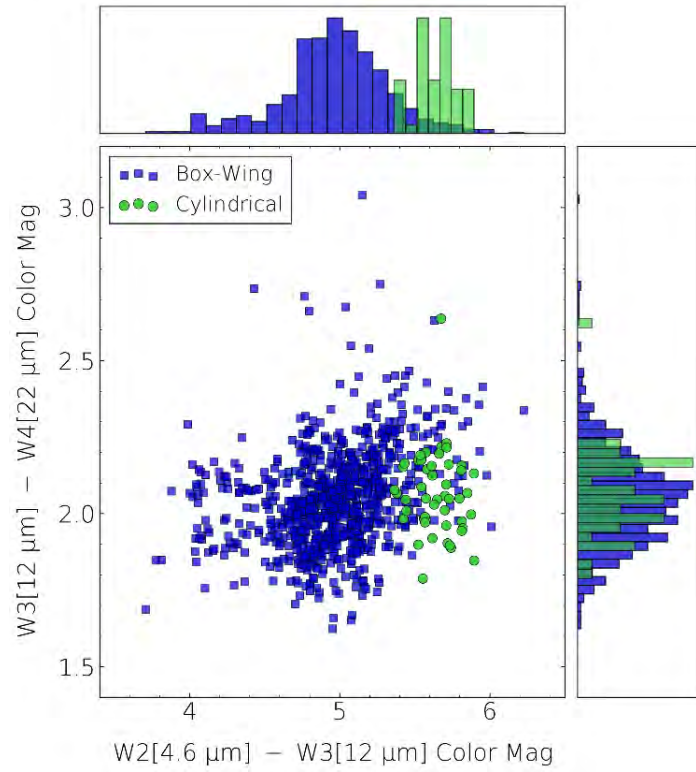
Figure 3.19: Colour indices of detected active box-wing and cylindrical satellites show some ability to discriminate between the two bus shapes [93].

3.6 Thermal Infrared Analysis of RSOs

WISE bands W2 - W4 are designed to observe energy in the thermal infrared regime. As described in Section 1.2.1, this allows for an estimation of RSO temperature to be obtained via measurement of streak irradiance. Due to time constraints, analysis of RSO temperature properties was not conducted for this thesis; photometry was instead chosen as the initial focus of characterisation efforts. A brief examination of literature pertaining to thermal infrared RSO characterisation is nonetheless included, to provide context for future research planned for the WISE database of imagery.

3.6.1 Temperature and RSO Size

Paxson et al. [94] conducted analysis of data from the Spatial Infrared Imaging Telescope (SPIRIT III) onboard the MSX satellite, in order to obtain various temperature measurements of space objects. SPIRIT III consists of four sensor channels (A - D), covering a thermal infrared bandwidth of 5.88 - 28.50 μm. RSOs were modelled as greybodies - that is, their emissivity did not vary with wavelength.

Three variations of models to determine temperature were developed - brightness temperature using one channel, colour temperature (index) using the comparison of two channels, and characteristic temperature using three or four channels [94]. Both the colour and characteristic temperature provided an estimate of the target size via its solid angle, however, the characteristic temperature was shown to be the most robust. Solid angle estimates were compared to radar cross section data from a radar observatory, and were found to provide reliable estimates of target size up to an altitude of 15,000km. It is believed that deviation between the RSO cross sections derived by radar and infrared measurements above 15,000km is attributable to the inaccuracy of radar above these altitudes. Infrared sensors, then, show promise in providing an accurate alternative over optical and radar for the estimation of target size in the GEO regime.

3.6.2 Thermal Infrared Characterisation

Early observations of GEO satellites using telescopes at the Universities of Arizona and Wyoming were conducted in 1992-1993 by Seniw [95], in the thermal infrared regime at 8 - 13 μm. Active, three-axis stabilised spacecraft were shown to exhibit large flux variance with change in phase angle. This was attributed to the highest cross sectional area (flat solar panels) being

observed at low phase angles, while at around 90° solar panels were viewed edge-on, with observation predominantly of the satellite bus. Spin-stabilised cylindrical satellites, conversely, exhibited relatively constant thermal flux at all phase angles, attributed to their cross-sectional area not changing based upon observational geometry. The contrast in flux variance between these two satellite shapes is shown in Figure 3.20.
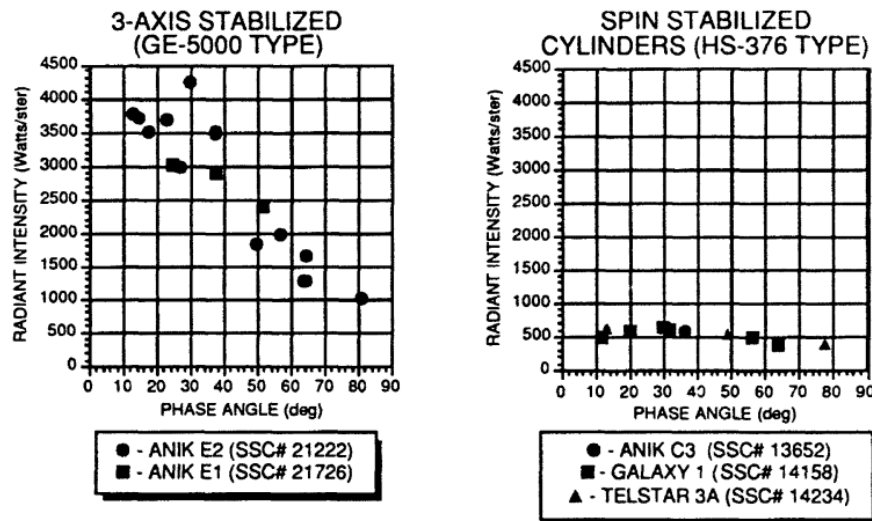
Figure 3.20: The thermal flux of 3-axis stabilised spacecraft varies with observational geometry due to the large winged solar panels, as compared to the relatively constant flux of spin-stabilised cylindrical satellites [95].

Skinner et al. have conducted extensive research of high-altitude RSOs, including an analysis of various observations made with the Broadband Array Spectrograph System (BASS) between 2007 and 2013 [81]. The authors were able to observe differences in the colour temperature of box-wing GEO satellites, based upon their operational status. For active satellites, flux was lowest as phase angle approached 90°, due to the edge-on observational geometry previously discussed. Colour temperature held an inverse relationship for these satellites, becoming higher as flux decreased; this was attributed to the observation of hot transmitter elements on the satellite buses. For inactive satellites, conversely, colour temperature decreased with flux, attributed to the lack of active electronic or radiating components on the bus. These observations show the potential of using temperature to characterise GEO RSOs.

3.7 Summary of Findings

Various streak detection methods, to identify both RSOs and asteroids, have been reviewed. While the reference image subtraction method utilised by Waszczak et al. [51] shows promise based upon its previous use with WISE imagery, a lack of C programming knowledge may prevent implementation within the thesis time-frames. The Hough and Radon transforms, as used by Ciurte and Danescu [56], will be tested to compare the relative trade-off between speed and accuracy. While the matched-filter process developed by Lévesque et al. [57] is not directly applicable due to the requirement of a-priori RSO knowledge, the implemented background subtraction may increase the ability to detect faint streaks. The same background subtraction process was used by Wallace et al. [63], along with other image processing techniques that perhaps show the most potential for application to WISE imagery.

Optical and infrared observations, both ground and space-based, exhibit the ability to reveal many identifying characteristics of RSOs. Infrared observations were typically shown to return brighter results than corresponding optical observations. WISE imagery, however, is limited to observations within a narrow range of phase angles. Despite this, the body of work by Lee et al. [45, 93] serves as an indicator of the potential for using WISE imagery to characterise RSOs. This potential should be explored, via an analysis of further RSO characteristics including operational status, age, size and type.

3.8 Summary of Thesis Goals

Based upon the broad thesis aims stated in Chapter 1, and upon the findings of this literature review, a summary of goals and questions that this thesis will seek to address is presented in Table 3.1.

Goal	Description
1	Through analysis of various streak detection methods, develop an algorithm (WISEstreakDET) to accurately detect streaks in WISE single-exposure database imagery.
2	Validate WISEstreakDET algorithm by comparing results to known star magnitudes.
3	Validate WISEstreakDET algorithm by reproducing and comparing results from previous research.
4	Compare the brightness of optical RSO photometric measurements to those in the IR.
5	Perform characteristic analysis of WISEstreakDET results.

Table 3.1: Summary of goals and questions that thesis will seek to address.

4 Streak Detection and Analysis Algorithm

The primary focus of this thesis is to address Goals 1 to 3, as stated in Section 3.8. Namely, to develop a streak detection algorithm for WISE imagery, and to validate this algorithm against known star magnitudes and previous research. This chapter, describing the process by which RSO streaks in WISE database imagery were detected and analysed, is therefore given the most consideration.

4.1 Algorithm Overview

The algorithm developed for this thesis and presented here is referred to as WISEstreakDET (WISE Streak Detection). The code primarily relies upon four concepts of image manipulation: background subtraction, thresholding, connectivity and image moments. These concepts, and those additional processes used to detect and analyse streaks, are summarised in the flowchart shown in Figure 4.1. A pictorial representation of the algorithm is shown in Figure 4.2, to provide context for the detailed explanation of each step given throughout this chapter.
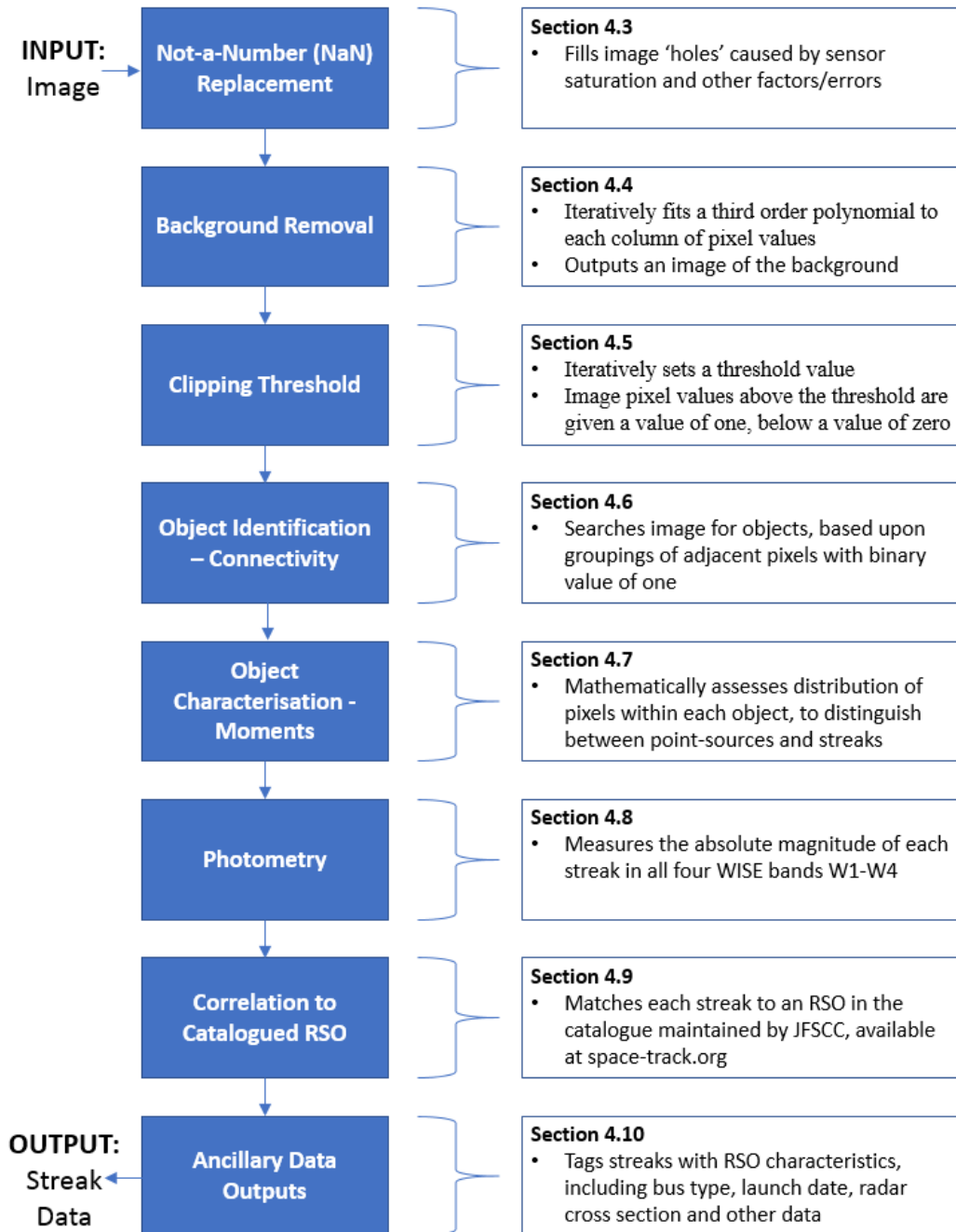
Figure 4.1: The concepts used within the WISEstreakDET algorithm, as described in detail throughout this chapter, are summarised in the above flowchart. The Section applicable to each concept is provided for reference.
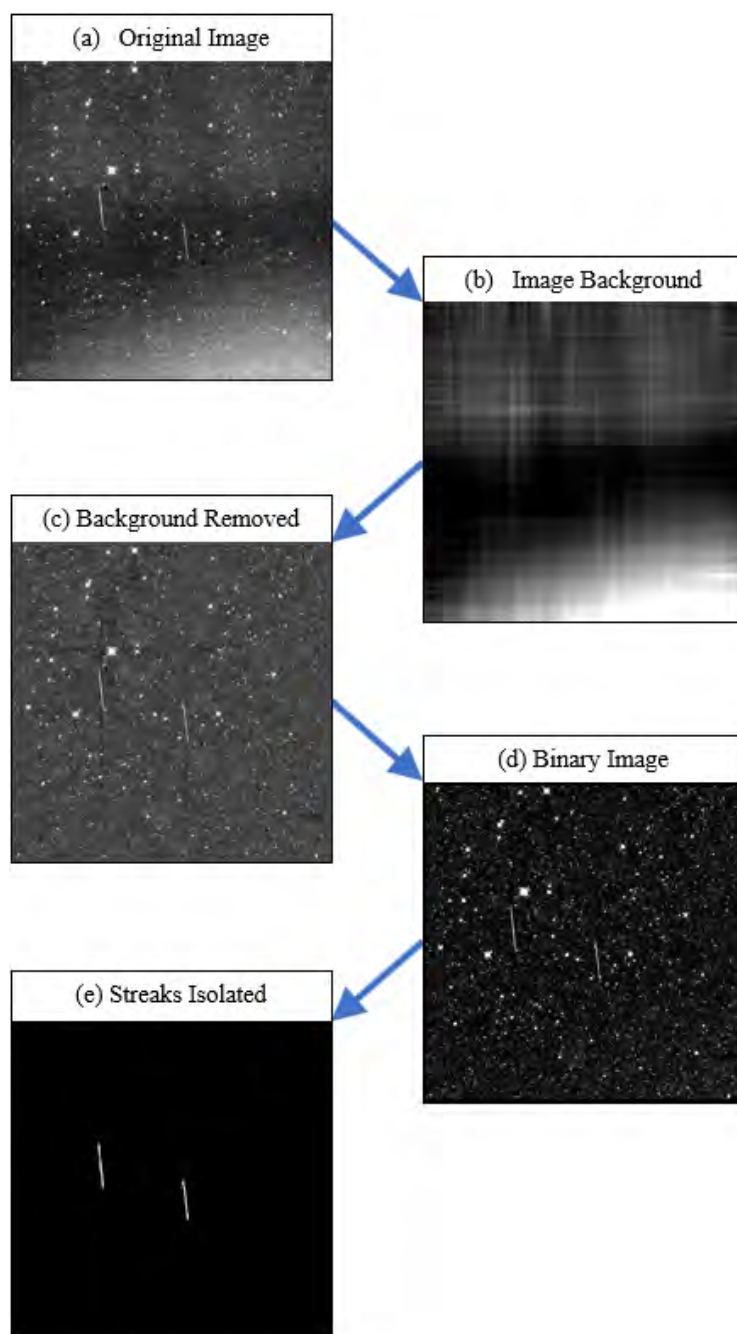
Figure 4.2: Pictorial representation of the WISEstreakDET algorithm. Adapted from Lévesque and Buteau [57], using WISE imagery processed with WISEstreakDET.

4.2   Preliminary Streak Detection

Prior to development of the final WISEstreakDET algorithm as outlined in Figure 4.1, several other streak detection processes were implemented in MATLAB and tested against WISE database imagery. The most time was spent developing an algorithm based upon the Hough transform, as described in Section 3.1.2. Images were first manipulated using mathematical morphology processes, which aim to extract desired image components such as streaks. Various methods described in Gonzales et al. [96] were tested, with a combination of pixel dilation, Canny edge detection, and skeletonisation providing the best outcome.

However, it was found that this method of streak detection, when applied to the diverse set of WISE images, was overly susceptible to false positive detections. In particular, diffraction spikes and other straight-line artefacts were returned as streak candidates. See for example Figure 4.3, in which the diffraction spike from a bright point-source was detected. A false-positive detection process could have been implemented, however WISEstreakDET was observed to be much less susceptible, and as such no further effort was spent on development of the Hough transform.

(a)   (b)
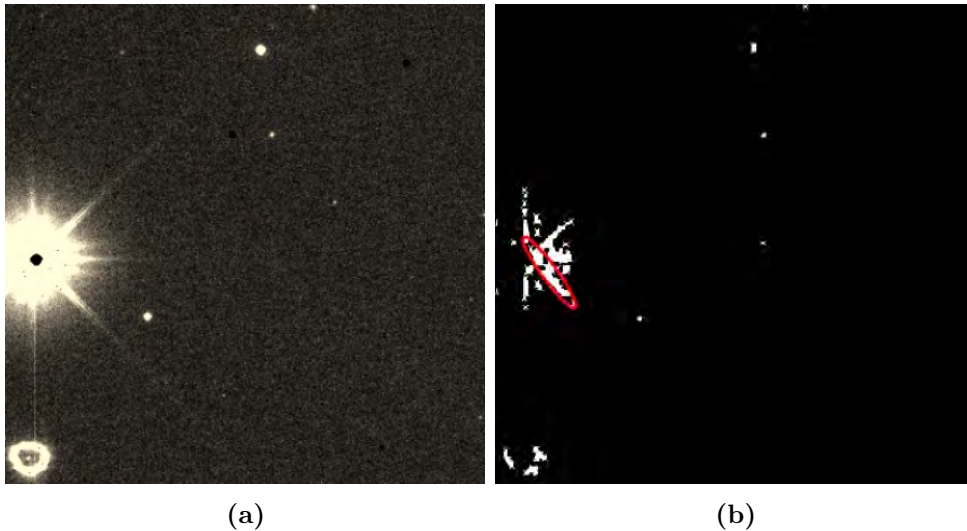
Figure 4.3: *(a)* WISE single-exposure image 01829b123, showing diffraction spikes from a bright point-source. *(b)* A preliminary algorithm based upon the Hough transform detects these straight line artefacts.

4.3   Not-a-Number Pixel Removal

During image capture, a bad pixel value may be recorded for several reasons, including pixel saturation, excessive noise, or highly positive/negative values caused by cosmic rays or sensor errors [44]. These bad pixel values are detected during the WISE image processing pipeline, and are replaced by a value of Not-a-Number (NaN). As a result, single-exposure images in the ALLWISE database contain numerous NaN pixel values. NaN's are often grouped, resulting in 'holes' within an image. Figure 4.4 shows an example of a point-source image, and the associated pixel values, including NaN's.

409.7	562.66	1039.2	944.33	743.01	650.62	517.16
517.72	1169	2823.1	3772.5	2084.2	1182	1115.6
911.51	1886.8	NaN	NaN	17011	NaN	1694.9
1266.2	3457.2	19254	NaN	NaN	15105	2093.3
1431.3	5217.7	NaN	NaN	NaN	10530	2420.2
1314.9	3367.2	12507	19296	18582	3519	1599.1
1181.5	1511.7	2385.2	2938.7	3152.6	1199.5	663.97

(a)   (b)
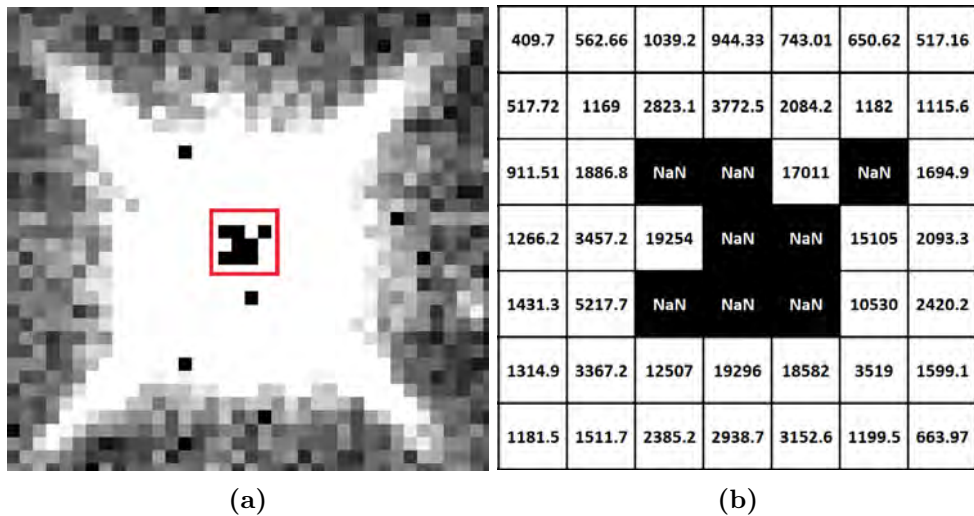
Figure 4.4: *(a)* WISE single-exposure image of a point-source, with NaN values producing visible 'holes'. *(b)* Pixel values within the red square - NaN values have been shaded black, reproducing the same shape observed on the point-source.

It is preferential to replace NaN values within an image prior to processing [97]. NaN values within a streak may lead to missed or incorrect detection, and the presence of NaN values would also lead to errors in the calculation of streak brightness (magnitude). Care must be taken, however, to ensure that the inserted values reflect those in surrounding pixels, to avoid the introduction of erroneous magnitude calculations. This process of accurately replacing NaN pixels based upon surrounding values is known as *inpainting* [97].

NaN values were inpainted in WISEstreakDET, prior to images being processed for the detection of streaks. Pre-existing, peer-reviewed code - *in-*

paint_nans - developed by D'Errico [98] and posted on MATLAB Central File-Exchange, was used for this purpose. *inpaint_nans* searches the entire image array for NaN values, then formulates a Partial Differential Equation (PDE). PDEs, unlike Ordinary Differential Equations (ODEs), contain multiple variables and are inherently more complex to solve. The code uses pixel values surrounding NaN 'holes' as boundary values, creating functions and derivatives at these points. The functions are then solved as a linear system of equations to produce the NaN pixel replacement values [98].

Figure 4.5a shows WISE image 01993a193-w2, prior to replacement of NaN pixel values. Several holes are evident along the length of each streak, upon point sources, and in areas of the sky. Figure 4.5b shows the same image following application of *inpaint_nans*, with holes filled.

(a) With NaN values   **(b)** NaN values replaced
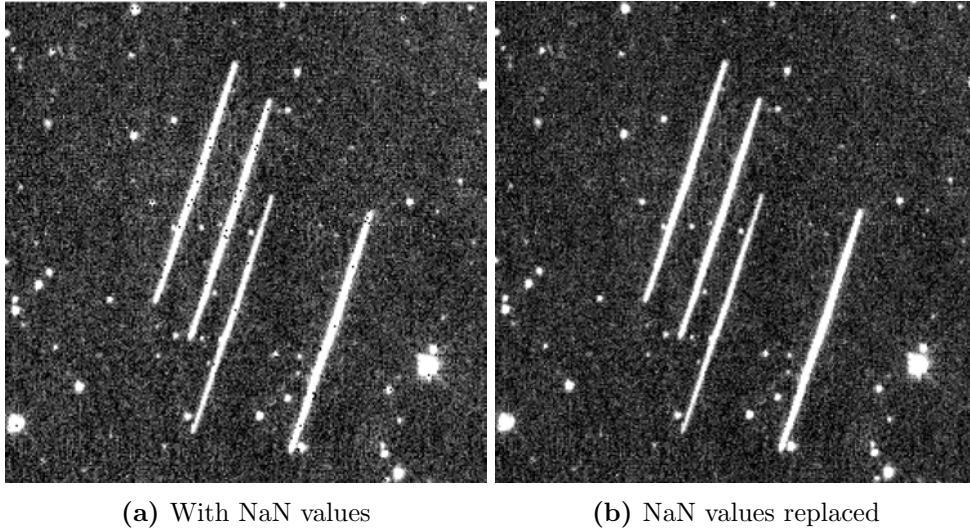
Figure 4.5: *(a)* WISE band W2 image 01993a193, prior to application of the NaN replacement algorithm. Several holes along the length of each streak, upon point sources, and in areas of the sky are evident. *(b)* The same image, following application of the NaN replacement algorithm, with holes filled.

4.4 Background Subtraction

When a pixel records flux from an RSO streak, it also records flux from nearby signal sources such as stars or cosmic rays, and from the sensor itself. This additional contribution is known as the background [9].

An astronomical image, such as those in the WISE single-exposure database being used for this research, may be considered as the combination of two components: signal (streaks and point-sources) and the background [57]. This is shown by Equation 4.1, where I is the image under analysis, S the signal sources, and B the background noise [58]. Therefore, to allow for the detection and measurement of streak flux (S), particularly those that are faint with low SNR, removal of image background (B) is desired. This section will focus upon the background, while residual noise will be dealt with in Section 4.6.

$$I = S + B \qquad (4.1)$$

Stationary, ground-based telescopes generally view the same segment of the night sky, and therefore witness a relatively constant level of background noise attributable to cosmic sources. Conversely, the WISE satellite was developed to capture imagery of the entire sky. As a consequence, the segment of celestial sphere visible in imagery, and therefore the number and brightness of cosmic sources, is highly variable. NASA produced five images of this background variance over the entire celestial sphere, one for each WISE band, and an amalgamation as shown in Figure 4.6 [44]. The Milky Way galactic plane is evident as the highest source of background, running horizontally across the image. The apparent path of the Sun (the Ecliptic) is observed as a golden swath passing through the centre, while the curved blue bands show elevated background as a result of residual Moon glow.
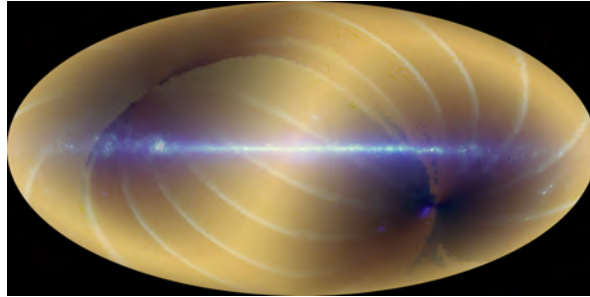
Figure 4.6: An image produced by NASA shows a summary of background noise variance in WISE imagery over the entire celestial sphere [44].

WISE captured images in four different bands of the infrared regime, with each band sensitive to different wavelengths of cosmic sources. This means that between bands, a large variance in background is evident, as shown in Figure 4.7

(a) W1 **(b)** W2

(c) W3 **(d)** W4
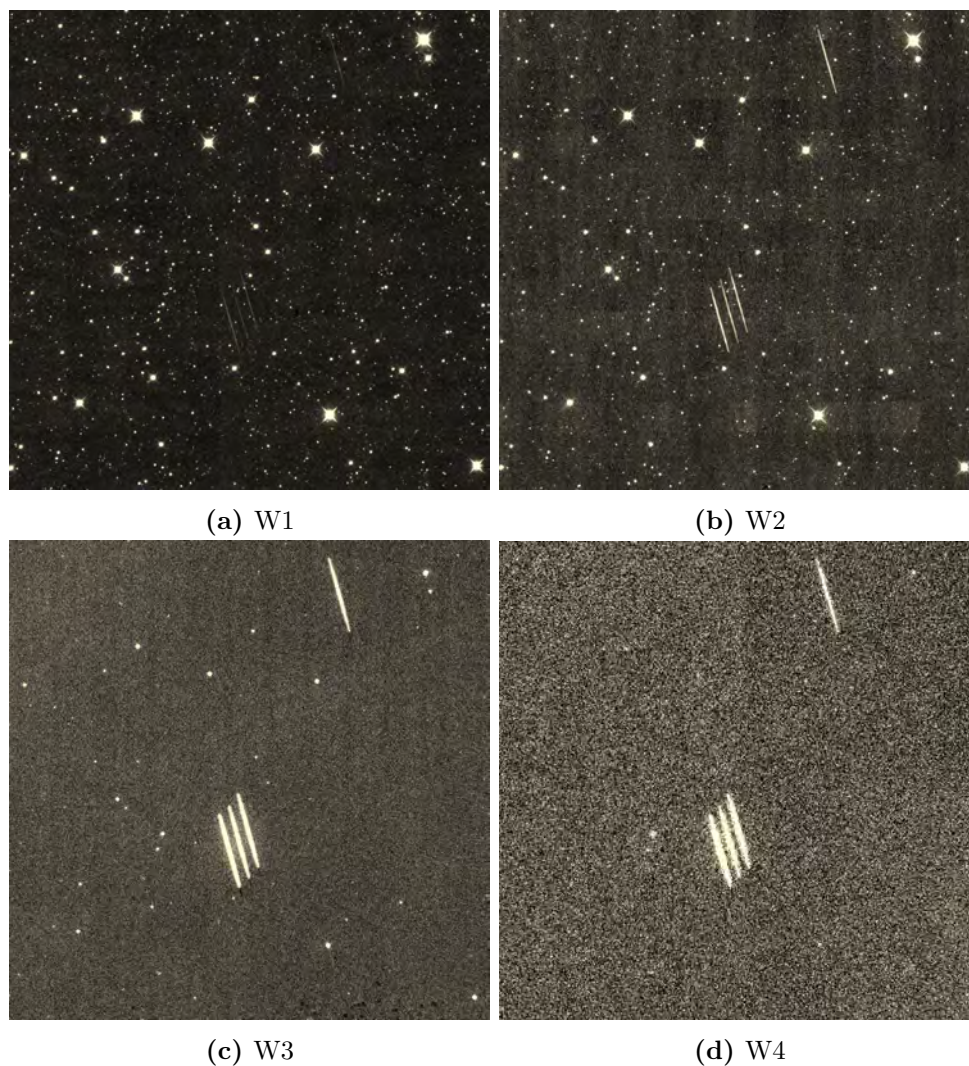
Figure 4.7: Wise single-exposure database imagery of frame 01992a095, in bands *(a)* W1, *(b)* W2, *(c)* W3 and *(d)* W4. A large variance in background is evident.

Due to this strong variance in background, WISEstreakDET required a process that accurately measures background levels in each individual image for subtraction purposes. To achieve this aim, MATLAB code developed by Lévesque and Buteau [57, 58] was obtained, and adapted to suit WISE imagery taken in multiple bands with differing exposure times and image size.

The background subtraction algorithm takes advantage of the fact that image background is typically smooth, and can therefore be modelled using polynomial fitting [57]. However, point-sources and streaks, being local sources of increased flux, interrupt this polynomial fitting process. Figure 4.8 shows two images, in bands W3 and W1, with a horizontal (image row) profile of pixel values taken along the given red line. These images demonstrate both the relatively constant nature of the background, and the interruption to the profile caused by point-source and streak flux. Figure 4.8 also demonstrates the particular importance of the background subtraction process in band W1, where streak signal is difficult to distinguish from the background level, and is dominated by point-source intensities.

(a) W3 Image

(b) W3 Line Profile

(c) W1 Image
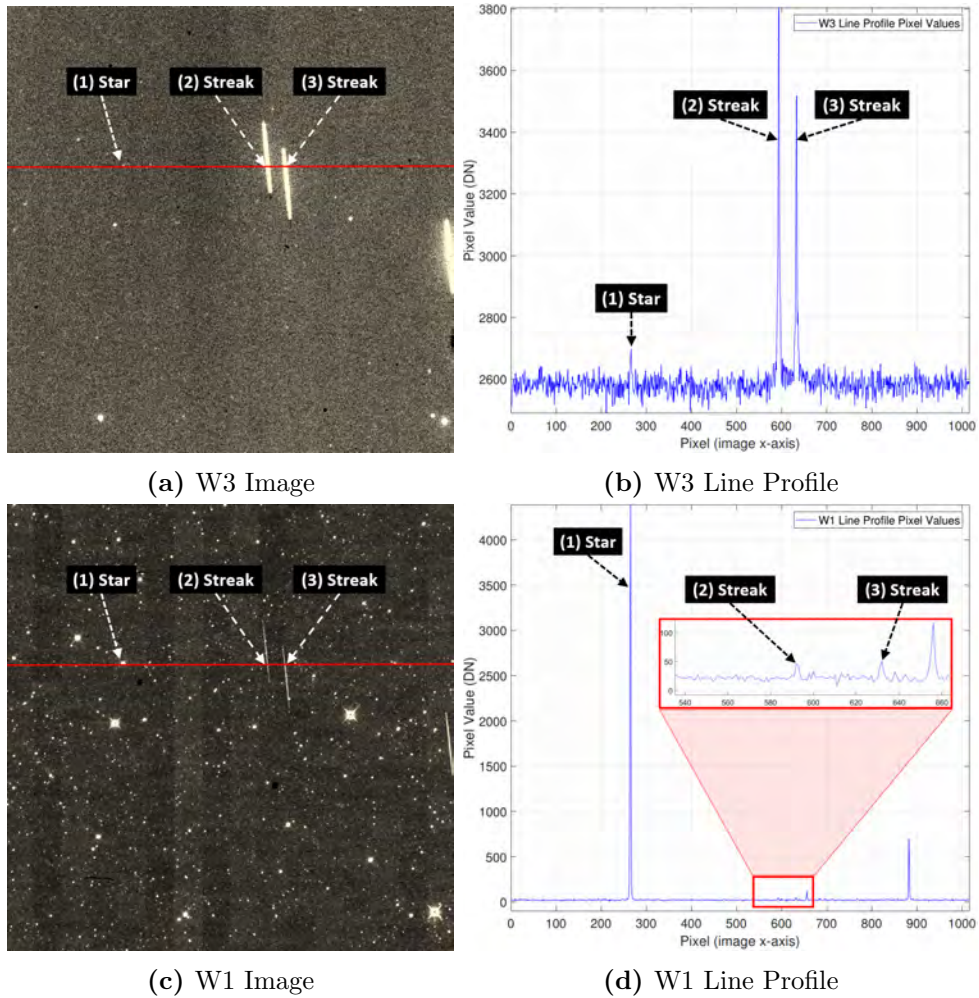
(d) W1 Line Profile

Figure 4.8: *(a)* Image frame 00808a115 in band W3, with *(b)* an associated horizontal (image row) line profile taken along the red line. Locations of a single point-source and two streaks are shown in the image, as well as their associated pixel values in the line profile. It can be seen that in band W3, streak signal is well above the background level, and also often stronger than point-source flux. In band W1 however, as shown in *(c)* and *(d)*, the same streaks are almost indistinguishable from the background, and are dominated by point-source flux. This demonstrates the particular importance of background subtraction in band W1.

To avoid the interruption to polynomial fitting caused by the presence of point-sources and streaks, the background subtraction algorithm utilises an iterative process [57]. For the first iteration, column (vertical) line profiles are taken over the entire image, and the pixel values stored in a matrix. For each column, a polynomial of the third order is determined via the best fit to data in the pixel value matrices. The general form of the third order polynomial is shown in Equation 4.2, where i is the image row, j the image column, and P_n the polynomial coefficients up to the order of n.

$$\text{pixel(i, j)} = P_{0j} + P_{1j}\ i + P_{2j}\ i^2 + P_{3j}\ i^3 \qquad (4.2)$$

The first iteration is highly influenced by the large pixel values of point-sources and streaks, affecting the initial fit. To account for this, the polynomial coefficients (P_n) of each column are compared, and their standard deviation determined (σ_P). Coefficients of adjacent columns are typically similar, due to the relatively constant nature of background noise. If adjacent values are quite dissimilar, this therefore indicates the presence of a strong source signal. The algorithm extracts these dissimilar polynomial coefficients if they differ by more than $3\sigma_P$, and replaces them by an interpolation of adjacent values.

Following adjustment of the first iteration to account for the presence of strong point-sources and streaks, a second iteration is carried out. This iteration attempts to ignore the contribution of remaining signal sources, by thresholding values to that of the first iteration plus a set constant. This constant was set to 50 by Lévesque and Buteau [57, 58], and was not adjusted for the purposes of WISE imagery. A third iteration is then conducted, setting a new threshold of 3σ above the background level determined by the second iteration.

The polynomial fits resulting from the third iteration are used to create a background image, of the same size as the input image. An example of such a background image is shown by Figure 4.2b. As per Equation 4.3, the individual pixel values of the background image (B) are subtracted from the corresponding input image pixel values (I) to create a background subtracted image, an example of which is shown by Figure 4.2c. For images containing a point-source or streak, pixel values now represent the signal (S) and any residual noise (n) not removed by the subtraction process. The entire background subtraction process is summarised in Figure 4.9.

$$\text{I} - \text{B} = \text{S} + \text{n} \qquad (4.3)$$
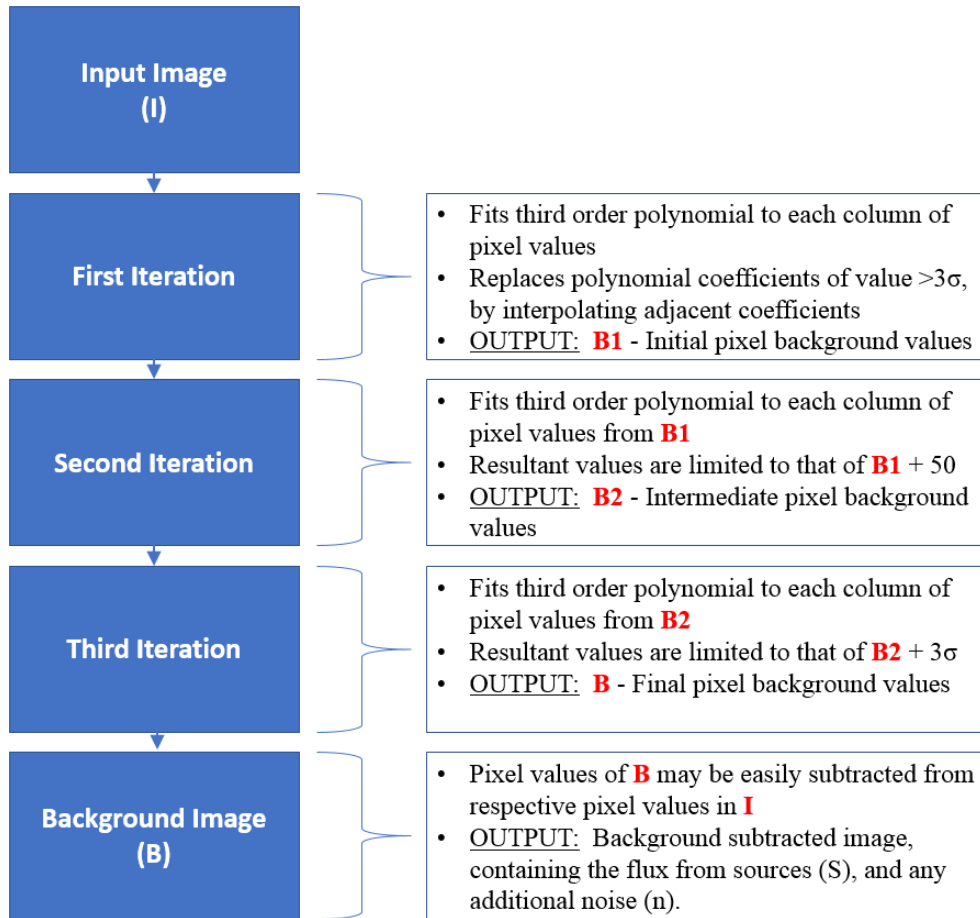
Figure 4.9: A summary of the background subtraction process, developed by Lévesque and Buteau [57] [58], and adjusted to suit WISE imagery taken in multiple bands with differing exposure times and image size.

4.5 Clipping Threshold

Now that the background (B) has been removed from the original image (I), pixels belonging to signal sources (S) need to be isolated from those attributable to remaining noise (n), per Equation 4.4. This is achieved via the elimination of noise pixels that are below a set threshold value - a process known as 'clipping' [99].

$$S = I - B - n \tag{4.4}$$

Setting the threshold value is a fine balance: if set too high, faint streaks will be clipped and therefore not detected; too low, and enough noise will remain between individual objects that they may be considered as one. A simple determination of the threshold value is possible by calculating the standard deviation (σ) of pixel values over the entire image, and clipping those pixels below a multiple of this σ value [99]. However, this process tends toward erroneously high threshold values, due to the presence of pixels in point-sources and streaks that possess exceedingly higher values than those in background removed noise.

Wallace [99] and Thorsteinson [37] developed an algorithm for use in the automated detection of streaks observed by DRDC. This algorithm allows for accurate determination of threshold values, via the implementation of an iterative process. The authors were generous enough to provide this algorithm, which was adapted for use with WISE imagery.

The clipping threshold algorithm first determines the standard deviation of the entire background subtracted image, denoted σ_{C1}. To discount strong point-sources and streaks, any pixels with a value greater than $1.5\sigma_{C1}$ above the mean background value determined in Section 4.4 are removed from consideration. The standard deviation of remaining pixels is then recalculated, denoted σ_{C2}. σ_{C1} and σ_{C2} are compared, and the entire process is repeated until the two standard deviation values differ by less than 10%. The initial clipping factor of $1.5\sigma_{C1}$ above the mean background was found by Wallace [99] and Thorsteinson [37] to strike the best balance between removing noise pixels, while retaining the ability to detect faint streaks. WISE imagery used in this research was extensively tested with various clipping factor values, and 1.5 was also found to be optimal.

Once the clipping threshold for an individual image has been determined, image pixels above the threshold are assigned a value of one, and those below

80

a value of zero. This has the effect of creating a binary image, in which ideally only the contribution of source flux remains. Depending upon the success of the clipping process, however, some noise will remain that will be dealt with in Section 4.6. An example of the resultant binary image is shown at Figure 4.2d.

Figure 4.10 provides an example of the importance of correctly setting the clipping threshold: two streaks within the band W3 image of frame 01274a129 are evident by strong peaks at x-axis pixel locations 740 and 775. The inset box provides a close-up view of the pixel values in close proximity to these streaks, in which the Gaussian nature of noise is evident. The upper black dashed line (erroneously high clipping threshold) shows how faint streaks may be clipped, while the lower black dashed line (erroneously low) shows how noise may be retained, potentially leading to the two streaks being 'connected' as one object. The solid green line at a value of 36 Digital Numbers (DN) represents the clipping value used for this particular image.
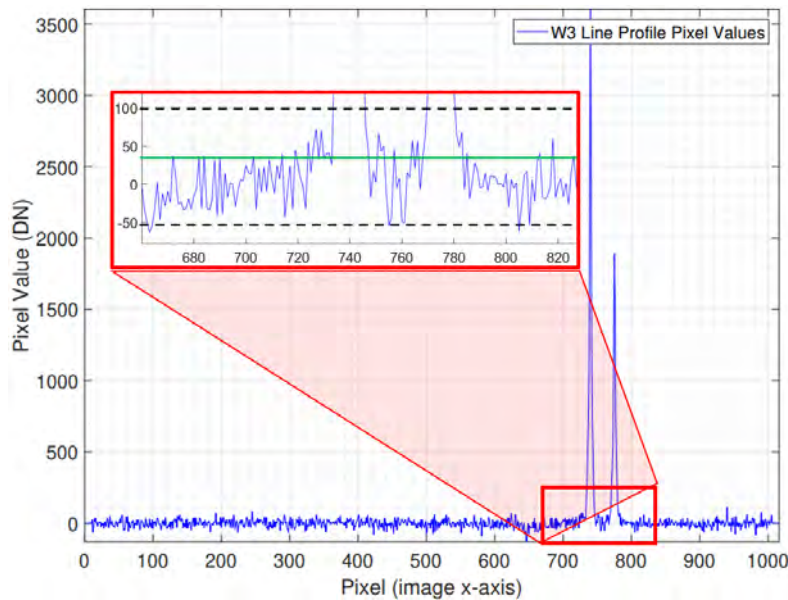
Figure 4.10: Image frame 01274a129 in band W3, with two streaks at x-axis values 740 and 775. The solid green line represents the ideal clipping value for this image, while the dashed black lines are examples of erroneously high and low clipping values.

4.6 Object Identification - Connected Pixels

In the previous step, pixels were assigned a value of one if above the set clipping threshold, or zero if below the threshold. This sought to discriminate pixels belonging to an object (point-source or streak) from those belonging to the background [100]. The next step is to identify individual objects - when multiple pixels form a group, based upon their 'connectedness'. Connectivity is defined as two pixels being adjacent, with a binary value of one.

Taking this concept further, a level of connectivity may be specified: 4-connected or 8-connected [101]. If *any* of the 4 pixels above, below or to the side of a central pixel with binary value of one also have the binary value one, as in Figure 4.11a, then those two pixels are said to be 4-connected. Similarly, if *any* of the eight pixels surrounding a central pixel with binary value of one also have the binary value one, as in Figure 4.11b, then those two pixels are said to be 8-connected.

(a) 4-connected   **(b)** 8-connected
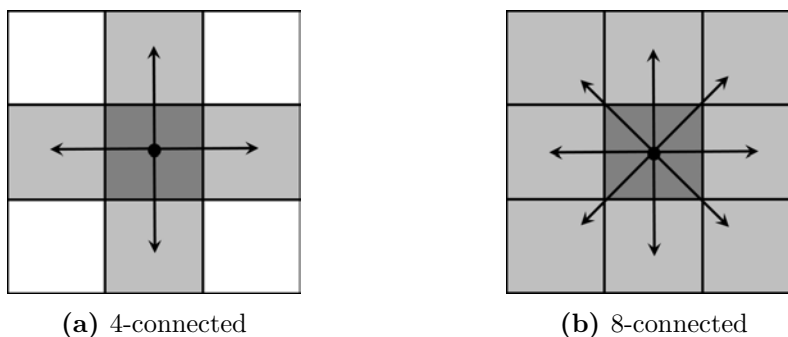
Figure 4.11: Tests to determine if adjacent pixels are *(a)* 4-connected, or *(b)* 8-connected.

The number of pixels in an object is affected by the specified level of connectivity. For example, the pixels with value of one in Figure 4.12a may be defined as both 4 and 8-connected, while those in Figure 4.12b are 8-connected only. For Figure 4.12c, the object will contain only the lower two pixels if 4-connected is specified, but all three pixels if 8-connected is specified.

(a) 4 and 8-connected   **(b)** 8-connected only   **(c)** Number of pixels in this object depends upon specified connectivity
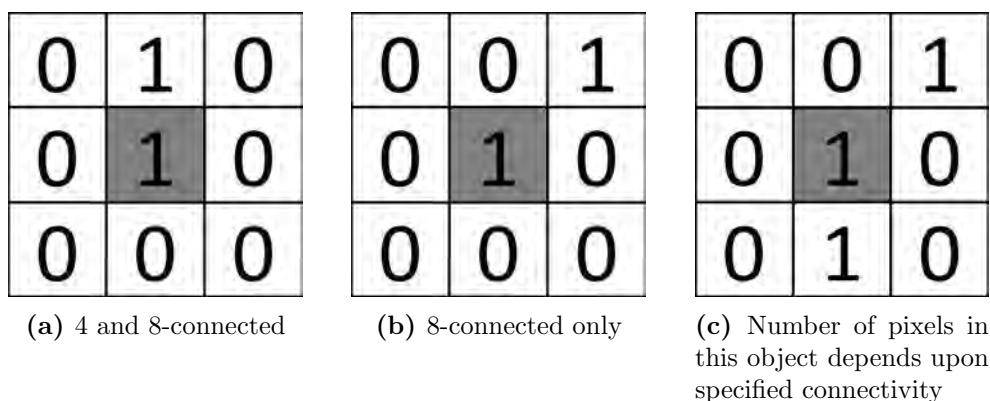
Figure 4.12: The grouping of pixels as an object depends upon the level of connectedness specified.

There is also an interdependence between the clipping threshold value, and the level of connectivity specified. If a lower clipping threshold value is set, more noise will remain after clipping. 4-connected is more suitable in this instance, as adjacent pixels are less likely to be grouped as objects, leaving noise pixels isolated for future removal. Conversely, if 8-connected is specified, the clipping value needs to be higher as any remaining noise is more likely to be classified as an object.

Following testing on images with known streaks of varying size and magnitude, 8-connectivity was specified for initial streak detection on band W3 images in WISEstreakDET. The clipping value of 1.5 std above the mean background value was selected to be high enough such that minimal noise remained after clipping. If fainter streaks are to be sought in subsequent research, consideration would be given to setting 4-connectivity as the requirement, and lowering the clipping threshold.

Some noise will remain following the background subtraction and clipping process, as shown in Figure 4.10. However, it is likely isolated and by definition random, and therefore its associated pixels are generally not well connected [99]. Remaining noise, that had been mis-classified as an object, was therefore further eliminated through a minimum pixel test. The number of pixels in each connected object is summed, and those objects with fewer than a set minimum are filtered out. This number was set at twenty pixels, allowing faint or distant RSOs to still be detected, while filtering out as much remaining noise as possible.

4.7 Object Characterisation - Moments

Following the connectivity tests, remaining groups of pixels are treated as objects. The next step is to discriminate point-source objects from streaks. This is achieved through the use of image moments, which analyse various characteristics of each object.

Image moments have been widely used in image processing for several decades, due to their relative mathematical simplicity and diversity of application [102, 103]. Early practical applications included letter recognition - for example identifying individual letters from digitised written texts. More recently, the rapidly developing field of machine learning, or artificial intelligence, makes use of image moments for pattern recognition and object detection purposes [104, 105].

Moment theory is based upon the distribution of objects in relation to a reference point or object [106]. While moment theory may be applied to objects in three-dimensional space, for the purposes of image processing in WISEstreakDET only the two-dimensional application will be considered. Image moments, when considering a two-dimensional binary image, look at the relative distribution and density of pixels assigned a value of one, in Cartesian space. An image moment may then be defined per Equation 4.5, where m is the moment of order $(p + q)$, x and y are the image row and column coordinates, and Ω the set of points (pixels) in the image plane [106].

$$\mathrm{m}_{pq} = \iint_{\Omega} x^p y^q \ f(x,y) dx dy \qquad (4.5)$$

The centroid location $(\bar{x}, \bar{y})$ of each object identified by WISEstreakDET was determined via the mean row and column values of its pixels. Once object centroids are known, moments may be calculated by adjusting Equation 4.5 to produce Equation 4.6.

$$\mathrm{m}_{pq} = \sum_{x,y \epsilon \Omega} (x - \bar{x})^p \ (y - \bar{y})^q \qquad (4.6)$$

Moments up to an order of two - that is m_{00}, m_{01}, m_{02}, m_{10}, m_{11} and m_{20} - define the basic object geometry being sought to discriminate point-sources from streaks. Specifically, individual moments and their combination may specify the characteristics cited in Equations 4.7 to 4.13 [103, 106, 107].

4.7.1 Zeroth Order Moment - Area

$$\text{Number of object pixels, or area:} \qquad m_{00} \qquad (4.7)$$

4.7.2 First Order Moments - Centre of Mass

$$\text{Centroid location:} \qquad \bar{x} = \frac{m_{10}}{m_{00}} \qquad (4.8)$$

$$\text{Centroid location:} \qquad \bar{y} = \frac{m_{01}}{m_{00}} \qquad (4.9)$$

4.7.3 Second Order Moments - Inertia

$$\text{Orientation:} \qquad \phi = \frac{1}{2}\tan^{-1}\left(\frac{2m_{11}}{m_{20} - m_{01}}\right) \qquad (4.10)$$

$$\text{Semi-major axis:} \qquad \alpha = \left(\frac{2[m_{20} + m_{02} + \sqrt{(m_{20} - m_{02})^2 + 4m_{11}^2}]}{m_{00}}\right)^{1/2} \qquad (4.11)$$

$$\text{Semi-minor axis:} \qquad \beta = \left(\frac{2[m_{20} + m_{02} - \sqrt{(m_{20} - m_{02})^2 + 4m_{11}^2}]}{m_{00}}\right)^{1/2} \qquad (4.12)$$

$$\text{Eccentricity:} \qquad e = \frac{\sqrt{(m_{20} - m_{02})^2 + 4m_{11}^2}}{m_{20} + m_{02}} \qquad (4.13)$$

The prevailing discriminator between point-source and streak objects is eccentricity (e) - a measure of how much a shape deviates from being a circle. As point-sources are typically of a circular shape, e is close to zero. Streaks, meanwhile, are typically more extended and linear, and therefore e is closer to 1. Following testing on over 100 images with known streaks of varying size and magnitude, 0.85 was chosen as a cut-off value, above which an object was classified as a streak, and below which it was classified as a point-source.

4.7.4 Adjusted Centroid

While the centroid coordinates determined by Equations 4.8 and 4.9 are useful for subsequent moment calculations via Equation 4.6, a more precise method is desired to accurately measure the streak magnitude and position relative to a coordinate system. This is achieved by assigning different 'weights' to streak pixels depending upon their intensity, and is known as the Weighted Centre of Gravity (WCoG) method [108].

The WCoG method is summarised by Equation 4.14, where $\hat{x}$ and $\hat{y}$ are the final weighted x and y centroid pixel locations, x and y the location of individual streak pixels, n the number of iterations (equal to the number of streak pixels), and $I_{x,y}$ the pixel intensity value at image coordinate x,y. In MATLAB, Equation 4.14 was implemented in an iterative fashion. The WCoG method works best when background noise is minimised [109] - for this reason, pixel intensities ($I_{x,y}$) were taken from the background subtracted image, as described in Section 4.4.

$$
\begin{aligned}
\hat{x} &= \frac{\sum\limits_{1}^{n} x\, I_{x,y}}{\sum\limits_{1}^{n} I_{x,y}} \\[2em]
\hat{y} &= \frac{\sum\limits_{1}^{n} y\, I_{x,y}}{\sum\limits_{1}^{n} I_{x,y}}
\end{aligned}
\tag{4.14}
$$

4.8 Photometry

Now that objects within an image have been classified as either streak or point-source, analysis of streaks may commence. For each streak, the magnitude as defined in Section 1.6 is calculated in all four WISE bands W1 - W4.

4.8.1 Streak Aperture and Sky Annulus

When determining the flux received from a source, in this case from a streak created by the relative movement of an RSO across WISEs field of view, there are two main methods available: fitting by point spread function (PSF) or through the use of a digital aperture [16]. The chosen method depends upon several variables, primarily the research objectives and whether images contain many, crowded sources [9]. Due to the inconsistent nature of imagery in the WISE database - namely four separate bands with varying background and number of sources - digital aperture photometry was implemented for the sake of consistency.

The streak characteristics determined by moments, as described in Section 4.7, were used to fit an ellipse around an individual streak to create digital apertures. Specifically, the centroid ($\hat{x}$ and $\hat{y}$), semi-major axis (α), semi-minor axis (β) and orientation (ϕ) are used in Equation 4.15 to create x and y coordinates of an ellipse fitted to an individual streak [110]. The number of points used to create the ellipse is determined by the index variable t, which in the case of WISEstreakDET was set to 0:2π:100.

$$
\begin{aligned}
x &= \beta\cos(t)\cos(\phi) + \alpha\sin(t)\sin(\phi) + \bar{x} \\
y &= \beta\cos(t)\sin(\phi) - \alpha\sin(t)\cos(\phi) + \bar{y}
\end{aligned}
\tag{4.15}
$$

Although the digital aperture has been created based upon geometry of the detected streak, some size adjustment was required. The exact 'border' of a streak is dependent upon the variables implemented in the process of clipping, connectedness and moments as described in Sections 4.5 to 4.7. Precisely fitting an ellipse therefore may lead to some flux from the streak being missed. This is a fine balance: too small an ellipse will lead to missed source flux, while too large an ellipse will lead to more background noise surrounding the streak being counted as source flux, decreasing the SNR [16]. Following testing on images with known streaks of varying size and magnitude, the source aperture

was created using Equation 4.15, with major-axis (α) and minor-axis (β) adjusted as per Table 4.1. This produced the highest SNR for each band in most images tested.

Band	Major-axis (α)	Minor-axis (β)
W1	1.2	1.1
W2	1.2	1.1
W3	1.2	1.6
W4	1.2	1.6

Table 4.1: Ellipses used for source apertures were multiplied by the factors above, in order to maximise SNR.

When the WISE IR sensor is capturing an image frame, it collects photons not only from the streak being analysed, but also from the astronomical sky in general. This is referred to as background, and as discussed in Sections 1.6 and 4.4 contains photons from the sensor itself, and astronomical sources near, behind and in front of the streak [16].

The background must therefore be ascertained, and removed from measurements, before a final determination of the total flux attributed to a streak is made. While the mean image background value determined in the background subtraction stage may be used for this purpose, an analysis of the background local to an individual streak is preferred [16]. To achieve this local background measurement, a 'sky annulus' is created surrounding the streak aperture. This annulus consists of the area between an inner ellipse, close to the streak aperture, and an outer ellipse. Similar to the streak aperture, size and placement is of importance: if the inner ellipse is too close to the streak, some source flux may be captured and recorded as background, while if the outer ellipse is too far from the streak the background may be too dissimilar to that near the streak [9].

Howell [16] states that in order to achieve a statistically significant measurement of the local background, the number of pixels contained within the sky annulus should be approximately three times the number of pixels within the streak aperture. Pixels in the aperture and annulus were counted by creating an image mask of each; all ellipse x and y coordinates and the associated internal area pixels were given a value of 1, and then summed. For the annulus, subtracting the number of pixels contained within the inner ellipse from the outer was required. Background annulus ellipses were then created, centred on the streak aperture with adjustments to the major-axis and minor-axis

such that the pixel number ratio was on average as close to three as possible. Over the 1696 valid streaks detected and analysed, an average ratio of 3.06:1 between number of sky annulus pixels and number of streak aperture pixels was achieved. Axes adjustment factors are listed in Table 4.2

Band	Major-axis (α) (inner / outer)	Minor-axis (β) (inner / outer)
W1	1.3 / 1.35	1.8 / 4.7
W2	1.3 / 1.35	1.8 / 4.7
W3	1.3 / 1.6	2.2 / 5.5
W4	1.3 / 1.6	2.2 / 5.5

Table 4.2: Ellipses used for sky annulus were multiplied by the factors above, in order to achieve statistically significant background estimation values.

Figure 4.13 shows the final streak apertures and sky annuli applied to images from all four WISE bands. The magenta cross in the middle of the streak represents the centroid location, the red ellipse represents the streak aperture, and the area between the two green ellipses represents the sky annulus.

(a) W1

(b) W2

(c) W3

(d) W4
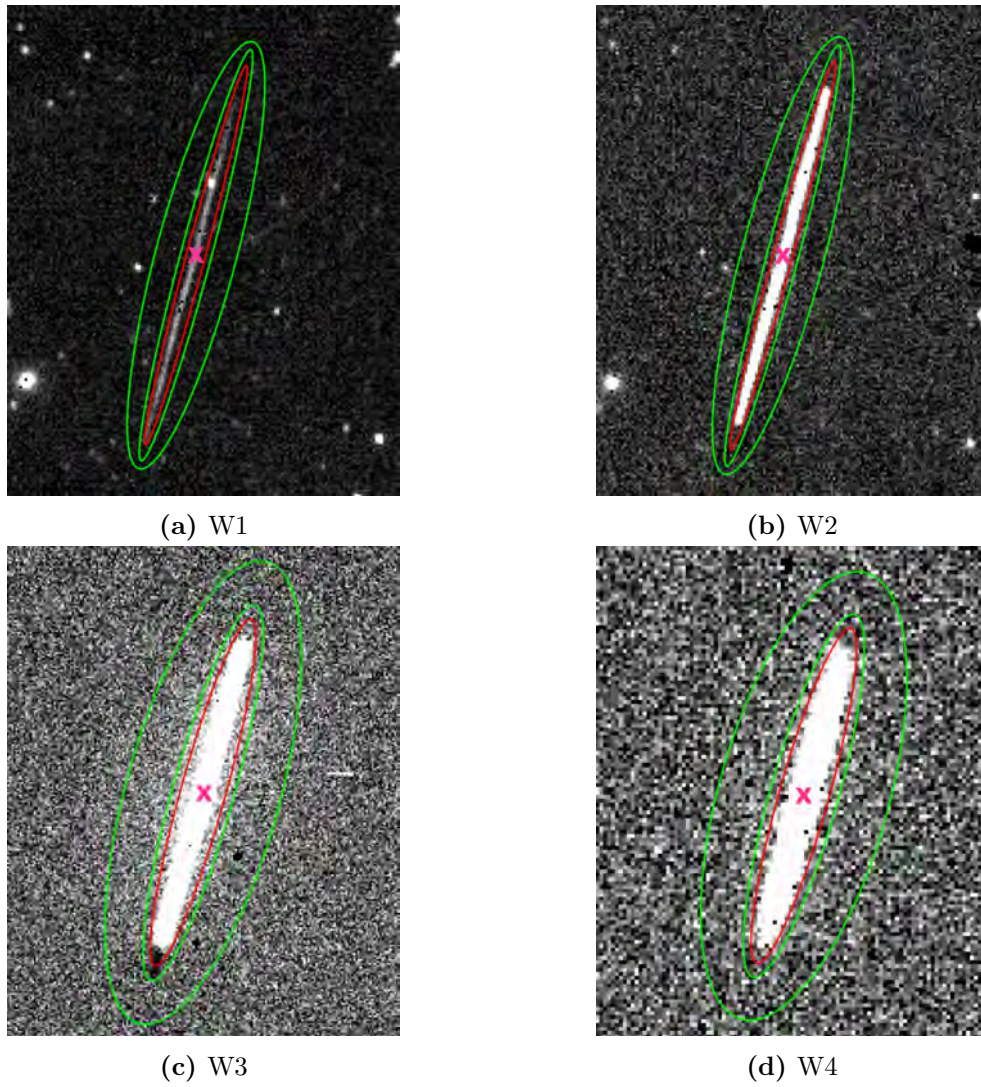
Figure 4.13: Centroid (magenta cross), streak aperture (inner red ellipse) and sky annulus (area between two outer green ellipses) are shown for a single streak. This single frame consists of images from WISE bands *(a)* W1, *(b)* W2, *(c)* W3 and *(d)* W4

An alternative means by which to measure the background is suggested by Chromey [9]: several sections of the image are selected, and the average pixel value within each section averaged. The median or modal value of these averaged sections is then taken as the overall background pixel value. This method carries the advantage of averaging out any bias that astronomical sources in close proximity to a streak aperture may induce. The downside, however, is that it may not provide a true estimation of the background value in proximity to a streak of interest, reducing the accuracy of magnitude measurements. In order to test the validity of this process, 100 equally distributed sky samples were taken, and both the median and modal values deduced. An example of these sky sections is shown in Figure 4.14. Upon analysis, there was not a statistically significant variation between the mean background pixel values calculated via the sky annulus method and the 100 sky section method. For this reason, the more traditional method of utilising a sky annulus in proximity to the streak of interest was adhered to.
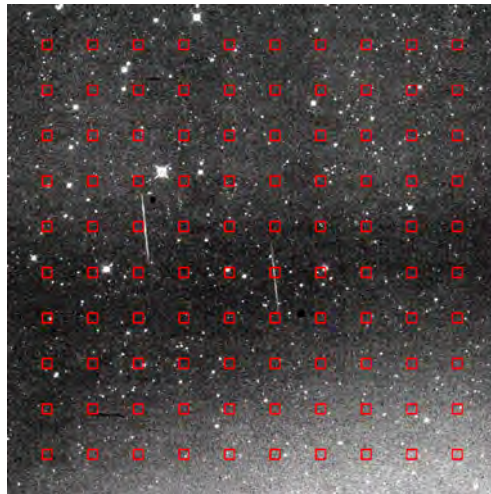
Figure 4.14: An image in WISE band W1, with 100 equally distributed sky sections shown by red boxes. Averaging the pixel value of each box, then determining the median or modal value over all boxes, is an alternate method to calculate the overall background pixel value. This method was not shown to significantly deviate from values calculated using the sky annulus method, and was therefore not used in final data output.

4.8.2 Magnitude

Before the magnitude of a streak may be measured, the mean background pixel value ($\bar{B}$) must be ascertained. This can be a simple process - all pixel values within the sky annulus are added together, and the total then divided by the number of pixels. However, a more statistically robust suggested by Howell [16] was implemented in WISEstreakDET.

Firstly, the median value of all sky annulus pixels is determined. Partial pixels were not of statistical concern and were therefore not considered, as the number of pixels within both the streak and sky annulus is quite large [16] Then, 'outlying' pixels with values greater than $\pm\, 3\sigma$ from the median sky annulus pixel value were removed. This seeks to eliminate the influence of point-sources, or bad pixels produced during image capture or read. This is of particular importance for determining streak magnitudes in bands W1 and W2, in which point-sources are numerous and often in close proximity to streaks. A histogram demonstrating the occurrence of outlying pixel values is shown in Figure 4.15. Should outlying values not be removed in this manner, the background level will be positively biased due to the influence of astronomical neighbours [9].
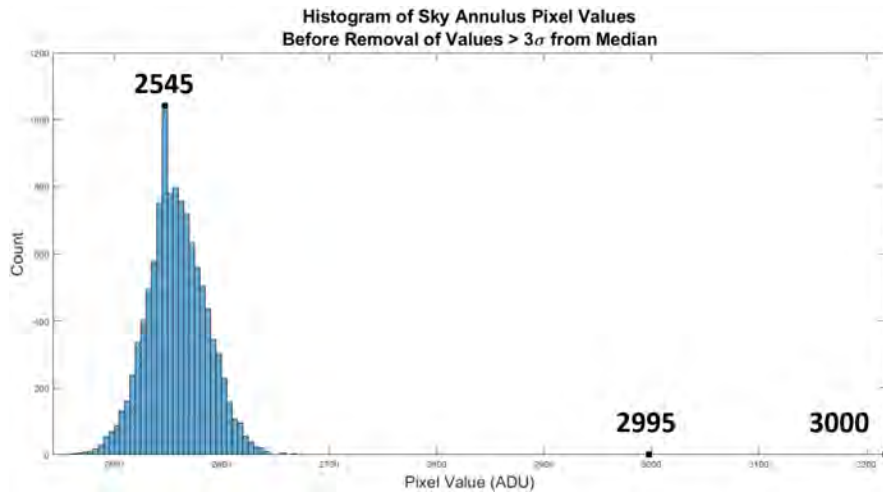
Figure 4.15: Histogram of pixels within the sky annulus, prior to removal of outlying pixel values ($> 3\sigma$ from median pixel value). Sample outlying values, potentially attributable to a neighbouring point-source, are shown on the right side of the histogram.

The final step in determining a value for $\bar{B}$ is to construct a histogram of pixel values remaining after removal of 3σ outliers. This histogram will be centred at the median of remaining pixel values; however, it will be ragged, with long tails, as a result of the relatively small sample size and bin width required. This is visually apparent in Figure 4.16. Histogram smoothing is therefore conducted to restore the distribution of values and shape of the histogram.
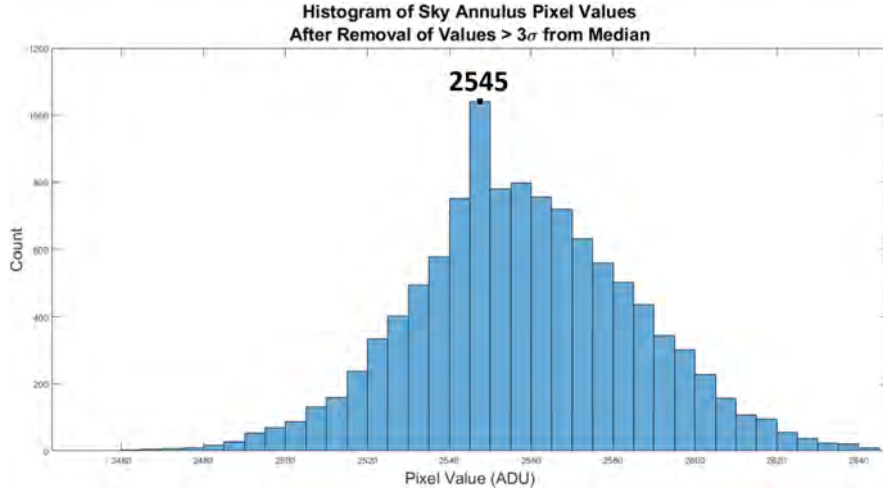
Figure 4.16: Histogram of pixels within the sky annulus, after removal of outlying pixel values ($> 3\sigma$ from median pixel value).

For the purposes of WISEstreakDET, a 'moving average' smoothing technique was implemented. Moving average, or moving window, arranges pixel values in ascending order and then inspects one pixel value at a time. This inspected value and a number of adjacent pixel values are averaged, and the output is used to replace the original pixel value being inspected. This is shown by Equation 4.16, where x is the input pixel value, y the output pixel value, i the sequential number of the input pixel value, j the window size (number of adjacent pixels to be considered), and M the specified size of the moving average filter [111]. The resultant histogram following this smoothing process is shown in Figure 4.17.

$$y[i] = \frac{1}{M} \sum_{j=0}^{M-1} x[i+j] \qquad (4.16)$$
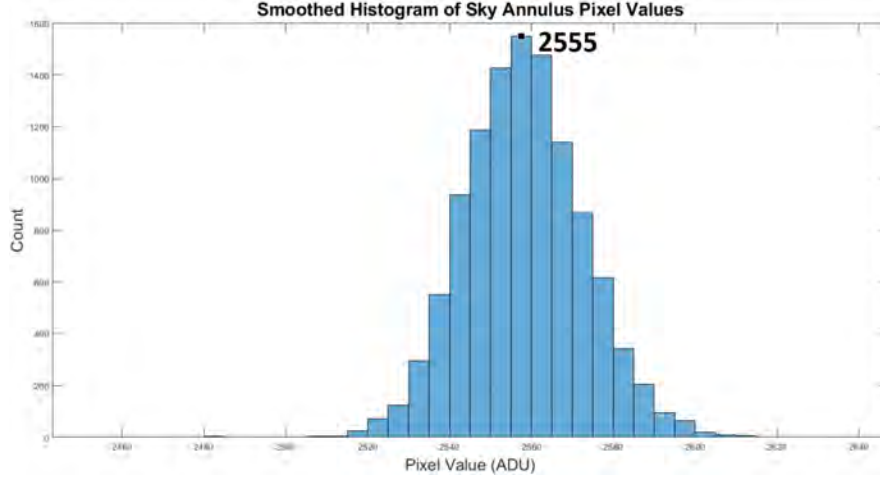
Figure 4.17: Histogram of pixels within the sky annulus, smoothed using a moving window process.

It can be seen from Figures 4.16 and 4.17 that the value of $\bar{B}$ was 2547.5 DN prior to smoothing, and 2557.5 DN after - a relatively minor change. However, small changes in the value of $\bar{B}$ can have a significant impact upon the accuracy of magnitude measurements, as $\bar{B}$ is eventually multiplied by the number of pixels in the streak aperture.

Now that the mean background pixel value, $\bar{B}$, has been determined for an individual streak, the magnitude of that streak may be calculated. The first step is to sum all pixel values contained within the streak aperture, denoted S [16]. As S is a sum of incident photons from both the streak and from the background, an intensity value I is determined using Equation 4.17, where n_{pix} is the number of pixels contained within the streak aperture.

$$I = S - (n_{pix})(\bar{B}) \tag{4.17}$$

Apparent magnitude for streaks is then determined using Equation 4.18, where m_b refers to the apparent magnitude, I the intensity, and ZP_b the zero-point in band b [44].

$$m_b = -2.5 \log_{10}(I_b) + ZP_b \tag{4.18}$$

The zero-point is a constant added to each measurement that allows for magnitudes to be calibrated to a standard photometric filter system [9]. Zero-

94

point values for each band in the single-exposure database used in this research are given in Table 4.3 [44].   These values were also listed in image FITS headers, allowing automated extraction for use in magnitude calculations in WISEstreakDET.

Band	ZP (mag)	ΔZP (mag)
W1	20.752	0.032
W2	19.596	0.037
W3	17.800	0.051
W4	12.945	0.063

Table 4.3: Instrumental zero-point values for each WISE band [44].

We have now measured both the flux attributed to the RSO of interest (S), and that of the background ($\bar{B}$). An indication of magnitude measurement quality may now be determined: the familiar term signal-to-noise ratio (SNR). However, SNR is not as simple as $S/\bar{B}$, as there are several contributors to the background that must be considered. One significant contributor is dark current, described in Section 1.3.1. Dark current is typically high in the infrared, particularly at longer wavelengths (W3 and W4). This introduces thermal noise during the readout process that is indistinguishable from source photons [17].

Equation 4.19 shows the well-known CCD equation, which is used in WISEstreakDET to determine the SNR of streak magnitudes, and subsequently their uncertainties [16]. S, $\bar{B}$ and n_{pix} are as previously defined, N_D is the total number of dark current photons per pixel, and N_R the total number of photons per pixel resulting from read noise. n_{pix} has already been determined when calculating S. N_D and N_R are reported in WISE technical documentation, based upon measured performance of the different detector focal plane array (FPA) types in use [44], and are summarised in Table 4.4. As N_D is measured in units of e$^-$/sec, multiplication by the exposure time is necessary to deduce the total dark current contribution.

$$\mathrm{SNR} = \frac{S}{\sqrt{S + n_{pix}\left(\bar{B} + N_D + N_R^2\right)}} \tag{4.19}$$

Parameter	HgCdTe FPA (W1 and W2)	Si:As FPA (W3 and W4)
Dark current (e^-/sec)	< 1	< 100
Read noise (e^-)	19	103

Table 4.4: Dark current and read noise values based upon measured performance of the HgCdTe and Si:As detector focal plane arrays (FPAs) [44].

While the SNR value provides an indication of magnitude measurement quality, an evaluation of measurement uncertainty is scientifically more useful. The relationship $\text{SNR} = 1/\sigma$ may be used to determine uncertainty, where σ is one standard deviation of the magnitude measurement for a particular streak [16]. A correction term of 1.0857 is applied, to account for the conversion from flux error to magnitude error. Equation 4.20 summarises the formula used in WISEstreakDET to measure streak magnitude uncertainty, denoted σ_{flux}. There is also an uncertainty term associated with the zero-point measurement for each WISE band, denoted σ_{ZP}; this is included in each image FITS header, and is added in quadrature to the magnitude uncertainty as shown in Equation 4.21 to arrive at the final measure of streak magnitude uncertainty, σ [9].

$$\text{SNR} = \frac{1}{\sigma_{\text{flux}}}$$
$$\Rightarrow \sigma_{\text{flux}} = 1.0857 \frac{1}{\text{SNR}} \tag{4.20}$$

$$\sigma = \sqrt{\sigma_{\text{flux}}^2 + \sigma_{\text{ZP}}^2} \tag{4.21}$$

4.9 RSO Correlation

Correlation refers to the process of matching a detected streak to a known RSO. A publicly available catalogue of RSOs is maintained by the Joint Force Space Component Commander (JFSCC), viewable online at space-track.org [112]. The purpose of the correlation algorithm, described in detail throughout this section, is to match RSO data from the JFSCC catalogue to streaks detected by WISEstreakDET.

4.9.1 Right-Ascension and Declination

In order to attempt correlation of an RSO streak to a catalogued object, the position of the RSO must be determined and translated to a standard coordinate system. As described in Section 1.4.4, the coordinate system most commonly utilised by astronomers is the equatorial system, referring to an RSOs position by right-ascension (RA or α) and declination (DEC or δ). This, therefore, is the coordinate system adhered to in determining streak position.

The first required input is the x and y coordinates of the streak centroid. These are obtained via the output of the WCoG centroid method, described in Section 4.7, and are denoted x_c and y_c (c for centroid). The next required input is the central pixel location of the image, denoted as x_o and y_o (o for origin). In the case of band W3 at 1016 x 1016 pixels, this equates to (x_o, y_o) = (508.5, 508.5). The next required input is the RA and DEC at the image centre, denoted as RA_o and DEC_o. Tthese are given in the FITS image header, and are automatically extracted for each image. The final required input is the image rotation value, denoted θ_R. This refers to the angle that the WISE sensor (and consequently the image) was rotated at image capture, relative to equatorial 'north' and 'east'.

Given these inputs, Equations 4.22 to 4.27 were implemented in code to determine the RA and DEC of the streak centroid. Notations are given in Table 4.5.

$$\Delta x = x_c - x_o$$
$$\Delta y = y_c - y_o \tag{4.22}$$

$$\Delta_{o,c} = \sqrt{\Delta x^2 + \Delta y^2} \qquad \text{(pixels)}$$
$$= \left(\sqrt{\Delta x^2 + \Delta y^2} \right) \times (s_p) \qquad \text{(arcseconds)} \tag{4.23}$$

97

$$\theta_{o,c} = tan\left(\frac{\Delta y}{\Delta x}\right) \tag{4.24}$$

$$\theta_{ALIGN} = \theta_{o,c} + \theta_R \tag{4.25}$$

$$\Delta\text{RA} = (\Delta_{o,c})\left(\frac{\cos(\theta_{ALIGN})}{3600}\right)$$
$$\Delta\text{DEC} = (\Delta_{o,c})\left(\frac{\sin(\theta_{ALIGN})}{3600}\right) \tag{4.26}$$

$$\text{RA} = \text{RA}_o - \Delta\text{RA}$$
$$\text{DEC} = \text{DEC}_o - \Delta\text{DEC} \tag{4.27}$$

Variable	Unit	Note
Δx / Δy	pixels	Distance along x-axis / y-axis between image origin and centroid
x_c / y_c	pixels	Centroid x / y axis location
x_o / y_o	pixels	Image centre x / y axis location
$\Delta_{o,c}$	arcseconds	Distance between image centre and centroid
$\theta_{o,c}$	degrees	Angle between image centre and centroid
θ_R	degrees	WISE sensor rotation at image capture
θ_{ALIGN}	degrees	Angle between image centre and centroid, aligned to relate x-axis to DEC, y-axis to RA
RA_o	decimal hours	Image centre RA
DEC_o	degrees	Image centre DEC
ΔRA	decimal hours	Centroid RA offset from RA_o
ΔDEC	degrees	Centroid DEC offset from DEC_o
s_p	arcseconds / pixel	The pixel scale, or number of arcseconds per image pixel

Table 4.5: Notation for Equations 4.22 to 4.27, used to convert the streak centroid pixel location to RA and DEC in the equatorial coordinate system.

4.9.2 Two-Line Elements

Now that the streak centroid RA and DEC have been determined, the coordinates must be compared to the position of all GEO RSO objects in orbit at the time of image capture. RSO positions are catalogued by JFSCC using Two-Line Elements (TLEs), as described in Section 1.4.

JFSCC provide an Automated Programming Interface (API), allowing for programmed, high-volume download of historical TLEs [113]. As GEO RSO streaks were the initial focus of this thesis, TLEs were requested for each RSO that met a set of GEO specific imposed conditions. TLE epoch was set between 10 December 2009 and 10 August 2010, corresponding to the date range of images in the initial dataset. To retrieve TLEs for GEO or

99

near-GEO objects only, the period was restricted to between 1400 and 1500 minutes. This period restriction was based upon Equation 1.11, in which the period of a GEO satellite was determined to be 1436 minutes. GEO satellites may be moved to a graveyard orbit upon retirement, up to a radius of 42,664 km, some 500km above the GEO radius; here, they may have periods as large as 1462 minutes, per Equation 4.28. The period restriction of 1400 to 1500 minutes therefore allowed capture of these GEO altitudes, with some tolerance above and below.

$$
\begin{aligned}
T_{\text{circular}} &= \frac{2\pi}{\sqrt{\mu}} \, r^{3/2} \\
&= \frac{2\pi}{\sqrt{398,600 \text{ km}^3/\text{s}^2}} \, (42,664 \text{ km})^{3/2} \\
&= 8.7701 \times 10^4 \text{ seconds} \\
&= 1462 \text{ minutes} \\
&= 24 \text{ hours } 22 \text{ minutes}
\end{aligned}
\tag{4.28}
$$

TLEs meeting the specified restrictions are then downloaded from space-track.org using the programmatic URL shown in Figure 4.18. Due to the large time period requested, many TLEs are returned for each individual RSO that meets the GEO specifications.

```
https://www.space-track.org/basicspacedata/query/class/tle/PERIOD/
1400--1500/EPOCH/2009-12-10--2010-08-10/orderby/NORAD_CAT_ID,EPOCH%
20desc/distinct/true/format/csv
```

Figure 4.18: The programmatic URL used to download TLEs specific to GEO satellites from the space-track.org API service [113]. The period range of 1400 to 1500 minutes was selected to RSOs in the GEO belt, and those that had been moved to a higher graveyard orbit. The epoch restriction covers the date range of images in the initial image dataset used in this thesis. The final URL components order the output by NORAD ID, removes duplicate TLEs, and delivers the output in Comma-Separated Value (CSV) format for download.

4.9.3 Correlation Algorithm

A TLE allows the position of an RSO to be determined only at the time of that TLE, known as the epoch. However, there will be some time variance

between the TLE epoch, and the epoch at which an image was captured. Therefore, the RSO position must be moved forward/backward in time to the image capture epoch, to predict if it falls within the WISE sensor field-of-view. This process is known as propagation [114], an example of which is shown in Figure 4.19 (adapted from [27]).
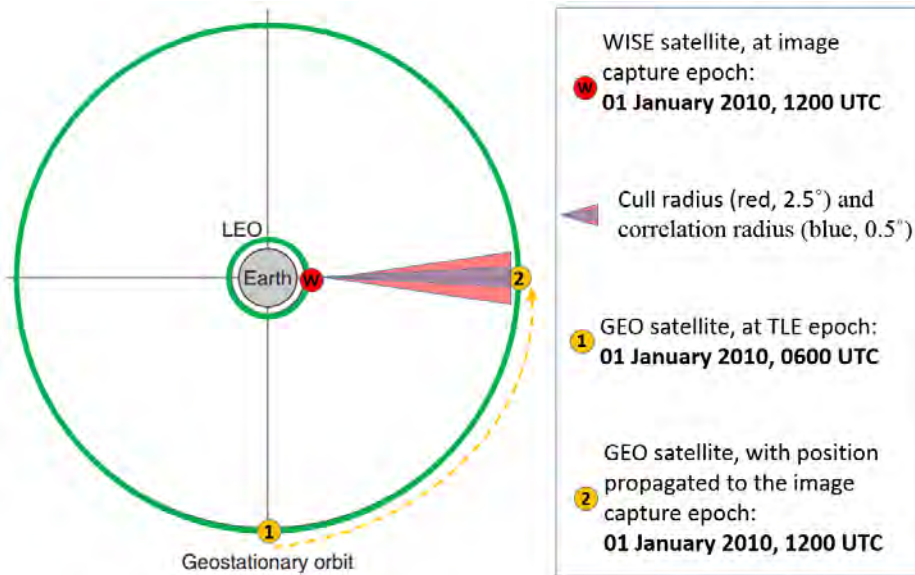
Figure 4.19: A polar view of the Earth, showing WISE (W) in a LEO orbit at the image capture epoch. A GEO satellite is shown at the TLE epoch (1), and at the predicted position once propagated to the image capture epoch (2) (figure adapted from [27])

When moving the position of an RSO forward/backward in time, the orbital perturbations described in Section 1.4 must be taken into account, else the predicted position will be inaccurate. TLEs are developed using the Simplified General Perturbations version 4 (SGP4) propagator, which takes these perturbation effects into account [114]. For this reason, the SGP4 model must also be used when propagating a TLE forward/backward in time.

The propagation algorithm utilised in WISEstreakDET is an adaptation of that used by Thorsteinson [37]. This algorithm implements the SGP4 propagator, and was written in C++ by Thorsteinson and others at Defence Research and Development Canada (DRDC). The algorithm was developed to correlate streak observations made by the Ground Based Optical (GBO) network, and later the Near Earth Orbit Surveillance Satellite (NEOSSat), to catalogued

101

RSOs. As the latest version was built for a space-based sensor (NEOSSat), the relative motion between observing and observed satellite is taken into consideration, making it an ideal candidate for use in WISE imagery.

The correlation algorithm implements a two-step process. First, the TLE file provided by the user is scanned, and each individual TLE is propagated to the image capture epoch. The SGP4 propagator outputs Cartesian position and velocity in the True Equator, Mean Equinox (TEME) reference frame [26]. For this reason, the propagated RSO position following the first step is also in the TEME reference frame. A 'cull radius' is set by the user, and the final stage of the first step is to disregard any propagated RSO positions that fall outside of this radius. In the second step, remaining RSO positions are transformed to the J2000 reference frame. This is a computationally expensive process, hence the need to cull RSO candidates in the first step. Once the reference frame transformation is complete, only those RSOs falling within a 'correlation radius' set by the user are returned as potential matches by the algorithm. An example of cull and correlation radii is shown by red and blue cones respectively in Figure 4.19, and by white dashed lines in Figure 4.20b.

In order to determine the best cull and correlation radii for use in WISEstreakDET, large radii were initially set in a batch of thirty images containing a single streak. For each image, the streak centroid RA and DEC were modelled at the image capture epoch in Analytical Graphics Inc Systems Tool Kit (STK). All GEO satellites were then displayed, along with the WISE sensor field of view. GEO satellites visible within the WISE sensor field of view were then compared to the correlation algorithm match candidates; cull and correlation radii were then gradually reduced to ease computational burden until agreement with the STK model was reached. The final parameters used were a cull radius of $2.5°$, and a correlation radius of $0.5°$. An example of STK modelling is shown in Figure 4.20

| (a) | (b) |
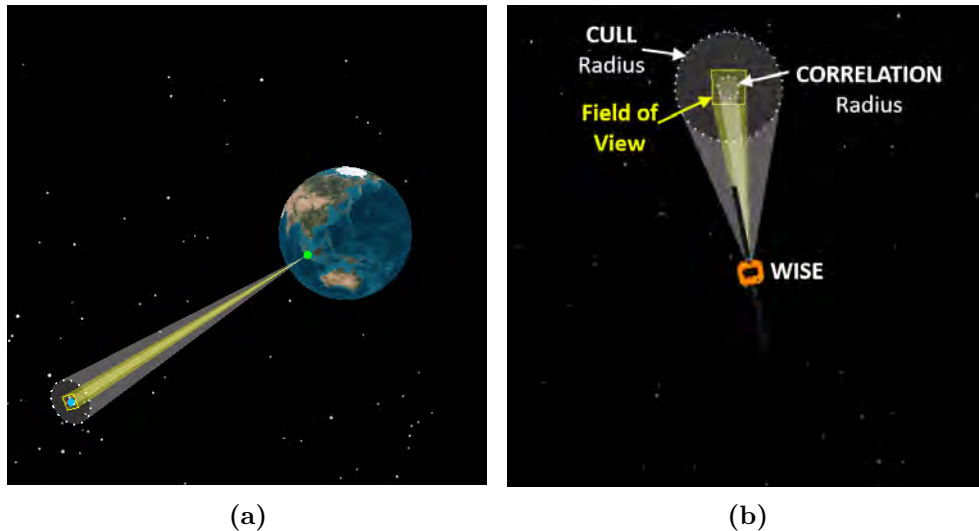
Figure 4.20: *(a)* WISE is shown in STK as a green dot near Earth in LEO, the sensor field of view by a yellow square, and the cull/correlation radii by the outer/inner white dashed circles. *(b)* Perspective from WISE.

4.9.4 Uncertainty in Correlation

In the case of images with a single streak, if more than one potential RSO match is returned by the correlation algorithm, the RSO candidate with the smallest angular separation to the streak centroid position is selected. However, 30% of images with streaks, as detected by WISEstreakDET, contained more than one streak. Often, this corresponded to capture of GEO RSOs in tightly clustered formations.

Due to the high demand for physical space in the GEO orbit belt, as well as the need for frequency deconfliction, GEO positions are allocated by the International Telecommunications Union (ITU) [115]. These allocated positions are within 'boxes' approximately 0.1° of latitude/longitude in size, corresponding to around 74 x 74 x 35km of physical space for collision avoidance. Furthermore, the demand for allocated space has led to a practice of co-locating satellites in GEO, often less than 0.05° of longitude apart [115]. Given the great distance of the GEO belt relative to WISE in LEO, such small separation between observed GEO satellite clusters leads to difficulty in distinguishing the identity of individual streaks.

A further cause of correlation uncertainty is that propagation models will inherently deviate from the realities of satellite perturbations. Therefore,

greater time variance between TLE and image epochs will decrease the accuracy of predicted RSO positions. For this reason, TLEs are updated at regular intervals based upon input from SSA sensors and satellite operators [61]. As previously mentioned, many TLEs exist for each individual RSO in the downloaded GEO TLE dataset. To minimise time variance between TLE and image, therefore minimising position uncertainty, a code segment was implemented that extracted only the TLE with closest epoch to image capture for each RSO. These individual TLEs were then placed in a text file that was unique to each streak, used as the TLE file by the correlation algorithm. As a result, the average variance between TLE and image epoch for correlated streaks in the dataset was 0.69 days, with a maximum variance of 9.68 days.

An example demonstrating potential error in RSO correlation is image frame 01274a129, in which four RSOs are in a tightly clustered formation as shown in Figure 4.21. For each of the four detected streaks, the correlation algorithm returned five potential RSO candidates, shown in Table 4.6. If IDs are assigned to each streak based upon the candidate with minimum angular separation to the streak centroid, duplicated ID assignment occurs, as evident in Figure 4.21a.

ID	RSO
26243	EUTELSAT-16C
25785	ASTRA-1H
29055	ASTRA-1KR
31306	ASTRA-1L
33436	ASTRA-1M

Table 4.6: Each of the four detected streaks in image frame 01274a129, as shown in Figure 4.21, had the five listed RSO candidates returned by the correlation algorithm.

A new method was therefore developed to assign IDs returned by the correlation algorithm when RSOs are tightly clustered. Firstly, adjacent streaks are tagged as a cluster if their centroids were within 0.15° of each other. The propagated position of each correlation candidate is then compared to the position of each streak centroid, and IDs assigned based upon sequenced RA values. For example, in the case of image frame 01274a129 as shown in Figure 4.21, the four closest TLE propagated positions to the four streak centroids were extracted. Tthe TLE propagated position for candidate ID 26243 (EUTELSAT-16C) was consequently disregarded as a potential match. The

(a) Duplicated IDs

(b) Unique IDs

(c) STK validation
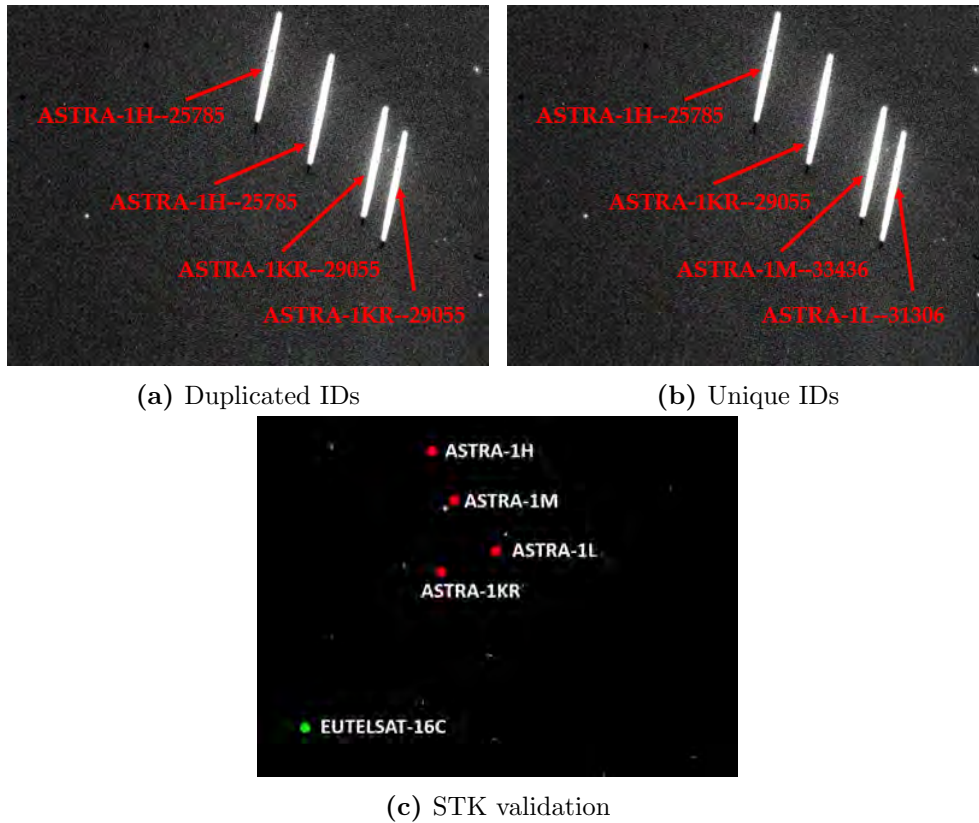
Figure 4.21: *(a)* Individual assignment of identity can lead to duplication. *(b)* Considering these four streaks as a cluster allows unique ID assignment, based upon relative RA distribution. (*c*) Modelling in STK shows an acceptable match to the final RSO IDs assigned by WISEstreakDET.

validity of removing EUTELSAT-16C is evident from its relative displacement, as modelled in STK and shown in Figure 4.21c. The four remaining candidates were then ordered by ascending RA, and assigned to the four streaks as they fell in order of ascending RA. Several image frames containing GEO clusters were modelled in STK following implementation of this method. RSO positions in STK predominately showed a positive match to the IDs assigned to streaks in WISEstreakDET, as shown in Figures 4.21b and 4.21c.

4.10 RSO Characteristics

To allow further analysis of detected streaks, the characteristics of correlated RSOs must be known. These include mass, bus type, shape, size and operational status. Several authoritative databases were utilised to compile these characteristics, for all GEO objects of interest, into a single Microsoft Excel spreadsheet. Once an ID had been assigned to a streak, WISEstreakDET consulted the Excel spreadsheet, and output the correlated RSO characteristics. The databases consulted, and their respective outputs, are outlined in Table 4.7.

Database	Note
Space-Track [112]	TLE data.
Celestrak [4]	RSO name, international designator (COSPAR ID), country of ownership, orbital period, radar cross section.
Jonathon McDowell [33, 34]	Satellite bus type, date of retirement.
ESA DISCOS [116] [117]	RSO type (satellite, rocket body or debris), launch date, radar cross section (min, max and average), mass, shape, dimensions (length, height and depth).

Table 4.7: Databases consulted to compile a list of individual RSO characteristics. This list was consulted by WISEstreakDET once an ID had been assigned to a streak, tagging that streak with the respective RSO characteristics.

4.11 Streak Detection and Magnitude Measurement Issues

WISEstreakDET was configured to first detect streaks in band W3, in which detection had proved to be most successful. For each streak detected in W3, a masked image was created for all other bands that blanked out all pixels except for those of the detected streak location and surrounding area. This sought to ensure that magnitude for the same streak was measured in each band before progressing to the next streak.

An example of this is at Figure 4.22, showing four streaks in band W4 of image frame 01274a129, and the associated masked image created for the furthest right streak. The full detection algorithm was then conducted for this blanked image, returning the magnitude, ID and RSO characteristics for that streak. If an image contained more than one streak, as in Figure 4.22, the algorithm returned control to the W3 image processing and created a new masked image for each streak to be processed in other bands. While this method works well in many cases, several issues were encountered that required remedy or exclusion of certain images.

(a)   (b)
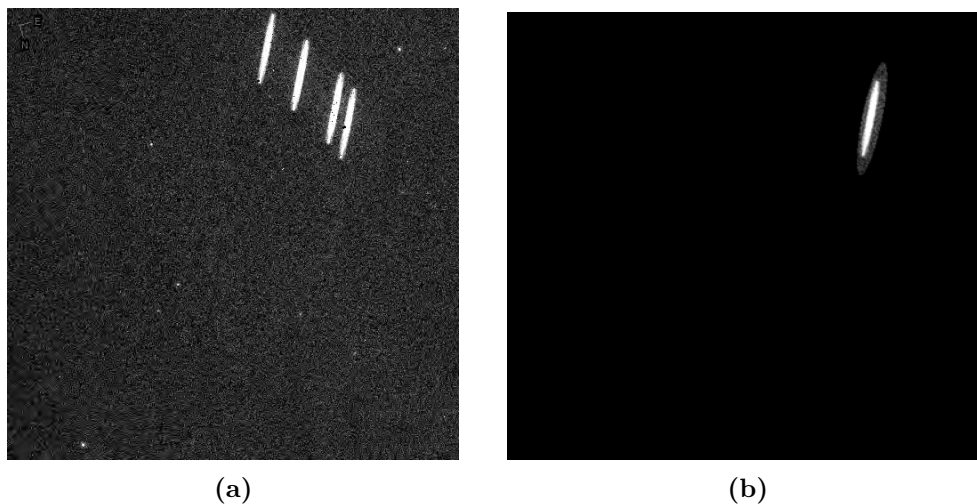
Figure 4.22: *(a)* When multiple streaks are detected in a W3 image, *(b)* a pixel mask around each streak is created before magnitude is measured.

4.11.1 Low W1 Streak Flux

RSO streaks in bands W2, W3 and W4 typically appear very bright, with flux well above the background. As such, WISEstreakDET was run in these bands using the pixel masking method previously described. Streak flux in band W1, however, was often so faint that distinguishing streak from background proved too difficult. The increased presence and relatively high flux of point-sources in W1 also provided a source of error in many cases.

A new method was therefore required to reliably detect streaks within W1 images. Transfer of the streak annulus from W3 or W4 to the W1 image was not possible, as bands W3 and W4 have different exposure times (8.8 seconds) compared to W1 (7.7 seconds). Streaks (and annuli) are therefore longer in W3 and W4 than they are in W1.

Band W2, however, has the same exposure time as W1. The streak annulus in this band was therefore used for magnitude determination in W1. A consequential error encountered from this was that the W2 annuli, though of the same size, were often offset from the streak in W1. Figure 4.23 demonstrates this issue. Offset annuli were evident by a low SNR in band W1 - for the streak in Figure 4.23, W1 SNR was 0.033 compared to the median W1 SNR value for all streaks of 45.16.

(a) (b)

Figure 4.23: *(a)* The W2 streak annulus used to measure magnitude in W1 is offset from the W1 streak, leading to incorrect magnitude measurement. *(b)* The W2 annulus captures the entire W2 streak.

To allow the W2 annuli to be used in W1 images, a method was devised to shift the W2 centroid (upon which the annuli are focussed) to the actual W1 centroid location. A constant direction of shift was not possible, as the offset varied depending upon the WISE observational geometry and RSO direction of travel. Accurate alignment of the W2 annuli onto streaks in W1 was therefore achieved using a line profile method. A line was fitted on the W1 image, centred at the W2 centroid location, and perpendicular to the W2 streak orientation. Pixel values along this line were assessed, and the W1 centroid assigned at the peak of the line profile. Figure 4.24 provides an example of this process.

The presence of stars along the line profile occasionally impacted upon the accuracy of the W1 annuli shifting process, as the relatively bright point-source would become the erroneous W1 centroid location. For this reason, W1 magnitude and SNR values were output using both the unadjusted W2 annuli, and the line profile shifted annuli. The W1 magnitude corresponding to the highest SNR value was retained, as from experimentation this was found to represent the most accurately fitted annuli.
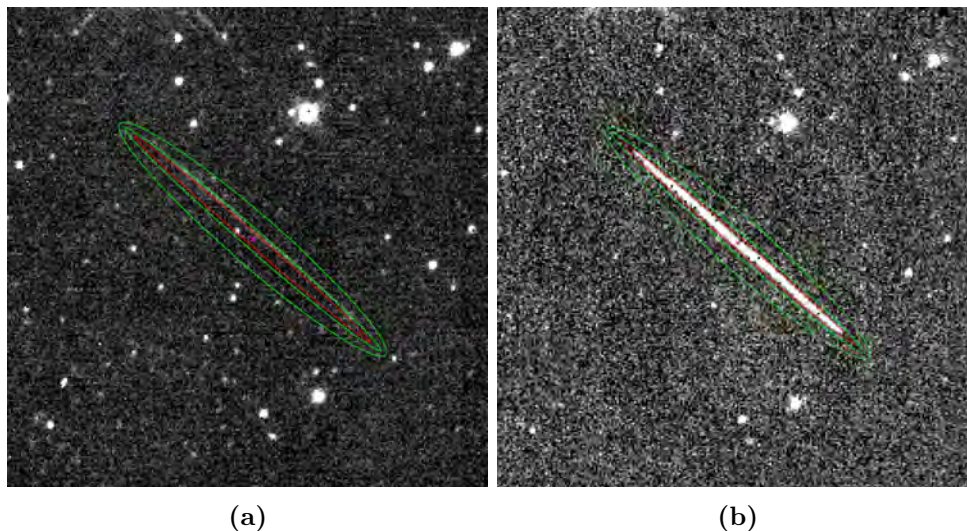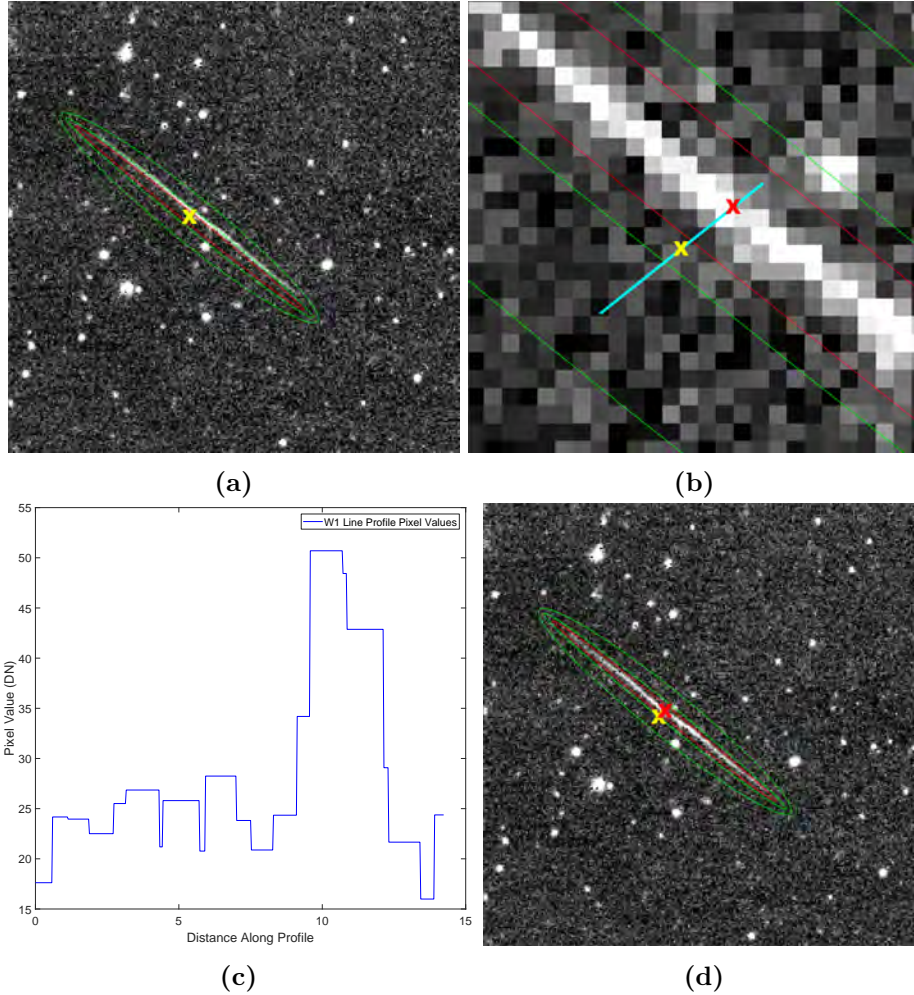
Figure 4.24: *(a)* The W2 streak annulus used to measure magnitude in W1 is offset from the W1 streak, leading to incorrect magnitude measurement. *(b)* A magnified view of the streak centre shows the W2 streak centroid (yellow cross), offset from the W1 streak. Pixel values along the cyan line profile are measured, with a new centroid (red cross) created at the location of maximum pixel intensity. *(c)* The two-dimensional profile of pixel intensity values used to determine the new centroid location. *(d)* The W1 streak is now correctly captured, following annulus adjustment based upon the new centroid location, allowing for accurate magnitude measurement.

110

4.11.2 W1 / W2 Partial Streak Detection

Another frequently encountered issue was partial streak detection in bands W1 and W2, caused by a portion of the streak being too similar to the background. As the annuli from W2 image streak detection were used in W1 images, this led to erroneous magnitude measurements in each of these bands. Figure 4.25 provides an example of a streak correctly detected and measured in band W3, with only partial detection in W1 and W2. To resolve this issue, the clipping threshold was adjusted from $1.5\sigma_{C1}$ to $0.8\sigma_{C1}$ for detection of streaks in band W2, and 4-connected specified in the W2 object identification stage. While this allowed a higher percentage of noise pixels to remain after clipping, it also retained faint streak pixels, reducing the incidence of partial detection.

(a)   (b)
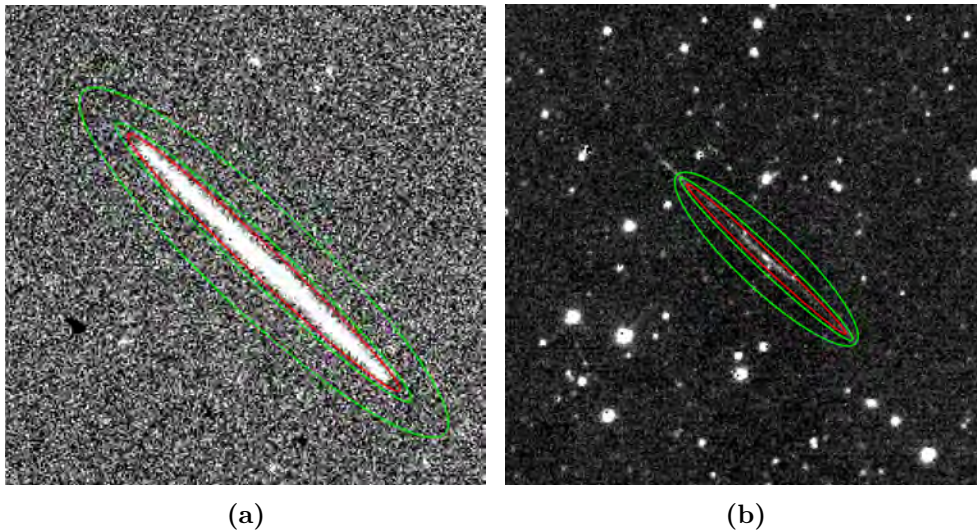
Figure 4.25: *(a)* A streak within image frame 05000a116 is accurately detected and measured in band W3. *(b)* The equivalent streak in band W1 is only partially detected, due to the streak pixels being too similar in value to the background.

This remedy was not enough to capture all streaks in W1 and W2, however, as some streak pixels in these bands were simply too close to the background; partial detection of streaks still occurred in these instances. To allow the images where this error occurred to be ascertained, the W2:W3 streak annulus major-axis ratio was calculated and output in the final data. Low ratio values were screened, and it was determined that a ratio of 0.75 or less - meaning that

the W2 streak annulus was less than 75% the length of W3 - corresponded to a partial detection in W1 and W2. These images were accordingly removed from consideration.

4.11.3   W1 / W2 Star Contamination

Star contamination in bands W1 and W2 provided another source of detection error. When stars are in close proximity to a streak in these bands, WISEstreakDET is unable to identify a sufficient gap of background pixels between them to identify streak and point-source as individual objects. Consequently, the streak and star are grouped together, and annuli are modelled off the subsequent erroneous moment calculations.

Figure 4.26 shows an example of a bright star in proximity to a single streak within image frame 06998a173 band W2. The streak aperture is clearly too wide and offset due to the presence of this point-source, leading to inaccurate magnitude measurement. Star removal processes, as implemented by Lévesque and Buteau [57] and others, were not implemented within WISEstreakDET due to time constraints. For this reason, bright point-source corruption of streaks was not able to be remedied. Instead, the W2:W3 streak annulus minor-axis ratio was calculated and output in the final data. It was determined that a ratio in excess of 0.88 - meaning that the width of a W2 streak annulus was greater than 88% of the width of the W3 annulus - corresponded to a point-source corrupted streak detection. These images were also accordingly removed from consideration.
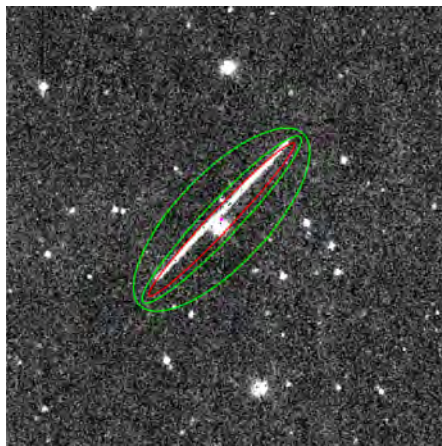
Figure 4.26: A bright point-source near the streak in image frame 06998a173 band W2 corrupts detection of the streak.

4.11.4   Border Proximity

A quality assurance measure was implemented, to detect streaks that were on or in close proximity to the image border. Should this occur, it may not be possible to ascertain the beginning or end point of a streak. It could therefore not be guaranteed that the entire flux of these streaks were collected when determining magnitude, impacting upon the validity of measurements.

To detect streak proximity to the border, edge detection pixel location values were set at $\pm$ ten pixels from the overall image size. In the case of WISE images in bands W1 to W3, at 1016 x 1016 pixels, the edge detection pixel x and y values were set at 11 and 1015. W4 band images, at 508 x 508 pixels, were given edge detection pixel x and y values of 6 and 503. The location of pixels attributed to a streak is known from their identification through connectivity tests, as described in Section 4.6. Should any of the streak pixel location values match the edge detection pixel location values, a flag would be annotated next to that streak in the final database. A total of 240 detected streaks were excluded from final analysis due to this quality assurance process.

4.11.5   Summary of Errors

Further sources of streak detection error were observed in WISEstreakDET, that were not able to be remedied, leading to a large number of images being removed from final consideration. All encountered errors and their potential causes are summarised in Table 4.8. Remedying some of these errors in future work would allow inclusion of a large number of streaks omitted in this research.

Error	Number Affected (%)	Potential Cause and Remedy
No ID assigned	519 (19.78%)	Potentially caused by sub-optimal correlation radius parameters, or by large time variance between TLE and image capture epochs, leading to disparity in predicted and detected RSO positions. Enlarging the correlation radii, and inclusion of a larger RSO set in the TLE database, may provide some remedy.
Streak on border	240 (9.15%)	Streaks on or in close proximity to an image border were discounted due to the potential for inaccurate magnitude measurement. No remedy to be sought.
W1 / W2 star corruption	71 (2.71%)	Point-sources in close proximity to a streak leads to the two objects being identified as one. This causes error in the moment calculations, as an ellipse is fitted to the combined shape, not solely the streak. Magnitude calculations are adversely affected. Star removal may provide remedy.
W1 / W2 partial detection	60 (2.29%)	Streak flux in these bands is low enough to at times be indistinguishable from the background. Lowering of the clipping threshold and specifying 4-connected to identify objects in W2, and transfer of the W2 annuli for use in W1, provides partial remedy.
W1 / W2 / W4 no magnitude output	38 (1.45%)	The cause for a value of zero to be assigned to magnitude in W1, W2 and/or W4 for these streaks is as yet undetermined.

Table 4.8: Several observed errors in the WISEstreakDET algorithm are presented, along with their potential causes and remedies. The number of streaks affected for each error are given, with a percentage in relation to the total number of streaks detected (2624) in the selected image database. Following omission of these erroneous streaks, a total of 1696 valid streaks remained.

5 Algorithm Validation and Optical Magnitude Comparison

Prior to conducting a characteristic analysis of RSOs, the accuracy and validity of WISEstreakDET was evaluated via two separate tests. The first test compared published star magnitudes to their magnitudes as measured with WISEstreakDET. The second test used WISEstreakDET to analyse a database of images examined in previous research, to compare the number of streaks detected, and their measured magnitudes.

Following validation of the WISEstreakDET algorithm, results were compared to optical observation data [67, 68, 70] reviewed in Chapter 3. Previous research [80] suggests that RSOs appear brighter in IR than the visible band. For the purposes of SSA, this may represent an advantage of IR over comparative optical sensors, particularly with respect to detection and tracking of faint RSOs. This comparison therefore aims to provide an initial indication of the value in utilising IR sensors for the purpose of SSA, which may assist in the requirements analysis phase of associated projects in future.

Finally, a summary of WISEstreakDET results is presented, to allow readers an insight into the statistical outcomes of this research.

5.1 Evaluation of Measured Stellar Magnitudes

WISEstreakDET was adjusted to detect and measure point-sources, rather than streak objects. This was achieved in the same manner as detecting streaks, instead filtering for objects with eccentricity *lower* than the set threshold described in Section 4.7. Due to the large number of point-sources in images, a width constraint was set to limit the quantity of data returned. An

example of point sources detected by the altered WISEstreakDET algorithm is shown at Figure 5.1.
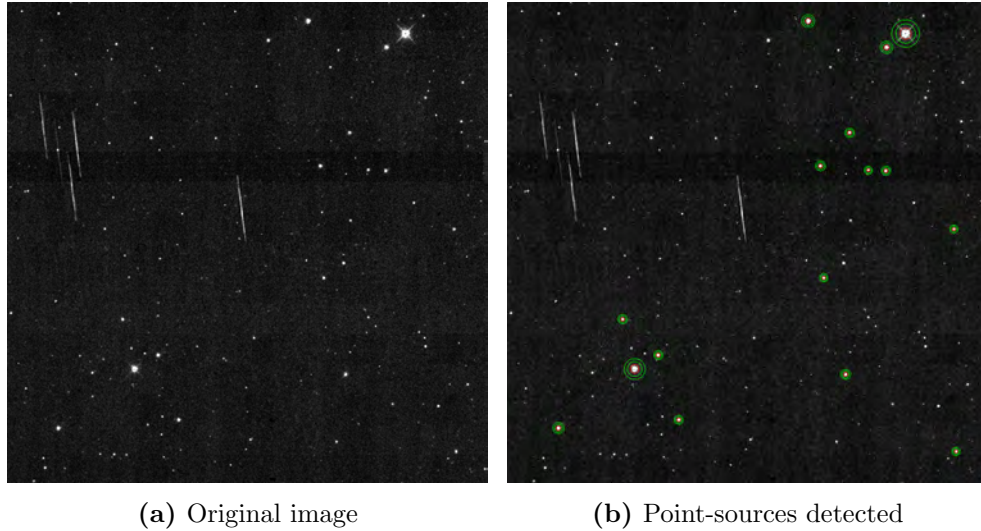

(a) Original image   **(b)** Point-sources detected

Figure 5.1: *(a)* Image frame 1009b135 in band W2 *(b)* WISEstreakDET was adjusted to detect and measure point-sources rather than streaks. Not all point-sources are detected, due to a width constraint placed to limit the quantity of output data.

The NASA Infrared Processing and Analysis Centre (IPAC) maintains a source catalogue, containing position, magnitude, astrometric and photometric uncertainties, and quality flags for 563,921,584 objects detected in WISE imagery [46]. The list of point-source positions (RA and DEC) detected by the altered WISEstreakDET algorithm were placed into an ASCII table format, for uploading to the source database. A list of matched point-sources with associated magnitude and other data was returned.

Several point-sources detected by the altered WISEstreakDET algorithm were omitted, such as when a star fell on the image border, had low SNR, or when the WISEstreakDET and IPAC centroid differed in RA by more $0.05°$. The range of point-source magnitudes was limited to that detected in the initial set of results (4.96 to 10.51). IPAC also issued chi-squared statistics - the deviance between expected and observed results - for each source measurement. IPAC states that sources with listed chi-squared values of greater than four were likely cosmic rays or other artefacts [44], and as such these results were also omitted from WISEstreakDET point-source data.

116

Following the omission of erroneous or invalid data, a sample size of 3,377 point-sources remained. The magnitudes as reported by both WISEstreakDET and the IPAC source catalogue were then compared.

5.1.1 Results

Figure 5.2 shows the W2 apparent magnitude difference between point sources measured by WISEstreakDET, and their value in the IPAC source database. IPAC published magnitudes are shown along the x-axis, and the sigma to WISEstreakDET measurements on the y-axis. The higher a data point is vertically positioned, the greater the difference between measured and published magnitude for an individual star.

Within the range of point-sources measured by WISEstreakDET, the probability of magnitude error greater than 0.1 is 1.66%, while the probability of error greater than 0.3 is 0.03%.
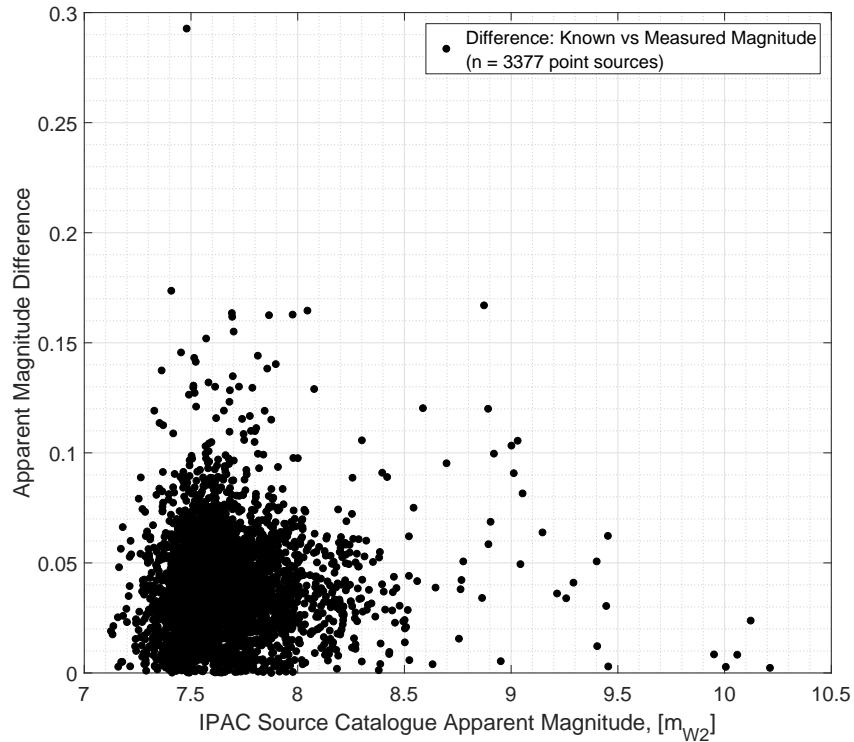
Figure 5.2: Variation between point-source magnitudes from the IPAC database and algorithm measurements.

The linear comparison of algorithm derived and IPAC source magnitudes in Figure 5.3 shows that WISEstreakDET returns relatively accurate measurements across the full range of magnitudes. One observation is that WISEstreakDET tends to return slightly fainter magnitudes than published. This may suggest that the digital apertures are slightly too small or off-centre, meaning that not all of the stellar flux is measured. Alternatively, background values may be overestimated, potentially as a result of stars or other flux sources within the sky aperture.

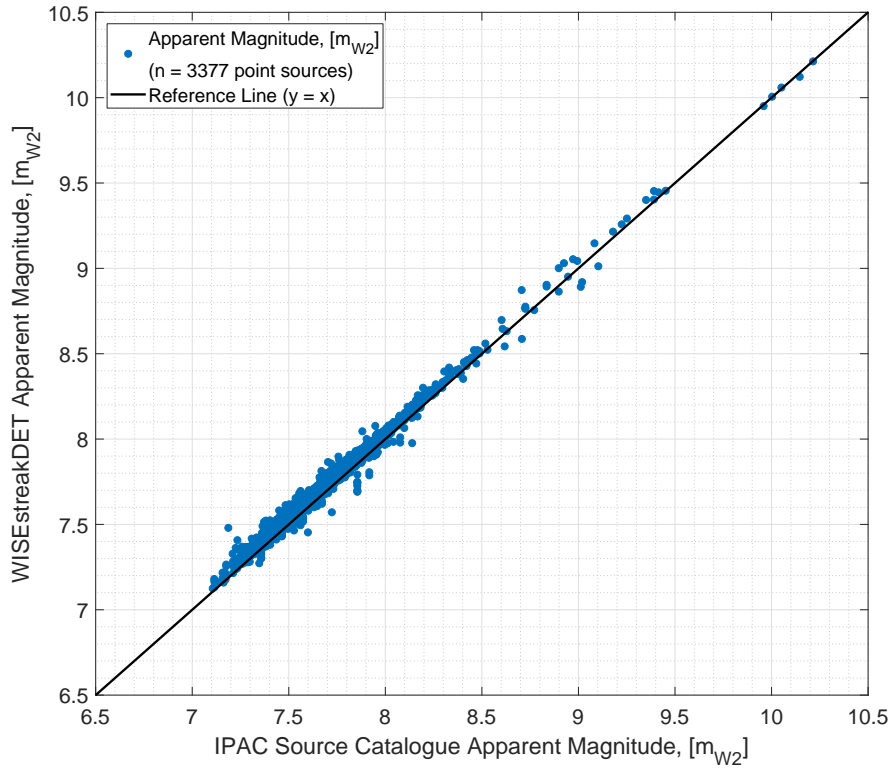**Figure 5.3:** Linear comparison of point-source magnitudes from the IPAC database and from algorithm measurements.

Despite this observation, the average magnitude disparity between WISEstreakDET measurements and published magnitudes is 0.04. This is considered sufficiently close to the average IPAC database uncertainty of 0.02, allowing progression to the next validation test.

5.2 Comparison of Results with Previous Research

Previous research conducted by Lee et al. [45], of the University of Michigan, is described in Section 3.5.1. The list of images used by this team, consisting of 20,552 frames for a total of 82,208 images over the four WISE bands, was acquired and downloaded using the method described in Section 2.3. These images were then scanned with WISEstreakDET, and the results compared to those of Lee et al. [45].

5.2.1 Detections and RSO Magnitude Comparison

Lee et al. [45] detected streaks using the open source software *Source Extractor* [52], with photometric measurements obtained with a custom-built streak aperture-fitting algorithm. Using this method, 861 valid GEO streaks were reported, with their magnitudes and other data generously provided by the authors for validation of this research.

WISEstreakDET, using the same database subset of 82,208 WISE images, detected and measured 1,696 valid GEO streaks. This may suggest that an algorithm purpose-built to detect streaks within a particular database of images has increased sensitivity to open source software.

Table 5.1 provides a comparison of magnitudes measured by each algorithm. WISEstreakDET tended to provide slightly fainter magnitudes than the method used by Lee et al., as was observed in the stellar magnitude comparison. Colour index values varied between more blue (smaller index value) and more red (larger index value). The predominate cause of magnitude variation between the algorithms is most likely the difference in sample sizes. Overall, with a maximum magnitude difference of 0.24 (in band W2) over a reasonably large sample size, the two independently conducted experiments using the same dataset may be considered in agreement.

Magnitude / Colour	Lee et al. [45]	WISEstreakDET	Difference
W1	10.31 ± 0.10	10.43 ± 0.03	0.12
W2	7.76 ± 0.05	8.00 ± 0.01	0.24
W3	2.76 ± 0.01	2.80 ± 0.01	0.04
W4	0.71 ± 0.02	0.86 ± 0.03	0.15
W1-W2	2.55	2.43	-0.12
W1-W3	7.55	7.63	0.08
W1-W4	9.60	9.58	-0.02
W2-W3	5.00	5.20	0.20
W2-W4	7.05	7.14	0.09
W3-W4	2.05	1.94	-0.11

Table 5.1: Comparison of independently obtained results from previous research conducted by Lee et al. [45], and this research, using the same dataset of images. Sample sizes are 861 and 1,696, respectively. **Note:** Colour index uncertainty values were not available from the research conducted by Lee et al., and were therefore not included in the table.

5.2.2 Colour-Colour Plot Comparison

Lee et al. [45] also presented their results in comparison to previous research conducted by Wright el al. [39] and Masiero et al. [92]. The research and outcomes presented by these authors are discussed in Section 3.5.1.

5.2.2.1 Stars and Galaxies

Lee et al. [45] concluded that GEO spacecraft occupy a difference colour subspace than the stars and galaxies analysed by Wright el al. [39]. This was attributed to the differing mechanisms by which flux is produced between artificial satellites and astronomical objects. The same colour-colour plot produced by Wright el al. [39] was re-produced by Lee et al. [45] from 63 observed GEO satellite streaks, and from 1,557 GEO satellite streaks observed in this research. All three colour-colour plots are shown in Figure 5.4

(a) Wright el al. [39]
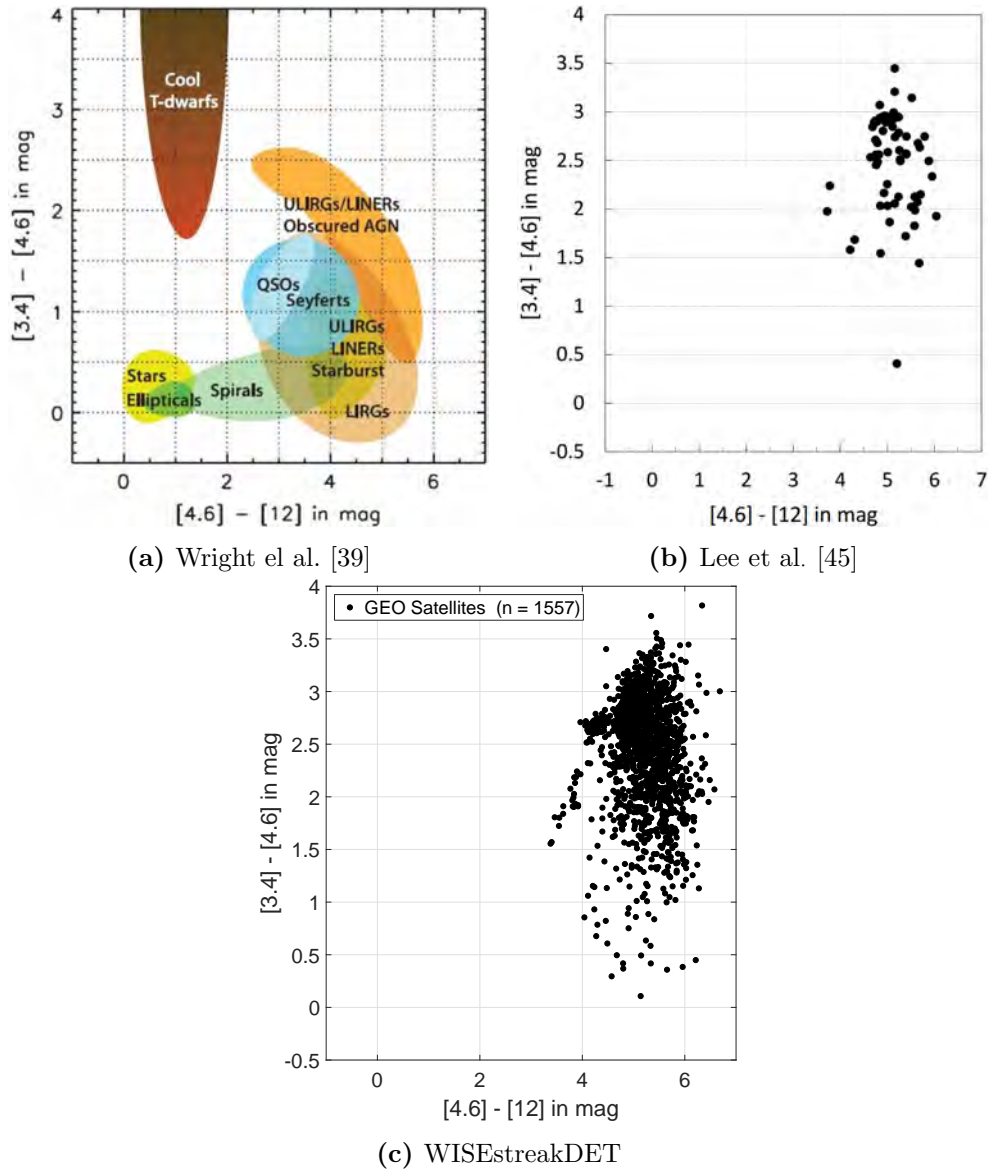

(b) Lee et al. [45]

(c) WISEstreakDET

Figure 5.4: *(a)* Wright el al. [39] produced a WISE colour index plot of stars and galaxies. *(b)* Lee et al. [45] reproduced this plot, from observations of 63 GEO satellite streaks, concluding that they fall in a unique subspace. *(c)* WISEstreakDET data falls at the same focus point, with a wider distribution.

The WISEstreakDET data points plot in the same focal point as the results from Lee et al. [45], further validating the conclusion of these authors, and WISEstreakDET measurements. However, due to the larger sample size in this research, there is a wider distribution of data. For this reason, while GEO spacecraft are largely observed to be distinct from the stars and galaxies plotted by Wright et al. [39], there is some overlap, reducing the veracity of the outcome.

5.2.2.2 Near Earth Objects

Masiero et al. [92] presented research on WISE observations of asteroids, specifically Main Belt Asteroids (MBAs), Trojans and Near Earth Objects (NEOs). These observations were plotted using several WISE colours, shown in Figures 5.5a and 5.6a respectively. The colour index plots were reproduced by Lee et al. [45], shown in Figures 5.5b and 5.6b, again using data from the image subset containing observations of 63 GEO satellite streaks. It was observed by the authors that GEO satellites fall in the colour index subspace occupied by the overlap of MBAs and NEOs.

WISEstreakDET data was again plotted in the same colour index space, shown in Figures 5.5c and 5.6c. Once again, while the same focal point of data as that of Lee et al. [45] is observed, the spread is wider due to the larger sample size of this research. Therefore, although the same conclusion regarding GEO satellites and NEOs may be drawn, it is not as explicit as for previous published research.

(a) Masiero et et al. [92]

(b) Lee et al. [45]

(c) WISEstreakDET

Figure 5.5: *(a)* Masiero et et al. [92] produced a colour index plot of asteroids, specifically MBAs (black), Trojans (green) and NEOs (magenta). *(b)* Lee et al. [45] reproduced this plot, from observations of 63 GEO satellite streaks, concluding that they fall at the junction of MBAs and NEOs. *(c)* WISEstreakDET data falls at the same focus point, with a wider distribution.

(a) Masiero et et al. [92]

(b) Lee et al. [45]
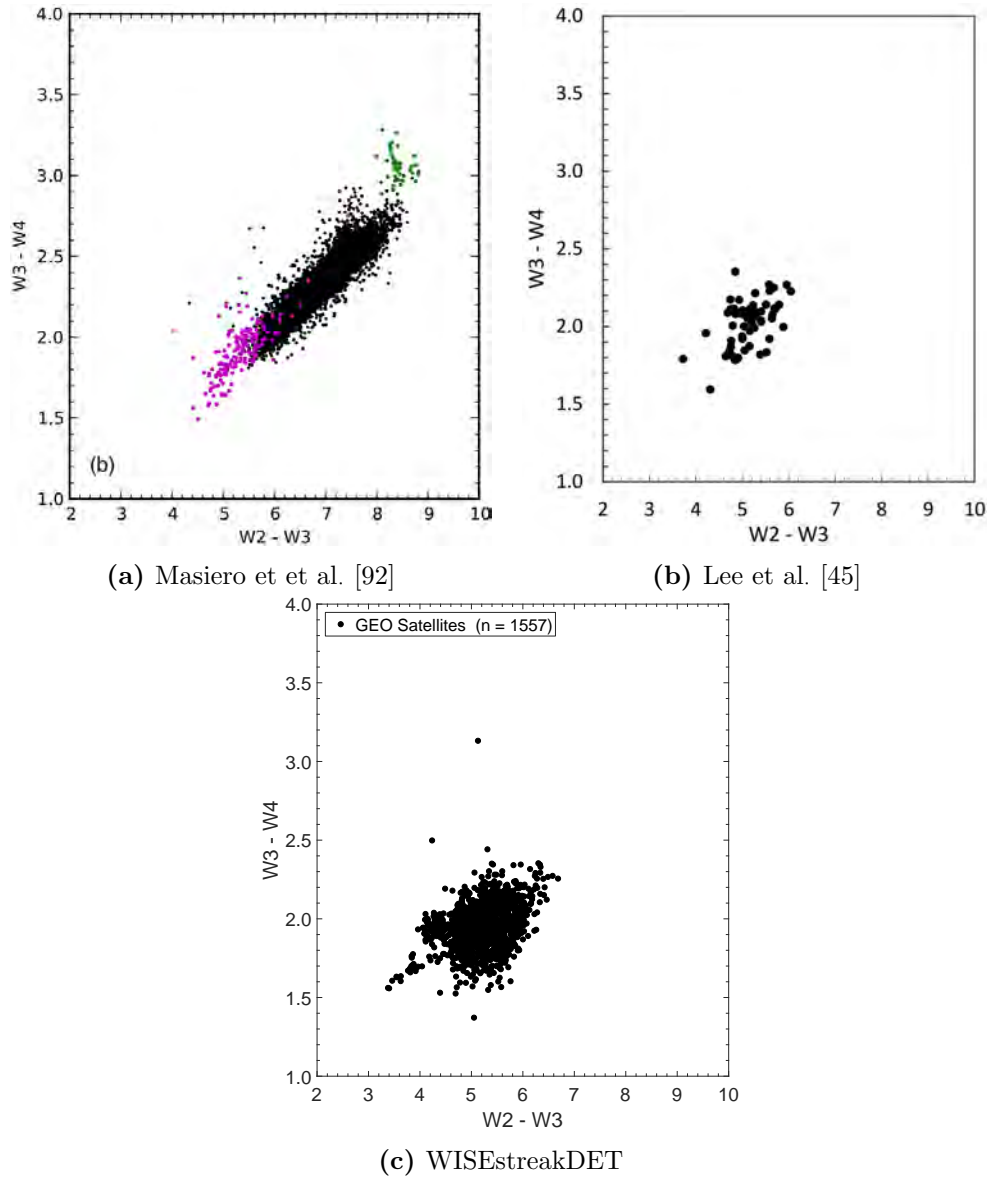

(c) WISEstreakDET

Figure 5.6: *(a)* Masiero et et al. [92] produced a colour index plot of asteroids, specifically MBAs (black), Trojans (green) and NEOs (magenta). *(b)* Lee et al. [45] reproduced this plot, from observations of 63 GEO satellite streaks, concluding that they fall at the junction of MBAs and NEOs. *(c)* WISEstreakDET data falls at the same focus point, with a wider distribution.
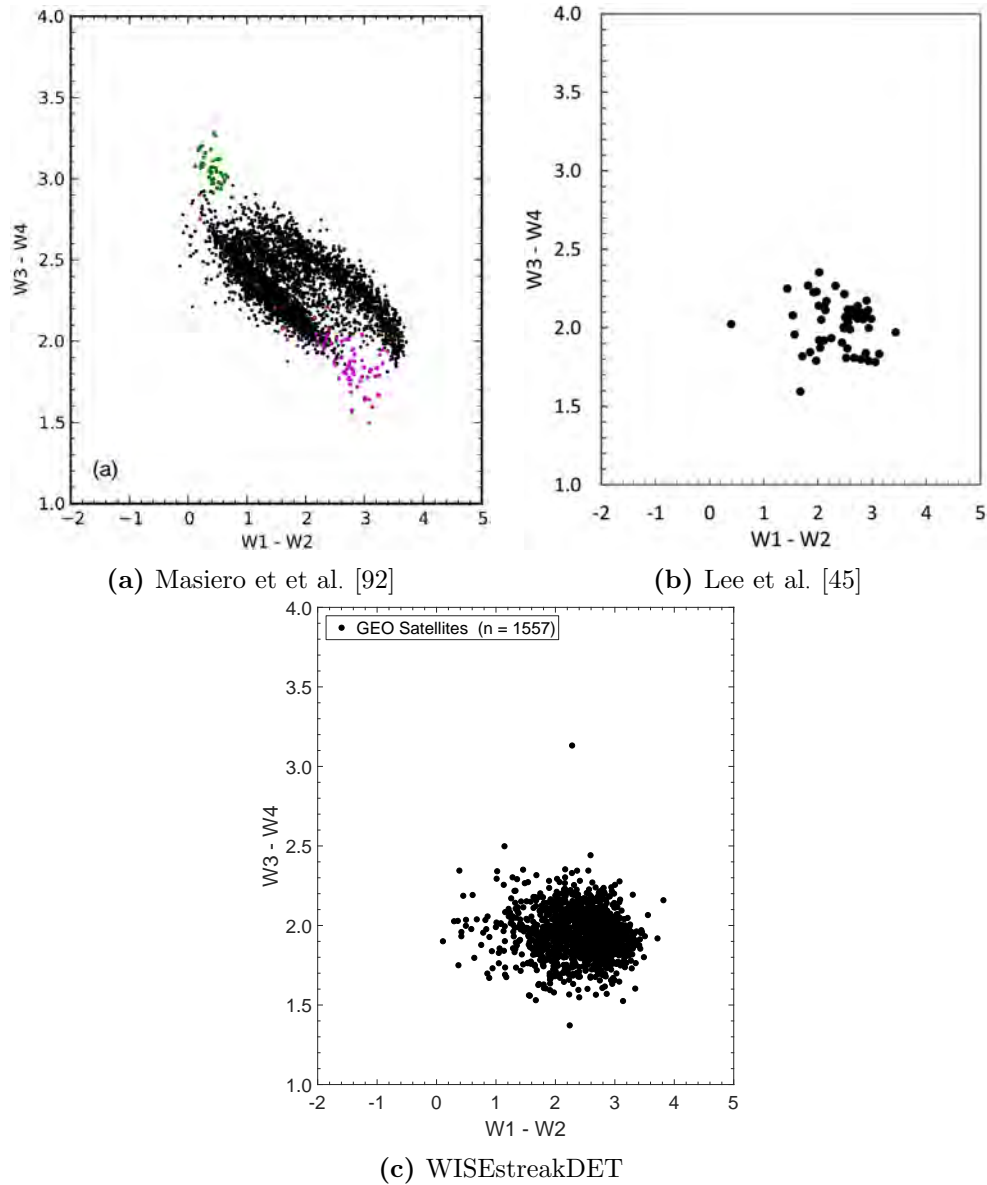
5.3 Comparison to Optical Photometry

Stokes et al. [70] presented photometric results obtained from the Space-Based Visible (SBV) sensor, on board the Midcourse Space Experiment (MSX) satellite. This research is examined in Section 3.3.1. Figure 5.7 shows photometric data captured by the SBV against satellites with bus type HS-601, as a function of phase angle [70].

(a) Three-axis stabilised satellites
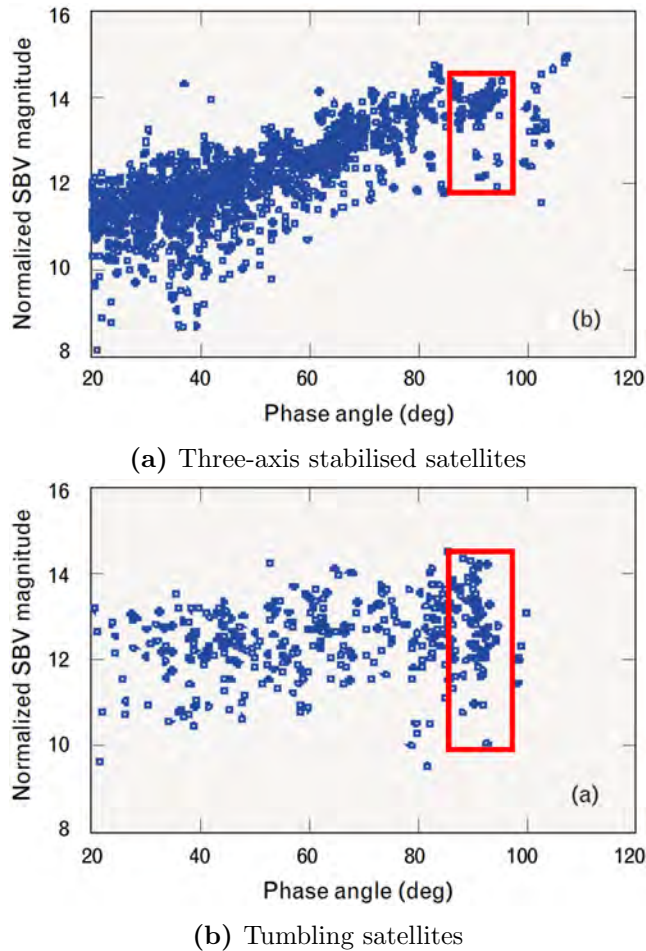

(b) Tumbling satellites

Figure 5.7: Optical photometry measurements of RSOs with HS-601 bus type [70]. Data captured by the SBV sensor, on board the MSX satellite. The red box indicates the comparative phase-angle range observed in data from this thesis.

Scott and Wallace [68] also present optical measurements of the HS-601 bus. These observations were made with the Space Surveillance Observatory (SSO) at DRDC Ottawa in 2008, and are shown in Figure 5.8a. Cognion [67] presents optical observations made in 2013 with a small-aperture telescope in Kihei, Maui. Figure 5.8b shows these results, with the orange circles representing HS-601 data points. As per the results of Stokes et al., raw data was not available, and as such values were inferred from plot data points.
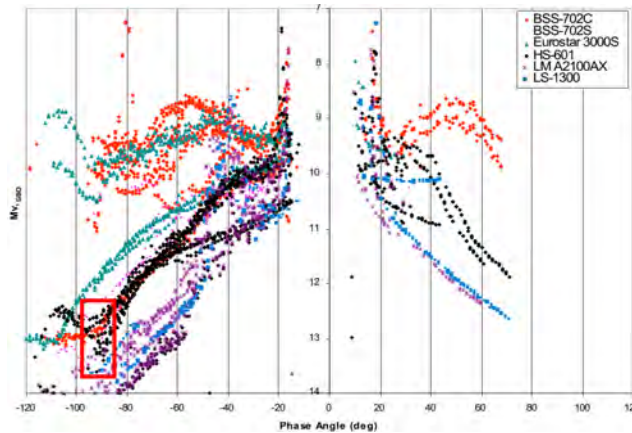
(a) Scott and Wallace [68]
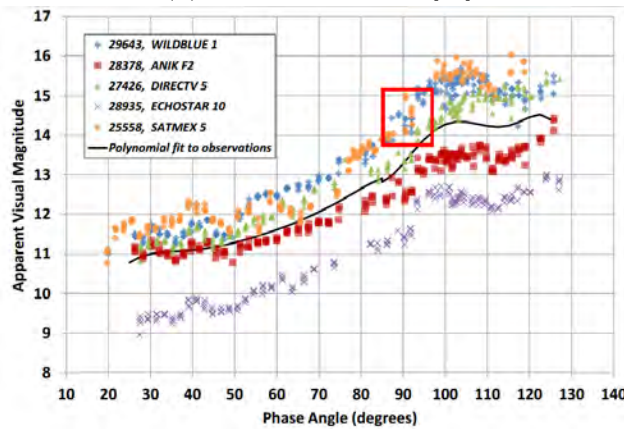
(b) Cognion [67]

Figure 5.8: Optical photometry measurements of RSOs with HS-601 bus type. The red box in each plot indicates the comparative phase-angle range observed in data from this thesis. Data reported by *(a)* Scott and Wallace [68] is shown by black diamonds, and *(b)* Cognion [67] by orange circles.

5.3.1 Results

From the subset of images analyses, 181 RSO streaks were correlated to satellites with HS-601 bus type. These observations ranged in phase angle from 85.92° to 97.79°. Within this phase angle range, the combined work of Stokes et al. [70], Scott and Wallace [68] and Cognion [67] produced approximately 184 observations of satellites with HS-601 bus type, in the visible band.

Observations in the visible band were collated, and plotted against the four individual WISE bands W1 to W4. This is shown in Figure 5.9. When comparing optical and IR observations, it is evident that similar RSOs appear brighter in IR wavelengths than in the visible spectrum, particularly for the longer wavelength bands W3 and W4.
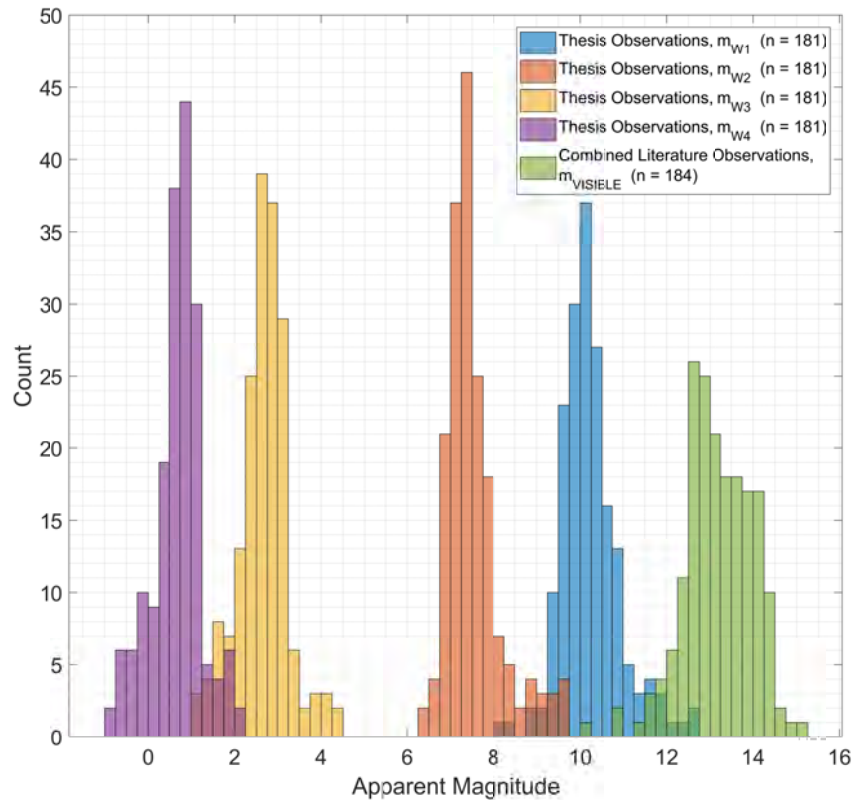

Figure 5.9: Observations of satellites with HS-601 bus type, comparing the four WISE bands to combined visual measurements by [70], Scott and Wallace [68] and Cognion [67]. Observations in the four WISE bands are typically brighter (smaller apparent magnitude) than comparative optical observations.

5.4 Conclusion

In this chapter, the precision of WISEstreakDET was evaluated by validating magnitude measurements against published stars and previous research. Stellar magnitudes as measured by WISEstreakDET were shown to be accurate, with an average sigma of 0.04 to the IPAC database. WISEstreakDET also detected more streaks than open source software for the same subset of images, and magnitudes of the independently conducted experiments agreed. This provides confidence in the data generated by this algorithm, and paves the way for the characterisation of RSOs in the four WISE bands.

As an initial evaluation of the SSA capability of WISE infrared bands, WISEstreakDET magnitudes were compared to optical observations of similar RSOs. It was demonstrated that all four WISE bands, but particularly W3 and W4, appear brighter than observations in the visible spectrum. Infrared sensors therefore show promise for detecting RSOs that may appear too faint for optical telescopes.

Finally, to allow readers an insight into the statistical outcomes of this research, data from the initial set of analysed images was collated, the results of which are presented in Table 5.2.

Variable	Note		
WISE Frames Analysed	20,552, each frame containing one image per band W1 - W4 for a total of 82,208 images		
Total Valid Streaks Detected	1696		
Magnitude (Average / Range)	**W1**	10.43 ± 0.03	6.59 : 13.36
	W2	8.00 ± 0.01	4.96 : 10.51
	W3	2.80 ± 0.01	0.94 : 5.41
	W4	0.86 ± 0.03	-0.88 : 5.00
Type	Satellites: 1557 (91.80%), Rocket Bodies: 136 (8.02%), Debris: 3 (0.18%)		
Streaks Per Image	Zero: 17636 (85.81%), One: 2360 (11.48%), Two: 430 (2.09%), Three: 90 (0.44%), Four: 27 (0.13%), Five: 7 (0.03%), Six: 2 (0.01%).		
Eccentricity	Average of 0.973. Cut-off set at 0.85. 97.11% of streaks carried eccentricity values greater than 0.90.		
Epoch Difference	Average time between image capture and TLE epoch of 0.69 days. Minimum difference of 25.90 seconds, maximum difference of 9.67 days.		
Phase Angle	Average of 92.54°, minimum of 85.92°, maximum of 97.79°.		
Status	Active: 1190 (70.17%), Retired: 503 (29.65%), Uncertain: 3 (0.18%)		

Table 5.2: Statistical analysis and commentary of initial results.

6   Infrared RSO Characterisation

Following the validation of WISEstreakDET as discussed in Chapter 5, research progressed to an evaluation of infrared photometric characterisation. Through the use of a correlation algorithm, as described in Section 4.9, each streak detected by WISEstreakDET was associated with a catalogued RSO. Consultation of the various databases described in Section 4.10 allowed specific characteristics, such as bus type, mass, shape and launch date, to be associated with each streak. By comparing magnitude and colour index values of streaks to their associated characteristics, some generalisations may be uncovered that allow the identity of an unknown observed RSO to be discerned. This is the ultimate objective in pursuing this research.

6.1   Experimental Aims and Objectives

This chapter aims to evaluate the four WISE infrared bands for characterisation purposes. Each section will seek to analyse a different RSO characteristic, and will involve several experiments as summarised in Table 6.1. Section 6.2 focusses upon satellite shape, and includes a comparison of box-wing and cylindrical satellites, as well as an evaluation of satellite size. Section 6.3 focusses upon status, including the difference between active and retired satellites, and the effect of RSO age. Finally, Section 6.4 focusses upon RSO type, comparing various satellites and rocket bodies. The chapter will end with a summary of findings, with the objective of advising the SSA community of the potential benefit of a space or ground-based infrared sensor for the purposes of space surveillance. Analysis conducted without merit for inclusion in the thesis body are included in Appendix A.

Section	Experiment
6.2 Satellite Shape	6.2.1 – Comparison of active box-wing satellites
	6.2.3 – Comparison of active cylindrical satellites
	6.2.3 – Comparison of active box-wing and cylindrical satellites
	6.2.4 – Comparison of satellite size
6.3 RSO Status	6.3.1 – Comparison of active and retired box-wing satellites
	6.3.2 – Comparison of active and retired cylindrical satellites
	6.3.3 – Comparison of satellite age
6.4 RSO Type	6.4.1 – Comparison of retired box-wing satellites and rocket-bodies
	6.4.2 – Comparison of retired cylindrical satellites and rocket-bodies
	6.4.3 – Comparison of rocket body types

Table 6.1: Summary of experiments within each section of this chapter.

6.1.1   A Note on Plots and Data

There are two ways in which photometric measurements may be presented: magnitude values alone, plotted as histogram counts, or colour index values plotted against one another (colour-colour plots). Throughout analysis, it was observed that colour-colour plots provided an enhanced ability to differentiate between RSO characteristics. For that reason, magnitude histograms will only be included if they exhibit a particularly useful representation of data.

Using photometric magnitudes of the four available WISE bands, a total of six colours may be produced, leading to 15 available colour-colour plot combinations. For each RSO characteristic analysed, all 15 plots were produced; typically, plots showing the greatest level of differentiation between data points were chosen for inclusion in this document. Some examples of colour-colour plots with minimal differentiation will also be shown to demonstrate instances when they do not provide meaningful information. The 15 available colour-colour plot combinations are listed in Table 6.2. Vertical and horizontal error-bars are shown on all colour-colour plots, representing the uncertainty of colour measurements.

Colour 1	Colour 2
W1 - W2	W1 - W3
W1 - W2	W1 - W4
W1 - W2	W2 - W3
W1 - W2	W2 - W4
W1 - W2	W3 - W4
W1 - W3	W1 - W4
W1 - W3	W2 - W3
W1 - W3	W2 - W4
W1 - W3	W3 - W4
W1 - W4	W2 - W3
W1 - W4	W2 - W4
W1 - W4	W3 - W4
W2 - W3	W2 - W4
W2 - W3	W3 - W4
W2 - W4	W3 - W4

Table 6.2: Using photometric magnitudes of the four WISE bands, six colour indices may be produced, leading to a total of fifteen possible colour-colour plot combinations.

6.2 Evaluation of Active Satellite Shapes

To evaluate the potential to differentiate between different satellite buses, the magnitudes and colour indices of various satellites with box-wing and cylindrical configurations were plotted. Only active satellites were considered, as unstable satellites and debris may exhibit increased variance in magnitude that could contaminate results of this experiment.

Of the 1696 total streaks detected, 1188 were correlated to active satellites. Of these, 1060 were box-wing, 107 were cylindrical, and 21 possessed unique shapes that could not be categorised as either.

6.2.1 Comparison of Active Box-Wing Satellites

Of the 1060 active box-wing satellites analysed, there were 56 different bus variants. The five bus variants with the most observations are listed in Table 6.3, and due to time restraints, are the only subjects of this experiment. Future analysis may consider the remaining bus variants to assess the ability for differentiation.

Bus Variant	# Observations
Boeing HS-601	148
SSL-1300	157
Lockheed Martin A2100	65
Boeing BSS-702HP	62
Lockheed Martin A2100AX	57

Table 6.3: The five active box-wing satellite bus variants with the most observations in this database. Note: HS-601 includes the HS-601HP, as the HP model represents primarily electrical component changes.
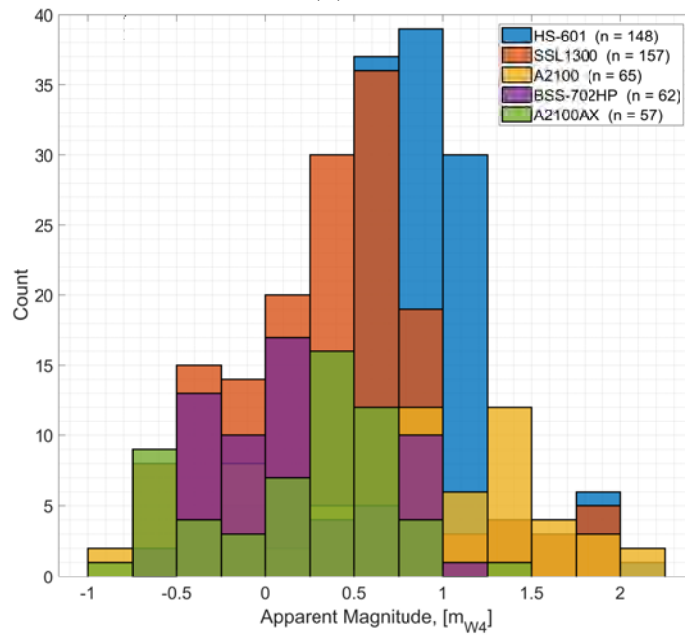
6.2.1.1 Magnitude

Figure 6.1 shows magnitude histograms for bands W1 and W4. In bands W3 and W4, the distribution of magnitudes for each of the five box-wing bus variants is largely the same, with much overlap. The five variants also appear similar in bands W1 and W2, though BSS-702HP buses are often brighter than the four other variants.
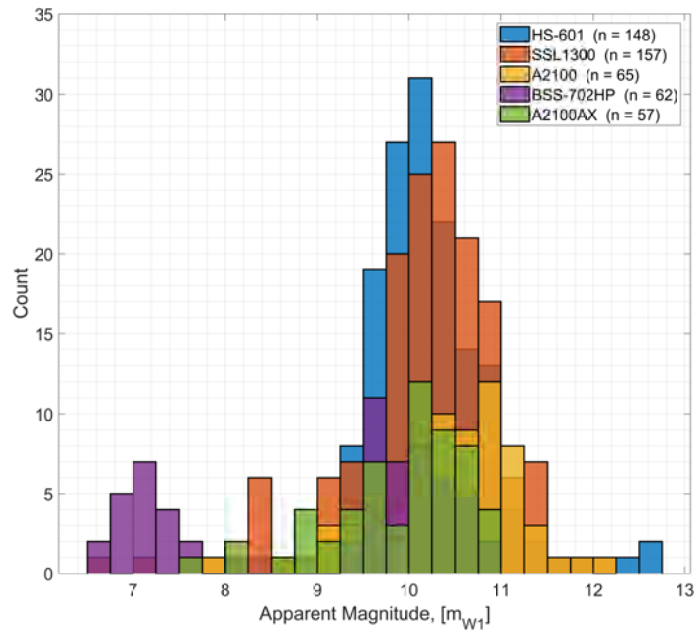
(a) W1

(b) W4

Figure 6.1: Magnitudes of various active box-wing satellites, as detected and measured by WISEstreakDET, in bands *(a)* W1 and *(b)* W4. Limited ability to discriminate between bus types is evident in bands W1 and W2.

134

6.2.1.2 Colour-Colour Plots

All fifteen colour-colour plot combinations were produced for the five variants of box-wing buses. Two examples are given in Figures 6.2 and 6.3, showing most and least differentiation of data respectively. It was observed that while the majority of data points overlap, many of the plots contained isolated BSS-702HP and HS-601 colour-colour values.
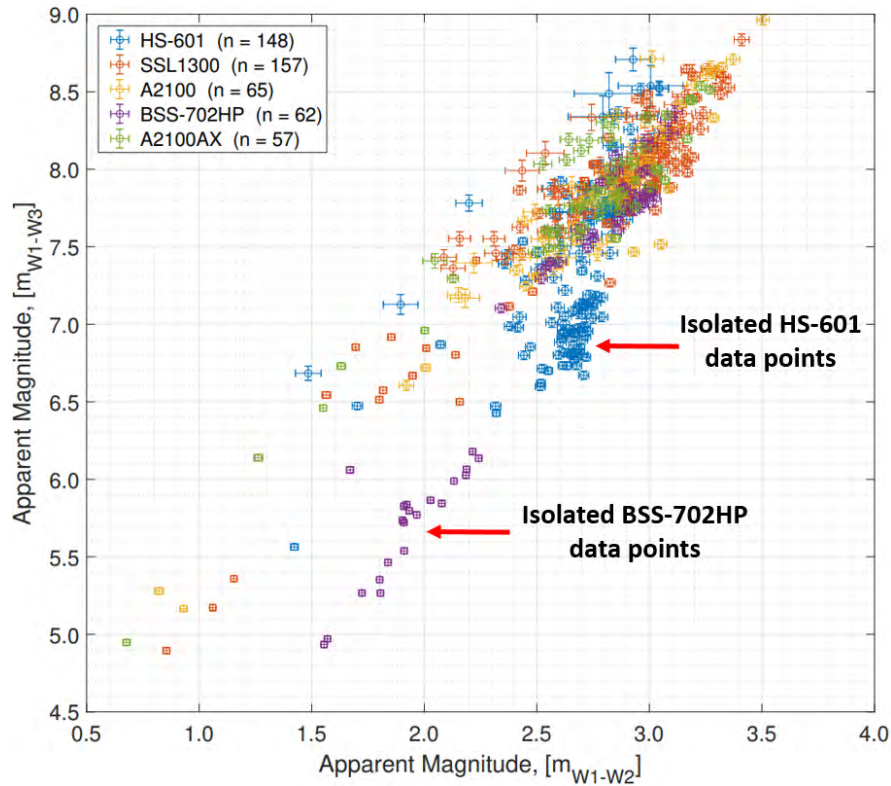

Figure 6.2: W1-W2 *vs* W1-W3 colour-colour plot of active box-wing satellites. Many data points associated with BSS-702HP and HS-601 buses are isolated.
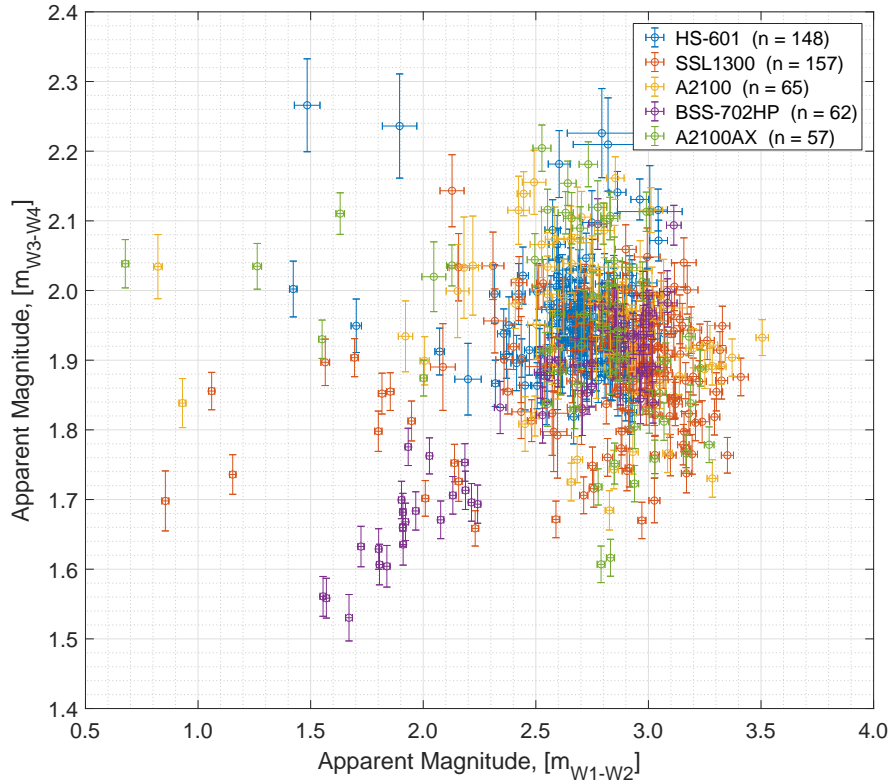
Figure 6.3: W1-W2 *vs* W3-W4 colour-colour plot of active box-wing satellites. This colour-colour combinations shows the least amount of differentiation between bus types.

The isolation of BSS-702HP data points may be explained by the unique configuration of solar concentrators used by Boeing in the production of this bus. As seen in Figure 6.4, these concentrators run along both edges of the satellite wings, and are almost orthogonal to the solar panels. Due to the observational geometry of WISE producing phase-angles near 90°, solar panel flux contribution is minimised. This geometry may, however, increase the flux contribution from the concentrators, differentiating BSS-702HP bus brightness from other bus variants. This is a similar conclusion as was drawn by Payne et al. [66], as examined in Section 3.6.
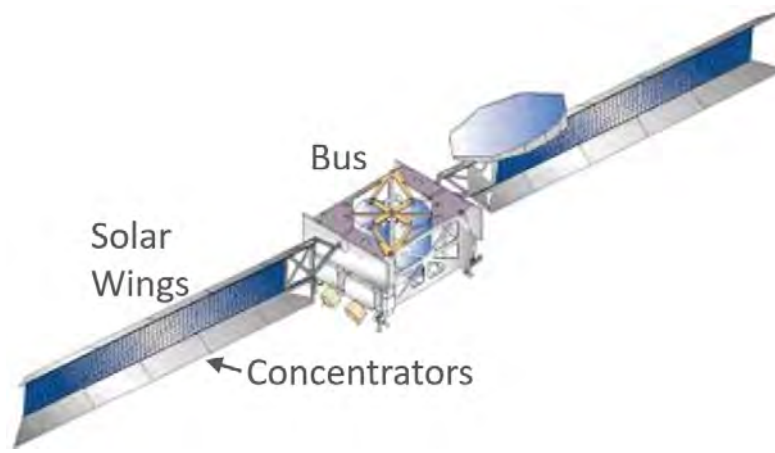
Figure 6.4: The Boeing BSS-702HP bus is shown, with concentrators running along the wing edges almost orthogonal to solar panels. This may explain the variance in BSS-702HP colours compared to other bus variants (adapted from [118]).

Another observation from Figure 6.2 is that data points for all satellites are quite widely distributed. One potential reason for this may be the change in Sun-RSO-sensor geometry as the Sun changes position over the course of a year. This change in flux with seasonal geometry, at constant phase angle, was discussed in Section 3.6. To test this theory, BSS-702HP data was plotted based upon the date of image capture, ranging from January to August of 2010. All 15 colour-colour plots were produced, with W1-W2 *vs* W1-W3 shown as an example in Figure 6.5. As can be seen, flux does not appear to be correlated to seasonal geometry.
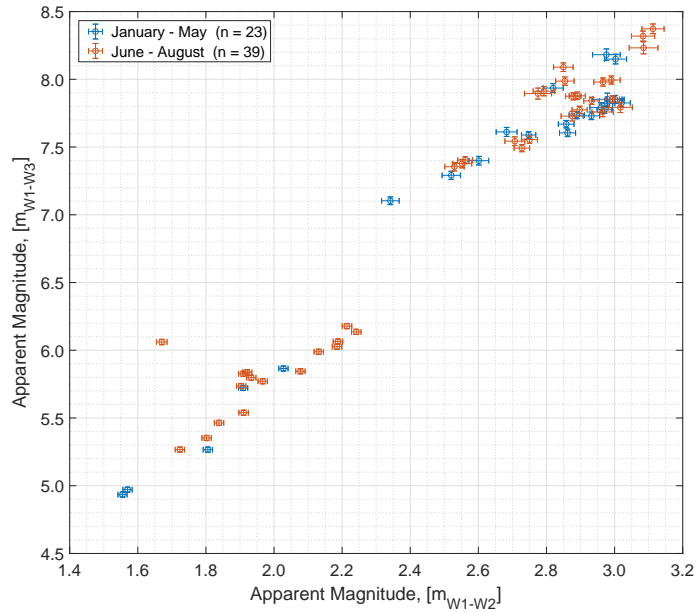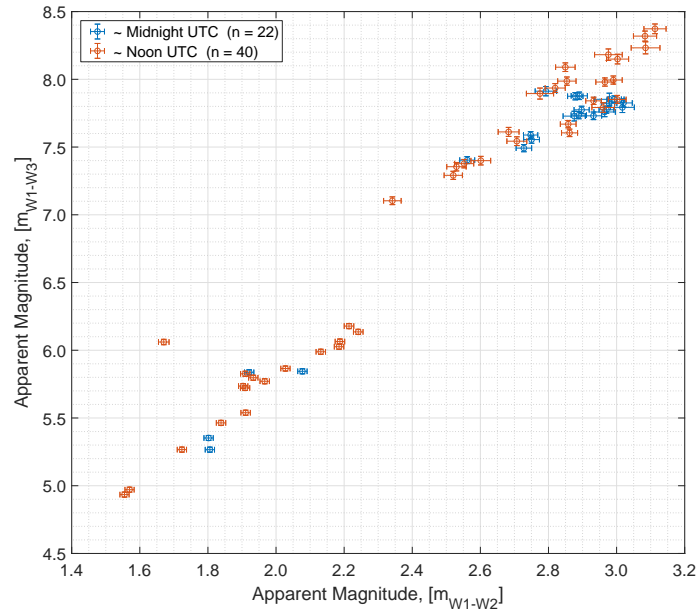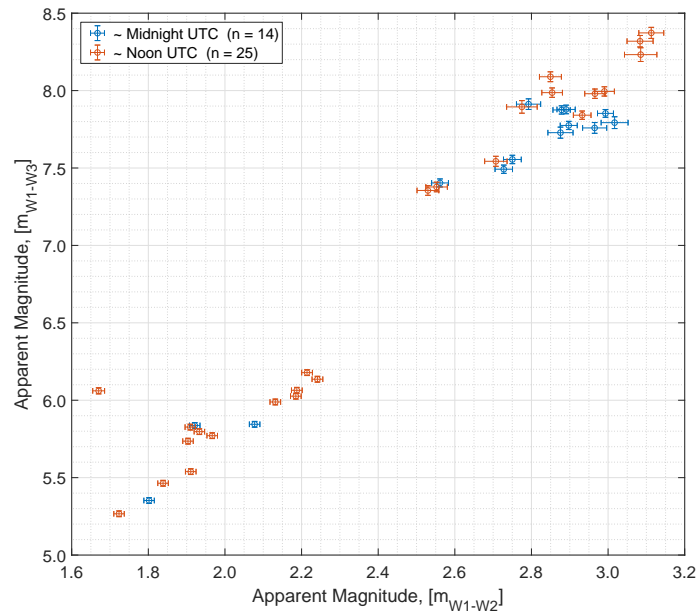
Figure 6.5: Colour-colour plots of active satellites with the Boeing BSS-702HP bus show no clear correlation between flux and time of year (seasonal geometry).

Due to the orbital geometry of the WISE satellite, it was noticed that images of GEO satellites tended to be isolated within two separate periods of the day - around noon and midnight UTC. WISE may be viewing GEO satellites with different observational geometry at these times, and as such, BSS-702HP data was plotted as a function of image time to assess correlation with time-of-day. All 15 colour-colour plots were produced, with W1-W2 *vs* W1-W3 again provided as an example. Figure 6.6a shows observations over the entire Jan-Aug period, while Figure 6.6b is isolated to the Jun-Aug period to examine a combined effect of time-of-year and time-of day. As can be seen, neither time-of-day or seasonal geometry seem to account for the wide distribution of flux seen in colour-colour plots.

(a) January to August

(b) June to August

Figure 6.6: Colour-colour plots of active BSS-702HP satellites show no clear correlation between flux and time-of-day. Seasonal geometry influence is evaluated by comparing *(a)* all observations, January to August, and *(b)* just June to August.

139

Other explored factors, including RSO size, age and phase angle, did not seem to account for the spread of data points. For the BSS-702HP data, one interesting observation was discovered. The solar concentrators on early builds of this satellite bus suffered from an inherent design flaw: excessive out-gassing of materials led to fogging of the concentrators, reducing their efficiency and consequently limiting the power available to satellite systems [119]. Figure 6.7 plots just active satellites with the BSS-702HP bus, comparing those with and without the design flaw. It can be seen that almost all observations of early models with the design flaw are bluer (smaller colour index) than newer models in which the flaw was rectified. As previously stated, such conclusions need to be considered in respect of the limitations of WISE data - a small number of data points, at near constant phase angle. Analysis of the entire WISE dataset, or confirmation with a photometric light curve from a different sensor, may increase the veracity of this and other outcomes.
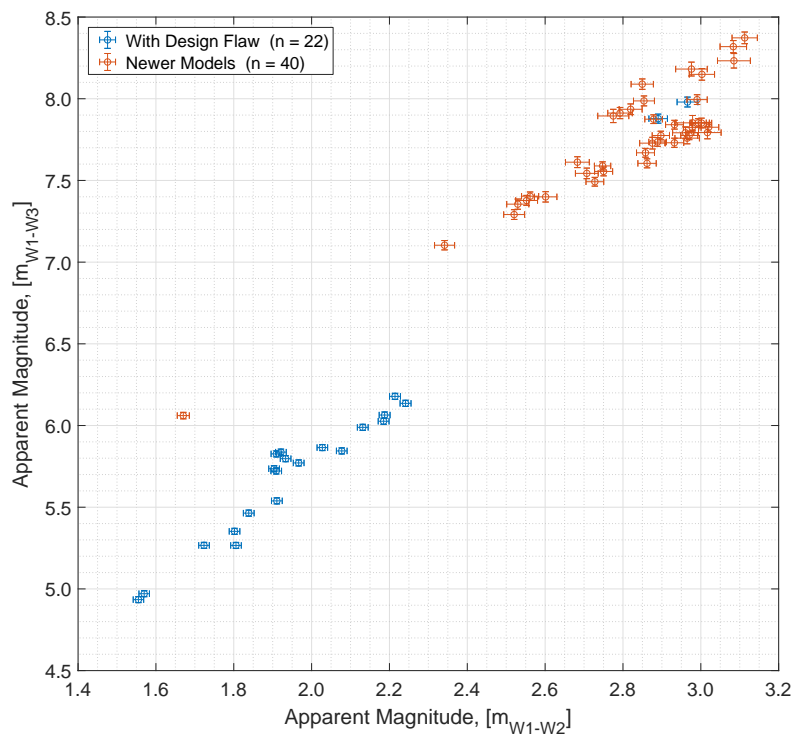

Figure 6.7: A colour-colour plot of active satellites with the Boeing BSS-702HP bus shows a potential correlation between flux and an early design flaw in the solar concentrators of these buses.

6.2.2 Comparison of Active Cylindrical Satellites

Of the 107 active cylindrical satellites analysed, there were 12 different bus variants. The five bus variants with the most observations are listed in Table 6.4, and are the subject of this experiment.

Bus Variant	# Observations
Russian Satellite Communications Company (RSCC) Ekspress	20
Boeing HS-376	16
Boeing HS-376HP	21
Boeing HS-376W	13
Meteosat Second Generation (MSG)	9

Table 6.4: The five active cylindrical satellite bus variants with the most observations in this database.

6.2.2.1 Colour-Colour Plots

All fifteen colour-colour plot combinations were produced for the five variants of box-wing buses. All appeared similar in regards to the amalgamation of data, with two examples given in Figures 6.8 and 6.9.
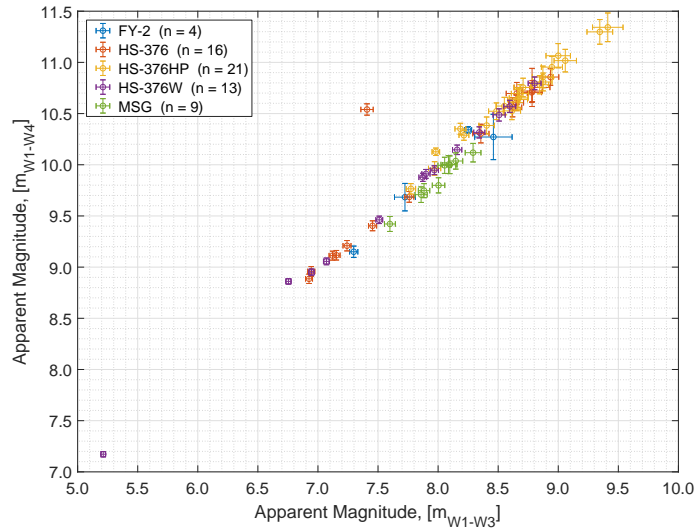
Figure 6.8: W1-W3 *vs* W1-W4 colour-colour plot of active cylindrical satellites.
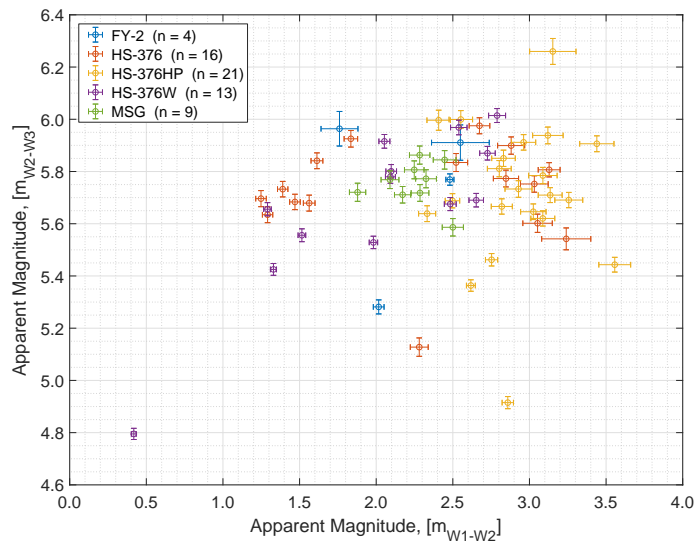

Figure 6.9: W1-W2 *vs* W2-W3 colour-colour plot of active cylindrical satellites.

It was observed that while some plots contained limited grouping of data points for individual variants - in particular satellites with the MSG bus - for

the most part data points were amalgamated. This is likely a consequence of the similarities in shape and configuration between various cylindrical bus variants. Although containing different payloads and sizes, as can be seen from Figure 6.10, the general appearance of these satellites is the same. It is noted that there is also a very limited amount of observations - this is due to the popularity of box-wing design reducing the number of cylindrical satellites still in service. Once again, analysis of the entire WISE dataset may give a more complete indication of the ability to differentiate between active cylindrical satellites.

(a) Boeing HS-376   (b) MSG

Figure 6.10: Cylindrical satellite buses, for example *(a)* the Boeing HS-376 and *(b)* MSG, often share very similar configurations [118].

6.2.3 Comparison of Active Cylindrical and Box-Wing Satellites

It has so far been observed that colour-colour plots provide some ability to differentiate between different active box-wing satellite variants, while cylindrical satellite variants are largely indistinguishable.

This experiment will seek to holistically compare active box-wings to cylinders, to ascertain if a general ability to characterise an unknown satellite as one or the other exists.

6.2.3.1 Colour-Colour Plots

Figures 6.11 and 6.12 provide examples of colour-colour plots comparing active box-wing and cylindrical satellites, with the least and most differentiation of data respectively.
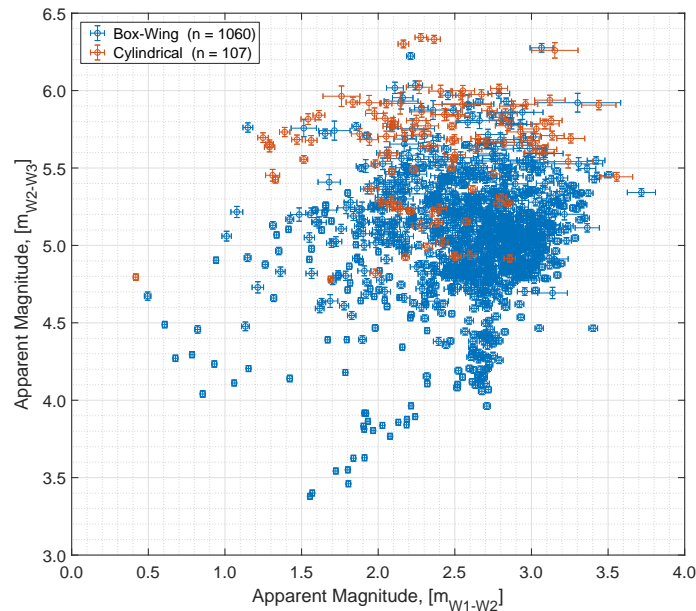

Figure 6.11: W1-W2 *vs* W2-W3 colour-colour plot of active satellites, showing some delineation of data points.
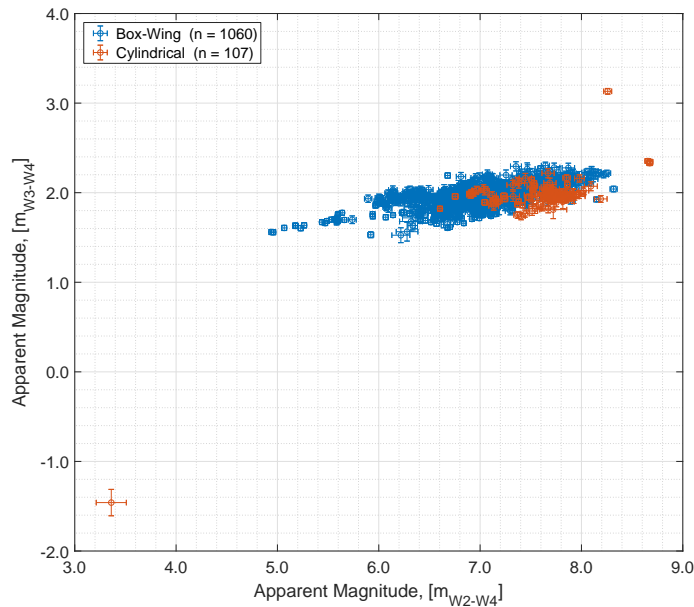
Figure 6.12: W2-W4 *vs* W3-W4 colour-colour plot of active satellites, showing grouping of box-wing and cylindrical shape variants. The two groups largely overlap.

Some colour-colour plots, such as in Figure 6.12, exhibit a grouping of cylindrical satellite data points. Again, this is likely due to the similarity in design of these satellite bus variants. Box-wing satellites, meanwhile, exhibit a wide distribution of data points, representing the great variance in shape, size, material and apertures present within this category. As there is always overlap between box-wing and cylindrical satellites, a general ability to characterise an unknown satellite as one or the other from WISE data does not exist.

A constructive summary to the comparison between active box-wing and cylindrical satellite variants may be this - many variants appear similar, though when comparing just two different satellites there is often a distinct difference in occupied colour-colour space. See Figure 6.13 as an example, which compares the Boeing BSS-702HP and HS-376 bus variants (box-wing and cylindrical respectively). There is a clear delineation of colour-colour data points.

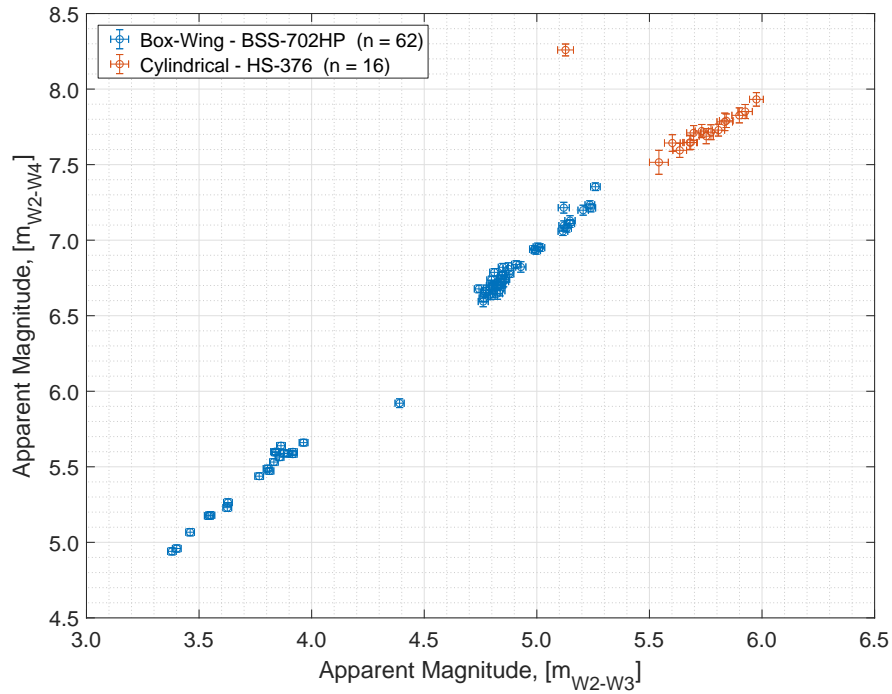**Figure 6.13:** W1-W2 *vs* W2-W3 colour-colour plot comparing box-wing BSS-702HP and cylindrical HS-376 satellite buses.

Figure 6.13 shows that WISE photometric data can potentially be used for determining satellite identity, despite the inability to produce RSO light-curve shapes as Scott and Wallace [68] did with Anik-F1 and Anik-F1R. This therefore shows promise for the utility of multi-band infrared characterisation of RSOs.

6.2.4 Comparison of Satellites Size

Average Radar Cross Section (RCS) values for RSOs analysed by WISEstreakDET were obtained via the ESA DISCOS service [116, 117]. Of the 1189 active satellites in the database, the minimum RCS was 3.25 m^2, the average 34.38 m^2, and the maximum 284.48 m^2. This breadth of values presents another opportunity for differential characterisation.

Stokes et al. [70], using SBV satellite data, observed that large satellites appear brighter than smaller satellites. This experiment will seek to test this generalisation, with a comparison of active box-wing satellites, active cylindrical satellites, and rocket-bodies.

6.2.4.1 Magnitude

Table 6.5 summarises the average magnitude for three different active box-wing satellites, with large, medium and small RCS values. All measured magnitudes for these satellites are shown in Figure 6.14. It can be seen that the outcome agrees with the generalisation made by Stokes et al. [70] - larger satellites appear brighter than smaller satellites. This is the case in all four WISE bands, though only bands W1 and W4 are shown for brevity.

Satellite	RCS (m^2)	W1	W2	W3	W4
Thuraya	284.48	8.54	6.48	1.75	-0.07
Intelsat	32.17	10.61	7.74	2.7	0.78
Beidou	12.79	11.44	8.76	3.42	1.39

Table 6.5: The average magnitude in each WISE band is shown for three different active satellites, with large, medium and small RCS.
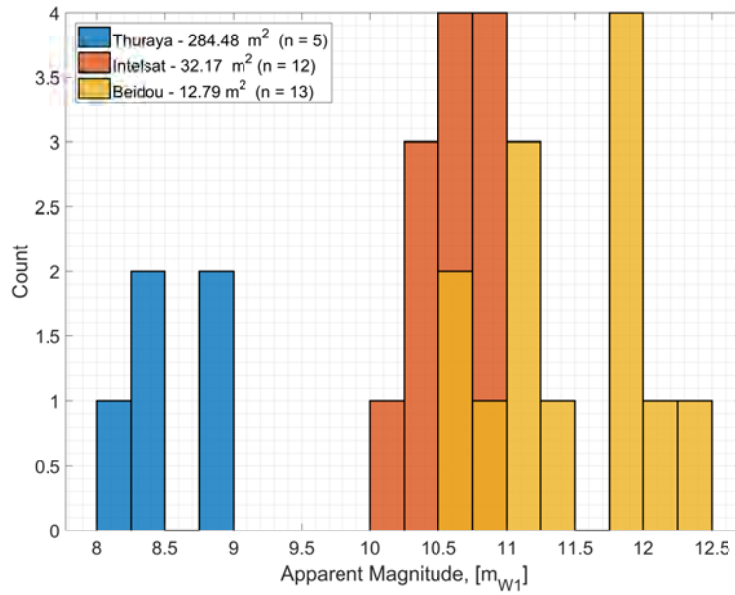
(a) W1
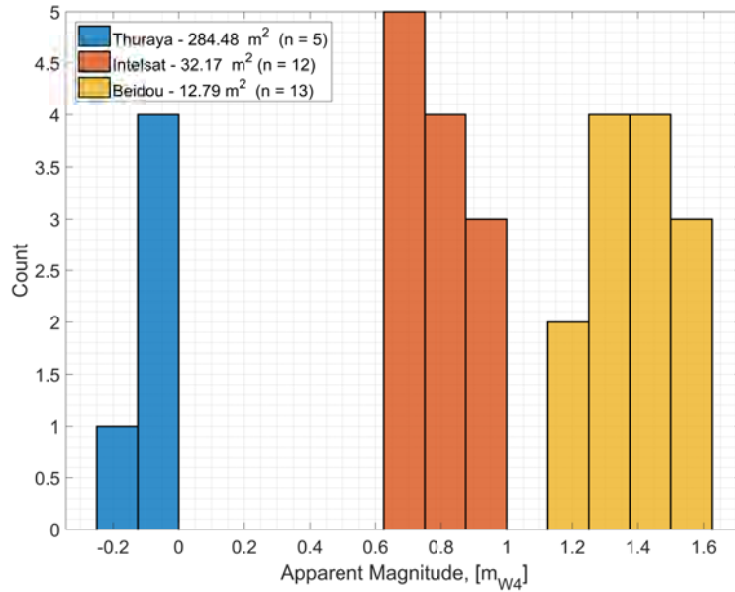
(b) W4

Figure 6.14: The magnitudes of a large, medium and small active box-wing satellite, in bands *(a)* W1 and *(b)* W4.

The magnitude of all active box-wing satellites were then plotted as a function of their respective RCS values. All four bands appear similar, with band W2 shown as an example in Figure 6.15. There is a large vertical spread of data points - this is likely attributable to variance in solar illumination geometry and satellite configuration for satellites of similar RCS. Despite this, a clear trend of increasing brightness with increasing satellite RCS is evident, as shown by the red polynomial line of best fit. Of note, data points corresponding to the Thuraya-2 satellite were not included, as their large RCS values detracted from the clarity of plots. The outcome with these data points included remained unchanged. The small sample size also needs to be taken into consideration, warranting confirmation with further research.
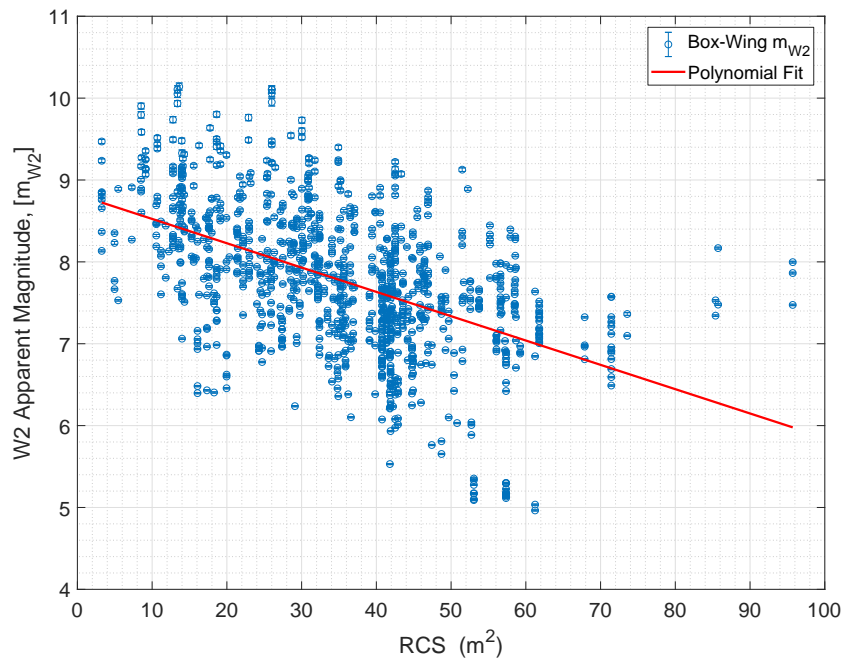
Figure 6.15: The magnitude of active box-wing satellites shows a positive correlation between RCS and brightness.

Similar plots were constructed for the 107 active cylindrical satellites and 136 rocket bodies observed by WISEstreakDET. Again, all bands appear similar, with W1 and W3 provided as examples for each in Figures 6.16a to 6.16b. Although the sample size for both cylindrical satellites and rocket bodies is relatively small, the positive correlation between RCS and brightness is again observed.
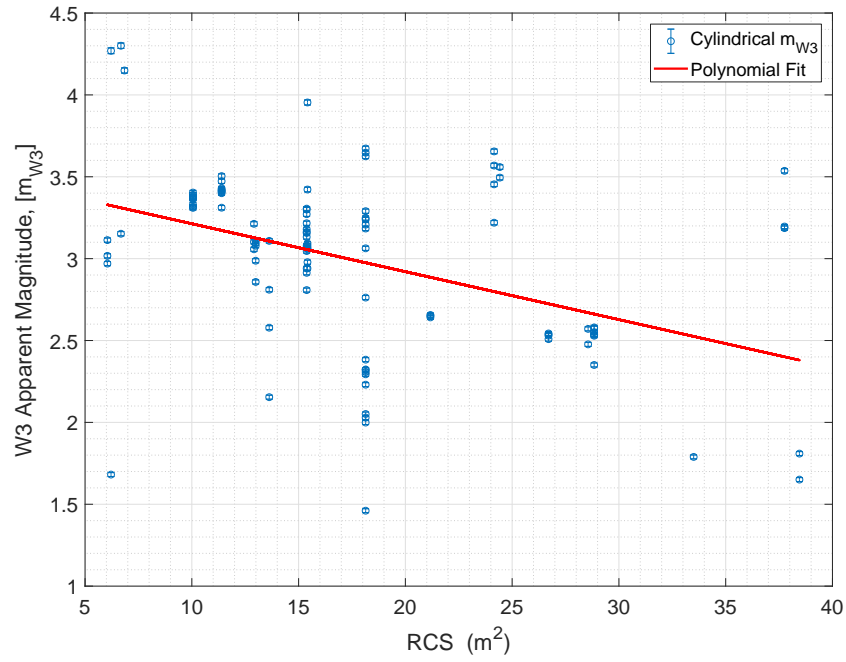
(a) Active cylindrical satellites, band W3
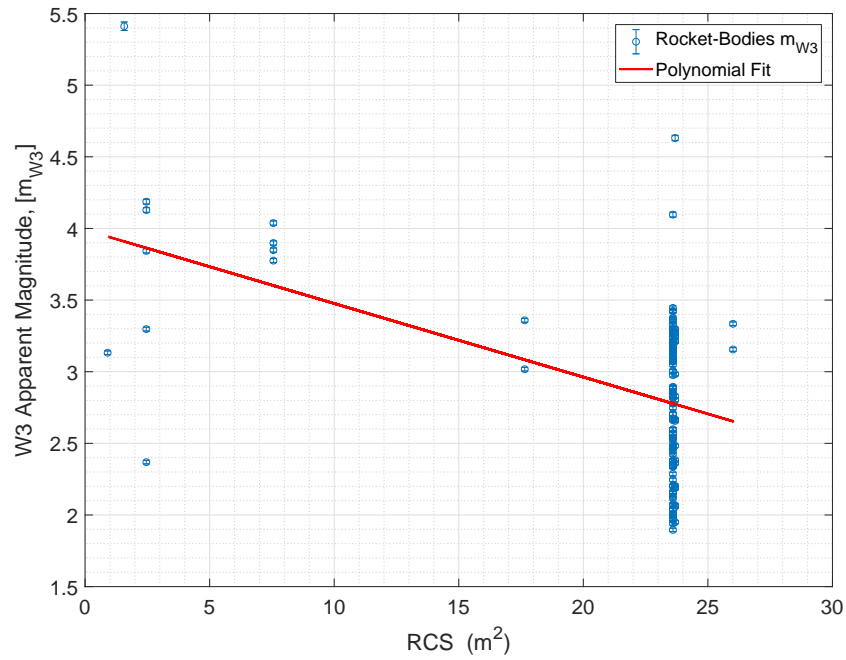
(b) Rocket bodies, band W3

Figure 6.16: The magnitude of *(a)* active cylindrical satellites and *(b)* rocket bodies shows a positive correlation between RCS and brightness.

150

The polynomial fit for rocket bodies may be less reliable than for satellites, as type SL-12 accounts for 123 of the 136 rocket bodies observed. This can be seen in Figure 6.16b as a grouping of data points with RCS values of around 23.5 m^2. The large vertical spread of SL-12 data points - almost 3 magnitudes - is in itself an interesting observation. As these are all the same rocket-body type, shape and size are relatively constant. Other factors, such as time spent in space or solar illumination geometry may account for the flux variance.

A further observation is that for rocket bodies, the correlation between RCS and brightness is weakest in band W1. This is evident from the relatively flat polynomial fit in Figure 6.17, not observed for W1 active satellite measurements. As W1 is in the reflective infrared regime, this result may be associated with the paint or surface material of the various rocket bodies. SL-12 surface properties were not found in literature, however spectroscopic observations by Abercromby et al. [89] suggest that it is not white paint. Research by Cowardin et al. [120] on SL-8 rocket bodies showed that white rocket bodies displayed diffuse reflectance, and grey rocket bodies specular. If SL-12s exhibit specular reflection, the WISE observational geometry of around 90° phase angle may lead to reduced flux toward the WISE sensor, accounting for the lower average flux compared to other rocket body types in band W1.
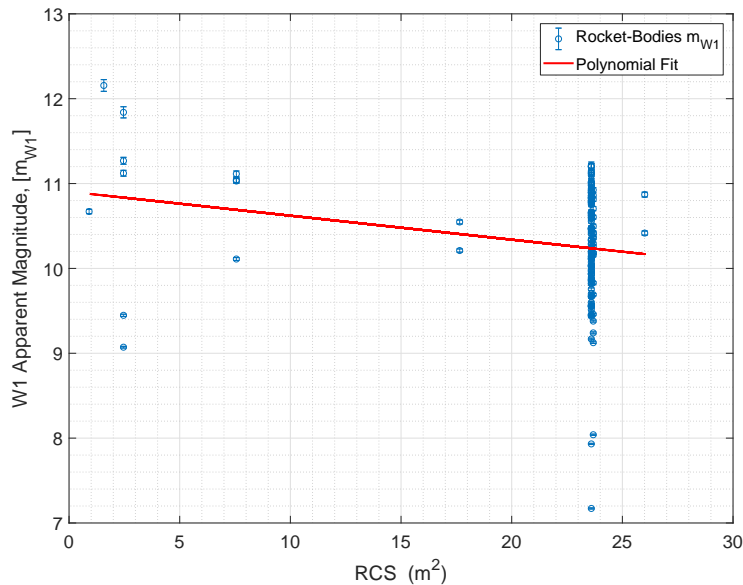
Figure 6.17: The W1 magnitude of rocket bodies shows a weaker correlation between RCS and brightness than for other bands.

6.2.5 Summary

To summarise the evaluation of active satellite shapes, four main observations have been made. Firstly, there is a limited ability to distinguish between some variants of active box-wing satellites using colour-colour plots. This ability is not apparent with active cylindrical satellite variants, likely due to the similarity in shape and configuration of these spacecraft. When holistically comparing active box-wing and cylindrical satellites, a grouping of colour-colour data points was evident for cylinders, however this grouping is amalgamated with box-wing data points. Therefore there is no general capability to distinguish between the two. Finally, a strong positive correlation between RSO size and brightness was observed.

6.3 Evaluation of Satellite Status

As described in Section 1.5.4, the operational status of a satellite - active or retired - may be an indicator of the orbital stability of that satellite. For GEO satellites in particular, once moved to a graveyard orbit and no longer actively controlled, satellites are subject to orbital perturbations that may lead to tumbling or generally unstable profiles. This disparity between stable and unstable flight profiles may provide another opportunity for characterisation.

6.3.1 Comparison of active and retired box-wing satellites

From the subset of WISE images analysed, 1232 box-wing satellites were detected. Of these, 1060 were active, 170 retired, and two unknown.

6.3.1.1 Magnitude

Figure 6.18 shows the magnitude histograms in band W3, comparing active and retired box-wing satellites. Remaining bands share the same appearance, and have not been shown for the sake of brevity.

As can be seen from the overlap of histogram data, there is no clear delineation between active and retired box-wing satellites. The left-side histogram tails for active box-wings in bands W1 and W2 show that some active satellites appear brighter than all retired satellites. This is more likely to be a factor of the higher sample size of active satellites than a detectable characteristic in these two bands.
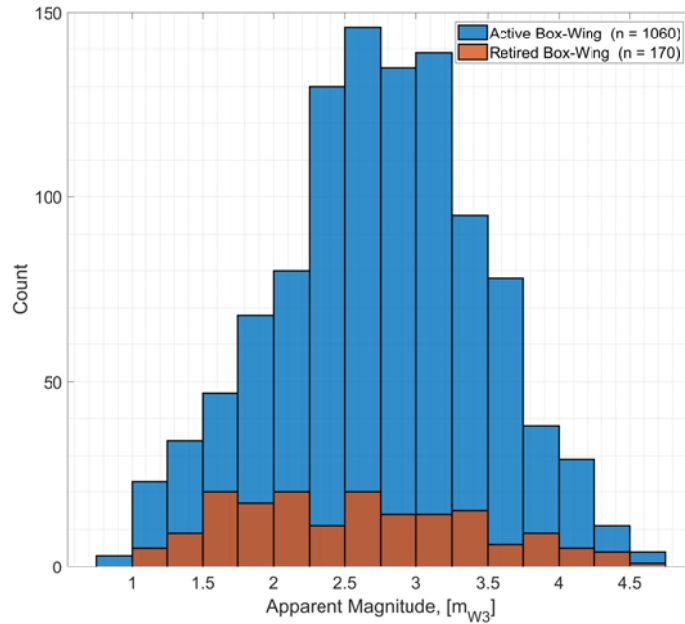
Figure 6.18: There is no clear delineation between the relative magnitudes of active and retired box-wing satellites.

6.3.1.2   Colour-Colour Plots

Colour-colour plots comparing active and retired box-wing satellites also failed to demonstrate any clear ability for differentiation. The W2-W3 *vs* W2-W4 plot shown in Figure 6.19a does exhibit clustering of retired satellites, however in a space also occupied by active satellites. Figure 6.19b is more representative of the majority of colour-colour plots, with data points amalgamated and with no apparent clustering or delineation. It was observed that active satellites always have some data points that are more blue than retired satellites. It is suggested that this is a result of the limited amount of representative data points, and not a generalisation that active satellites appear brighter than retired.
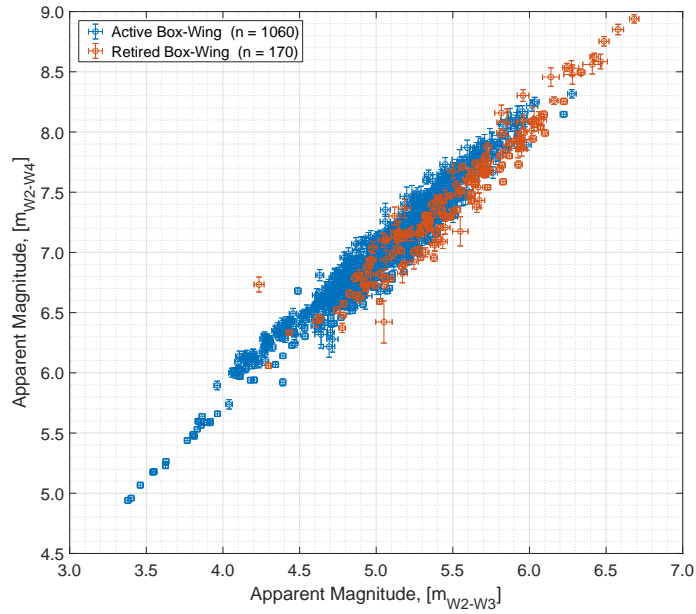
(a) W2-W3 *vs* W2-W4
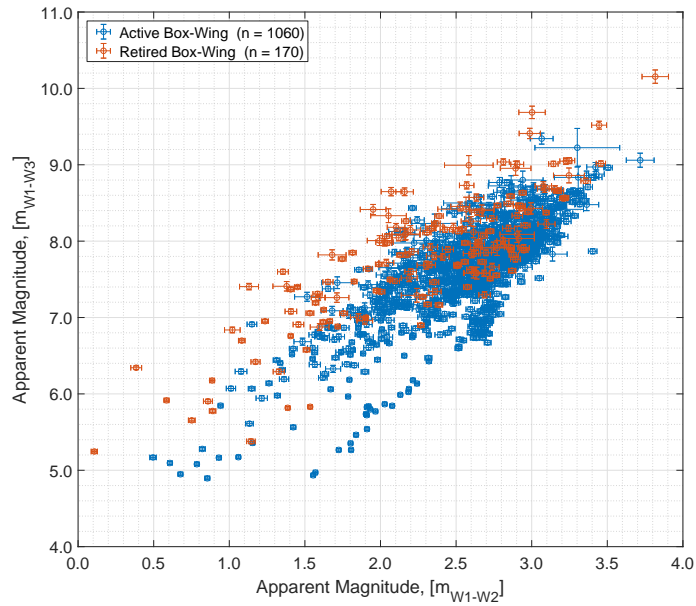
(b) W1-W2 *vs* W1-W3

Figure 6.19:   Colour-colour plots comparing active and retired box-wing satellites. Some clustering is apparent in *(a)*, with *(b)* representative of the majority of plots.

6.3.2 Comparison of active and retired cylindrical satellites

From the subset of WISE images analysed, 283 cylindrical satellites were detected. Of these, 107 were active, 175 retired, and one unknown.

Results for the comparison of active and retired cylindrical satellites are much the same as for box-wings - no clear ability to differentiate based upon operational status is evident. For the sake of brevity, only one magnitude histogram and colour-colour plot are shown, in Figures 6.20 and 6.21 respectively. The remainder of plots provide the same outcome.
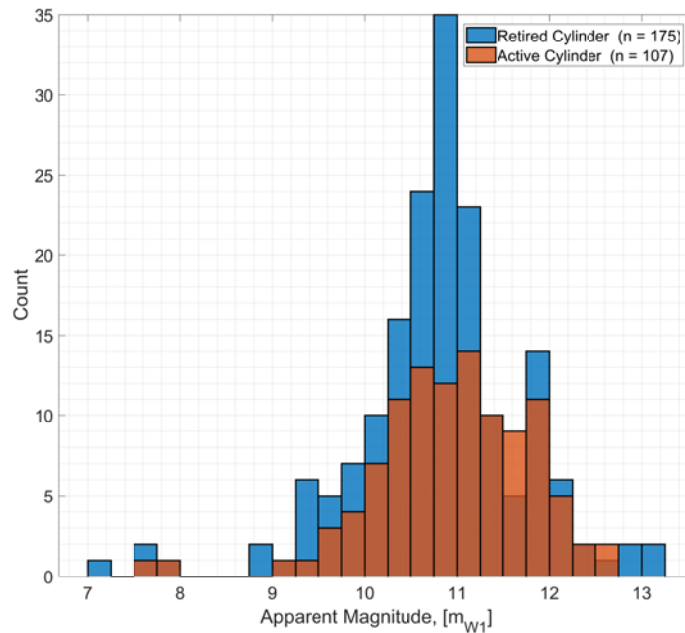
Figure 6.20: There is no clear delineation between the relative magnitudes of active and retired cylindrical satellites.

156
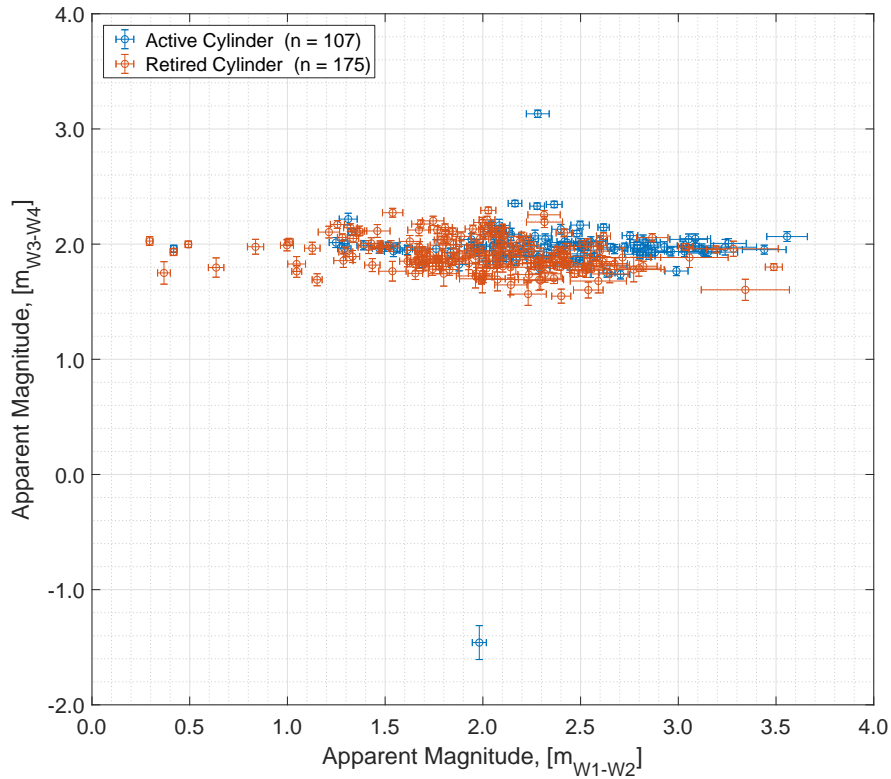
Figure 6.21: W1-W2 *vs* W3-W4 colour-colour plot comparing active and retire cylindrical satellites.

The lack of differentiation between active and retired satellites - for both box-wing and cylindrical shaped buses - is likely due the limited number of observations in WISE imagery, and the consequent inability to produce light curves.

It is predicted that light curves would more clearly show a distinction, due to the reflecting/emitting surface of a tumbling retired satellite constantly changing. This may produce a light curve that exhibits more rapid oscillation of flux than for active, stable satellites. WISE observations, conversely, represent satellite flux in at a single point of time - such oscillations are therefore not able to be readily observed.

6.3.3   Comparison of Satellite Age

As described in Section 1.4, unlike LEO satellites which are typically de-orbited, retired GEO satellites are placed into a 'graveyard' orbit, offset from the active GEO belt. Rocket bodies and debris often also remain on or near the GEO belt for some time. GEO RSOs analysed by WISEstreakDET therefore may be newly launched, or the remains of early GEO satellite launches. For this reason, age statistics vary significantly, once again presenting an opportunity for differential characterisation.

Frith et al. [87] reported a correlation between the mean J-K (1.22 - 2.19 μm) colour values of HS-376 satellites and their respective ages - the longer a spacecraft has been in space, the more red (large) its colour index. This experiment will seek to determine if similar correlations exist using WISE data.

RSO age was determined using the launch date, as provided by the ESA DISCOS service [116, 117]. Age is then defined as the time between date of launch, and date of image capture.

6.3.3.1   Replication of HS-376 Observations

The nearest WISE bands to J and K, as used by Frith et al. [87], are W1 and W2. Therefore, a comparison is made between these two colours. Frith et al. [87] focussed solely upon retired HS-376 buses, however to allow for a more complete analysis, both active and retired HS-376 buses observed with WISEstreakDET were examined.

The J-K results are shown in Figure 6.22, W1-W2 results for retired HS-376s in Figure 6.23, and W1-W2 results for active HS-376s in Figure 6.24. The W1-W2 colours for retired HS-376s shared the same trend as previous research - colours are more red for the older satellites. However, active HS-376s exhibited the opposite correlation.
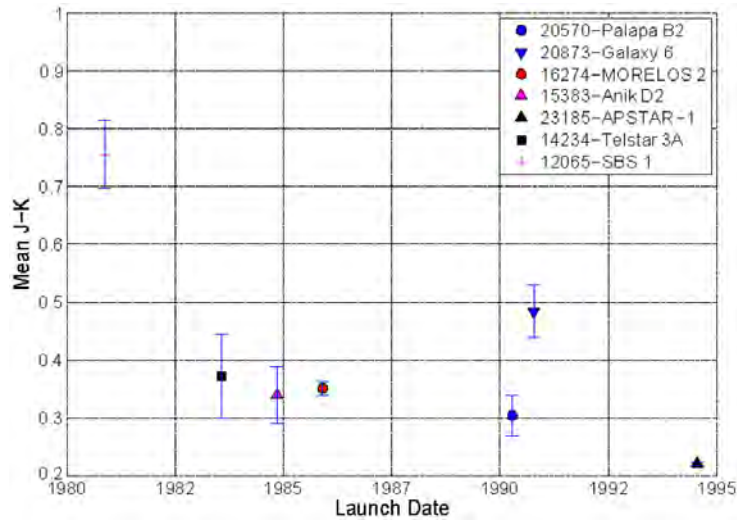
Figure 6.22: Observations by Frith et al. [87] suggest that mean J-K colour index values become more red (larger) with increase in spacecraft age.
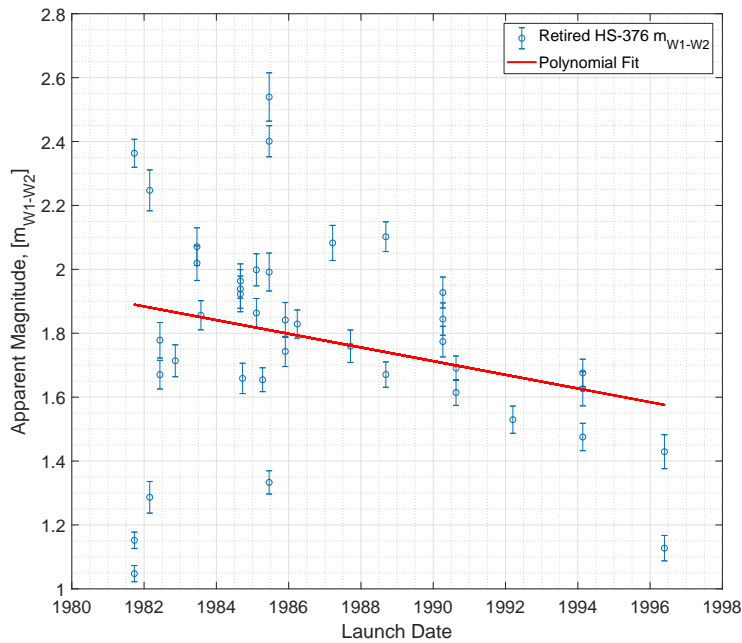
Figure 6.23: The W1-W2 colour index values of retired HS-376 buses also show a tendency to become more red with age.
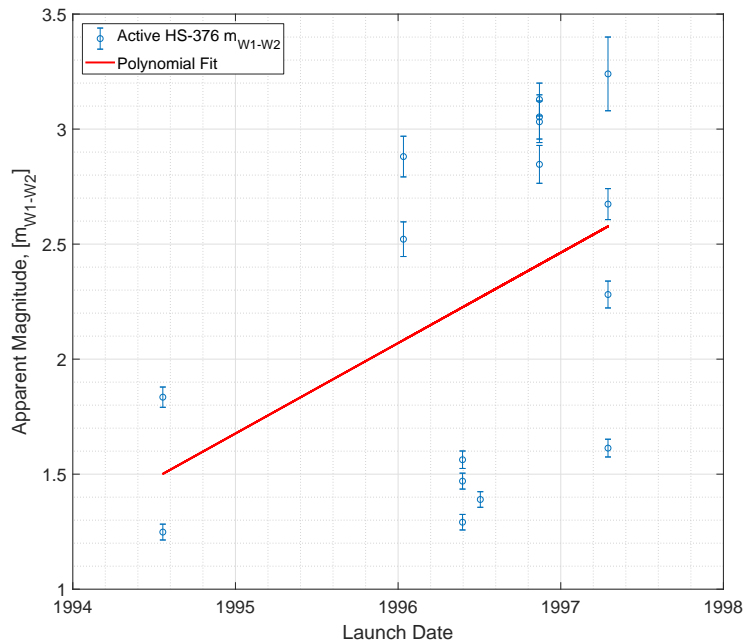
Figure 6.24: The W1-W2 colour index values of active HS-376 buses also show a tendency to become more red with age.

Active HS-376 results are less reliable than those of retired HS-376s, reducing the confidence of the reversed correlation observed in Figure 6.24. Firstly, the sample size is smaller - 16 active HS-376s, compared to 40 retired. Secondly, the last satellite to utilise the HS-376 bus was launched in 1997, leading to a small range of launch dates among active satellites. This reduced x-axis spread is likely to have a great influence on the polynomial fit of data.

The remaining five WISE colours were also plotted for retired HS-376s, to examine if colour became more red with age as observed in J-K and W1-W2. W1-W3, shown in Figure 6.25a, exhibited the same relationship. However, the remaining four colours exhibited a reversed correlation, with colour being more blue for older satellites. W2-W4 is provided as an example in Figure 6.25b
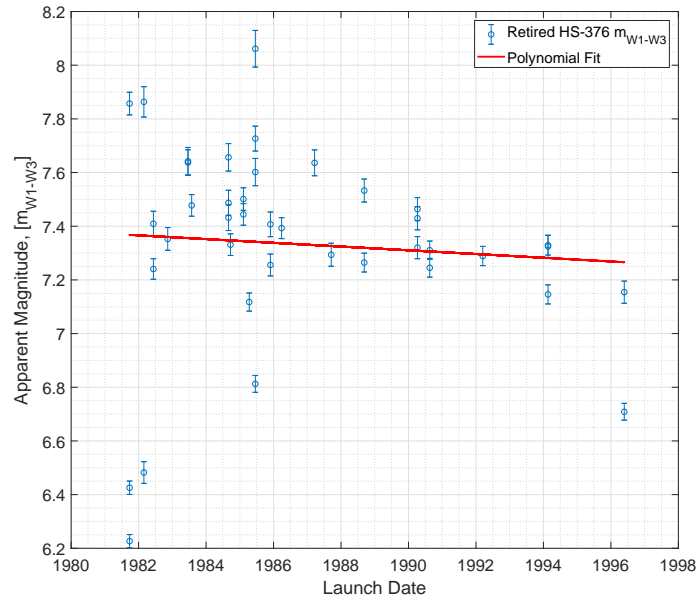
(a) W1-W3
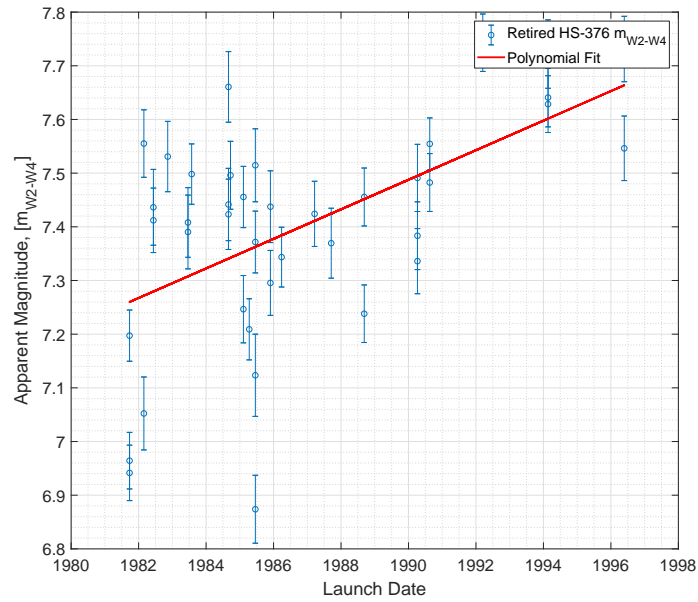
(b) W2-W4

Figure 6.25: *(a)* Some colours of retired HS-376 buses, such as W1-W3, show a tendency to become more red with age. *(b)* Other colours, such as W2-W4 show a reverse correlation.

161

This result may indicate a correlation that is dependent upon the wavelength of observation. For reflective infrared, such as the J-K colour index used by Frith et al. [87] and colours including band W1 for this research, older satellites typically appear more red. For thermal infrared, and particularly the passive thermal bands W3 and W4, older satellites tend to appear more blue.

The cause of this varying correlation may be a result of the reflectivity and emissivity of materials changing in different ways with age. Further analysis, including different bus types and using spectral observations, may confirm this conclusion.

6.3.3.2 Ageing of Active Box-Wings, Cylinders and Rocket Bodies

Following the somewhat ambiguous results for HS-376 buses, the colours of all active box-wings, cylinders and rocket bodies were plotted as a function of their respective ages, to determine if a general correlation to age could be established. This experiment was limited to active satellites, instead of retired, as this is of most interest to the SSA community.

A summary of results is presented in Table 6.6, showing whether older RSOs tend to become more red or blue. Some colours exhibited a flat polynomial fit, suggesting that there was no correlation between age and colour - these are also listed in the summary of results. An example of each RSO type, for the W2-W3 colour, is given in Figures 6.26a, 6.26a and 6.27

Colour	Active Box-Wing	Active Cylinders	Rocket Bodies
W1-W2	-	-	Red
W1-W3	Blue	Red	Red
W1-W4	Blue	Red	Red
W2-W3	Blue	Red	-
W2-W4	Blue	Red	-
W3-W4	Blue	-	-

Table 6.6: Summary of WISE colour index values as a function of age. If blue, this means that colour values become smaller as the given RSO type ages. If red, colour values become larger. A dash means that there was no observed correlation between colour and age.
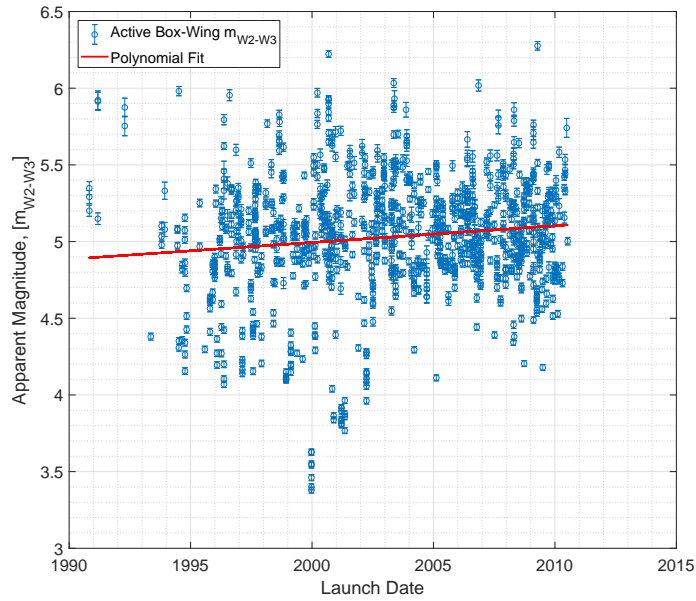
(a) Active box-wing satellites, W2-W3
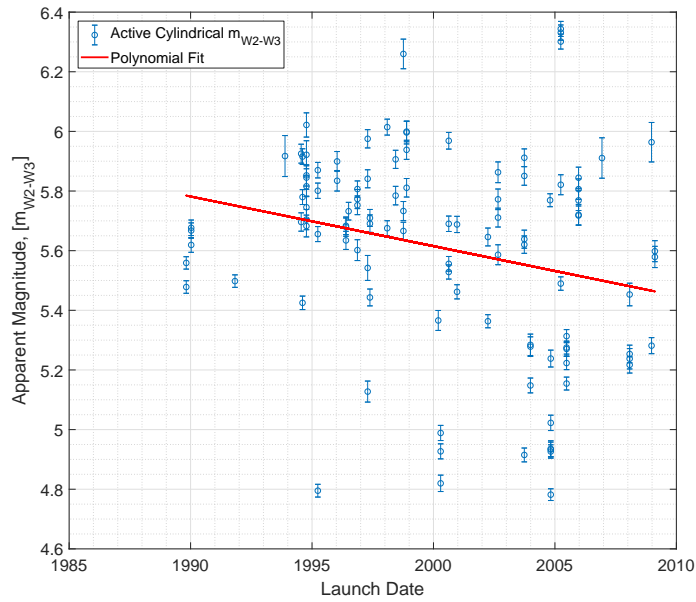
(b) Active cylindrical satellites, W2-W3

Figure 6.26: *(a)* The W2-W3 colour index values of active box-wing satellites show a tendency to become more blue with age. *(b)* Active cylindrical satellites show a reverse correlation.
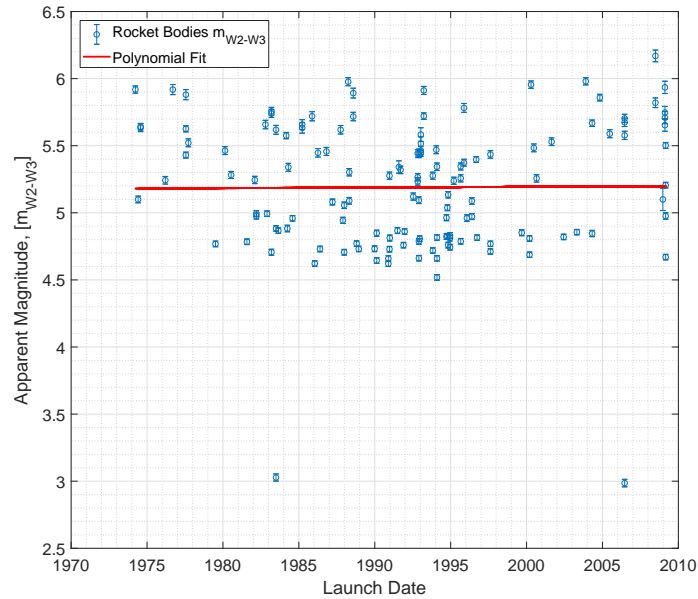
Figure 6.27: The W2-W3 colour index values of rocket bodies show no correlation with age.

It is interesting to note that active box-wings colours tended to become more blue with age, while active cylinders and rocket bodies become more red. A preliminary attribution may be that large, winged solar panels age differently than the curved panels of cylinders and the surface materials of rocket bodies. Further research into the manner by which the reflectivity and emissivity of each surface type ages is warranted.

6.4 Evaluation of RSO Type

To evaluate the potential to differentiate between satellites and rocket bodies, the magnitudes and colour indices each were plotted. Only retired satellites were considered, as the need to differentiate between active satellites and rocket bodies is less likely among the SSA community.

6.4.1 Comparison of retired box-wing satellites and rocket-bodies

Of the 1696 total streaks detected, 177 were correlated to retired box-wing satellites, and 136 to rocket bodies.

6.4.1.1 Magnitude

A comparison of retired box-wing satellite and rocket body magnitudes shows that while the two RSO types are largely similar, some satellites appear brighter than rocket bodies. This is evident in all bands except W1, for which there is no clear difference in recorded magnitudes. Magnitude histograms for bands W1 and W3 are shown in Figure 6.28.
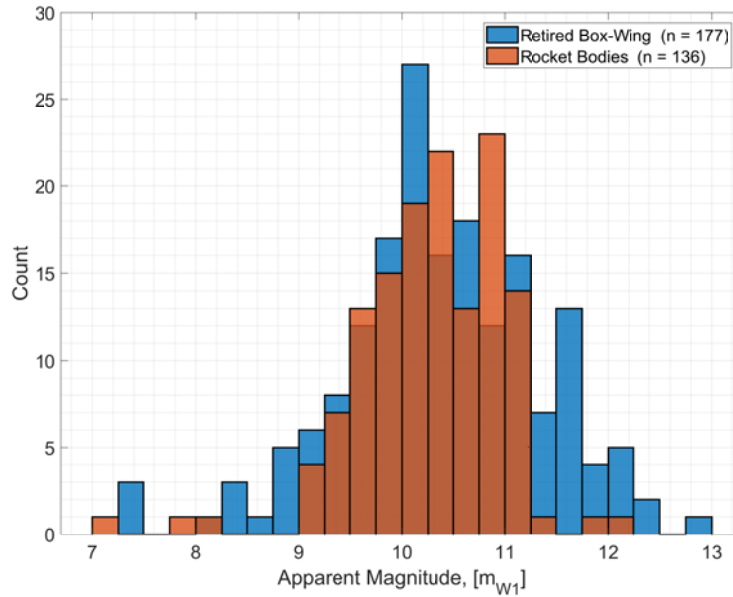
(a) W1
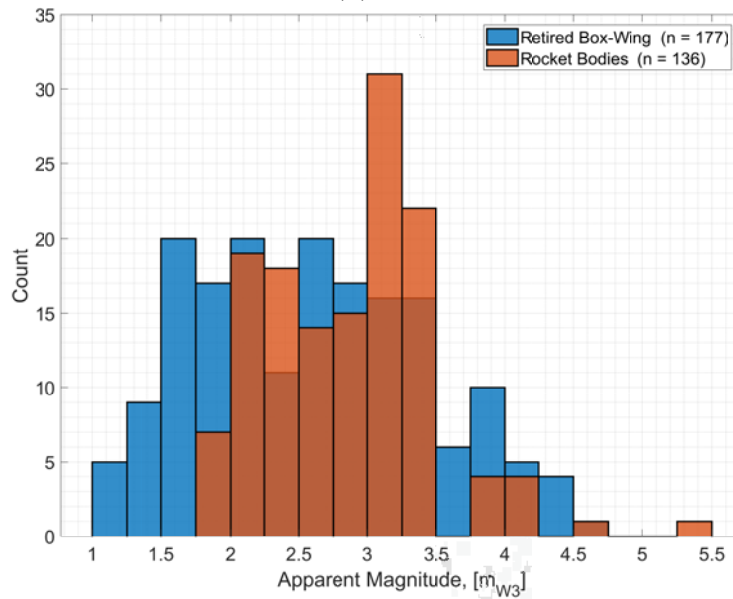
(b) W3

Figure 6.28: The magnitudes of retired box-wing satellites and rocket bodies are very similar in *(a)* band W1, while in bands W2-W4 some box-wings appear brighter, as is shown for *(b)* band W3.

6.4.1.2 Colour-Colour Plots

Colour-colour plots also show very little ability to differentiate between retired box-wing satellites and rocket bodies. Two examples are given in Figures 6.29 and 6.30, showing the most and least differentiation of data respectively.
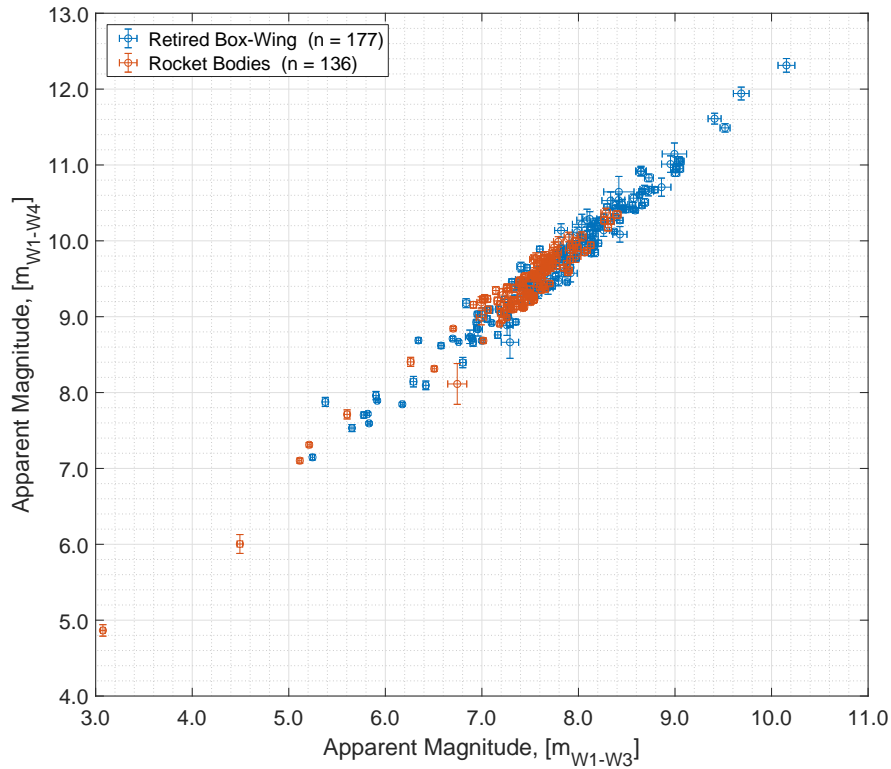
Figure 6.29: The W1-W3 *vs* W1-W4 colour-colour plot comparing retired box-wing satellites and rocket bodies shows limited ability to differentiate between the two RSO types.
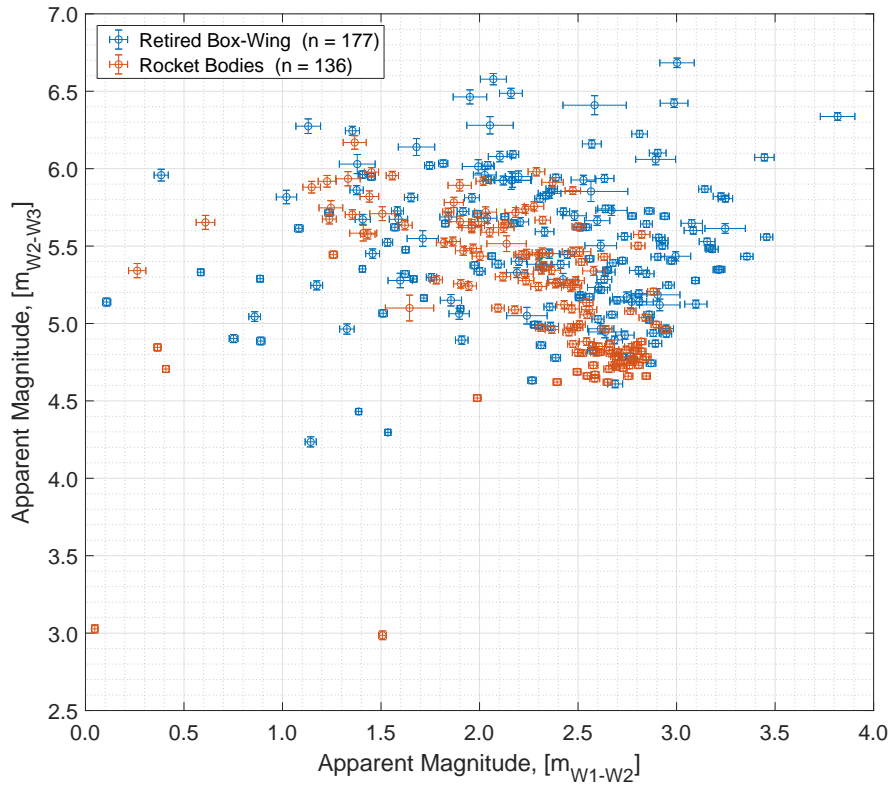
Figure 6.30: The W1-W2 *vs* W2-W3 colour-colour plot comparing retired box-wing satellites and rocket bodies show limited ability to differentiate between the two RSO types.

The distribution of data points is typically wider for satellites than for rocket bodies, as seen clearly in Figure 6.29. This is likely attributable to the greater variance in shape, size and appendages of satellites.

6.4.2 Comparison of retired cylindrical satellites and rocket-bodies

Of the 1696 total streaks detected, 175 were correlated to retired cylindrical satellites, and 136 to rocket bodies.

6.4.2.1 Magnitude

A comparison of retired cylindrical satellite and rocket body magnitudes reveals much the same result as for the last experiment - some satellites appear

brighter than rocket bodies, except in band W1 where the two RSO types exhibit a similar range of magnitudes. Histograms for bands W1 and W3 are shown in Figure 6.31.
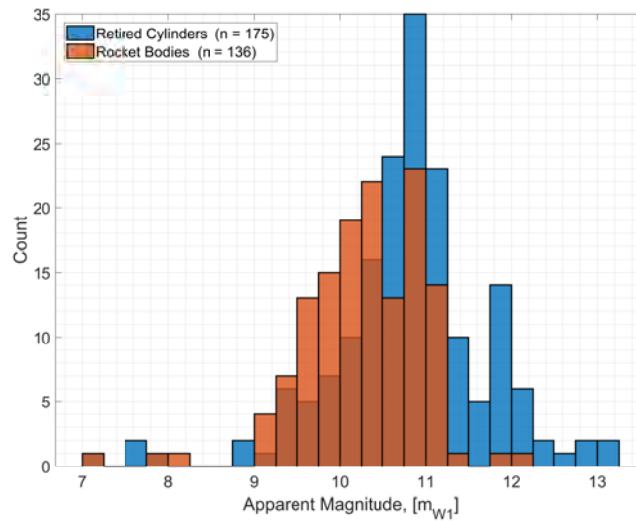
(a) W1
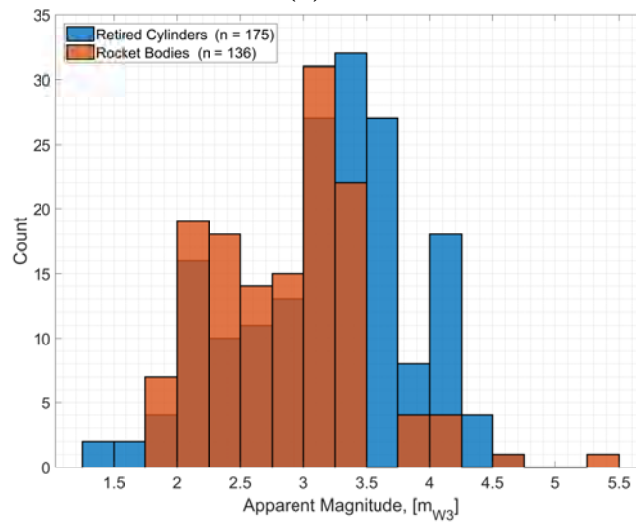
(b) W3

Figure 6.31: The magnitudes of retired cylindrical satellites and rocket bodies are very similar in *(a)* band W1, while in bands W2-W4 some box-wings appear brighter, as is shown for *(b)* band W3.

6.4.2.2 Colour-Colour Plots

The data points of colour-colour plots, while mostly being amalgamated, do show more potential for differentiation than for the box-wing comparison. Two examples are given in Figures 6.32 and 6.33.
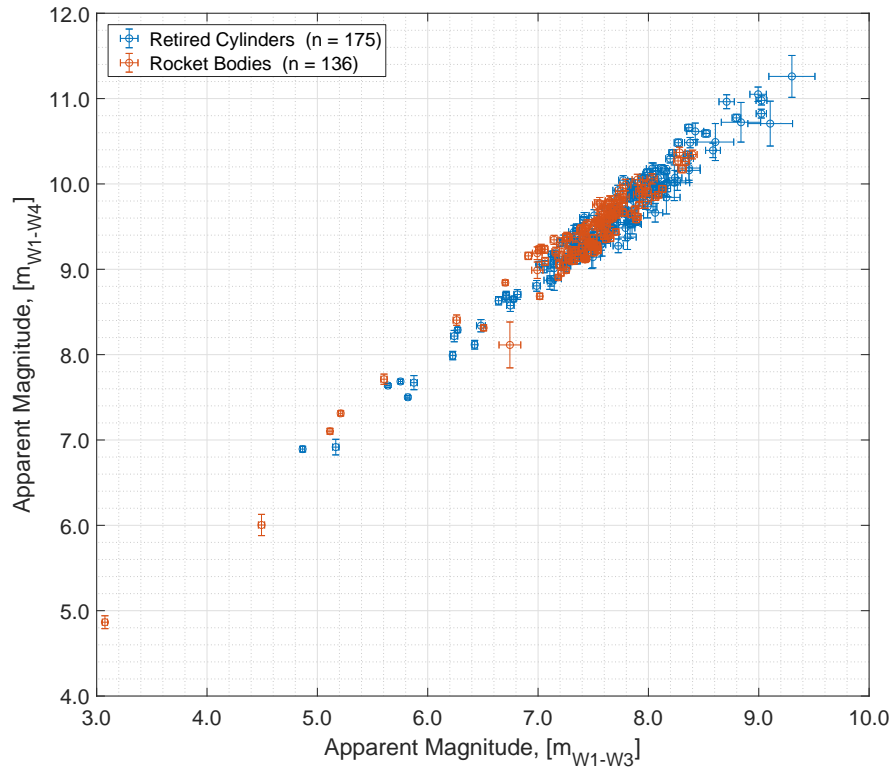
Figure 6.32: The W1-W3 *vs* W1-W4 colour-colour plot comparing retired cylindrical satellites and rocket bodies shows some ability to differentiate between the two RSO types.

170
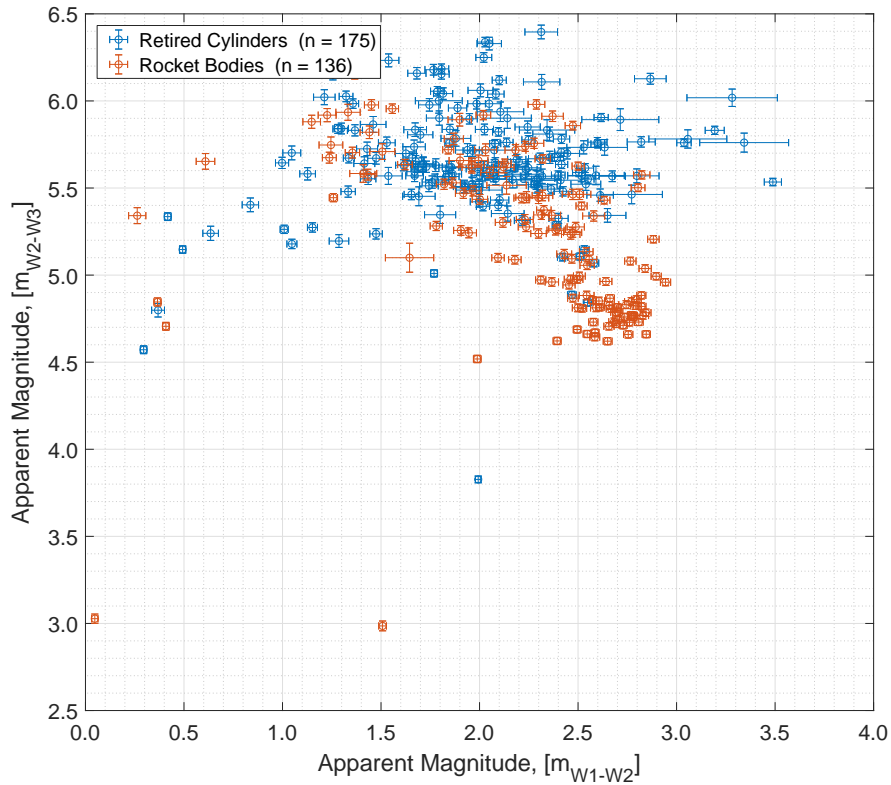
Figure 6.33: The W1-W2 *vs* W2-W3 colour-colour plot comparing retired cylindrical satellites and rocket bodies shows some ability to differentiate between the two RSO types.

The limited ability to differentiate between retired satellites and rocket bodies may once again be associated with the limited range of data points available for each. Creation of time-resolved light curves with a more complete set of WISE photometric results may lead to more differentiation between the RSO types.

6.4.3 Comparison of rocket body types

In addition to the 136 rocket bodies detected in the original image dataset, 14 Breeze-M rocket body measurements were taken using WISEstreakDET, in collaboration with measurements by Lee et al. [45] for an upcoming Committee on Space Research (COSPAR) conference paper. These additional measure-

ments have been included in the present analysis. In total, six different rocket body sub-types were observed, summarised in Table 6.7.

Rocket Body	Observations	Typical Mass (kg)	Average RCS (m^2)
SL-12	123	2120 - 2440	23.60 - 26.01
Breeze-M	18	1600	7.56
IUS Stage 2	5	1140	2.46
Titan 3C	2	1487	17.65
Fengyun 2E AKM	1	729	1.57
Himawari 5 AKM	1	27	0.91

Table 6.7: Summary of the rocket body types observed and characterised by WISEstreakDET. Note: AKM stands for Apogee Kick Motor, used for propulsion into final orbit [121].

6.4.3.1 Magnitude

Figure 6.34 shows the magnitudes of each rocket body type, in bands W2 and W4. Histograms for all four WISE bands appeared similar, with two shown for brevity. Some SL-12 rocket bodies appear brighter than other types in all bands except W4. The magnitude range of other rocket body types typically overlap, except for the Fengyun 2E which is the least bright in all bands. Sample sizes for all but the SL-12s is low, however are included for indicative purposes - future analysis of the full WISE imagery database may reveal a more complete comparison.
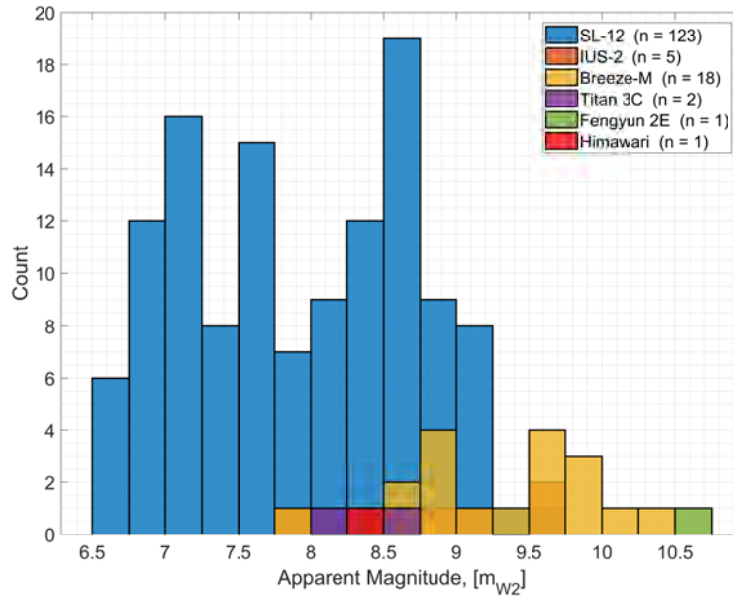
(a) W2
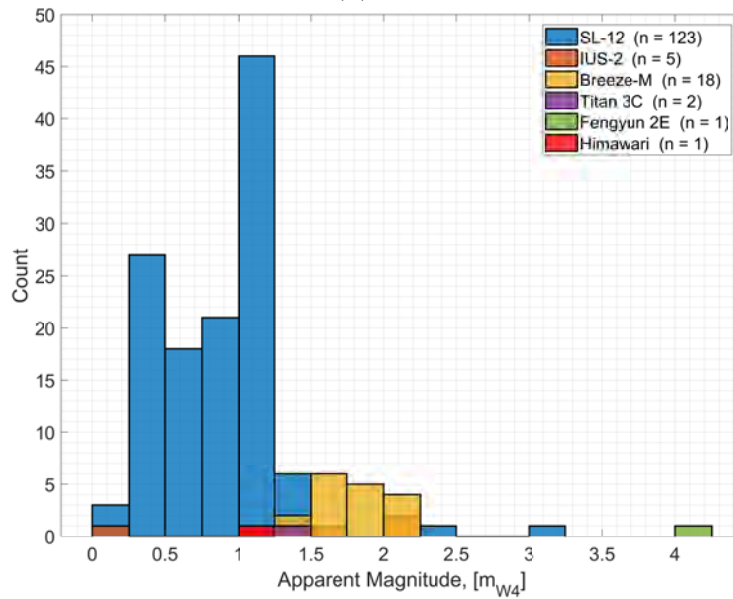
(b) W4

Figure 6.34: The magnitudes of six rocket body types, in bands *(a)* W2 and *(b)* W4, show a large overlap, however SL-12s are often brightest in all bands, and the Fengyun 2E the least bright.

6.4.3.2   Colour-Colour Plots

Colour-colour plots, despite displaying a reasonable overlap of data points, do exhibit some ability to delineate between the six rocket body types. As can be seen in Figures 6.35 and 6.36, SL-12 and Titan rocket bodies in particular tend to plot in different subspaces than do Breeze-M. This may be due to size - Breeze-M are less than half the size of SL-12 and Titan - or a factor of the different surface materials of these rocket bodies.
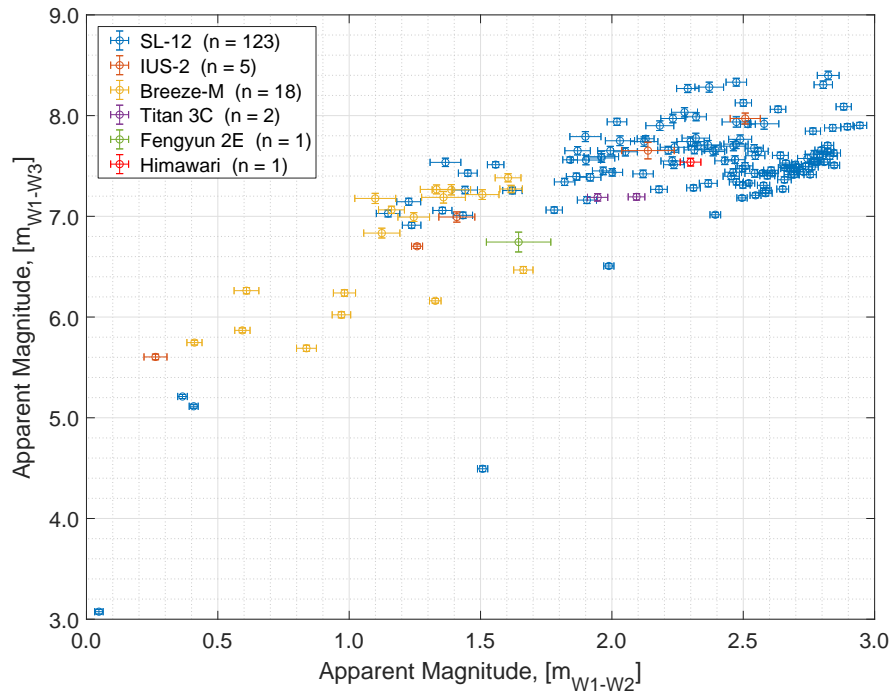
Figure 6.35: The W1-W2 *vs* W1-W3 colour-colour plot shows some ability to differentiate between six rocket body types, in particular SL-12, Titan and Breeze-M.
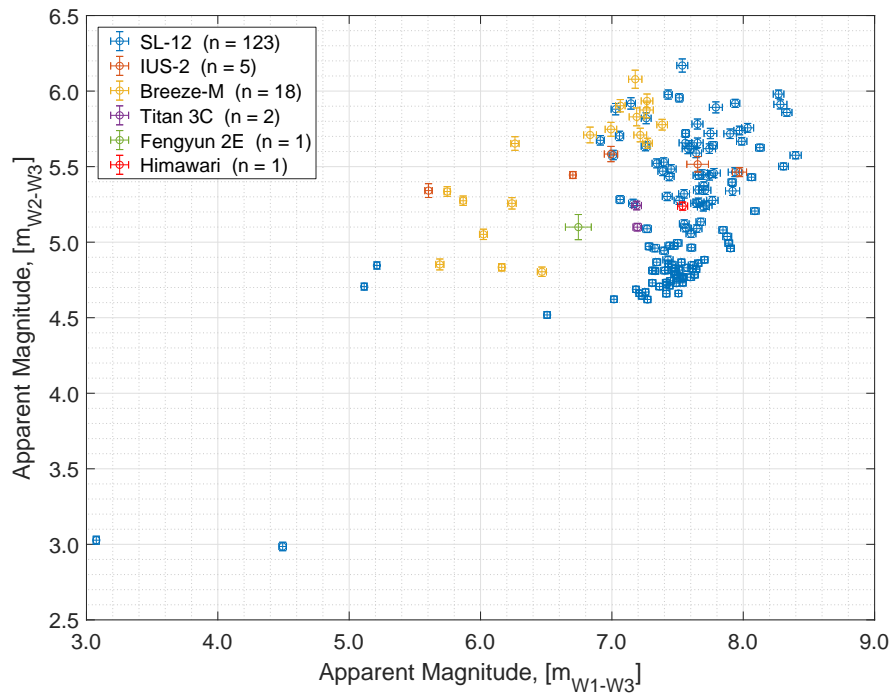
Figure 6.36: The W1-W3 *vs* W2-W3 colour-colour plot shows some ability to differentiate between six rocket body types, in particular SL-12, Titan and Breeze-M.

6.5 Conclusion

This chapter has attempted to utilise data from the 1696 valid streaks detected and analysed by WISEstreakDET. Using the database sources listed in Section 4.10, RSO shape, size, operational status, age and type were examined, using both the magnitudes and colours of measured data.

Several of there characteristics were able to be differentiated through the use of colour-colour plots and index values. These outcomes will be summarised in the following chapter.

The most important outcome from this analysis is that clear conclusions are not yet able to be drawn, as a result of the limited number of observations in the initial subset of WISE imagery that was analysed. The review of literature in Chapter 3 showed that time-resolved light curves provide a more complete representation of RSO characteristics. Nevertheless, WISE imagery shows much promise, and analysis of the full image database is likely to provide a similarly complete representation.

7 Conclusion

Space situational awareness is becoming increasingly important. The escalating number of resident space objects - satellites, rocket bodies and debris - raises the probability of damage to space assets that are heavily relied upon in everyday life. RSOs are monitored and characterised by various sensors, predominantly exploiting the microwave, radio and optical segments of the electromagnetic spectrum.

This thesis focusses upon an evaluation of the infrared regime, to determine ways by which ground or space-based infrared sensors may contribute to space surveillance. To achieve this, a streak detection algorithm was developed to identify serendipitous RSO streaks in WISE imagery. Photometric measurements in the four available WISE bands were then obtained, allowing evaluation of infrared RSO characterisation.

This chapter summarises the main conclusions of the thesis, providing an indication of the utility of infrared SSA sensors. Recommendations for future work are also provided, such that the present research may be built upon.

7.1 Summary of Conclusions

7.1.1 Streak Detection

The algorithm developed for this thesis, WISEstreakDET, was tailored to detect and measure streaks in the WISE database of imagery. The algorithm's ability to detect streaks was evaluated via a comparison to previous research, using the same subset of 82,208 images. Overall, WISEstreakDET detected 1,696 valid GEO streaks, compared to the 861 detected with open source software in previous research.

7.1.1.1 Future Work

Despite detecting an increased number of valid RSO streaks compared to previous research, an additional 928 streaks were detected and deemed invalid. The predominate cause of this was an inability to correlate streaks with a known RSO. An increase in correlations may be achieved via further analysis of optimal cull and correlation radii, as used in the correlation algorithm within WISEstreakDET.

The matched filter algorithm developed by Lévesque et al. [57–62] was not utilised for this research, as there was no a-priori knowledge of RSO position and orbital trajectory in WISE imagery. However, the exceptional ability of this algorithm to detect faint streaks would be beneficial in overcoming the detection issues observed for low SNR streaks in bands W1 and W2. Initial detection of streaks with WISEstreakDET in band W3 could be conducted, with position and orientation data then fed to the matched filter algorithm for detection and measurement in remaining bands.

Development of a new streak detection algorithm that makes use of artificial neural networks, also known as machine learning, is also recommended. Neural networks learn over time - in the context of streak detection, advising the algorithm when it makes a correct or incorrect detection would lead to increases in detection accuracy. This may particularly enhance the ability to identify very faint RSO streaks, that are not detected due to the inherent weaknesses of threshold processes when differentiating signal from background. The level of operator input in the streak detection process may also be greatly reduced, improving the turn around time between image capture and confirmation of streak detection.

7.1.2 Data Validation

To evaluate the validity of WISEstreakDET magnitude measurements, a comparison was made to the magnitudes of a published star catalogue and RSOs in previous research. 3,377 stars were measured using WISEstreakDET, and compared to the published IPAC source catalogue. An average magnitude sigma of 0.04 was observed. Using the same subset of 82,208 images, RSOs measured by WISEstreakDET were then compared to measurements in previous research. An average magnitude sigma of 0.14 was observed.

It was observed that WISEstreakDET, when compared to the IPAC database and previous research, had a tendency to return slightly fainter magnitude measurements. However, the sigma of 0.04 and 0.14 respectively was consid-

ered acceptable, paving the way for research into RSO characterisation in the four WISE bands.

7.1.3 RSO Brightness

A comparison of magnitude between WISE infrared and optical bands clearly showed that similar RSOs appear brighter in IR wavelengths than in the visible spectrum. While bands W3 and W4 were the brightest, observation at these wavelengths requires cryogenic cooling, which adds cost and maintenance considerations to any sensor design comparison. For space-based sensors, depletion of cryogen also limits the available observation window.

The observed advantage over optical sensors shows promise for a multi-band infrared sensor observing wavelengths in the regions of W1 and W2 to be particularly well suited for a space surveillance system aimed at detecting faint objects.

7.1.4 Utility of IR Sensors for SSA

An extensive evaluation of the ability for WISE infrared bands to characterise RSOs was conducted. To achieve this, magnitude histograms and colour-colour plots were created and analysed. WISE photometric measurements were not able to be used to create light curves, as is typically seen in the SSA community for characterisation purposes. However, several notable outcomes were identified that may be used to direct the priorities of future infrared SSA observations.

7.1.4.1 Identification of Bus Shape

A comparison of active box-wing and cylindrical satellites was made, to see if different satellites of the same shape could be distinguished, or if a general ability to determine satellite shape existed. Different cylindrical satellites, due to their generally similar design philosophy, were not able to be distinguished from one another. As a result of the varying design of box-wing satellites, however, a limited ability to differentiate bus types was observed. The variance in WISE colours for BSS-702HP bus types, depending upon their manufacture pre or post an identified design flaw, was of particular interest.

7.1.4.2 Identification of RSO Size

RSO size was evaluated, based upon radar cross section values, to determine if a correlation with WISE photometric magnitude existed. It was

observed that larger satellites typically appeared brighter than smaller satellites, in all four WISE bands. For different satellites of similar size, there was a large distribution in measured magnitude, likely as a result of variation in solar illumination geometry and satellite configuration. However, overall a clear linear relationship between size and magnitude was established.

7.1.4.3   Identification of RSO Operational Status

The operational status of satellites - either active or retired - was compared for both box-wing and cylindrical shaped buses. Following analysis of magnitude histograms and colour-colour plots, it was determined that WISE observations do not provide a definitive ability to differentiate between active and retired satellites. It is predicted that infrared light curves would more clearly show a distinction.

7.1.4.4   Identification of RSO Age

Previous research indicated a correlation between reflective infrared colour and satellite age. It was observed that the longer a retired HS-376 satellite had been in space, the more red (larger) its colour index value. This experiment was repeated for retired HS-376 satellites detected and measured with WISEstreakDET. A similar relationship was observed for colours including the reflective infrared W1 band, however for the thermal infrared bands, the reverse correlation was observed. This outcome may indicate that the reflectivity and emissivity of spacecraft materials change in different ways with age.

Active box-wing satellites, cylindrical satellites and rocket bodies were then evaluated. While the colours of rocket bodies and active cylindrical satellites tended to show a similar relationship to previous research, becoming more red with age, active box-wings exhibited the reverse correlation by becoming more blue. This may be attributed to a variance in ageing of the large, winged solar panels in active box-wings.

7.1.4.5   Identification of RSO Type

Retired box-wing and cylindrical satellites were compared to rocket body types, to establish if an ability existed to differentiate between the different RSO types. While some satellites appeared brighter than all rocket bodies, it was determined that WISE observations do not provide a definitive ability to differentiate between satellites and rocket bodies. Some differentiation

between rocket body types, however, was evident. In particular, SL-12 and Titan rocket bodies tended to occupy a different space of colour-colour plots than Breeze-M rocket bodies. This may be attributed to Breeze-Ms being less than half the size of these other rocket bodies, or a factor of the different surface materials of each.

7.1.4.6 Future Work

The results presented in this thesis represent analysis of just a fraction of the WISE imagery database. In total, almost six million single-exposure images, in the four infrared bands W1 - W4, are available. The next stage of this research involves acquisition of the entire image database. Focus will initially remain within the GEO regime, to build a more complete picture of GEO RSO characteristics in the infrared. In-depth verification of the results presented in this thesis would also then be possible. Of particular interest, due to the increased brightness of RSOs in WISE bands, would be a quantitative analysis of debris populations in the GEO regime.

Following this, research may progress to the detection and measurement of RSOs in other orbital regimes above LEO. Alternative astronomical sensor databases may also be considered, such as those of satellites observing in ultraviolet wavelengths, or the aircraft based NASA Stratospheric Observatory for Infrared Astronomy.

7.2 Concluding Remarks

While several notable observations have been made in this thesis, they are made in the context of the limitations of WISE data. As WISE is not a dedicated SSA sensor, the number of observations for individual RSOs is restricted. So too is the range of solar illumination geometry.

However, the validation of streak detection and photometric measurement performed by WISEstreakDET provides confidence in the initial outcomes presented. Future work, in particular the attainment of infrared light curves, will assist in confirming the validity of these outcomes, and further establish the utility of infrared sensors for space surveillance.

Bibliography

[1]   A. Snow, A. Den Boer, and L. Alexander. Design and Optimization of a Disaggregated Constellation for Space Situational Awareness. In *Proceedings of the 2015 AIAA Conference on Small Satellites*, Logan, UT, USA, 2015.

[2]   M. Skinner, T. Kelecy, S. Gregory, J. Toth, D. Liang, D. Yamanaka, S. Kent, R. Tjoelker, D. Margineantu, A. Allison, et al. Commercial Space Situational Awareness: An Investigation of Ground-Based SSA Concepts to Support Commercial GEO Satellite Operators. In *Proceedings of the 2013 AMOS Technologies Conference*, Maui, Hawai'i, USA, 2013.

[3]   W. Shelton. Sustaining GPS for National Security. Technical report, Air Force Space Command, Los Angeles, CA, USA, 2011.

[4]   T. Kelso. *CelesTrak Satellite Catalog*. Center for Space Standards and Innovation. Retrieved from `https://www.celestrak.com/satcat/search.asp`, August 2017.

[5]   M. Baird. Maintaining Space Situational Awareness and Taking It to the Next Level. Technical report, *Air Force Research Institute*, Maxwell AFB, AL, USA, 2013.

[6]   B. Weeden, P. Cefola, and J. Sankaran. Global Space Situational Awareness Sensors. In *Proceedings of the 2010 AMOS Technologies Conference*, Maui, Hawai'i, USA, 2010.

[7]   J. Forshaw, G. Aglietti, N. Navarathinam, H. Kadhem, T. Salmon, A. Pisseloup, E. Joffre, T. Chabot, I. Retat, R. Axthelm, et al. RemoveDEBRIS: An In-Orbit Active Debris Removal Demonstration Mission. *Acta Astronautica*, 127:448–463, 2016.

[8]   IPAC. *Cool Cosmos: Mulitiwavelength Astronomy*. Caltech Infrared Processing and Analysis Center (IPAC). Retrieved from `http://coolcosmos.ipac.caltech.edu/cosmic_classroom/multiwavelength_astronomy/multiwavelength_museum/m51.html`, March 2018.

[9]   F. R. Chromey. *To Measure the Sky: An Introduction to Observational Astronomy*. Cambridge University Press, Cambridge, UK, 2010.

[10]   K. Witek, T. Piotrowski, and A. Skwarek. Analysis of Polymer Foil Heaters as Infrared Radiation Sources. *Materials Science and Engineering*, 177(15):1373–1377, 2012.

[11]   M. S. Bessell. Standard Photometric Systems. *Annual Review of Astronomy and Astrophysics*, 43:293–336, 2005.

[12]   É. Papp and T. Cudahy. Hyperspectral Remote Sensing. *Geophysical and Remote Sensing Methods for Regolith Exploration*, 144:13–21, 2002.

[13]   S. Price. History of Space-Based Infrared Astronomy and the Air Force Infrared Celestial Backgrounds Program. Technical report, Air Force Research Lab, Hanscom Air Force Base, MA, USA, 2008.

[14]   C. Elachi and J. van Zyl. *Introduction to the Physics and Techniques of Remote Sensing*. Wiley-Interscience, Hoboken, NJ, USA, 2nd edition, 2006.

[15]   W. Rees. *Physical Principles of Remote Sensing*. Cambridge University Press, Cambridge, UK, 3rd edition, 2013.

[16]   S. Howell. *Handbook of CCD Astronomy*. Cambridge University Press, Cambridge, UK, 2nd edition, 2006.

[17]   G. H. Rieke. Infrared Detector Arrays for Astronomy. *Annual Review of Astronomy and Astrophysics*, 45:77–115, 2007.

[18]   D. Joyce. An Introduction to Infrared Detectors. In *National Optical Astronomy Observatory (NOAO) Gemini Data Workshop*, Tucson, AZ, USA, 2010.

[19]   R. Mason, A. Wong, T. Geballe, K. Volk, T. Hayward, M. Dillman, S. Fisher, and J. Radomski. Observing Conditions and Mid-IR Data Quality. In *Observatory Operations: Strategies, Processes, and Systems II*, Marseille, France, 2008.

[20]   M. Macdonald and V. Badescu. *The International Handbook of Space Technology*. Springer Science & Business Media, Berlin, Germany, 1st edition, 2014.

[21]   N. Johnson. Protecting the GEO Environment: Policies and Practices. *Space Policy*, 15(3):127–135, 1999.

[22]   M. Moldwin. *An Introduction to Space Weather*. Cambridge University Press, Cambridge, UK, 1st edition, 2008.

[23]   H. Curtis. *Orbital Mechanics for Engineering Students*. Butterworth-Heinemann, Oxford, UK, 3rd edition, 2013.

[24]   IADC. Space Debris Mitigation Guidelines. Inter-Agency Space Debris Coordination Committee, Retrieved from `http://www.unoosa.org/documents/pdf/spacelaw/sd/IADC-2002-01-IADC-Space_Debris-Guidelines-Revision1.pdf`, 2007.

[25] The European Global Navigation Satellite Systems (GNSS) Service Centre. *Orbital and Technical Parameters*. Retrieved from `https://www.gsc-europa.eu/system-status/orbital-and-technical-parameters`, March 2018.

[26] D. Vallado. *Fundamentals of Astrodynamics and Applications*. Springer, New York, NY, USA, 3rd edition, 2007.

[27] W. Ley, K. Wittmann, and W. Hallmann. *Handbook of Space Technology*. John Wiley & Sons, Chichester, UK, 22nd edition, 2009.

[28] J. Palmer, B. Hennessy, M. Rutten, D. Merrett, S. Tingay, D. Kaplan, S. Tremblay, S. Ord, J. Morgan, and R. Wayth. Surveillance of Space using Passive Radar and the Murchison Widefield Array. In *Proceedings of the 2007 IEEE Radar Conference*, Seattle, WA, USA, 2017.

[29] P. Kervin, D. Hall, M. Bolden, and J. Toth. Phase Angle: What is it Good For? In *Proceedings of the 2010 AMOS Technologies Conference*, Maui, Hawai'i, USA, 2010.

[30] T. Iida. *Satellite Communications: System and its Design Technology*. IOS Press, Tokyo, Japan, 1st edition, 2000.

[31] C. Hoeber. SSL - Yesterday, Today and Tomorrow. In N. Allen and D. Sachdev, editors, *Recent Successful Satellite Systems: Visions of the Future*, chapter 1, pages 1–42. American Institute of Aeronautics and Astronautics, Reston, VA, USA, 2017.

[32] Boeing. *Select Products in Boeing History*. Retrieved from `http://www.boeing.com/history/products/#/space`, January 2018.

[33] J. McDowell. Personal communication. Harvard-Smithsonian Center for Astrophysics. Satellite Database (in preparation), November 2017.

[34] J. McDowell. *Geostationary Orbit Catalog*. Harvard-Smithsonian Center for Astrophysics. Retrieved from `http://www.planet4589.org/space/log/geo.log`, January 2018.

[35] T. Grimwood. Personal communication. The Union for Concerned Scientists (UCS) Satellite Database, January 2018.

[36] B. Wallace, E. Steinbring, G. Fahlman, B. Leckie, T. Hardy, M. Fletcher, M. Pennington, K. Caputa, R. Carlberg, B. Croll, et al. Site Testing for a Far-North Optical/Infrared Telescope. In *Proceedings of the 2008 AMOS Technologies Conference*, Maui, Hawai'i, USA, 2008.

[37] S. Thorsteinson. Space Surveillance from a Microsatellite: Metric Observation Processing from NEOSSat. Master's thesis, Royal Military College of Canada, 2017.

[38] M. Seeds and D. Backman. *The Solar System*. Nelson Education, Boston, MA, USA, 7th edition, 2011.

[39] E. L. Wright, P. R. M. Eisenhardt, A. K. Mainzer, M. E. Ressler, R. M. Cutri, T. Jarrett, J. D. Kirkpatrick, D. Padgett, R. S. McMillan, M. Skrutskie, et al. The Wide-field Infrared Survey Explorer (WISE): Mission Description and Initial On-Orbit Performance. *The Astronomical Journal*, 140(6):1868–1881, 2010.

[40] M. F. Larsen, H. Latvakoski, A. K. Mainzer, S. Schick, and J. Drake. Wide-Field Infrared Survey Explorer Science Payload Update. In *Proceedings of Space Telescopes and Instrumentation 2008: Optical, Infrared, and Millimeter*, Marseille, France, 2008.

[41] NASA. Wide-field Infrared Survey Explorer Launch. Technical report, Jet Propulsion Laboratory, Berkeley, CA, USA, 2009.

[42] F. Liu, W. Irace, and E. Wright. Development and Operation of the Wide-Field Infrared Survey Explorer Mission. In *Proceedings of the 2011 IEEE Aerospace Conference*, Big Sky, MT, USA, 2011.

[43] A. Mainzer, J. Bauer, R. Cutri, T. Grav, J. Masiero, R. Beck, P. Clarkson, T. Conrow, J. Dailey, P. Eisenhardt, et al. Initial Performance of the NEOWISE Reactivation Mission. *The Astrophysical Journal*, 792 (1):30, 2014.

[44] R. M. Cutri, E. L. Wright, T. Conrow, J. Bauer, D. Benford, H. Brandenburg, J. Dailey, P. R. M. Eisenhardt, T. Evans, S. Fajardo-Acosta, et al. *Explanatory Supplement to the WISE All-Sky Data Release Products*. Caltech Infrared Processing and Analysis Center (IPAC). Retrieved from `http://wise2.ipac.caltech.edu/docs/release/allsky/expsup/index.html`, September 2017.

[45] C. H. Lee, P. Seitzer, R. M. Cutri, C. J. Grillmair, and T. Schildknecht. Infrared Photometry of GEO Spacecraft with WISE. In *Proceedings of the 2016 AMOS Technologies Conference*, Maui, Hawai'i, USA, 2016.

[46] IPAC. *ALLWISE Source Catalogue*. Caltech Infrared Processing and Analysis Center (IPAC). Retrieved from `http://irsa.ipac.caltech.edu/cgi-bin/Gator/nph-scan?submit=Select&projshort=WISE`, February 2018.

[47] IPAC. *IRSA Catalog Search Service Application Program Interface (API)*. Caltech Infrared Processing and Analysis Center (IPAC). Retrieved from `https://irsa.ipac.caltech.edu/applications/Gator/GatorAid/irsa/catsearch.html`, September 2017.

[48] IPAC. *IRSA WISE Image Service*. Caltech Infrared Processing and Analysis Center (IPAC). Retrieved from `http://irsa.ipac.caltech.edu/applications/wise/`, July 2017.

[49] D. Bédard, G. A. Wade, and K. Abercromby. Laboratory Characterization of Homogeneous Spacecraft Materials. *Journal of Spacecraft and Rockets*, 52(4):1038–1056, 2015.

[50] J. Keesee. Spacecraft Thermal Control Systems. Technical report, *Massachusetts Institute of Technology*, Cambridge, MA, USA, 2003. URL `https://ocw.mit.edu/courses/aeronautics-and-astronautics/16-851-satellite-engineering-fall-2003/lecture-notes/l23thermalcontro.pdf`.

[51] A. Waszczak, T. Prince, R. Laher, F. Masci, B. Bue, U. Rebbapragada, T. Barlow, J. Surace, G. Helou, and S. Kulkarni. Small Near-Earth Asteroids in the Palomar Transient Factory Survey: A Real-Time Streak-Detection System. *Publications of the Astronomical Society of the Pacific*, 129(973), 2017.

[52] E. Bertin and S. Arnouts. SExtractor: Software for Source Extraction. *Astronomy and Astrophysics Supplement Series*, 117(2):393–404, 1996.

[53] R. Laher, J. Surace, C. Grillmair, E. Ofek, D. Levitan, B. Sesar, J. van Eyken, N. Law, G. Helou, N. Hamam, et al. IPAC Image Processing and Data Archiving for the Palomar Transient Factory. *Publications of the Astronomical Society of the Pacific*, 126(941):674–710, 2014.

[54] R. Laher. Personal communication. Caltech Infrared Processing and Analysis Center (IPAC), September 2017.

[55] G. Vosselman, S. Dijkman, et al. 3D Building Model Reconstruction From Point Clouds and Ground Plans. *International Archives of Photogrammetry Remote Sensing and Spatial Information Sciences*, 34(3): 37–44, 2001.

[56] A. Ciurte and R. Danescu. Automatic Detection of MEO Satellite Streaks from Single Long Exposure Astronomic Images. In *Proceedings of the 2014 IEEE Computer Vision Theory and Applications (VISAPP) Conference*, Lisbon, Portugal, 2014.

[57] M. Lévesque and S. Buteau. Image Processing Technique for Automatic Detection of Satellite Streaks. Technical report, *Defence Research and Development Canada (DRDC) Valcartier*, Quebec, QC, Canada, 2007.

[58] M. Lévesque and S. Buteau. Evaluation of the Iterative Method for Image Background Removal in Astronomical Images. Technical report, *Defence Research and Development Canada (DRDC) Valcartier*, Quebec, QC, Canada, 2008.

[59] M. Lévesque and M. Lelièvre. Improving Satellite-Streak Detection by the Use of False Alarm Rejection Algorithms. Technical report, *Defence Research and Development Canada (DRDC) Valcartier*, Quebec, QC, Canada, 2008.

[60] M. Lévesque. Automatic Reacquisition of Satellite Positions by Detecting Their Expected Streaks in Astronomical Images. In *Proceedings of the 2009 AMOS Technologies Conference*, Maui, Hawai'i, USA, 2009.

[61] M. Lévesque. Image and Processing Models for Satellite Detection in Images Acquired by Space-Based Surveillance-of-Space Sensors. Technical report, *Defence Research and Development Canada (DRDC) Valcartier*, Quebec, QC, Canada, 2010.

[62] Martin P Lévesque. Detection of Artificial Satellites in Images Acquired in Track Rate Mode. In *Proceedings of the 2011 AMOS Technologies Conference*, Maui, Hawai'i, USA, 2011.

[63] B. Wallace, R. Scott, and A. Spaans. The DRDC Ottawa Space Surveillance Observatory. In *Proceedings of the 2007 AMOS Technologies Conference*, Maui, Hawai'i, USA, 2007.

[64] A. Masevich and N. Slovokhotova. Artificial Satellite Tracking: 1957-1967. Technical report, Foreign Technology Division, Wright-Patterson Air Force Base, OH, USA, 1968.

[65] M. Hejduk. Catalogue-Wide Satellite Photometric Behaviour Paradigms. In *Proceedings of the 2013 AMOS Technologies Conference*, Maui, Hawai'i, USA, 2010.

[66] T. Payne, S. Gregory, and K. Luu. Electro-Optical Signatures Comparisons of Geosynchronous Satellites. In *Proceedings of the 2006 IEEE Aerospace Conference*, Big Sky, MT, USA, 2006.

[67] R. Cognion. Observations and Modeling of GEO Satellites at Large Phase Angles. In *Proceedings of the 2013 AMOS Technologies Conference*, Maui, Hawai'i, USA, 2013.

[68] R. Scott and B. Wallace. Satellite Characterization Using Small Aperture Instruments at DRDC Ottawa. In *Proceedings of the 2008 AMOS Technologies Conference*, Maui, Hawai'i, USA, 2008.

[69] R. Scott. *A Method for Optical Tracking of On-Orbit Servicing Operations in Geostationary Orbit Using Speckle Interferometry*. PhD thesis, Carleton University, Ottawa, Canada, 2015.

[70] G. Stokes, C. von Braun, R. Sridharan, and J. Sharma. The Space-Based Visible Program. *The Lincoln Laboratory Journal*, 11(2):205–239, 1998.

[71] J. Stuart, A. Wiseman, and J. Sharma. Space-Based Visible End of Life Experiments. In *Proceedings of the 2008 AMOS Technologies Conference*, Maui, Hawai'i, USA, 2008.

[72] eoPortal. *MSX (Midcourse Space Experiment)*. Earth Observation Portal (eoPortal) Directory. Retrieved from `https://directory.eoportal.org/web/eoportal/satellite-missions/m/msx`, April 2018.

[73] R. Scott, B. Wallace, and D. Bedard. Space-Based Observations of Satellites From the MOST Microsatellite. Technical report, *Defence Research and Development Canada (DRDC) Ottawa*, Ottawa, ON, Canada, 2006.

[74] M. Morton and T. Roberts. Joint Space Operations Center (JSpOC) Mission System (JMS). Technical report, Air Force Space Command, Peterson AFB, CO, USA, 2011.

[75] R. Scott, K. Bernard, and S. Thorsteinson. Combined Space-Based Observations of Geostationary Satellites. In *Proceedings of the 2016 AMOS Technologies Conference*, Maui, Hawai'i, USA, 2016.

[76] H. Walker. A Brief History of Infrared Astronomy. *Astronomy & Geophysics*, 41(5):5–10, 2000.

[77] J. Lambert, T. Osteen, and B. Kraszewski. Determination of Debris Albedo from Visible and Infrared Brightnesses. In *Proceedings of the 1993 International Society for Optics and Photonics Space Debris Detection and Mitigation Conference*, Orlando, FL, USA, 1993.

[78] J. M. Beckers. Daytime Observations With Extra Large Telescopes in the Thermal Infrared Using Laser Guide Star Adaptive Optics. In *Second International Conference on Adaptive Optics for Extremely Large Telescopes*, Victoria, BC, Canada, 2011.

[79] K. Jim, B. Scott, and R. Knox. Simulations of Non-Resolved, Infrared Imaging of Satellites. In *Proceedings of the 2009 AMOS Technologies Conference*, Maui, Hawai'i, USA, 2009.

[80] B. Gibson, K. Jim, R. Cognion, and E. A. Pier. Optical-Infrared Colors of GEO Satellites. In *Proceedings of the 2013 AMOS Technologies Conference*, Maui, Hawai'i, USA, 2013.

[81] M. A. Skinner, R. W. Russell, T. Kelecy, S. Gregory, R. J. Rudy, D. L. Kim, and K. Crawford. Observations in the Thermal IR and Visible of a Retired Satellite in the Graveyard Orbit, and Comparisons to Active Satellites in GEO. *Acta Astronautica*, 105(1):1–10, 2014.

[82] M. A. Skinner, R. W. Russell, R. J. Rudy, D. J. Gutierrez, D. L. Kim, K. Crawford, S. Gregory, and T. Kelecy. Time-Resolved Infrared Spectrophotometric Observations of High Area to Mass Ratio (HAMR) Objects in GEO. *Acta Astronautica*, 69(11):1007–1018, 2011.

[83] M. Skinner, R. Russell, T. Kelecy, S. Gregory, R. Rudy, D. Gutierrez, D. Kim, and K. Crawford. Further Analysis of Infrared Spectrophotometric Observations of High Area to Mass Ratio (HAMR) Objects in GEO. *Acta Astronautica*, 80:154–165, 2012.

[84] S. Lederer, J. Frith, H. Cowardin, and B. Buckalew. NASA Newest Orbital Debris Ground-based Telescope Asset: UKIRT. In *Proceedings of the 2014 AMOS Technologies Conference*, Maui, Hawai'i, USA, 2014.

[85] K. Abercromby, B. Buckalew, P. Abell, and H. Cowardin. Infrared Telescope Facility's Spectrograph Observations of Human-Made Space Objects. In *Proceedings of the 2015 AMOS Technologies Conference*, Maui, Hawai'i, USA, 2015.

[86] S. Lederer, H. Cowardin, B. Buckalew, J. Frith, P. Hickson, L. Pace, M. Matney, P. Anz-Meador, P. Seitzer, E. Stansbery, et al. NASA's Orbital Debris Optical and IR Ground-based Observing Program: Utilizing the MCAT, UKIRT, and Magellan Telescopes. In *Proceedings of the 2016 AMOS Technologies Conference*, Maui, Hawai'i, USA, 2016.

[87] J. Frith, P. Anz-Meador, H. Cowardin, B. Buckalew, and S. Lederer. Near-Infrared Color vs Launch Date: An Analysis of 20 Years of Space Weathering Effects on the Boeing 376 Spacecraft. In *Proceedings of the 2015 AMOS Technologies Conference*, Maui, Hawai'i, USA, 2015.

[88] I. S. Robinson and A. Klier. Wideband Hyperspectral Imaging for Space Situational Awareness. In *Proceedings of the 2006 AMOS Technologies Conference*, Maui, Hawai'i, USA, 2006.

[89] K. J. Albercromby, P. Abell, and E. Barker. Reflectance Spectra Comparison of Orbital Debris, Intact Spacecraft, and Intact Rocket Bodies in the GEO Regime. In *Fifth European Conference on Space Debris*, Darmstadt, Germany, 2009.

[90] E. Gaposchkin and R. Bergemann. Infrared Detections of Satellites with IRAS. Technical report, Massachusetts Institute of Technology Lincoln Lab, Lexington, MA, USA, 1995.

[91] M. Aggarwal, A. Batra, P. Guggilla, M. Edwards, B. Penn, and J. Currie Jr. Pyroelectric Materials for Uncooled Infrared Detectors: Processing, Properties, and Applications. Technical report, NASA Marshall Space Flight Center, Huntsville, AL, USA, 2010.

[92] J. Masiero, A. Mainzer, T. Grav, J. Bauer, R. Cutri, J. Dailey, P. Eisenhardt, R. McMillan, T. Spahr, M. Skrutskie, et al. Main Belt Asteroids with WISE/NEOWISE. I. Preliminary Albedos and Diameters. *The Astrophysical Journal*, 741(2):68–87, 2011.

[93] C. Lee, P. Seitzer, R. Cutri, C. Grillmair, T. Schildknecht, J. Murray-Krezan, and D. Bédard. Distinguishing Active Box-Wing and Cylindrical Geostationary Satellites using IR Photometry with NASA's WISE Spacecraft. In *Proceedings of the 2017 AMOS Technologies Conference*, Maui, Hawai'i, USA, 2017.

[94] C. Paxson, H. E. Snell, J. M. Griffin, K. Kraemer, S. Price, M. Kendra, and D. Mizuno. Space Object Temperature Determination From Multi-Band Infrared Measurements. In *Proceedings of the 2008 AMOS Technologies Conference*, Maui, Hawai'i, USA, 2008.

[95] W. Seniw. LWIR Observations of Geosynchronus Satellites. In *Proceedings of the 1993 Space Surveillance Workshop*, MIT Lincoln Laboratory, Cambridge, MT, USA, 1993.

[96] Gonzalez R., Woods R., and Eddins S. *Digital Image Processing using MATLAB*. Pearson Education, Upper Saddle River, NJ, USA, 1st edition, 2004.

[97] M. Pesenson, I. Pesenson, S. Carey, B. McCollum, and W. Roby. High-Dimensional Data Reduction, Image Inpainting and their Astronomical Applications. In *Proceedings of Astronomical Data Analysis Software and Systems XVIII - ASP Conference Series No.411*, San Francisco, CA, USA, 2009.

[98] J. D'Errico. *inpaint_nans*. MATLAB Central File Exchange, Aug. 2012. https://www.mathworks.com/matlabcentral/fileexchange/4551-inpaint-nans.

[99] B. Wallace. Automated Streak Detection Using Image Segmentation and Moments. Technical report, *Defence Research and Development Canada (DRDC) Ottawa*, Ottawa, ON, Canada, 2016.

[100] K. Wu, E. Otoo, and K. Suzuki. Optimizing Two-Pass Connected-Component Labeling Algorithms. *Pattern Analysis and Applications*, 12(2):117–135, 2009.

[101] Azriel Rosenfeld. Connectivity in Digital Pictures. *Journal of the ACM (JACM)*, 17(1):146–160, 1970.

[102] M. Hu. Visual Pattern Recognition by Moment Invariants. *IRE Transactions on Information Theory*, 8(2):179–187, 1962.

[103] R. Prokop and A. Reeves. A Survey of Moment-Based Techniques for Unoccluded Object Representation and Recognition. *CVGIP: Graphical Model and Image Processing*, 54(5):438–460, 1992.

[104] Min Peng, Chongyang Wang, Tong Chen, and Guangyuan Liu. NIR-FaceNet: A Convolutional Neural Network for Near-Infrared Face Identification. *Information*, 7(4):61, 2016.

[105] W. Yau, D. Kumar, S. Arjunan, and S. Kumar. Visual Speech Recognition Using Image Moments and Multiresolution Wavelet Images. In *Proceedings of the 2006 International Conference on Computer Graphics, Imaging and Visualisation*, Sydney, NSW, Australia, 2006. IEEE.

[106] M. Pawlak. *Image Analysis by Moments : Reconstruction and Computational Aspects*. Oficyna Wydawnicza Politecjmiki Wrocawskiej, Wroclaw, Poland, 2006.

[107] M. Stojmenovic and A. Nayak. Direct Ellipse Fitting and Measuring Based on Shape Boundaries. In *Proceedings of the 2007 Advances in Image and Video Technology Conference*, Santiago, Chile, 2007.

[108] S. Thomas, T. Fusco, A. Tokovinin, M. Nicolle, V. Michau, and G. Rousset. Comparison of Ccentroid Ccomputation Algorithms in a Shack-Hartmann Sensor. *Monthly Notices of the Royal Astronomical Society*, 371(1):323–336, 2006.

[109] A. Vyas, M. Roopashree, and B. Prasad. Advanced Methods for Improving the Efficiency of a Shack-Hartmann Wavefront Sensor. In R. Tyson, editor, *Topics in Adaptive Optics*, chapter 8, pages 167–196. InTech, 2012.

[110] D. Kalman. The Most Marvellous Theorem in Mathematics. *Journal of Online Mathematics and its Applications*, 8, 2008.

[111] S. Smith. *Digital Signal Processing: A Practical Guide for Engineers and Scientists*. Elsevier, Burlington, MA, USA, 2013.

[112] Joint Forces Space Component Commander (JFSCC). *Space-Track*. United States Air Force. Retrieved from `https://www.space-track.org`, August 2017.

[113] Joint Forces Space Component Commander (JFSCC). *API Use Guidelines*. United States Air Force. Retrieved from `https://www.space-track.org/documentation`, November 2017.

[114] F. Hoots and R. Roehrich. Spacetrack Report No. 3: Models for Propagation of NORAD Element Sets. Technical report, *Aerospace Defense Command, United States Air Force*, Colorado Springs, CO, USA, 1980.

[115] R. Scott and B. Wallace. Small Aperture Telescope Observations of Co-located Geostationary Satellites. In *Proceedings of the 2009 AMOS Technologies Conference*, Maui, Hawai'i, USA, 2009.

[116] Q. Funke. Personal communication. European Space Agency, December 2017.

[117] European Space Agency. *Database and Information System Characterising Objects in Space (DISCOS)*. Retrieved from `https://discosweb.esoc.esa.int/web/guest/home`, December 2017.

[118] G. Krebs. *Gunter's Space Page*. Retrieved from `http://space.skyrocket.de`, April 2018.

[119] D. McKnight. Examination of Spacecraft Anomalies Provides Insight Into Complex Space Environment. *Acta Astronautica*, 2017.

[120] H. Cowardin, G. Ojakangas, M. Mulrooney, S. Lederer, and J. Liou. Optical Signature Analysis of Tumbling Rocket Bodies via Laborat ory Measurements. In *Proceedings of the 2012 AMOS Technologies Conference*, Maui, Hawai'i, USA, 2012.

[121] M. Shan, J. Guo, and E. Gill. Review and Comparison of Active Space Debris Capturing and Removal Methods. *Progress in Aerospace Sciences*, 80:18–32, 2016.

Appendices

A Data Analysed Without Merit for Inclusion

A.1 Phase Angle Analysis

The phase angle of measurements taken by WISE was limited, due to the geometry between Sun, observed satellite and WISE sensors. For the initial dataset of images analysed, the minimum observed phase angle was $85.92°$, and the maximum $97.79°$.

Figure A.1 shows magnitude in the four WISE bands as a function of phase angle. Due to the limited range, a clear observation of flux change with varying phase angle was not evident.

(a) W1

(b) W2

(c) W3

(d) W4

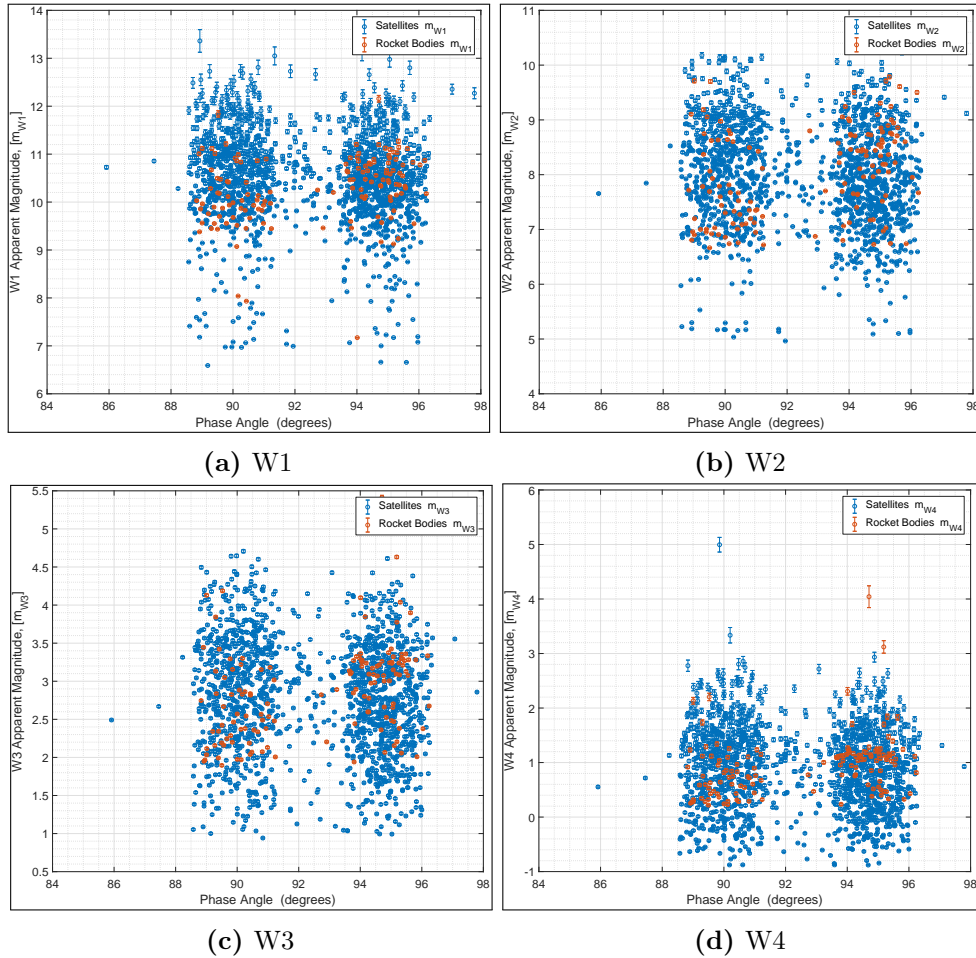**Figure A.1:** Due to the limited range of observational phase angles in WISE imagery, a relationship between flux and phase angle is not evident.

A.2 Time of Year Analysis

Four band WISE imagery in the ALLWISE database was captured in the period between December 2009 and August 2010. An analysis was conducted to determine if macro-level flux variation was evident over this time period.

Figure A.2 shows magnitude in the four WISE bands as a function of image capture date (day of the year). A clear observation of flux change with time was not evident.
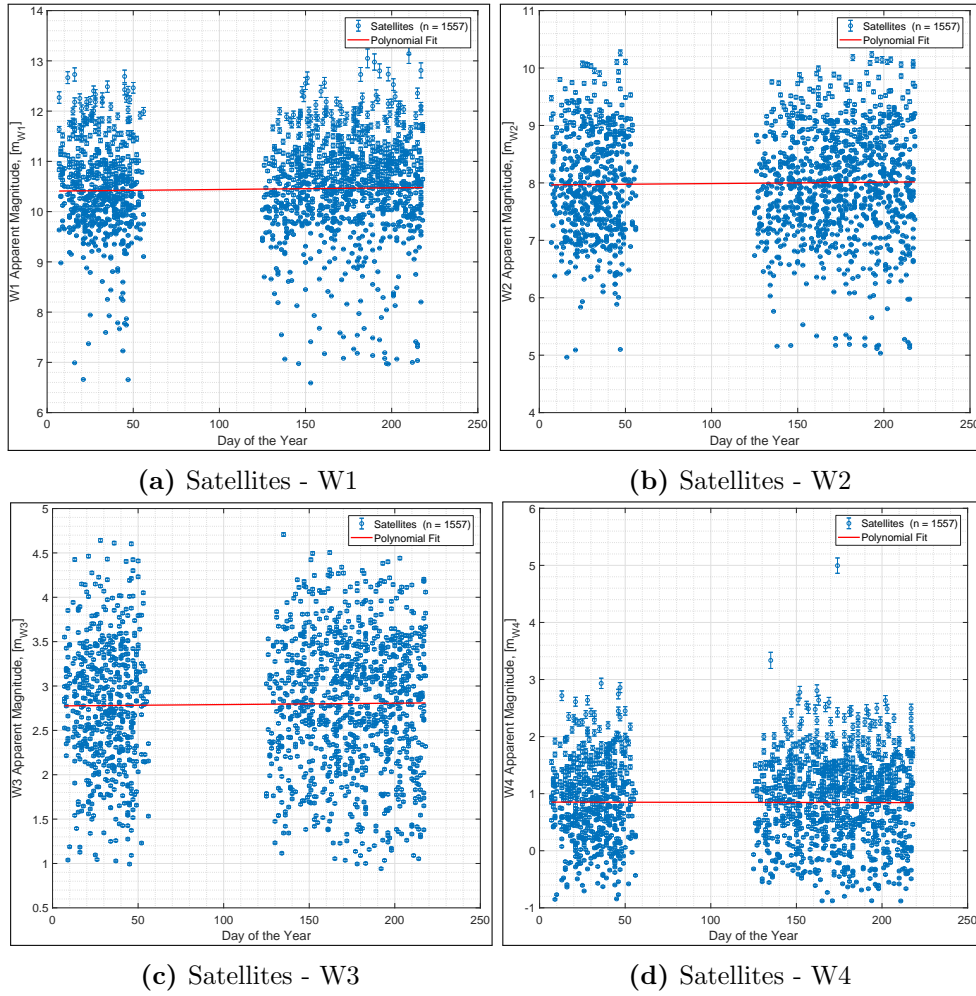
(a) Satellites - W1

(b) Satellites - W2

(c) Satellites - W3

(d) Satellites - W4

Figure A.2: A flux change over the time period of image capture is not evident for satellites.

(a) Rocket Bodies - W1

(b) Rocket Bodies - W2

(c) Rocket Bodies - W3

(d) Rocket Bodies - W4

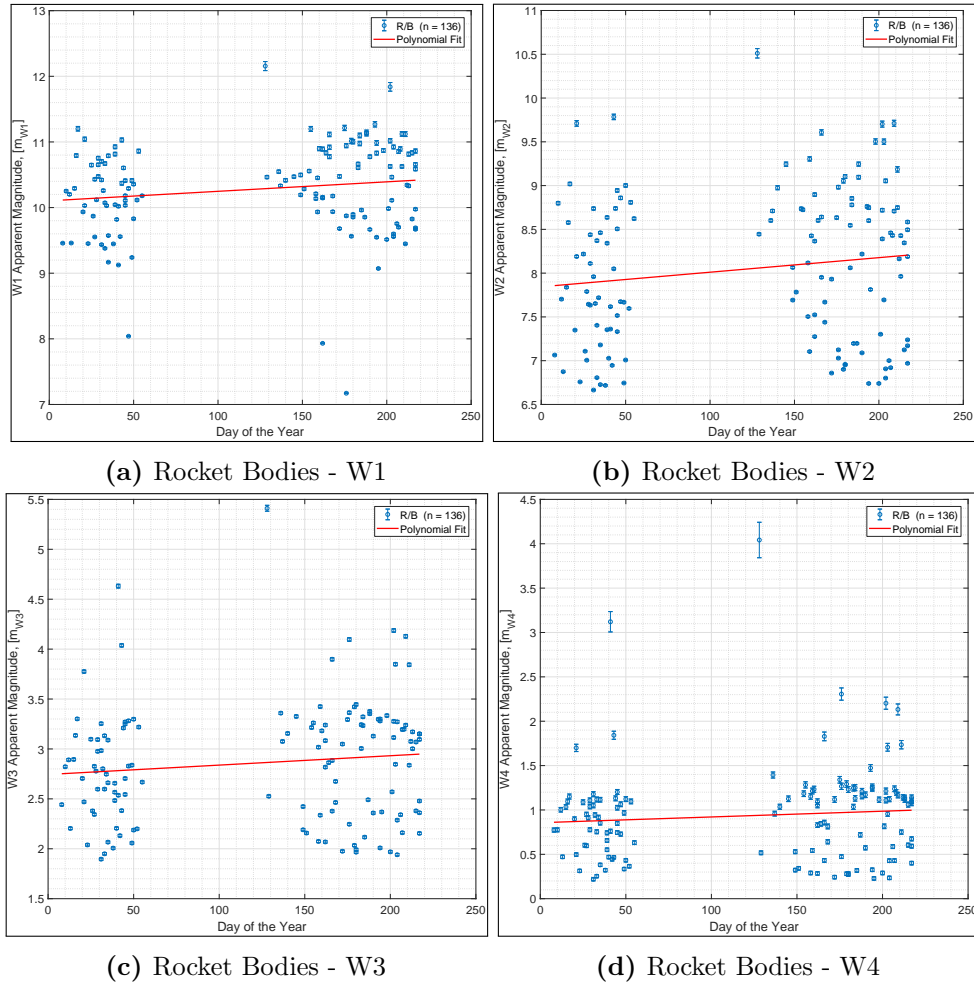**Figure A.3:** A flux change over the time period of image capture is not evident for rocket bodies.

B Curriculum Vitæ

Name:	Joshua Fitzmaurice	
Place of birth:	Devonport, TAS, Australia	
Year of birth:	1984	

Post-secondary education and degrees:	**Master of Science Candidate** Royal Military College of Canada Kingston, ON, Canada	**2016-2018**
	Master of Business Candidate University of New South Wales Canberra, ACT, Australia	**2012-2016**
	Diploma of Project Management Federation Training Sale, VIC, Australia	**2014**
	Advanced Diploma of Air Force Studies School of post-graduate studies, RAAF Wagga Wagga, NSW, Australia	**2012**
	Certificate IV in Training and Assessment Federation Training Sale, VIC, Australia	**2012**
	Bachelor of Science Physics & Mathematics University of New South Wales Canberra, ACT, Australia	**2003-2005**

Employment history:	**Aircrew Training Systems Lead** Capability Acquisition and Sustainment Group Canberra, ACT, Australia	**2015-2016**
	Aviation Standardisation Officer School of Air Warfare Sale, VIC, Australia	**2014**
	Aviation Instructor School of Air Warfare Sale, VIC, Australia	**2011-2013**
	Airborne Tactical Coordinator 11 Squadron Adelaide, SA, Australia	**2007-2011**
Honours and awards:	**Operational Service Medal** **Border Protection**	**2013**
	Afghanistan Medal Operations Slipper and Catalyst	**2010**
	Iraq Medal Operations Slipper and Catalyst	**2008**
	Australian Active Service Medal	**2008**